USGS
science for a changing world

In cooperation with the Interagency Ecological Program
for the San Francisco Bay–Delta Estuary

A Semi-Implicit, Three-Dimensional Model for Estuarine Circulation

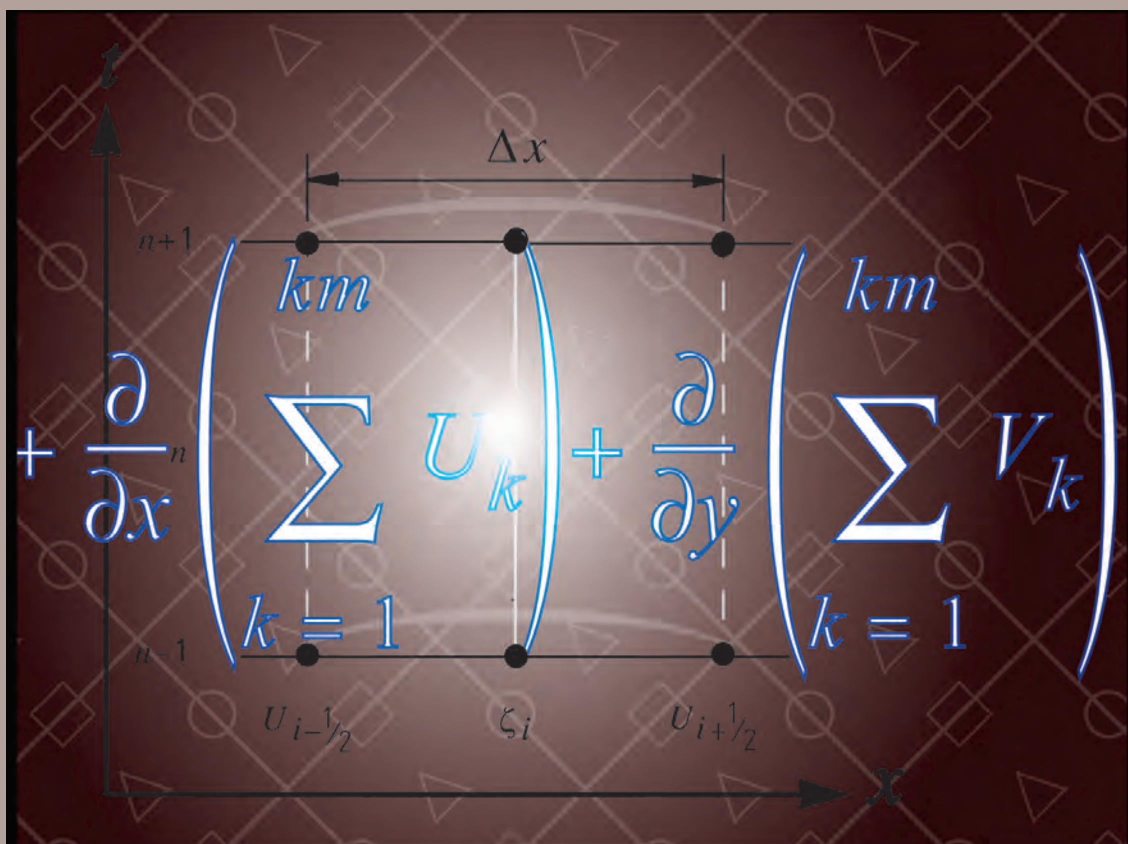

Open-File Report 2006–1004

U.S. Department of the Interior
U.S. Geological Survey

A Semi-Implicit, Three-Dimensional Model for Estuarine Circulation

By Peter E. Smith

Prepared in cooperation with the
Interagency Ecological Program for the San Francisco Bay–Delta Estuary

Open-File Report 2006–1004

U.S. Department of the Interior
U.S. Geological Survey

U.S. Department of the Interior
Dirk Kempthorne, Secretary

U.S. Geological Survey
P. Patrick Leahy, Acting Director

U.S. Geological Survey, Reston, Virginia: 2006
For sale by U.S. Geological Survey, Information Services
Box 25286, Denver Federal Center
Denver, CO 80225

For more information about the USGS and its products:
Telephone: 1-888-ASK-USGS
World Wide Web: http://www.usgs.gov/

Suggested citation: Smith, P.E., 2006, A Semi-Implicit, Three-Dimensional Model for Estuarine Circulation: U.S. Geological Survey Open-File Report 2006–1004, 176 p.

Preface

This report mostly is a republication of a Ph.D. thesis prepared by the author for the University of California, Davis, in 1997. Only minor changes in the original thesis were made; these changes did not change the substance of the report. The reference list and the discussions of the state of knowledge in 3-D estuarine modeling have not been upgraded beyond 1997. The intent of republishing this work is to make its content available in an online format as part of the U.S. Geological Survey Open-File Report series. The version of the computer model described in this report is applicable only to simple rectangular geometries. Since 1997, it has been entirely recoded using the latest (Fortran 95) programming enhancements and generalized for applications to estuaries that have arbitrary geometries, including islands and barriers, and multiple open boundaries. The model has been used successfully in several applications to different parts of the San Francisco Bay–Delta Estuary, California. Although the model was designed mostly to apply to estuaries, the University of California, Davis, has successfully applied it to studies of lakes (Clear Lake and Lake Tahoe, California) also. Additional publications describing the model and its applications will be forthcoming.

This page intentionally left blank.

Contents

Figures

Tables

Acronyms and Abbreviations

ADI, alternating-direction implicit
CFL criterion, Courant-Friedrich-Lewy criterion
ELM, Eulerian-Lagrangian Method
H.O.T., higher order terms
MICCG, modified incomplete Cholesky conjugate-gradient
NSPCG, non-symmetric preconditioned conjugate-gradient
PCGM, preconditioned conjugate-gradient method
RMS, root mean square
RMS_e, root mean square error
UCD, University of California at Davis
USGS, U.S. Geological Survey
1-D, one-dimensional
2-D, two-dimensional
3-D, three-dimensional

cm, centimeter
cm/sec, cm/s, centimeter per second
cm^2/sec, centimeter squared per second
ft, foot
ft^3/s, cubic foot per second
km, kilometer
kg/m, kilogram per meter
kg/m^3/cm, kilogram per cubic meter per centimeter
m, meter
m/s, m/sec, meter per second
m^3/s, cubic meter per second
s, second
sec^{-1}, per second

This page intentionally left blank.

A Semi-Implicit, Three-Dimensional Model for Estuarine Circulation

By Peter E. Smith

Abstract

A semi-implicit, finite-difference method for the numerical solution of the three-dimensional equations for circulation in estuaries is presented and tested. The method uses a three-time-level, leapfrog-trapezoidal scheme that is essentially second-order accurate in the spatial and temporal numerical approximations. The three-time-level scheme is shown to be preferred over a two-time-level scheme, especially for problems with strong nonlinearities. The stability of the semi-implicit scheme is free from any time-step limitation related to the terms describing vertical diffusion and the propagation of the surface gravity waves. The scheme does not rely on any form of vertical/horizontal mode-splitting to treat the vertical diffusion implicitly. At each time step, the numerical method uses a double-sweep method to transform a large number of small tridiagonal equation systems and then uses the preconditioned conjugate-gradient method to solve a single, large, five-diagonal equation system for the water surface elevation. The governing equations for the multi-level scheme are prepared in a conservative form by integrating them over the height of each horizontal layer. The layer-integrated volumetric transports replace velocities as the dependent variables so that the depth-integrated continuity equation that is used in the solution for the water surface elevation is linear. Volumetric transports are computed explicitly from the momentum equations. The resulting method is mass conservative, efficient, and numerically accurate.

1. Introduction

1.1 Background

Estuaries are a valuable natural resource. Each benefits the economy of the surrounding region, is important as habitat for living creatures, and is cherished for scenic and recreational qualities. The exhaustible nature of estuarine resources requires that they be afforded a high level of environmental protection. As centers of population growth, commerce, and industrial development, estuaries frequently are subjected to change related to the human activities that take place within and around their shorelines. Activities such as altering freshwater inflow, dredging channels, reclaiming tidal wetlands, discharging municipal and industrial wastes, and accidentally spilling toxic chemicals can degrade the quality of estuarine waters and adversely affect the biological populations that are part of the estuarine ecosystem. An evaluation of the environmental effects of an estuarine change usually requires an understanding of the physical processes of water circulation and mixing. The distribution and transport of estuarine salts, sediments, contaminants, and certain biological organisms (for example, plankton and larval fish) are governed by circulation and mixing. Water replacement rates (flushing times) in estuaries are determined by the cumulative effects of long-term circulation patterns and mixing processes.

The application of three-dimensional (3-D), hydrodynamic models for studies of circulation and mixing in estuaries and coastal seas is a relatively recent development. Over the last quarter century, advances in the design of numerical methods and the availability of more powerful computers have stimulated an increase in the use and development of 3-D models. Studies of Chesapeake Bay by Blumberg and Goodrich (1990) and Johnson and others (1993), Hudson-Raritan Estuary by Oey and others (1985a, b, c) and Blumberg and Galperin (1990), Delaware Bay by Galperin and Mellor (1990a, b) and Walters (1992, 1997), Galveston Bay by Wang (1994) and Berger and others (1994, 1995), Tampa Bay by Hess (1994), Puget Sound by Chu and others (1989), Massachusetts Bay by Blumberg and others (1993), San Francisco Bay by Smith and Cheng (1990) and Cheng and Casulli (1996), and Upper Narragansett Bay by Muin and Spaulding (1997b) are examples of applying a 3-D model to an estuary or a semi-enclosed bay in the United States. Many additional applications have taken place on estuaries in Europe, Asia, and Canada where efforts toward developing and improving multidimensional, numerical models for simulating shallow-water hydrodynamics have been even more significant than in the United States. With no real slowing in sight to the continued improvement and availability of low-cost computing facilities, the trend toward increasing use of 3-D models is likely to continue.

A significant trend, accompanying that in modeling, has taken place in estuarine hydrography toward the increased use and development of improved field instruments for measuring currents and salinity in estuaries. Instruments, such as shallow-water acoustic Doppler current profilers and fast-response conductivity-temperature-depth profilers, now make it possible to obtain field data on the vertical structure of velocity and salinity in estuaries that are more accurate and have greater vertical resolution than could be obtained previously for a reasonable cost. These advances in field measurements fulfill a critical need for data appropriate for skill assessment of 3-D models; many of the existing applications of 3-D models have been based on insufficient data to supply reasonable confidence in the predictive ability of the model.

Because there exists considerable temporal and spatial variability in the currents and water properties of most estuaries, field measurements alone are rarely dense enough in space and time to describe the circulation and mixing processes adequately; therefore, models are needed to interpret sparse observations. For studies of long-term transport in estuaries, one of the greatest needs is for predictions of water currents that are averaged in such a way as to filter out the tidal oscillations; these tidally averaged currents are referred to as residual currents. Three-dimensional models can be particularly useful for deriving complete distributions of residual currents (residual circulation) and can employ either Eulerian (averaging at a fixed point) or Lagrangian (averaging based on particle tracking) methods. The only other practical alternative to numerical modeling for estuarine investigations is physical scale modeling, which has well-known shortcomings involving both flexibility and cost.

Water motions in estuaries result primarily from the combined forcing of the tides, wind stress at the free surface, rotation of the Earth, and density gradients, caused primarily by salinity gradients. These driving forces are balanced by internal and bottom frictional forces. The simulation of 3-D estuarine flows is based on partial differential equations that describe the conservation of mass, momentum, and salt[1] for a turbulent, incompressible flow with a time-dependent free surface. Water depths in estuaries are generally much smaller than the wave length of the tidal oscillations on the free surface, so the flow is classified as shallow water. In such flows, the change of vertical velocities with time (vertical accelerations) is extremely small, and the vertical equation of motion is replaced by the hydrostatic approximation.

[1]If temperature simulations are considered, then an additional statement for conservation of thermal energy is required.

In the past, some hydrodynamic studies of estuaries have used two-dimensional (2-D) models in which the 3-D governing equations are averaged over either the vertical dimension (vertically averaged models) or the lateral dimension (laterally averaged models). The operation of 2-D models is less computer intensive than 3-D models, and 2-D models generally are easier to program. Studies using 2-D models also can be less time consuming than studies using 3-D models because the need to parameterize and calibrate either the vertical or horizontal mixing processes is avoided. The parameterization of vertical mixing, in particular, is one of the most challenging problems in the application of 3-D models to density stratified flows. Although 2-D models are useful in some applications, they are generally limited by fairly restrictive assumptions. Vertically averaged models require the estuarine density profile to be well mixed vertically. Estuaries typically undergo significant periods of time when they are stratified by freshwater inflows or weak tidal mixing. A vertically averaged model applied to a stratified estuary can compute fictitious horizontal density gradients between waters of different depths that cause significant errors in the model predictions and are difficult to detect; for this reason, applications of vertically averaged models, even to weakly stratified systems, should be avoided. Laterally averaged models require hydrodynamic variables that are homogenous across the estuarine cross section, which in a strict sense rarely exists in real estuaries. Only in estuaries of very small aspect ratio (the ratio of estuarine width to length) should the assumption of lateral homogeneity be considered, and even then the validity of the assumption should be checked.

Because significant variations in currents and salinity occur in all three spatial dimensions in most estuaries, 3-D models are needed. For example, tidal currents in estuaries that flow in opposite directions at different depths or travel in one way near a shoreline and in the opposite way near the center of a channel are not uncommon. The density gradients that occur in estuaries are severe enough to affect the longitudinal and transverse circulations and the vertical mixing. Today hydraulic engineers increasingly are being asked to use models as part of chemical or biological studies to analyze and to predict the transport and mixing of contaminants or biological organisms. In these studies, a model is most valuable when it correctly simulates the actual physical processes causing the transport and mixing of substances and organisms in the estuary under investigation. Because of the different length scales that typically characterize the vertical and horizontal dimensions in most estuaries, the processes of transport and mixing can be separated into those components that vary horizontally but are vertically uniform, and those that vary vertically as well as horizontally. The first category includes residual flows driven by the tides interacting with the estuarine geometry, river inflows, depth-integrated wind-driven flows, and tidal trapping by shoreline irregularities or side embayments (Fischer and others, 1979). The second category includes vertical variations in wind-driven flows, vertical turbulent diffusion of mass and momentum, mixing caused by differential velocities over the water column depth (shear flow dispersion), and the vertical density-driven (or gravitational) circulation (*fig. 1.1*). If both horizontal and vertical processes of transport and mixing are important in an estuary, a 3-D model must be used. If the density-driven circulation is important, the 3-D model equations for the circulation and the salt distribution must be coupled and solved simultaneously. The coupling of equations results in significantly increased running costs of a 3-D model, but usually coupling is required in estuarine modeling. Ultimately, constructing a model that is capable of correctly simulating all the important mechanisms causing transport and mixing in any real estuary is a formidable challenge, but recent progress in 3-D modeling is moving closer to that goal.

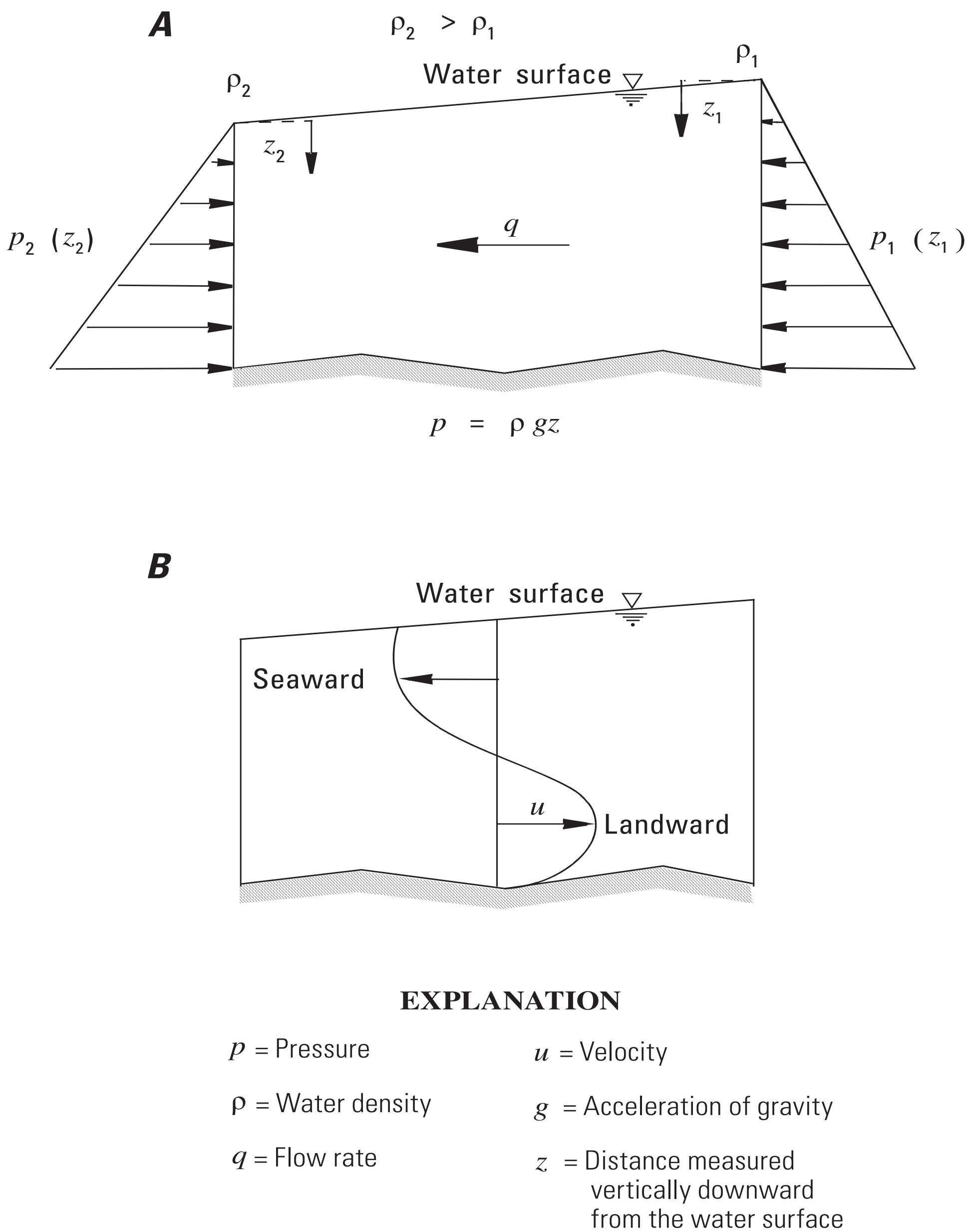

Figure 1.1. Density-driven (gravitational) circulation in an estuary caused by the longitudinal density gradient ($\rho_2 - \rho_1$).
The pressure distribution on the faces of a control volume are shown in *(A)* based on the hydrostatic law ($p = \rho g z$). In the surface layers of the water column, the water surface slope causes the net pressure force to be seaward. In the bottom layer, the effect of the longitudinal density gradient on the pressure distribution causes the net pressure force to be landward. The resulting velocity profile is two-layered, as shown in *(B)*. The importance of the density-driven circulation as a transport mechanism in many estuaries is one reason why a 3-dimensional model is needed. (All quantities shown are tidally-averaged.)

1.2 Objective, Scope, and Organization of this Work

The objective of this report is to describe the development and testing of a new finite-difference method for the numerical computation of 3-D flow in estuaries. The numerical formulation is believed to be an advance over techniques used for existing 3-D hydrodynamic models for estuarine and coastal seas. Because field-scale simulations of estuaries using 3-D models are still constrained by the limitations of modern-day computers, special effort was made to develop an efficient computational scheme that will be useful for lengthy (seasonal) simulations, but without loss of numerical accuracy.

Referring to the computer program here as a model is somewhat premature, despite the use of that term in the title and elsewhere in this report. A model in the engineering sense usually implies a computer program that is ready for applications to real systems. The present computer program is not that far advanced.[2] The program is tested in three dimensions on a closed rectangular basin of constant depth only; the nontrivial task of generalizing the coding to treat estuaries of irregular geometry with open boundaries remains to be accomplished. The speedy accomplishment of this task, however, is planned, and no real difficulties are anticipated.[3] The computer program is intended for eventual use on real systems and was designed and coded with that end result in mind.

The motivation for developing the numerical model described here is eventual use in 3-D (three-dimensional) hydrodynamic simulations of San Francisco Bay and Delta to study the effects of varying amounts of freshwater inflow on circulation and mixing in the estuary. Because the emphasis of this research is applied, more discussion is included that is related to the equation development and the assumptions that are built into the model than would typically be included in a strictly mathematical treatise.

The report is organized into seven chapters. In the next section of this chapter, the progress in 3-D modeling over the last quarter century is reviewed; following that is a discussion of the new 3-D model formulation and its advantages over those already in use. In Chapter 2, the governing equations, boundary conditions, and assumptions and approximations for the estuarine model are discussed thoroughly. In Chapter 3, the model equations are developed for a horizontally layered grid system by averaging the 3-D governing equations over each layer. The layer-averaged formulation of the equations helps to ensure that mass and momentum are conserved in the model. Chapter 4 details the finite-difference formulation used in the model, which is based on a semi-implicit method. The semi-implicit numerical method is introduced in section 4.2 using two different schemes to solve equations for unsteady flow in one dimension; then the complete details for the semi-implicit discretization of the equations in three dimensions are given beginning in section 4.3. Chapter 5 presents the numerical experiments used to test the model, starting with two cases in one dimension followed by one case in three dimensions. The report concludes with a summary (Chapter 6) and the list of references (Chapter 7).

1.3 Acknowledgments

The research for this report was supported under a cooperative agreement between the U.S. Geological Survey and the Interagency Ecological Program for the San Francisco Bay–Delta Estuary. Special thanks are due Randy Brown (retired) of the California Department of Water Resources and Jim Arthur (retired) of the U. S. Bureau of Reclamation for their role in providing the support from their respective agencies. I also thank Henry Wong of the U.S. Bureau of Reclamation who helped with some of the computer graphics and original typing of the report.

[2] Note that "present" refers to 1997 (see Preface).

[3] As of 2006, this task has been completed. The model has been applied to several real estuaries and lakes and tested using a suite of analytical solutions.

As noted in the preface, this report is mostly a republication of the author's Ph.D. thesis prepared for the University of California at Davis (UCD) in 1997. I thank my thesis committee chair at UCD, Professor Bruce E. Larock, for his advice and encouragement during the course of the research and for his valuable reviews of drafts of the manuscript. Professor Ian P. King also provided valuable review comments on the final draft.

I thank Ralph Cheng of the USGS for introducing me to the field of estuarine hydrodynamics and for generously sharing his knowledge of numerical modeling. It was through Ralph Cheng that I met Professor Vincenzo Casulli (University of Trento, Italy) while Vincenzo was on sabbatical leave to the USGS. From Vincenzo I learned much about the semi-implicit numerical scheme; I thank him very much for his generous advice and help. I also thank John Donovan of the USGS for his skillful help with some of the typing and preparation of the figures for the original thesis.

1.4 Progress on Three-Dimensional Modeling

The first 3-D models used to simulate tidal motions in estuaries and coastal seas appeared in the early 1970s (Heaps, 1972; Leendertse and others, 1973; Sündermann, 1975). In the quarter century since that time, significant advances have been made in the fundamental numerical algorithms and equation formulations used in these models. The models of today are more realistic and numerically efficient than those from a quarter century ago.

The earliest 3-D circulation models actually were developed in the 1960s for applications to oceans and lakes. The well known ocean model by Bryan (1969) and the lake model by Liggett (1969) were based on an assumption known as the rigid-lid approximation in which the free surface is held constant and the surface gravity waves (including ocean tides and lake seiches) are filtered out of the solutions. By eliminating the fast-moving gravity waves, these models were able to employ large time steps so that long-term simulations of large regions could be done economically. For studying large-scale oceanic circulation on a coarse numerical grid, rigid-lid models generally are adequate and are still being developed for modern applications (for example, Haidvogel and others, 1991; Gerdes, 1993). For lakes, rigid-lid models should only be used in studies focusing on time periods much longer than the dominant seiching period of the lake (Sheng, 1986b). Sheng and others (1978) compared a rigid-lid model with a model that solves directly for the variable free surface (free-surface model) and showed the rigid-lid model gave poor results for periods of active seiching of Lake Erie under spatially and temporally varying winds. A study by Huang and Sloss (1981) used a rigid-lid model for Lake Ontario and obtained reasonably good results for the mean monthly circulation.

In many estuarine modeling studies, the free-surface tidal motions are themselves of primary interest, and the rigid-lid approximation clearly is not suitable. In modeling studies for which the interest is in residual motions, Nihoul and Ronday (1975) and Durance (1976) pointed out that the tidal motions must be taken into account because of the significant driving force they produce on the residual circulation through nonlinear interactions. Thus in nearly all estuarine and coastal modeling studies, a variable free surface is an essential feature of the model.

Leendertse and others (1973) and Leendertse and Liu (1975, 1977) were the first to develop a 3-D model for estuaries and coastal seas incorporating a fully time-varying free-surface location and using standard finite-difference grid boxes in all three dimensions. This model was noteworthy, not only because it was developed first, but because it was very complete in the equation formulation, including nonlinear friction and advection, the effects of the Earth's rotation, horizontal shear stresses, arbitrary bottom topography, coupled simulation of salt and hydrodynamics, density-gradient forcing, and a physically realistic vertical turbulence parameterization (Leendertse and Liu, 1977). The details of the model formulation were thoroughly described in the series of Rand Corporation reports, which benefitted future investigators in the field. The significant drawback of the Rand model was its explicit,[4] finite-difference scheme that limited the size of the time step to the time a surface gravity wave takes to travel between two adjacent horizontal grid points—a limitation referred to as the Courant-Friedrich-Lewy (CFL or Courant) stability condition for the gravity waves. When using a high resolution numerical grid in an estuary with areas of deep water, this limitation can be very severe. As an example, in an application of the Rand model to San Francisco Bay using a horizontal grid size of $\Delta x = \Delta y = 1$ km, Leendertse and Liu (1975) used a time step of only 15 seconds. Because the 12.4-hour (M_2) tide is the dominant period in San Francisco Bay, a time step of up to one-half hour would theoretically be adequate for temporal resolution of the physics.

[4]An explicit numerical scheme is one in which the unknown hydrodynamic variables at any spatial point at time level n+1 may be computed entirely from known values at neighboring points from one or more previous time levels. In these schemes, each unknown value can be related to known values by a single algebraic equation and found directly (explicitly). In contrast, implicit schemes are ones in which the unknown variables at an entire row or mesh of points are obtained by the simultaneous solution of a system of algebraic equations. In the first version of the Rand model (Leendertse and others, 1973), all terms in the finite-difference equations were treated explicitly. In a later version of the Rand model (Leendertse and Liu, 1977), the vertical diffusion terms were converted to an implicit treatment for stability reasons.

Freeman and others (1972) presented a free-surface model for modeling the Great Lakes. This model generally resembled the Rand model except that the vertical coordinate z was transformed into a new “normalized” coordinate called sigma (σ).[5] The time step for this model was limited by the same gravity-wave CFL stability condition as the Rand model and therefore was not practical for long-term simulations, especially on the computers available at that time.

The model by Heaps (1972, 1974) differed significantly from the other early models in that it avoided the use of grid boxes in the vertical dimension and instead used a spectral method. In the spectral approach, the horizontal components of current are expanded in terms of a set of functions (called the basis set) through the water depth. A 3-D model using the spectral method is reduced essentially to a 2-D model that determines the variation in the coefficients of the basis functions over the horizontal dimension and through time. The spectral method does account directly for the temporal variation in the free surface and improves computational efficiency by reducting the dimension of the problem by one. Because the spectral method can represent the vertical profiles of horizontal currents as continuous functions, it can give superior numerical accuracy over the grid-box method (Davies and Stephens, 1983; Davies, 1991; Davies and Lawrence, 1994). Although efficient and numerically accurate, the early spectral models were not nearly as far advanced in equation formulation as the finite-difference models. The model by Heaps (1972) solved only a linear form of the governing equations and neglected advection, horizontal shear stresses, and density forcing terms. The vertical, internal shear stresses were parameterized with an eddy viscosity that remained constant over the depth and with time. Years later, strategies for obtaining solutions with nonlinearities, stratified density, and variations in the vertical eddy coefficients were devised. Good review papers on the progress in using spectral methods for representing the vertical current structure in 3-D models are by Heaps (1980), Davies (1987), and Davies and others (1997a).

The spectral method also can be used for the horizontal dimension (for example, Krauss and Wubber, 1982), but this approach generally is attractive only if the region being modeled has regular boundaries or can be transformed into one having regular boundaries (Davies, 1987). The set of basis functions in the spectral method can be chosen as piece-wise polynomial functions (either 2-D functions in the horizontal domain or 1-D functions in the vertical domain), in which case the method actually can be regarded as a finite-element method (for example, Koutitas and O’Connor, 1982).

A third category of spectral models uses a spectral approach in the time domain. These 3-D models are usually called harmonic models (for example, Lynch and Werner, 1987; Walters, 1992) and use a frequency-domain numerical scheme to replace the traditional time-stepping approach. Harmonic models also have previously been developed in two dimensions by Pearson and Winter (1977), Le Provost and Poncet (1978), Snyder and others (1979), Walters (1988), and Burau and Cheng (1989) among others. Because models that are spectral in time represent the unknowns of water level and velocity by summing harmonic functions with astronomical tidal frequencies, they are particularly well suited for studying the propagation and interactions of the astronomical constituents of the tide; these models are not particularly well suited for studies that deal with strong nonlinearities and aperiodic forcing.

Although there are many applications for which spectral models are useful, they are still not ideally suited for the most dynamically complex problems involving stratified estuaries with nonlinear effects that require an advanced parameterization of the turbulent processes. Therefore the discussion here is limited mostly to finite-difference models that are considered because of their generality.

[5]The σ transformation is widely used in 3-D models and is discussed in more detail in section 2.6.2 and Appendix C of this report.

In attempting to reduce the computation time of 3-D, explicit, finite-difference models while retaining free-surface effects, a so-called mode-splitting technique has been used by many investigators. Several variations of mode-splitting are used, but in general, mode-splitting is a separation of the 3-D governing equations into a set of equations describing the 2-D depth-mean flow (the external mode) and a set describing the vertical structure of flow (the internal mode). The time discretization for the gravity-wave terms in the external-mode equations can be either explicit or implicit; the internal-mode equations are treated explicitly except for the vertical diffusion terms, which usually are treated implicitly to avoid a time-step limitation in shallow water (Davies, 1985). By using an explicit time discretization for the external-mode gravity-wave terms, the time step must be small enough to satisfy the gravity-wave CFL condition. By applying a time-splitting algorithm, however, the internal-mode solution can be integrated by using a much larger time step than the external mode. Because the internal-mode solution can be expensive in terms of computation time, significant economies are gained by solving the internal mode explicitly with a large time step (usually at least an order of magnitude larger than the time step for the external mode). By using an implicit time discretization for the external-mode gravity-wave terms, the CFL limitation can be avoided, although this advantage is partially offset by the additional complexities involved in an implicit formulation (including the need to solve a matrix system of algebraic equations each time step). Implicit mode-splitting, however, allows the external and internal modes to be solved using the same long time step. Depending on the physical situation and the computer being used (parallel or sequential), either the explicit or the implicit time discretization method may be more computationally efficient with mode-splitting. In either case the use of mode-splitting will usually lead to solutions that are far more computationally efficient than those that solve the primitive 3-D equations directly using a fully explicit scheme.

Mode-splitting refers to models that solve the equations of both modes numerically and retain the three-dimensionality of the governing equations. Some models, such as early ones by Jelesnianski (1970), Forristall (1974), and Nihoul (1977), numerically solve a depth-integrated, 2-D model and then analytically solve a locally 1-D or "point" model for the vertical profiles of currents based on the classic Ekman theory (Welander, 1957); a model proposed by Tee (1979) is similar to these models although somewhat more flexible in the vertical formulation. These simple 3-D models (Tee, 1987) are not mode-splitting models in the sense used here. Because the simple models are constrained by assumptions, they are not suited to shallow-water estuaries that are stratified and involve nonlinear effects.

Simons (1973, 1974, 1980) is credited as the first to introduce the mode-splitting technique for use on modeling the Great Lakes. Later, Madala and Piacsek (1977) used it to develop an ocean model. This method has since been adopted by numerous other investigators for use in 3-D shallow-water circulation modeling (for example, Blumberg and Mellor, 1980, 1987; Wang, 1982; Sheng, 1983; Hess, 1985; Lardner and Smoczynski, 1990; Blumberg, 1991; Johnson and others, 1991; Hamrick, 1992; Jin, 1993; Chapman and others, 1996; Muin and Spaulding, 1997a). In fact, most 3-D shallow-water models now being used are mode-splitting models. The mode-splitting technique is also being implemented for modeling the large-scale circulation of the ocean (Killworth and others, 1991; Dukowicz and Smith, 1994; Semtner, 1995).

Although mode-splitting has become widely accepted in 3-D modeling, it has several important drawbacks that are often overlooked. If an explicit time discretization is used for both modes of a time-splitting scheme, the external mode (2-D) velocities must be the exact depth average of the internal mode (3-D) velocities; otherwise, the computations will become unstable. Dukowicz and Smith (1994) point out that it is necessary when using the explicit-leapfrog, finite-difference scheme to integrate the external-mode equations over a time interval corresponding to twice the internal mode time step to ensure that the time-averaged 2-D variables are properly centered in time and satisfy the continuity equation. Splitting methods, in general, have an increased amount of poorly understood errors associated with them; to keep these errors small, the maximum allowable time step for the internal mode calculations may have to be limited in certain cases. If an implicit time discretization is used for the external-mode gravity waves in a mode-splitting model, time-splitting errors can be eliminated if the external and internal mode time steps are chosen to be equal; however, the separate calculations of the 2-D and 3-D variables lead to difficulties in consistently representing the magnitude of the bottom frictional stress between the external and internal modes. The problem arises because, for consistency (and for true three-dimensionality), the 2-D external-mode equations must include bottom stress as a nonlinear function of the 3-D bottom velocity. The 3-D bottom velocity cannot be used implicitly in the external-mode computations without implementing some form of iteration involving the internal mode. To circumvent this problem, the bottom stress term must remain explicit in the external mode, which in shallow water and in the presence of strong currents can lead to a rather restrictive limitation on the time step for stability.

Instead of mode-splitting, some 3-D modelers have used other forms of splitting methods. For example, the latest versions of the 3-D Rand Corporation model (Leendertse, 1989) and the 3-D TRISULA model from Delft Hydraulics of the Netherlands (Uittenbogaard and others, 1992) are based on one of the best known splitting techniques—the alternating-direction-implicit (ADI) method. These models are basically 3-D extensions of ADI methods successfully used in two dimensions (Leendertse, 1967, 1987; Stelling, 1984). In each of these models, the vertical diffusion is treated implicitly. Leendertse (1989) is especially critical of the use of mode-splitting because it "degrades the accuracy of computation" to first order. The ADI models are formulated using essentially second-order accuracy numerics and are computationally efficient. These models also are unconditionally stable, which allows the use of large time steps. However, for large time steps, the ADI models may cause inaccuracies when dealing with flow domains where the bathymetry is complex, especially where one or more narrow channels within a modeled region are not aligned with the principal directions of the numerical grid. To eliminate these inaccuracies, either the time step or horizontal grid size of a simulation must be decreased, which can have a significant effect on model efficiency. This source of inaccuracy in ADI models is known as the ADI effect (Stelling and others, 1986) and is more likely to be significant in water bodies like estuaries, where typically there are deep-water shipping channels crossing through shoal areas, rather than in the coastal ocean.

A 3-D model presented by de Goede (1991) uses an implicit, time-splitting, finite-difference scheme that does not employ ADI methods so that inaccuracies caused by the ADI effect are absent, even for large time steps. The 3-D scheme has a strong resemblance to the 2-D scheme described in Wilders and others (1988). The 3-D scheme, which neglects advection, density-forcing, and horizontal shear stress terms, is based on a two-stage splitting procedure in which the first stage requires the solution of a large number of independent tridiagonal systems of equations involving the implicit treatment of vertical diffusion. In the second stage, the terms describing the propagation of the surface gravity waves (that is, the water surface pressure gradient in the momentum equations and the velocity divergence in the continuity equation) are treated implicitly. This stage results in a five-diagonal matrix system to be solved for the water surface elevation. Once the water- surface elevation is known, the velocities are computed explicitly. A later version of the model (de Goede, 1992, Chapter 7) includes advective terms, but the time-splitting procedure then is reduced to only first-order accuracy in time for the advection and bottom friction calculations, and the computational efficiency is reduced.

The special approach used by de Goede (1991) for the implicit treatment of the gravity-wave terms is also used in the 3-D finite-difference models of Backhaus (1985) and Casulli and Cheng (1992). These latter two models are referred to as semi-implicit and are appealing because they involve no mode-splitting, ADI, or other splitting procedure and yet still include implicit vertical diffusion. In three dimensions, semi-implicit schemes almost always are preferable, for reasons of computational efficiency, to the alternative of a fully implicit scheme (without splitting). When the 3-D equations are approximated using a fully implicit scheme, a coupled system of nonlinear equations for velocity and surface elevation formed at each time step requires enormous computer resources to solve.[6] For many practical problems, however, there simply is not enough benefit from using an implicit scheme for the advection, Coriolis, baroclinic (density-driven) pressure gradient, and horizontal shear stress terms of the governing equations to justify the extra computational expense (which is considerable). These terms are associated with slower phase speeds than the gravity waves and often do not result in a too-restrictive time step limitation for linear stability when calculated explicitly. Thus, in a semi-implicit, 3-D scheme, these terms are treated explicitly, and only the gravity-wave and vertical diffusion terms are treated implicitly.

Some authors have used the term semi-implicit loosely to refer to any method in which one or more terms in the governing equations are treated implicitly, and one or more terms are treated explicitly. Using this definition, all of the ADI methods can be classified as semi-implicit. Li and Zhan (1993) call their finite-element model semi-implicit, even though only the vertical diffusion and Coriolis terms are treated implicitly. Here, in the current report, semi-implicit is used specifically to refer to the basic approach originating with Kwizak and Robert (1971) in atmospheric modeling (see also Mesinger and Arakawa, 1976; Haltiner and Williams, 1980). The approach is based on treating two groups of terms differently: the gravity-wave terms in the model equations are treated implicitly to avoid the time-step limitation due to the gravity-wave CFL condition and other terms are treated explicitly. For multidimensional models, the gravity-wave terms should be treated implicitly in both horizontal coordinate directions at once, in contrast to the alternating-direction, semi-implicit scheme used by Wolf (1983).

[6]Fully implicit schemes are widely used in one-dimensional (1-D) hydrodynamic models, but only because 1-D problems generally require only minimal computer resources.

For shallow-water modeling, the great benefit of the semi-implicit approach is that the solution for the water surface elevation can be uncoupled from the solution for the velocity by inserting the equations of motion into the divergence terms of the depth-integrated continuity equation. This step results in a single system of linear equations that is solved at each time step for the new surface elevation over the entire domain. The coefficient matrix for the system is symmetric and positive-definite so that the equations can be solved efficiently using an iterative technique, such as the preconditioned conjugate-gradient method. Velocities in this approach are computed explicitly using the newly updated surface elevation. Compared with the fully implicit method (without splitting), the semi-implicit method requires not only considerably less computer time but also less memory and storage and is of similar accuracy. Because the semi-implicit method does not involve any ADI technique, it is not affected by any time-step limitation or inaccuracy related to the ADI effect.

The semi-implicit method has been successfully implemented by many authors in 2-D finite-difference models (for example, Backhaus, 1983; Duwe and others, 1983; Casulli, 1990; Muin and Spaulding, 1996). Benqué and others (1982) and Wilders and others (1988) have used the semi-implicit approach for the propagation of the gravity waves in the context of fully implicit splitting methods in two dimensions. The semi-implicit method has also been used for the 2-D external-mode computations in 3-D mode-splitting models (for example, Madala and Piacsek, 1977; Wang, 1982; Blumberg, 1991; Hamrick, 1992; Muin and Spaulding, 1997a). Muin and Spaulding (1996) comment that the semi-implicit method was preferred over an ADI method in their 2-D applications using nonorthogonal (boundary-fitted) grids; the ADI method gave accurate solutions only for orthogonal or slightly non-orthogonal grid systems.

Casulli and Cheng (1992) made a significant contribution to the implementation of the semi-implicit method in three dimensions. They devised a concise and accurate procedure to include implicit vertical diffusion in the 3-D scheme without resorting to any form of splitting method. Their procedure avoids the inconsistency in the treatment of the bottom frictional-stress condition referred to by Stronach and others (1993, p. 19) regarding an updated version of the Backhaus (1985) 3-D model. Using two executions of a tridiagonal-matrix (double-sweep) algorithm beneath each grid box in the horizontal plane, Casulli and Cheng (1992) formally transform each vertical set of x- and y-momentum equations into a matrix equation for the discrete horizontal velocities in each layer, expressed in terms of the unknown water surface pressure gradients. The matrix equations are then formally substituted into the depth-integrated continuity equation to eliminate the unknown vertical integrals of the 3-D horizontal velocities. The depth-integrated continuity equations for all horizontal grid boxes form a five-diagonal system of equations for the unknown water surface elevations over the entire domain. Once the matrix system for water surface elevation is solved using a conjugate-gradient method, the 3-D velocities are solved explicitly from the momentum equations with the newly determined water surface gradients inserted. The overall computational scheme is quite efficient.

The finite-difference scheme used by Casulli and Cheng (1992) is based on two time levels and uses an Eulerian-Lagrangian method (ELM) with linear interpolation for the treatment of the advective terms in the momentum equations. The scheme uses no coordinate transformations and solves the governing momentum equations in a nonconservative form that is consistent with the use of an ELM. The scheme is basically an extension of an earlier 2-D model by Casulli (1990) that has been used successfully (Cheng and others, 1993; Signell and Butman, 1992). The 3-D scheme has been used successfully for San Francisco Bay (Cheng and Casulli, 1996). A drawback of the Casulli and Cheng (1992) scheme is that it is only first-order accurate in the time discretization, which can cause artificial damping of tidal amplitudes and velocities. Casulli and Cattani (1994) present a modified version of the scheme in which the time discretization for the gradient of the free-surface elevation in the momentum equations and the velocity in the continuity equation can be centered in time, according to Crank and Nicolson (1947), to achieve second-order accuracy for these terms. This modification does improve the overall accuracy of the scheme, but for fully nonlinear problems, the finite-difference momentum equations are still first-order accurate in the advection and Coriolis terms and the bottom friction condition. The depth-integrated continuity equation also is first-order accurate in the representation used for the total depth of flow, which is evaluated backward-in-time. All terms in the two-level scheme could conceivably be centered in time if an iterative procedure was implemented, as will be discussed later. The scheme from Casulli and Cheng (1992) also has been implemented by Stansby and Lloyd (1995).

In this discussion, relatively little has been said regarding 3-D models that use the finite-element method (Zienkiewicz, 1977) for the numerical discretization in the horizontal plane. In general, the research on 3-D modeling has concentrated far more on the finite-difference method than the finite-element method.[7] This emphasis on the finite-difference method may in part be due to a perception that, at least until recently, finite-element models were not fully competitive with finite-difference models in terms of computational efficiency. Because research on the finite-element method for solving free-surface flow problems started much later than research on the finite-difference method, there has been a period in which finite-element models have been "catching up" with the finite-difference models in terms of both accuracy and efficiency. Of course, the advantage of the finite-element method has always been its flexibility in allowing unstructured grid networks that can be employed to represent shoreline curvature better and to increase grid-point density where needed. This advantage has become somewhat less significant, however, with the recent advances in curvilinear-coordinate, finite-difference models.

The progress on 3-D finite-element models followed most of the same trends as for 3-D finite-difference models. Two early 3-D models (Kawahara and others, 1982; Shubinski and Walton, 1982) use explicit time discretizations with simple elements, even though the finite-element method does not lead naturally to explicit procedures; both these models use a multilevel, finite-difference approach in the vertical dimension. The model by Koutitas and O'Connor (1982) uses a time-splitting method (fractional step approach) to separate the horizontal computations from the vertical computations, which are both done using finite elements. The model by King (1985) uses the rather costly approach (in terms of computer time) of solving the nonlinear, 3-D equations using a fully implicit, time-stepping scheme without any form of splitting procedure; to improve computational efficiency of simulations, the model allows the convenient coupling of 1-, 2-, and 3-D elements so that the user can limit the 3-D analysis to the region in

[7] Of seventeen 3-D models surveyed in a review paper by Cheng and Smith (1990), only three used the finite-element method for the numerical discretization in the horizontal plane; the other models used the finite-difference method.

which it is needed. Lynch and Werner (1987) and Walters (1992) chose an efficient spectral (harmonic) approach in the time domain for their 3-D finite-element models. These models separate the horizontal and vertical components of the solution much like mode-splitting models except that no time-stepping is employed. The model by Lynch and Werner (1987) is linear and allows either analytical or numerical (finite- element) solutions in the vertical dimension. The model by Walters (1992) includes nonlinear terms. Lynch and Werner (1991) use mode-splitting in a nonlinear, time-stepping, 3-D finite-element model in which the external mode is solved by way of a semi-implicit method with a wave-equation rearrangement of the governing equations. The wave-equation rearrangement has been prevalent in 2-D modeling (for example, Lynch and Gray, 1979; Kinnmark, 1986) and suppresses short wavelength solution oscillations that have long been the bane of finite-element modelers. In the external mode of the model by Lynch and Werner (1991), the friction and nonlinear part of the water surface slope term must be treated explicitly. A new approach for 3-D modeling has been demonstrated by Luettich and others (1994): velocity is replaced with shear stress as the dependent variable in the internal-mode computations of a mode-splitting, finite-element model. The rationale for changing variables is that, because shear stress normally varies more slowly near sheared boundaries, it can be resolved more readily than velocity. Luettich and others (1994) solve the external mode by using a harmonic model. Additional references on finite-element models can be found in the review papers by Westerink and Gray (1991) and Davies and others (1997).

1.5 The Present [1997] Model

Numerous factors were considered in the design of the 3-D model described herein. Because the model will be used for calculations of the circulation in real estuaries under varying conditions, the equation formulation must be complete, incorporating a time-varying free surface, nonlinearities, and horizontal density-gradient forcing for prognostic purposes (a baroclinic model). The numerical scheme must be flexible enough to accept an advanced turbulence parameterization suitable for stratified flows later and be capable of providing accurate simulations under both periodic forcing from tides and aperiodic forcing by freshwater inflows and the wind. The shallowness of estuarine basins also requires using a quadratic (rather than linear) stress law for the bottom frictional-boundary condition. Owing to these very general requirements, the use of any of the various spectral approaches in time or space was not considered. Because the new 3-D finite-difference techniques (semi-implicit and ADI) obviate the need for mode-splitting to deal efficiently with gravity-wave propagation, the finite-difference approach was chosen for the numerical approximations in the new model.

The objectives in the design of the numerical scheme for the model were that it be efficient for long-term (at least seasonal) simulations of estuaries and second-order accurate in the truncation errors to ensure that solutions are not overly damped or diffused by artificial viscosity. Implementing the numerical scheme using the conservation form of the governing equations for both the flow and salt transport also was considered desirable. Mass and momentum are more readily conserved by the conservation form of the basic equations, and the depth-integrated continuity equation is linear.

Presently, the differences in the computational efficiencies of the new finite-difference, the ADI (Leendertse, 1989; Uittenbogaard and others, 1992), and the semi-implicit (Casulli and Cheng, 1992) methods are difficult to assess and depend on the geometry and hydrodynamic conditions of the particular water body under study. As de Goede (1992) points out, semi-implicit methods require solving a pentadiagonal matrix system using a two-dimensional structure, whereas the ADI schemes solve only simple tridiagonal systems. The ADI schemes, however, may be limited because of geometry to a certain maximum time step for accuracy (the so-called ADI effect). The semi-implicit methods do not suffer from the ADI effect, but they may have a known time-step limitation related to the explicit treatment of other terms. The dependence on geometry and bathymetry by the ADI scheme is a disadvantage because errors due to the ADI effect can go undetected by an unaware user and cause misinterpretation of model results. Ultimately the decision was made to implement the semi-implicit approach in the new model. To simulate the hydrodynamics of a geometrically complex estuary, such as the Suisun Bay region of San Francisco Bay, the semi-implicit scheme may indeed be the most efficient approach.

The semi-implicit scheme implemented herein closely follows the approach outlined by Casulli and Cheng (1992) for the implicit inclusion of vertical diffusion in a 3-D calculation without recourse to mode-splitting. The details of the overall scheme, however, differ from those in Casulli and Cheng (1992) in many significant ways. The time integration used here is a three-time-level, semi-implicit, leapfrog-trapezoidal method. Except for a small amount of first-order error introduced by the uncentered (in time) treatment of horizontal diffusion for stability considerations, the scheme is second-order accurate in the truncation errors of the finite-difference approximations in both space and time. All terms (other than horizontal diffusion), as well as nonlinear coefficients, are centered in time during the leapfrog and trapezoidal steps of the scheme to achieve second-order accuracy in time. The accurate evaluation of the nonlinearities in the equation of motion is important, because nonlinearities have a significant effect on the tidally averaged circulation in shallow estuaries. The governing equations for the multilevel scheme are prepared in a conservative form by integrating them over the height of each layer. The layer-integrated, volumetric transports replace velocities as the dependent variables so that the depth-integrated continuity equation that is used in the solution for the water surface elevation is linear. The advection terms in the momentum and salt-transport equations are solved using explicit, leapfrog-trapezoidal integration rather than an ELM as used by Casulli and Cheng (1992). The leapfrog-trapezoidal approach does very well with the conservation of salt, which can be a problem with the ELM approach. The global matrix solution for water surface elevation in the new model is implemented using the conjugate-gradient method with a modified incomplete Cholesky preconditioner (Axelsson and Lindskog, 1986). This method was selected after testing a number of other preconditioners and acceleration methods.

In the initial design of the 3-D model, it was not obvious whether a two- or three-time-level time-integration scheme would be the better choice for optimal computational efficiency, accuracy, and stability. Both approaches are used in existing semi-implicit models. The nonlinear terms can be time centered in the context of a two-level scheme by iterating to a solution and averaging the old and new time levels. Duwe and others (1983) suggested a two-iteration (two-step) procedure in a 2-D, two-level, semi-implicit model and found it improved accuracy and stability for the simulation of markedly nonlinear flows. Of course, iteration significantly increases the computer time of a model simulation and therefore is costly in three dimensions. A three-level, semi-implicit, leapfrog scheme is attractive because all terms can be readily centered in time without iteration. However, leapfrog schemes have been used extensively in atmospheric modeling and are known occasionally to exhibit instabilities that are thought to be caused by strong nonlinearities; a widely cited example is Lilly (1965, p. 23). To suppress nonlinear instabilities, the addition of an intermittent two-level, trapezoidal step, following a leapfrog step, has been successful (Mesinger and Arakawa, 1976). The combined scheme is referred to as leapfrog-trapezoidal. A semi-implicit, leapfrog-trapezoidal scheme was tested in an early version of the model described herein (Smith and Larock, 1993) and is also used in the 3-D model by Hamrick (1992).

One goal of the research in this report was to investigate two- and three-time-level integration schemes for use in the 3-D, semi-implicit model. The two types of integration schemes were thoroughly tested and compared using numerical experiments with the 1-D equations representing open channel flow; the results are presented in Chapter 5. A similar comparison using the full 3-D equations would have proven too laborious, so it was not pursued. The 1-D testing shows in many instances that the three-level, leapfrog scheme can be used without a trapezoidal step and can provide second-order accuracy with excellent efficiency. With strong nonlinearities present in the bottom friction term, the two-level scheme without iteration gives poor results owing to the first-order approximation of that term. Both schemes are comparable in efficiency and accuracy when iteration is used. Iteration extends the stability of both schemes. On the basis of the 1-D model testing it was decided to use the three-level scheme in the 3-D model. A numerical experiment using the 3-D model is included in Chapter 5.

The 3-D equations solved herein use standard Cartesian coordinates, which were simplest for developing the numerical scheme. A variety of coordinate transformations from the Cartesian system are prevalent today in multidimensional modeling, and these are discussed in some detail in Chapter 2.

The horizontal location of variables on the 3-D numerical grid is the staggered arrangement known as an Arakawa C-grid (Mesinger and Arakawa, 1976). Most of the finite-difference schemes that have been developed for hydrodynamic modeling of estuaries and coastal seas have been based on this grid (Lardner and Song, 1992). It has the advantage that difference quotients are easily centered in space to obtain second-order accuracy. Stelling (1984, p. 102) discusses some of the other advantages of using a staggered grid, versus a nonstaggered grid, in terms of efficiency, minimizing spurious oscillations, and simplicity of implementing boundary conditions.

2. Governing Equations and Boundary Conditions

2.1 Introduction

This chapter develops the governing equations and boundary conditions used in the 3-D circulation model. The assumptions and approximations inherent in the development of the equations are highlighted to ensure that the model is applied properly. In section 2.2, the basic 3-D equations for the instantaneous flow that describe exactly the fluctuating turbulent variables are presented. Because the instantaneous-flow equations have long been recognized as intractable for applications to rivers and estuaries, the time-averaged 3-D equations for the mean-flow (turbulent-averaged) variables are introduced in section 2.3. In this section, the closure problem resulting from the equation-averaging process is discussed, and the concepts of an eddy viscosity and eddy diffusivity are introduced. In section 2.4, the boundary conditions for an estuarine flow are specified. In section 2.5, a scaling analysis is used to estimate the relative magnitude of the various terms in the differential equations for an estuary, using San Francisco Bay as an example. Finally, section 2.6 discusses the horizontal and vertical coordinate transformations that are used in some existing 3-D models. These coordinate transformations are offered only as background because they are not used in the present model.

2.2 Instantaneous-Flow Equations

In estuaries, the flows are almost always turbulent. The exact equations describing the instantaneous turbulent motion originate from the conservation laws for mass, momentum, and salt. These equations are introduced in the following three sections.

The reference frame is a right-handed, Cartesian coordinate system with axes x_i $(i = 1, 2, 3)$ oriented such that the positive x_1-axis is directed horizontally to the east, the positive x_2-axis is directed horizontally to the north, and the positive x_3-axis is directed vertically upward along the line of action of gravity (*fig. 2.1*). In an estuary, the boundary is continuously in motion because of the earth's rotation. It is convenient to choose a reference frame at rest relative to the boundaries of the estuary rather than one that is fixed in space (relative to the fixed stars). The reference frame is therefore chosen to be fixed on the earth's surface and rotating with the earth's axis at an angular velocity Ω equal to 1 revolution per sidereal[8] day (7.29×10^{-5} radian/second).

The horizontal scale of many estuaries is sufficiently large that the earth's rotation will introduce a significant term in the equation of motion. The area is not so large, however, that the curvature of the earth's surface must be considered. The plane $x_3 = 0$ is therefore considered to be a tangent plane to the geoid and coincides with mean sea level.

[8]"One sidereal day = 23 hours 56 minutes 4 seconds = 86,164 seconds is the time required for the earth to rotate once about its axis, relative to the fixed stars. Since the earth revolves about the sun it must turn a little further to point back to the sun and complete one solar day—hence the solar day is a little longer than the sidereal day" (Pond and Pickard, 1986, p. 38).

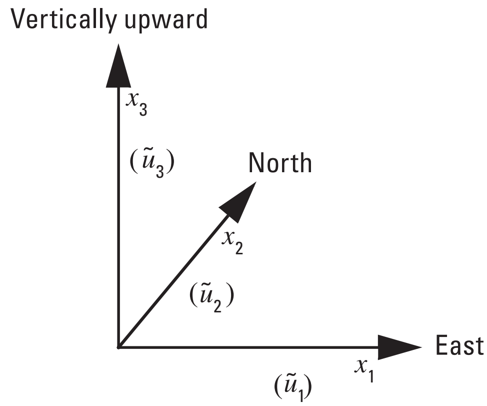

Figure 2.1. Orientation of Cartesian coordinate system with corresponding velocity components $\tilde{u}_i$ (i = 1, 2, 3).

2.2.1 Mass Conservation

The principle of conservation of mass requires the net flux of mass through a control volume fixed to the rotating reference frame to be balanced by the net rate of change of the mass within the volume. The basic differential equation which expresses this principle is (Currie, 1974)

$$\frac{\partial\tilde{\rho}}{\partial t} + \frac{\partial(\tilde{\rho}\tilde{u}_i)}{\partial x_i} = 0\,, \tag{2.1}$$

where

$\tilde{u}_i$ are the instantaneous velocity components,

$\tilde{\rho}$ is the instantaneous density,

x_i are the Cartesian coordinates, and

t is time.

This equation is written using Einstein's summation convention (Spain, 1960) in which a repeated subscript in any term indicates a summation over the three coordinate directions. This convention is used elsewhere in this chapter when it affords greater brevity than other notation.

Because equation 2.1 is written as a partial differential equation, it is assumed that the velocity is a continuous function. For this reason, equation 2.1 is often referred to as the equation of continuity, or simply the continuity equation.

In discussing the continuity equation, it is convenient to introduce the concept of the substantial derivative, which for density is expressed as

$$\frac{D\tilde{\rho}}{Dt} = \frac{\partial\tilde{\rho}}{\partial t} + \tilde{u}_i\frac{\partial\tilde{\rho}}{\partial x_i}\,. \tag{2.2}$$

This expression describes the rate of change in density of a given mass of fluid as it is followed through the flow. Using the substantial derivative, equation 2.1 can be rewritten as

$$\frac{1}{\tilde{\rho}}\frac{D\tilde{\rho}}{Dt}+\frac{\partial \tilde{u}_i}{\partial x_i} = 0 . \tag{2.3}$$

Because the compressibility of water is small, it is usually assumed that $D\tilde{\rho}/Dt = 0$ for water flows of constant density everywhere, so that equation 2.3 can be simplified to

$$\frac{\partial \tilde{u}_i}{\partial x_i} = 0 . \tag{2.4}$$

When the estuarine water density is a function of salinity, temperature, and pressure, it is not correct to equate $D\tilde{\rho}/Dt$ to zero simply by invoking incompressibility. The formal definition of incompressibility requires only that the fluid density not be affected by changes in pressure, which is not equivalent to the statement that $D\tilde{\rho}/Dt = 0$ if the density of the moving fluid element is changed by the molecular conduction of heat or the exchange of water molecules for salt ions. However, for estuaries, these effects are miniscule and can be safely ignored when considering mass or volume conservation. Therefore, equation 2.4 can in fact be used as a good approximation to the instantaneous equation for mass conservation in estuaries.

2.2.2 Momentum Conservation

The principle of conservation of linear momentum arises from Newton's second law of motion and requires that the change of momentum in a control volume fixed to the rotating reference frame be equal to the net influx of momentum into the control volume and the sum of the forces acting on it. In the form of a differential equation, this principle results in the following instantaneous equation of motion for estuaries (Pritchard, 1971a):

$$\frac{\partial(\tilde{\rho}\tilde{u}_i)}{\partial t}+\frac{\partial(\tilde{\rho}\tilde{u}_i\tilde{u}_j)}{\partial x_j} = -\frac{\partial \tilde{p}}{\partial x_i}-2\varepsilon_{ijk}\Omega_j\tilde{\rho}\tilde{u}_k+\tilde{\rho}g_i+\tilde{\rho}\nu\frac{\partial^2\tilde{u}_i}{\partial x_j\partial x_j} , \tag{2.5}$$

where

g_i is the local acceleration of gravity in the direction x_i,

$\tilde{p}$ is the instantaneous pressure,

Ω_j is the component of the angular velocity of the earth in the direction x_j,

ν is the coefficient of (molecular) kinematic viscosity (assumed constant), and

ε_{ijk} is the alternating tensor defined by the relations $\varepsilon_{123} = \varepsilon_{231} = \varepsilon_{312} = 1$, $\varepsilon_{213} = \varepsilon_{132} = \varepsilon_{321} = -1$, and $\varepsilon_{ijk} = 0$ if two or more subscripts are equal.

Equation 2.5 is the famous Navier-Stokes equation in tensor notation including gravitational and Coriolis body-force terms; the tensor equation represents three scalar equations corresponding to the three possible values of the free subscript *i*.

It is common to simplify the two terms on the left side of equation 2.5 by first expanding, using the product rule for differentiation, into the form

$$\tilde{\rho}\frac{\partial\tilde{u}_i}{\partial t} + \tilde{u}_i\frac{\partial\tilde{\rho}}{\partial t} + \tilde{u}_i\frac{\partial(\tilde{\rho}\tilde{u}_j)}{\partial x_j} + \tilde{\rho}u_j\frac{\partial\tilde{u}_i}{\partial x_j}. \tag{2.6}$$

The second and third terms of this expression sum to zero, because they represent the continuity equation (eq. 2.1) multiplied by the velocity. Using this simplification, the equation of motion becomes

$$\tilde{\rho}\frac{\partial\tilde{u}_i}{\partial t} + \tilde{\rho}\tilde{u}_j\frac{\partial\tilde{u}_i}{\partial x_j} = -\frac{\partial\tilde{p}}{\partial x_i} - 2\varepsilon_{ijk}\Omega_j\tilde{\rho}\tilde{u}_k + \tilde{\rho}g_i + \tilde{\rho}\nu\frac{\partial^2\tilde{u}_i}{\partial x_j\partial x_j}. \tag{2.7}$$

On the left side of equation 2.7 are the inertia or acceleration terms that represent the rate of change of linear momentum of a unit volume of the fluid. The first term is a temporal acceleration, and the second is the advective acceleration. The right side of equation 2.7 lists the forces causing the acceleration. The first term is the pressure force term, which in an estuary can result from horizontal gradients in the water surface, density, and atmospheric pressure. The second term is the Coriolis body-force term, which is derived in detail in Appendix A. The Coriolis force is actually a pseudoforce that arises solely as a result of the rotating reference frame. (In an estuary in the northern hemisphere, the Coriolis force acts perpendicular to, and to the right of, the velocity vector; it is proportional to the magnitude of the velocity.) The third term on the right side of equation 2.7 is the gravity body-force term, which in the chosen reference system is defined by $\tilde{\rho}g_i = (0, 0, -\tilde{\rho}g)$. The fourth term is the viscous-shear term and represents internal forces in the fluid resulting from the fluid viscosity.

A widely used approximation to equation 2.7, first introduced by Boussinesq (1903), is known as the Boussinesq approximation. It consists essentially of neglecting variations in density insofar as they affect the mass of the fluid but retaining them where they affect the weight.

To clarify the Boussinesq approximation, the relations $\tilde{\rho} = \rho_0 + \tilde{\rho}'$ and $\tilde{p} = p_0 + \tilde{p}'$ can be substituted into equation 2.7, where ρ_0 and p_0 are the reference values of density and pressure that satisfy hydrostatic equilibrium such that $\partial p_0/\partial x_i = -\rho_0 g_i$, and $\tilde{\rho}'$ and $\tilde{p}'$ are small deviations from the reference values caused by the fluid motion and stratification in combination. The result, after cancelling terms and dividing by ρ_0, is (similar to Turner [1973], p. 9)

$$\left(1+\frac{\tilde{\rho}'}{\rho_0}\right)\left(\frac{\partial\tilde{u}_i}{\partial t} + \tilde{u}_j\frac{\partial\tilde{u}_i}{\partial x_j}\right) = -\frac{1}{\rho_0}\frac{\partial\tilde{p}'}{\partial x_i} - 2\varepsilon_{ijk}\Omega_j\left(1+\frac{\tilde{\rho}'}{\rho_0}\right)\tilde{u}_k + \frac{\tilde{\rho}'}{\rho_0}g_i + \left(1+\frac{\tilde{\rho}'}{\rho_0}\right)\nu\frac{\partial^2\tilde{u}_i}{\partial x_j\partial x_j}. \tag{2.8}$$

Here the density ratio $\tilde{\rho}'/\rho_0$ appears as only a small correction to the inertia, Coriolis, and viscous-shear terms, but it is of great importance to the gravity term where it appears alone. The Boussinesq approximation neglects the effect of density variations in each term except for the gravity term. This simplification allows an average value for the density of the flow to be used in the horizontal momentum equations (x_1- and x_2-directions) where the gravity term is zero; the actual density must be considered only in the x_3-equation. Equation 2.7 with the Boussinesq approximation becomes

$$\rho_0\frac{\partial\tilde{u}_i}{\partial t} + \rho_0\tilde{u}_j\frac{\partial\tilde{u}_i}{\partial x_j} = -\frac{\partial\tilde{p}}{\partial x_i} - 2\varepsilon_{ijk}\Omega_j\rho_0\tilde{u}_k + \tilde{\rho}g_i + \rho_0\nu\frac{\partial^2\tilde{u}_i}{\partial x_j\partial x_j}. \tag{2.9}$$

In a stratified estuarine flow, the lighter (lower density) water near the surface will actually tend to accelerate faster under an applied pressure gradient than the heavier (higher density) water near the bottom. This influence of the vertical density variation on the fluid inertia is neglected in the Boussinesq approximation. For the normal range of stratification in estuaries this is equivalent to less than a 2 percent correction. It therefore appears reasonable to neglect this factor in calculating the inertial response of the flow. A recent evaluation of the Boussinesq approximation in ocean models is given by Mellor and Ezer (1995).

2.2.3 Dissolved Species Conservation

The principle of conservation of salt in an estuary requires the time rate of change in salt mass within a control volume to be balanced by the net flux of salt from the control volume. For a control volume at rest relative to the estuary, the salt flux is composed of both advection (transport by the motion of the fluid) and molecular diffusion (transport by molecular motions). The differential equation expressing the conservation principle for the instantaneous salt concentration $\tilde{s}$ is known as the advection-diffusion equation and may be written as (Fischer and others, 1979)

$$\frac{\partial\tilde{s}}{\partial t} + \frac{\partial(\tilde{u}_i\tilde{s})}{\partial x_i} = \lambda\frac{\partial^2\tilde{s}}{\partial x_i \partial x_i}. \tag{2.10}$$

The coefficient λ is called the molecular diffusivity (assumed constant) and has units of $(\text{length})^2/\text{time}$. The molecular-diffusion term involving λ is based on Fick's law of diffusion (Fischer and others, 1979, p. 30–34), which relates the mass flux to the concentration gradient of the solute. Molecular diffusion is a result of the random scattering of solute particles by the constant motion and collision of molecules in the fluid; in equation 2.10, the rate of molecular diffusion in a moving fluid is assumed to equal the rate for a fluid at rest. In turbulent estuarine flows, the contribution of molecular diffusion to the salt flux is almost always insignificant, and the advection by the instantaneous velocity is the dominant mechanism. In section 2.3.1, the concept of turbulent diffusion is introduced; it is many times more efficient in promoting the mixing of salt than is molecular diffusion.

2.2.4 Equation of State

To close the set of governing equations 2.4, 2.9, and 2.10, an equation of state in the form

$$\tilde{\rho} = f(\tilde{s}, \tilde{\Theta}) \tag{2.11}$$

is needed to relate the density to salinity and temperature $(\tilde{\Theta})$ The density represented by $\tilde{\rho}$ is normally chosen to be the potential density (Pond and Pickard, 1986, p. 8), which is computed as a function of salinity and potential temperature at atmospheric pressure rather than actual temperature. Potential density is used to eliminate any effect of the compressibility of water when comparing water densities at significantly different depths.[9] The equation of state used in the model is given in Appendix B.

[9]The distinction of using potential density instead of actual density is not important in estuaries unless the water depths exceed about 100 m. For a change in pressure of 100 m of water, the density of sea water (s ~ 35) changes by approximately 0.5 kg/m^3, which is roughly equivalent to the effect caused by a change in salinity at constant pressure of 0.6. Because a vertical density distribution caused by the compressibility of water does not affect the water-column stability, the potential density is the correct indicator of stability.

In some cases, the temperature variations in an estuary may be small, in which case the effect of temperature variations on density will be minimal. Under these conditions it is acceptable to specify either a constant or slowly varying temperature distribution rather than compute the temperature distribution using the model. In the model described herein, the temperature distribution is assumed to be constant for the entire water body. Temperature predictions can easily be added to the model by including an equation for the conservation of thermal energy similar in form to equation 2.10, but with $\tilde{\Theta}$ substituted for $\tilde{s}$ and appropriate terms for heat sources and sinks.

2.3 Mean-Flow Equations

Although equations 2.4, 2.9, and 2.10 describe the fluid motion and salt transport for both laminar and turbulent flows, it is not practical to use them in numerical calculations of turbulent flow. Turbulence in estuaries occurs over a wide range of eddy sizes; the largest scales are comparable to the basin dimensions and the smallest scales are determined by the fluid viscosity. The length, time, and velocity scales of the smallest eddies are referred to as the Kolmogorov microscales; for the open ocean, Fischer and others (1979, p. 58) estimate these scales to be about 0.1 cm, 1 s, and 0.1 cm/s, respectively. In an estuarine flow, these scales should be close to the same values. For numerical predictions, it is not practical on even the fastest computers to use such small spatial and temporal increments to determine the motions of the smallest three-dimensional eddies. Fortunately, the details of the fluctuating turbulent motion are rarely of interest in estuarine modeling studies. It is therefore common practice to average the instantaneous-flow and -transport quantities to separate the essentially stochastic (random) motions of the turbulence from the deterministic motions of the mean flow.

One rigorous approach to the averaging of instantaneous quantities is to resort to the statistical method of ensemble averaging as described by Pritchard (1971a) for the 3-D estuarine model equations and as used in formal textbooks on the theory of turbulence (Monin and Yaglom, 1971, 1975). Ensemble averages have the advantage of encompassing all time scales of the stochastic motion, but they have the disadvantage that they cannot be measured in the field or laboratory. Bedford and others (1987) have introduced generalized filtering methods that incorporate high-order averages of the instantaneous quantities over both the space and time dimensions. These generalized filtering methods are theoretically appealing, but they introduce many additional terms into the governing equations that are not conveniently included in a model formulation; further research demonstrating the improvements to real predictions by using generalized filtering methods is needed before their use can be justified.

The averaging that is used here is the conventional time averaging suggested in the late nineteenth century by Osborne Reynolds (Reynolds, 1894). It represents a field situation in which measurements are made at a fixed point in a water body and time averaged over some period (usually minutes) to determine a mean quantity. Reynolds suggested decomposing the instantaneous quantities into mean and fluctuating parts. For the instantaneous velocity, pressure, density, and salinity, the decomposition is

$$\tilde{u}_i = u_i + u'_i \ , \quad \tilde{p} = p + p' , \quad \tilde{\rho} = \rho + \rho' , \quad \tilde{s} = s + s' , \tag{2.12}$$

where the mean quantities are defined by these time averages:

$$u_i = \frac{1}{T}\int_t^{t+T} \tilde{u}_i \, dt \ , \quad p = \frac{1}{T}\int_t^{t+T} \tilde{p} dt \ , \quad \rho = \frac{1}{T}\int_t^{t+T} \tilde{\rho} dt \ , \quad s = \frac{1}{T}\int_t^{t+T} \tilde{s} dt \ . \tag{2.13}$$

The size of the averaging interval T is difficult to prescribe exactly, but in general it must be long compared to the time scale of the individual fluctuations but small compared to the time scale at which the unsteady mean flow is varying. In estuaries where the astronomical tides are a primary source of unsteadiness, the mean flow can vary significantly in just 15 minutes. The minimum required value for T will vary between flows and can truly be determined only by experiment. Indeed, a criticism of the time average is that T cannot always be chosen to include all of the time scales of the stochastic (turbulent) motion. An argument also can be made that an average should be taken in space as well as time to average the instantaneous quantities over the spatial turbulent eddy structure. The Reynolds time average, however, still is used extensively in practice and has not yet been shown to be inadequate in a significant way.

Substituting the relations 2.12 into equations 2.4, 2.9, and 2.10 and time averaging each term in the way indicated by 2.13 yields the mean-flow and transport equations (For details, see most texts on fluid mechanics or turbulence such as Sabersky, Acosta, and Hauptmann, 1971; Hinze, 1975; and Tennekes and Lumley, 1972):

Continuity equation,

$$\frac{\partial u_i}{\partial x_i} = 0 \, ; \tag{2.14}$$

Momentum equation,

$$\rho_0 \frac{\partial u_i}{\partial t} + \rho_0 u_j \frac{\partial u_i}{\partial x_j} = -\frac{\partial p}{\partial x_i} - 2\varepsilon_{ijk}\Omega_j \rho_0 u_k + \rho g_i + \rho_0 \frac{\partial}{\partial x_j}\left(\nu \frac{\partial u_i}{\partial x_j} - \overline{u_i' u_j'} \right) ; \tag{2.15}$$

Salt transport equation,

$$\frac{\partial s}{\partial t} + \frac{\partial u_i s}{\partial x_i} = \frac{\partial}{\partial x_i}\left(\lambda \frac{\partial s}{\partial x_i} - \overline{u_i' s'} \right) ; \tag{2.16}$$

Equation of state,

$$\rho = \mathrm{f}(s, \Theta) \, . \tag{2.17}$$

These equations are identical in form to the instantaneous equations except for the extra terms $\overline{u_i' u_j'}$ and $\overline{u_i' s'}$ that have been introduced by the Reynolds averaging process (the overbar represents the Reynolds time average). These terms originate with the nonlinear advection terms and are non-zero because correlations exist between the fluctuating velocities and between the velocities and salt fluctuations. In a physical sense, these terms, when multiplied by density, represent fluxes of momentum and salt associated with the turbulent fluctuations. The momentum flux acts as an effective stress on the fluid that is analogous to the viscous stress in gases caused by momentum flux associated with molecular fluctuations. The presence of the heretofore undetermined turbulent stress and salt transport terms in the mean flow equations make the number of unknowns greater than the number of equations. Resolving this imbalance between equations and unknowns is the problem of turbulence closure.

2.3.1 Turbulence Closure

Turbulence closure is achieved by introducing additional equations, either algebraic or differential, governing the turbulent stress and salt transport terms. It is possible to use the instantaneous equations to develop additional differential transport equations that describe exactly the behavior of the individual turbulent stress and salt transport terms, but these equations contain new unknowns involving averages of the triple products (triple correlations) of the fluctuating quantities. Transport equations for the triple correlations have also been derived, but quadruple correlations are then introduced and closure is still not obtained. The process of introducing additional higher-order correlation equations can go on indefinitely, but the number of unknowns will always exceed the number of equations until some further approximation is introduced to provide the necessary additional equations to close the system. The infinite system of equations is referred to as the Friedmann-Keller system.

The suite of possible turbulence closure schemes or models is large, and the interested reader is referred to state-of-the-art reviews by Reynolds (1976), Rodi (1980a), and the American Society of Civil Engineers (1988). Reviews of models pertaining specifically to turbulence closure in stratified environmental flows and estuaries are given by Rodi (1980b, 1987), Blumberg (1986), Viollet (1988), and Davies and others (1995, 1997b). A paper by Nunes Vaz and Simpson (1994) compares seven different turbulent closure schemes for the modeling of estuarine stratification.

The most basic classification scheme for turbulence models is based on whether the model employs Boussinesq's (1877) well-known eddy viscosity concept. The models that do not use an eddy viscosity are usually based on approximations to the exact transport equations for the turbulent stresses and are called second-order-closure schemes (Rodi, 1980a, p. 33). Although second-order-closure schemes have great potential and are gaining in popularity, the eddy-viscosity approach is still the most widely used approach and is the approach used here. Among eddy-viscosity models there is a great difference from the simplest to the most complex models. In this report, a complex turbulence model is not introduced because the primary purpose is to present a numerical scheme for the 3-D model equations. Nothing in the numerical scheme, however, presents any conceptual difficulty in introducing a more complex turbulence model later.

The turbulent processes themselves in estuaries are very complex, especially when density stratification occurs. Turbulence can originate near the estuary bed, in the interior of the fluid where density-gradient effects and internal waves are important, and near the free surface caused by wind waves and wind-generated surface drift. For a discussion of the physical processes related to turbulence and mixing in estuaries see, for example, Bowden (1977) and Abraham (1988).

2.3.1.1 Eddy Viscosity

The eddy-viscosity concept is based on an analogy with Stokes' viscosity law for viscous stress in laminar flow. The turbulent stress is equated to a product of the eddy viscosity and a fluid-deformation tensor. For three-dimensional flows this is expressed as (Rodi, 1980a, p.10)

$$-\overline{u'_i u'_j} = \nu_t\left(\frac{\partial u_i}{\partial x_j} + \frac{\partial u_j}{\partial x_i}\right) - \frac{2}{3}K\delta_{ij}\ , \tag{2.18}$$

where

v_t is the eddy viscosity,

δ_{ij} is the Kronecker delta (defined as $\delta_{ij} = 1$ for $i = j$ and $\delta_{ij} = 0$ for $i \neq j$), and

K is the kinetic energy per unit mass of the fluctuating turbulent motion and is equal to $(\overline{u'_i u'_i}/2)$.

Because in estuaries the turbulent stresses per unit mass are almost always much larger than the laminar stresses per unit mass ($\nu\partial u_i/\partial x_j$ in eq. 2.15), the laminar stresses generally are neglected.

Using equation 2.18 to replace the turbulent stress in equation 2.15, the turbulent stress term in the x_1-direction becomes

$$\frac{\partial(-\overline{u_1' u_1'})}{\partial x_1}+\frac{\partial(-\overline{u_1' u_2'})}{\partial x_2}+\frac{\partial(-\overline{u_1' u_3'})}{\partial x_3} \tag{2.19}$$

$$=\frac{\partial}{\partial x_1}\left[2\nu_t\frac{\partial u_1}{\partial x_1}-\frac{2}{3}K\right]+\frac{\partial}{\partial x_2}\left[\nu_t\left(\frac{\partial u_1}{\partial x_2}+\frac{\partial u_2}{\partial x_1}\right)\right]+\frac{\partial}{\partial x_3}\left[\nu_t\left(\frac{\partial u_1}{\partial x_3}+\frac{\partial u_3}{\partial x_1}\right)\right].$$

The kinetic energy per unit mass K is a scalar sum of normal turbulent stresses and therefore acts similar to a pressure. Because the gradient of $\frac{2}{3}K$ generally is small compared to the pressure-gradient term in equation 2.15, it can be neglected. It also is common to neglect the horizontal gradient of the vertical velocity, $\partial u_3/\partial x_1$, in 2.19 because it too is small. The stress terms in the x_1-momentum equation then appear as

$$\frac{\partial}{\partial x_1}\left[2\nu_t\frac{\partial u_1}{\partial x_1}\right]+\frac{\partial}{\partial x_2}\left[\nu_t\left(\frac{\partial u_1}{\partial x_2}+\frac{\partial u_2}{\partial x_1}\right)\right]+\frac{\partial}{\partial x_3}\left[\nu_t\frac{\partial u_1}{\partial x_3}\right]. \tag{2.20}$$

For the x_2-momentum equation, the corresponding result is

$$\frac{\partial}{\partial x_1}\left[\nu_t\left(\frac{\partial u_2}{\partial x_1}+\frac{\partial u_1}{\partial x_2}\right)\right]+\frac{\partial}{\partial x_2}\left[2\nu_t\frac{\partial u_2}{\partial x_2}\right]+\frac{\partial}{\partial x_3}\left[\nu_t\frac{\partial u_2}{\partial x_3}\right]. \tag{2.21}$$

Because the gradients of the turbulent stresses in the x_3-momentum equation are all small compared with the gravitational acceleration g, they generally are neglected entirely.

The expressions 2.20 and 2.21 are one form of the stress terms. Another form for these terms can be obtained by first rearranging the right side of 2.19 (omitting $\partial\left(\frac{2}{3}K\right)/\partial x_1$) as follows:

$$\frac{\partial}{\partial x_1}\left[2\nu_t\frac{\partial u_1}{\partial x_1}\right]+\frac{\partial}{\partial x_2}\left[\nu_t\left(\frac{\partial u_1}{\partial x_2}+\frac{\partial u_2}{\partial x_1}\right)\right]+\frac{\partial}{\partial x_3}\left[\nu_t\left(\frac{\partial u_1}{\partial x_3}+\frac{\partial u_3}{\partial x_1}\right)\right] \tag{2.22}$$

$$=\frac{\partial}{\partial x_j}\left(\nu_t\frac{\partial u_1}{\partial x_j}\right)+\frac{\partial}{\partial x_j}\left(\nu_t\frac{\partial u_j}{\partial x_1}\right)$$

$$=\frac{\partial}{\partial x_j}\left(\nu_t\frac{\partial u_1}{\partial x_j}\right)+\nu_t\frac{\partial}{\partial x_1}\left(\frac{\partial u_j}{\partial x_j}\right)+\frac{\partial u_j}{\partial x_1}\frac{\partial \nu_t}{\partial x_j}.$$

In this last expression, the second term equals zero by the continuity equation (eq. 2.14), and the third term can be neglected if the gradients of the eddy viscosity are assumed to be small.[10] After these simplifications, the stress terms in the x_1- and x_2-momentum equations, respectively, can be written as

[10]In an estuary of large horizontal extent, horizontal gradients of the eddy viscosity generally are small. The vertical gradient of the eddy viscosity, $\partial\nu_t/\partial x_3$, may not be small, but it is multiplied in equation 2.22 by $\partial u_3/\partial x_1$, the horizontal gradient of the vertical velocity, which as noted previously can be neglected.

$$\frac{\partial}{\partial x_1}\left(\nu_t \frac{\partial u_1}{\partial x_1}\right) + \frac{\partial}{\partial x_2}\left(\nu_t \frac{\partial u_1}{\partial x_2}\right) + \frac{\partial}{\partial x_3}\left(\nu_t \frac{\partial u_1}{\partial x_3}\right) \tag{2.23}$$

and

$$\frac{\partial}{\partial x_1}\left(\nu_t \frac{\partial u_2}{\partial x_1}\right) + \frac{\partial}{\partial x_2}\left(\nu_t \frac{\partial u_2}{\partial x_2}\right) + \frac{\partial}{\partial x_3}\left(\nu_t \frac{\partial u_2}{\partial x_3}\right) \quad . \tag{2.24}$$

The form of 2.23 and 2.24 does not preserve the symmetry of the turbulent stress tensor because the right sides of $-\overline{u_1' u_2'} = \nu_t(\partial u_1/\partial x_2)$ and $-\overline{u_2' u_1'} = \nu_t(\partial u_2/\partial x_1)$ are no longer equal as they should be. For this reason, the form of 2.20 and 2.21 sometimes is preferred. It turns out, however, that the loss of symmetry in the stress tensor generally is not a serious concern for estuarine modeling.

When 2.20 and 2.21 or 2.23 and 2.24 is introduced into equation 2.15, the problem of turbulence closure is shifted to that of defining the distribution of the eddy viscosity. Unlike the molecular viscosity, the eddy viscosity is not a fluid property but instead varies throughout the flow field as a function of the length and velocity scales of the turbulent eddies. Because the largest-scale eddies are primarily responsible for the turbulent transport of momentum and salt, these largest eddies influence most the magnitude of v_t. The geometry of the estuary determines to a great extent the size of the largest eddies. Because of the striking disparity between the length scales of the horizontal and vertical dimensions of most estuaries, the intensity and size of the horizontal eddies are much greater than those of the vertical eddies. The turbulent motions under these conditions are said to be anisotropic (direction dependent). It is typical to define separate horizontal and vertical eddy viscosities, A_H and A_V, to account for the anisotropy. The turbulent stress terms in the form of 2.23 and 2.24 then become

$$\frac{\partial}{\partial x_1}\left(A_H \frac{\partial u_1}{\partial x_1}\right) + \frac{\partial}{\partial x_2}\left(A_H \frac{\partial u_1}{\partial x_2}\right) + \frac{\partial}{\partial x_3}\left(A_V \frac{\partial u_1}{\partial x_3}\right) \tag{2.25}$$

and

$$\frac{\partial}{\partial x_1}\left(A_H \frac{\partial u_2}{\partial x_1}\right) + \frac{\partial}{\partial x_2}\left(A_H \frac{\partial u_2}{\partial x_2}\right) + \frac{\partial}{\partial x_3}\left(A_V \frac{\partial u_2}{\partial x_3}\right). \tag{2.26}$$

For estuaries, a possible range of magnitudes is 10^3 to 10^6 cm^2/s for A_H and 1 to 500 cm^2/s for A_V.

Because of the large horizontal extent of flow in most estuaries, the horizontal variations in mean-flow quantities generally are much more gradual than the vertical variations. As a result, the four terms in 2.25 and 2.26 involving horizontal gradients of mean velocities ordinarily are much smaller than the two terms involving vertical gradients. (This will be demonstrated also in Section 2.5 using scale analysis.) Each of the terms in 2.25 and 2.26 represent momentum diffusion due to turbulence in addition to their interpretation as stresses. Horizontal momentum diffusion generally is less significant in estuaries than vertical momentum diffusion.

Some amount of horizontal momentum diffusion must be present in numerical calculations to reproduce horizontal circulations in side bays, as shown theoretically by Flokstra (1976), and through numerical experiments by Ponce and Yabusaki (1980, 1981). For this reason, the horizontal, momentum-diffusion terms should not be omitted from a model even if they are relatively small. In some models, horizontal diffusive transport is introduced through either a diffusive numerical scheme or a smoothing procedure. It is better to choose a numerical scheme that is free of numerical diffusion and introduce a proper amount of physical diffusion with the appropriate terms in the governing equations. Horizontal diffusion terms are easily included in an estuarine model because refined modeling of the distribution of A_H generally is not warranted. For flows with constant or slowly varying geometries, a constant value for A_H often is satisfactory. For flows with more complex geometries, approaches such as those proposed in papers by Smagorinsky and others (1965) and Leith (1968) that relate the magnitude of A_H to the size of the largest eddies being resolved by a model and to the local deformation field or vorticity, respectively, can be used.

The assumption of a constant vertical eddy viscosity generally is not adequate for a realistic description of the vertical, turbulent-momentum diffusion in estuaries. In open channel flows that are steady and neutrally buoyant (unstratified), theory and experiment show that A_V has a nearly parabolic distribution over the depth with the maximum value occurring near mid-depth (Nezu and Rodi, 1986). In a density stratified flow, A_V is reduced near the stratification so that the vertical distribution becomes bimodal, with maxima above and below the density gradient and a minimum at the gradient itself (Bowden, 1977). The effect of stratification can be represented by empirical stability functions Φ_M of the type

$$A_V = A_{V_0}\,\Phi_M(Ri) \quad , \tag{2.27}$$

where A_{V_0} is the neutral value of the eddy viscosity without stratification and Ri is the gradient Richardson number defined as

$$Ri = -\frac{g}{\rho}\frac{\partial\rho}{\partial x_3}\left[\left(\frac{\partial u_1}{\partial x_3}\right)^2 + \left(\frac{\partial u_2}{\partial x_3}\right)^2\right]^{-1} . \tag{2.28}$$

The Richardson number represents a ratio of gravity to inertial forces and characterizes the importance of buoyancy effects. The subscript M in equation 2.27 identifies the stability function for momentum diffusion which can be expressed in the form

$$\Phi_M(Ri) = (1+\beta_1 Ri)^{\alpha_1} \tag{2.29}$$

as proposed by Munk and Anderson (1948).[11] In equation 2.29, β_1 and α_1 are coefficients that generally are chosen to fit whatever data is available. A review by Delft Hydraulics Laboratory (1974) reports that values of $\beta_1 = 10$ and $\alpha_1 = -0.5$, used by Munk and Anderson (1948), best fit most of the experimental data available for large Ri ($Ri \geq 0.7$); for $Ri < 0.7$, the scatter in the data was so great that no best fit could be selected. Because values of Ri below 0.7 are common in environmental flows, it is understandable that numerous values for β_1 and α_1 have been reported in the literature. Blumberg (1986, p. 87, table 4.1) gives a partial summary of previously reported values for β_1 and α_1.

The vertical distribution of A_{V_0} in equation 2.27 can be determined by using the well-known mixing-length model that originated with Prandtl (1925). The mixing-length model relates the eddy viscosity under unstratified conditions to the gradients of velocity in the mean flow and a single parameter known as the mixing length Λ. For general 3-D flows, the mixing-length model is (Rodi, 1980, p. 18)

[11]Other functional forms for Φ_M have been given by Blumberg (1977) and Henderson-Sellers (1982), but these have not been as widely used as 2.29.

$$A_{V_0} = \Lambda^2\left[\left(\frac{\partial u_i}{\partial x_j} + \frac{\partial u_j}{\partial x_i}\right)\frac{\partial u_i}{\partial x_j}\right]^{1/2}. \quad (2.30)$$

For flows where the most significant velocity gradients are the vertical gradients, $\partial u_1/\partial x_3$ and $\partial u_2/\partial x_3$, the expression can be approximated by

$$A_{V_0} = \Lambda^2\left[\left(\frac{\partial u_1}{\partial x_3}\right)^2 + \left(\frac{\partial u_2}{\partial x_3}\right)^2\right]^{1/2}. \quad (2.31)$$

The mixing-length Λ can be a parameter adjusted during model calibration or defined beforehand by using the following formula for unstratified, open channel flow:

$$\Lambda = \kappa z'\left(1 - \frac{z'}{H}\right)^{1/2}, \quad (2.32)$$

where

κ is the von Kármán constant (~ 0.41),

z' is the vertical distance measured from the estuarine bottom to the point considered, and

H is the total water depth.

Equation 2.32 is derived by assuming the logarithmic velocity law for steady, open-channel flow (Keulegan, 1938) applies over the entire depth of flow.[12] Even without density stratification, the velocity profiles in unsteady, estuarine flows are often non-logarithmic owing to the effects of accelerations and secondary currents that are induced by a non-uniform channel geometry or transverse density gradients. Velocity profiles are also affected if flows are carrying sufficiently high sediment loads that sediment grains in suspension damp the vertical components of turbulent fluctuations. For these reasons, equation 2.32 must be considered as approximate for use in estuaries.

Wind blowing across an estuary can affect the magnitude of the eddy viscosity by inducing vertical shear in the horizontal velocities ($\partial u_1/\partial x_3$ and $\partial u_2/\partial x_3$) from surface drift and by causing surface waves that produce oscillatory water motions. The effect of velocity shear on the eddy viscosity is incorporated in equation 2.31 as the shear is developed from the wind stress boundary condition imposed at the free surface. Wind-wave effects, however, must be simulated by a separate wave-current interaction model such as those discussed by Grant and Madsen (1979, 1986), Spaulding and Isaji (1987), Signell and others (1990), and Davies and others (1993). Wind waves in estuaries generally have periods below 10 seconds so their effect on water movements is within the time scale considered as turbulence. Water movements are influenced by surface waves to a depth below the free surface of about one-half their wave length. In shallow water, if wave-induced oscillatory water motions are non-zero at the estuarine bottom, the turbulence is enhanced, which in turn effects bottom friction and ultimately the wind-driven flow field (Davies and others, 1993). Wave conditions are a function of wind speed, duration, and fetch, so a separate wave model is needed for hydrodynamic simulations to predict wave conditions from meteorological data and information on the geometry of the water body. Because the formulations for wave and wave-current interaction models are rather specialized subjects, they are not considered here. However, for realistic applications of a 3-D estuarine model during wind conditions (especially in shallow waters), a wind-wave component should be included in the model.

[12]Nezu and Rodi (1986, p. 338, eq. 10) have refined equation 2.32 by including a wake function in the region away from the boundary ($z'/H > 0.2$) to account for deviations from the logarithmic law in steady, open-channel flow. The Nezu and Rodi refinement is not needed here, considering the approximate nature of equation 2.32 for estuarine flows.

2.3.1.2 Eddy Diffusivity

The turbulent transport of mass (in this case salt) in estuaries is closely analogous to the turbulent transport of momentum. The analogy, referred to as the Reynolds analogy, is indicated by the similar roles played by the mass flux term $\overline{u'_i s'}$ in equation 2.16 and the momentum flux term $\overline{u'_i u'_j}$ in equation 2.15 (Sayre, 1975). Similar to the way in which the eddy viscosity is introduced with equation 2.18 by relating the turbulent transport of momentum to the gradients of mean velocity, an eddy diffusivity is introduced to relate the turbulent transport of salt to the gradient of the salt concentration

$$\overline{u'_i s'} = D\frac{\partial s}{\partial x_i}, \tag{2.33}$$

where D is the eddy diffusivity for salt mass.

The numerical value of D, like the eddy viscosity, depends on the direction of the turbulent transport, and therefore horizontal and vertical eddy diffusivities, D_H and D_V, are defined.[13] The turbulent salt flux terms in equation 2.16 then become

$$\frac{\partial}{\partial x_i}(-\overline{u'_i s'}) = \frac{\partial}{\partial x_1}\left(D_H\frac{\partial s}{\partial x_1}\right) + \frac{\partial}{\partial x_2}\left(D_H\frac{\partial s}{\partial x_2}\right) + \frac{\partial}{\partial x_3}\left(D_V\frac{\partial s}{\partial x_3}\right). \tag{2.34}$$

For estuaries, a possible range of magnitudes is 10^3 to 10^6 cm^2/s for D_H and 10^{-1} to 500 cm^2/s for D_V. Because the molecular diffusivity for salt ($\lambda \sim 10^{-5}$ cm^2/s) is at least four orders of magnitude smaller than the smallest possible eddy diffusivity, the molecular diffusion term in equation 2.16 can safely be neglected.

The values of the horizontal and vertical eddy diffusivities can be related to the corresponding values of the eddy viscosities by defining horizontal and vertical turbulent Schmidt numbers

$$Sc_H = \frac{A_H}{D_H} \quad \text{and} \quad Sc_V = \frac{A_V}{D_V}. \tag{2.35}$$

When momentum transfer is unaffected by mass transfer, it can be assumed that the Reynolds analogy is complete and the Schmidt numbers equal unity. For estuaries, $Sc_H = 1.0$ is generally a reasonable assumption, but the vertical mass transfer of salt can cause significant vertical density stratification that alters the momentum transfer and the value of Sc_V. To account for the variation in Sc_V, a separate stability function for salt diffusion can be introduced as

$$D_V = D_{V_0}\Phi_s(Ri), \tag{2.36}$$

[13] D is actually a second rank, symmetric tensor, D_{ij}. If the coordinate axes are chosen to coincide with the principal axes of the flow (and therefore the principal axes of the diffusion tensor), the tensor is diagonal, although not isotropic, in which case

$$D_{ij} = \begin{bmatrix} D_H & 0 & 0 \\ 0 & D_H & 0 \\ 0 & 0 & D_V \end{bmatrix}.$$

where D_{V_0} is the neutral value of the eddy diffusivity without stratification. By using the Reynolds analogy, D_{V_0} can be equated to A_{V_0} as defined by equation 2.31. The form of $\Phi_s(Ri)$, as proposed by Munk and Anderson (1948), is

$$\Phi_s(Ri) = (1 + \beta_2 Ri)^{\alpha_2}, \tag{2.37}$$

where β_2 and α_2 are coefficients chosen by Munk and Anderson: $\beta_2 = 3.33$ and $\alpha_2 = -1.5$. The numerical values for β_2 and α_2 are not universal constants, and in all cases they should be checked against available data and adjusted as necessary. According to 2.29 and 2.37 (and using the coefficients chosen by Munk and Anderson [1948]), the vertical turbulent Schmidt number Sc_V increases with Ri and with the amount of stable stratification. Officer (1977, p. 17, table 1.2) published values from six estuaries for the inverse of the vertical turbulent Schmidt number ($= D_V/A_V$) which, when inverted into Schmidt numbers, lie in the range of 10 to 0.83.[14] For a Richardson number of 0.5, the Munk and Anderson formulas predict that $Sc_V = 1.8$.

2.3.2 Treatment of the Pressure Term

The shallow-water flows considered herein are assumed to be essentially horizontal and, therefore, vertical accelerations and velocities are negligible compared to gravity. As a result of this assumption, only the pressure and gravity terms are retained in the x_3-momentum equation, which then reduces to the hydrostatic pressure equation.[15] The Coriolis terms in the horizontal momentum equations that involve the vertical velocity u_3 can also be neglected, as discussed in Appendix A. By incorporating these simplifications and representing the turbulence fluxes as shown previously, equations 2.14 to 2.16 can be written in coordinates $(x, y, z) = (x_1, x_2, x_3)$ as

$$\frac{\partial u}{\partial x} + \frac{\partial v}{\partial y} + \frac{\partial w}{\partial z} = 0, \tag{2.38}$$

$$\frac{\partial u}{\partial t} + \frac{\partial uu}{\partial x} + \frac{\partial uv}{\partial y} + \frac{\partial uw}{\partial z} - fv = -\frac{1}{\rho_0}\frac{\partial p}{\partial x} + \frac{\partial}{\partial x}\left(A_H\frac{\partial u}{\partial x}\right) + \frac{\partial}{\partial y}\left(A_H\frac{\partial u}{\partial y}\right) + \frac{\partial}{\partial z}\left(A_V\frac{\partial u}{\partial z}\right), \tag{2.39}$$

$$\frac{\partial v}{\partial t} + \frac{\partial uv}{\partial x} + \frac{\partial vv}{\partial y} + \frac{\partial vw}{\partial z} + fu = -\frac{1}{\rho_0}\frac{\partial p}{\partial y} + \frac{\partial}{\partial x}\left(A_H\frac{\partial v}{\partial x}\right) + \frac{\partial}{\partial y}\left(A_H\frac{\partial v}{\partial y}\right) + \frac{\partial}{\partial z}\left(A_V\frac{\partial v}{\partial z}\right), \tag{2.40}$$

$$0 = -\frac{1}{\rho_0}\frac{\partial p}{\partial z} - \frac{\rho}{\rho_0}g \text{, and} \tag{2.41}$$

$$\frac{\partial s}{\partial t} + \frac{\partial us}{\partial x} + \frac{\partial vs}{\partial y} + \frac{\partial ws}{\partial z} = \frac{\partial}{\partial x}\left(D_H\frac{\partial s}{\partial x}\right) + \frac{\partial}{\partial y}\left(D_H\frac{\partial s}{\partial y}\right) + \frac{\partial}{\partial z}\left(D_V\frac{\partial s}{\partial z}\right), \tag{2.42}$$

where u, v, and w are the velocities in the x, y, and z directions and f is the Coriolis parameter (see Appendix A). The hydrostatic pressure equation is 2.41, which has been substituted for the z-momentum equation. The advective acceleration terms ($\partial uu/\partial x$, $\partial uv/\partial y$, $\partial uw/\partial z$, and so forth) in equations 2.39 and 2.40 are written in a conservative form (or divergence from) similar to that used in equation 2.5. This form is obtained by adding the continuity equation (eq. 2.38), multiplied by the appropriate velocity component, to the left side of the momentum equations (similar to eq. 2.6).

[14]The values for A_V and D_V reported by Officer (1977) were for tidally averaged conditions.

[15]Casulli and Stelling (1996) present a 3-D model in which the hydrostatic pressure assumption is not introduced and give examples showing when the non-hydrostatic pressure component should not be neglected.

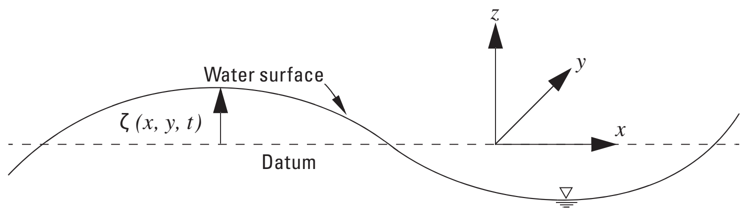

Figure 2.2. Sketch defining the free-surface elevation ζ.

Using the hydrostatic equation, the horizontal pressure gradient terms in the momentum equations, $(\partial p/\partial x)/\rho_0$ and $(\partial p/\partial y)/\rho_0$, can be reformulated in terms of the gradients of the water surface elevation and density. Integrating 2.41 from a depth z to the free (water) surface, where $z = \zeta(x, y, t)$ (*fig. 2.2*), gives

$$\int_z^{\zeta} \frac{\partial p}{\partial z}\, dz' = -g \int_z^{\zeta} \rho\, dz' . \tag{2.43}$$

Then carrying out the left-side integration and assuming the pressure at the free surface equals p_a, the atmospheric pressure, yields

$$p_a - p = -g \int_z^{\zeta} \rho\, dz' \cdot \tag{2.44}$$

Now differentiating 2.44 with respect to x and y and applying Leibnitz' rule to move the differentiation inside the integral term leaves

$$\frac{\partial p}{\partial x} = \frac{\partial p_a}{\partial x} + g\rho_s \frac{\partial \zeta}{\partial x} + g \int_z^{\zeta} \frac{\partial \rho}{\partial x}\, dz' \tag{2.45}$$

and

$$\frac{\partial p}{\partial y} = \frac{\partial p_a}{\partial y} + g\rho_s \frac{\partial \zeta}{\partial y} + g \int_z^{\zeta} \frac{\partial \rho}{\partial y}\, dz' \qquad , \tag{2.46}$$

where ρ_s is the surface density. If one assumes $\rho_s = \rho_0$ to the same order of approximation as the Boussinesq approximation, then the pressure gradient terms become

$$\frac{1}{\rho_0}\frac{\partial p}{\partial x} = \frac{1}{\rho_0}\frac{\partial p_a}{\partial x} + g\frac{\partial \zeta}{\partial x} + g\frac{1}{\rho_0}\int_z^{\zeta} \frac{\partial \rho}{\partial x}\, dz' \tag{2.47}$$

and

$$\frac{1}{\rho_0}\frac{\partial p}{\partial y} = \frac{1}{\rho_0}\frac{\partial p_a}{\partial y} + g\frac{\partial \zeta}{\partial y} + g\frac{1}{\rho_0}\int_z^{\zeta}\frac{\partial \rho}{\partial y}\,dz' \cdot \tag{2.48}$$

The integral terms in equations 2.47 and 2.48 are referred to as baroclinic terms and increase with depth[16] under most conditions. Because the baroclinic terms require a complete specification of the density field, they couple the hydrodynamic solution to the solution for the salt field. The importance of these terms accounts for the primary difference between modeling an estuary and a river of homogeneous density. In an estuary, the horizontal density gradients often are an important driving force for the flow, as illustrated for the longitudinal density gradients in *figure 1.1*.

The water surface slope terms in equations 2.47 and 2.48 are referred to as the barotropic terms and are constant with depth. These incorporate the important driving force of the tide.

The terms in equations 2.47 and 2.48 involving the gradients of atmospheric pressure generally are neglected in estuarine models, using the rationale that no significant gradients of atmospheric pressure are produced because of the relatively small size of estuaries. Changes in atmospheric pressure cause the water level in most estuaries to adjust "coherently" (uniformly) over the entire estuary. Normal variations in atmospheric pressure of ±20 millibars cause variations in estuarine water levels of approximately $\mp$20 cm; these variations are introduced into a numerical simulation through the open boundary conditions rather than through the governing equations themselves. Gradients of atmospheric pressure generally are important only in wide-area models of the coastal or open ocean when, for example, storm-surge predictions are attempted. If the atmospheric pressure terms are neglected, it then is common to assume the pressure at the free surface corresponds to zero "gage" pressure.

Substituting equations 2.47 and 2.48, without the atmospheric pressure gradient terms, into equations 2.39 and 2.40 gives

$$\frac{\partial u}{\partial t} + \frac{\partial uu}{\partial x} + \frac{\partial uv}{\partial y} + \frac{\partial uw}{\partial z} - fv = -g\frac{\partial \zeta}{\partial x} \tag{2.49}$$

$$-g\frac{1}{\rho_0}\int_z^{\zeta}\frac{\partial \rho}{\partial x}\,dz' + \frac{\partial}{\partial x}\left(A_H\frac{\partial u}{\partial x}\right) + \frac{\partial}{\partial y}\left(A_H\frac{\partial u}{\partial y}\right) + \frac{\partial}{\partial z}\left(A_V\frac{\partial u}{\partial z}\right)$$

and

$$\frac{\partial v}{\partial t} + \frac{\partial uv}{\partial x} + \frac{\partial vv}{\partial y} + \frac{\partial vw}{\partial z} + fu = -g\frac{\partial \zeta}{\partial y} \tag{2.50}$$

$$-g\frac{1}{\rho_0}\int_z^{\zeta}\frac{\partial \rho}{\partial x}\,dz' + \frac{\partial}{\partial x}\left(A_H\frac{\partial v}{\partial x}\right) + \frac{\partial}{\partial y}\left(A_H\frac{\partial v}{\partial y}\right) + \frac{\partial}{\partial z}\left(A_V\frac{\partial v}{\partial z}\right).$$

These are the forms of the *x*- and *y*-momentum equations that apply to estuarine tidal flows influenced by density variations.

[16]For the case of a vertically well-mixed estuary, the density is independent of z and the baroclinic terms increase linearly with depth.

2.4 Boundary Conditions

To complete the system of mean-flow equations introduced in section 2.3, it is necessary to specify the boundary conditions for an estuarine flow. For a 3-D model application, boundary conditions must be specified at the free surface, bottom, shoreline, and open boundaries of the estuary. In this report, it is assumed that all boundaries other than the free surface are fixed and do not change with time. This eliminates any consideration of vertical movement of the bottom profile caused by sediment transport or the lateral movement of shoreline boundaries caused by wetting and drying of tidal flats. The treatment of these moving boundaries involves topics that are outside the scope of this report. It also is assumed that the estuary bottom is impermeable and that the effects of precipitation and evaporation at the free surface are negligible. The 3-D model test cases included in this report do not involve open boundaries, so the formulation of a generalized open boundary condition is not discussed here. It is recognized, however, that the proper specification of open boundary conditions is a challenging problem in modeling.

2.4.1 Free Surface

Hydrodynamic boundary conditions at the free surface require that kinematic and dynamic conditions be satisfied. These conditions are discussed below. The boundary condition for the salt transport equation requires zero salt flux ($\partial s/\partial z = 0$) at the free surface.

2.4.1.1 Kinematic Surface Condition

The kinematic surface condition is derived by balancing the mass fluxes into and out of a control volume enclosing a thin layer of fluid mass immediately below the free surface. *Figure 2.3* illustrates the velocities on the faces of the control volume at one instant in time. The change in mass within the control volume during a time interval Δt ($\partial\zeta/\partial t \times \rho\Delta x\Delta y\Delta t$) must equal the net inflow of mass to the control volume minus the net outflow. The flow through a fluid surface is the product of the velocity normal to the surface, and the area. Mathematically, the mass balance (after canceling density[17]) can be expressed as

$$\begin{aligned}\frac{\partial\zeta}{\partial t}\Delta x\Delta y\Delta t \;=\;& \left(u-\frac{1}{2}\frac{\partial u}{\partial x}\Delta x\right)\left(\Delta z-\frac{1}{2}\frac{\partial\zeta}{\partial x}\Delta x\right)\Delta y\Delta t+\left(v-\frac{1}{2}\frac{\partial v}{\partial y}\Delta y\right)\left(\Delta z-\frac{1}{2}\frac{\partial\zeta}{\partial y}\Delta y\right)\Delta x\Delta t\\ &-\;\left(u+\frac{1}{2}\frac{\partial u}{\partial x}\Delta x\right)\left(\Delta z+\frac{1}{2}\frac{\partial\zeta}{\partial x}\Delta x\right)\Delta y\Delta t-\left(v+\frac{1}{2}\frac{\partial v}{\partial y}\Delta y\right)\left(\Delta z+\frac{1}{2}\frac{\partial\zeta}{\partial y}\Delta y\right)\Delta x\Delta t\\ &+\;\left(w-\frac{1}{2}\frac{\partial w}{\partial z}\Delta z\right)\Delta x\Delta y\Delta t\ .\end{aligned} \tag{2.51}$$

Dividing through the above equation by $\Delta x\Delta y\Delta t$, then cancelling terms and neglecting the small term involving $\partial w/\partial z$ which vanishes as $\Delta z \rightarrow 0$, gives the kinematic condition for the free surface:

$$\frac{\partial\zeta}{\partial t}+u\frac{\partial\zeta}{\partial x}+v\frac{\partial\zeta}{\partial y}-w \;=\; 0 \qquad \text{on} \qquad z \;=\; \zeta(x, y, t)\ . \tag{2.52}$$

This form of the kinematic condition requires that evaporation and precipitation at the free surface be negligible and also ignores the effects from any mass of water that may break away from the free surface as spray during especially rough seas.

[17]Any effects of density variations on the mass balance are neglected using similar arguments made earlier in developing the continuity equation. The flow also is assumed incompressible.

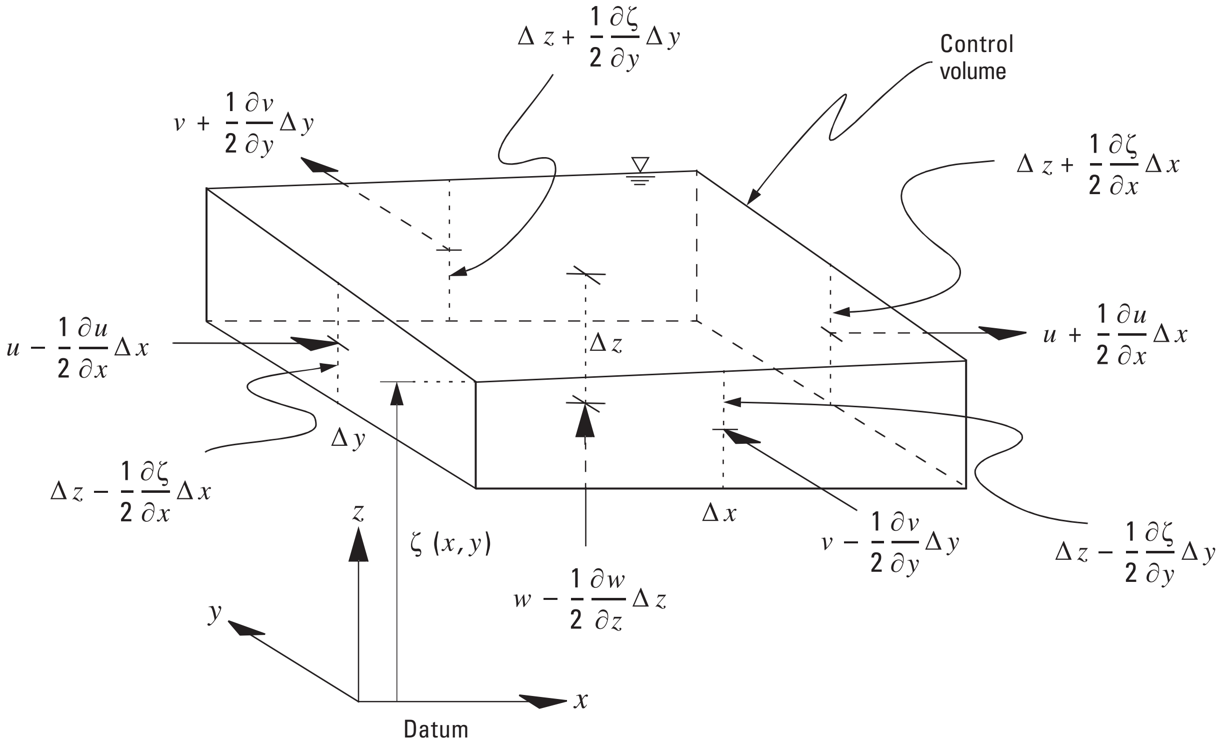

Figure 2.3. Velocities for mass flux balance on a surface control volume in three dimensions. Expressions in the form $u + \frac{1}{2}\frac{\partial u}{\partial x}\Delta x$ represent the velocities on each control volume face. Expressions in the form $\Delta z + \frac{1}{2}\frac{\partial \zeta}{\partial x}\Delta x$ represent the heights of each vertical control volume face.

2.4.1.2 Dynamic Surface Condition

The derivation of the dynamic surface condition is similar in method to the derivation of the kinematic condition. The equation of motion ($\Sigma F = ma$) is applied to a control volume enclosing a thin fluid layer at the surface (*fig. 2.4*). Viscous normal and shearing stresses act on the vertical and bottom faces of the fluid layer, and the free surface is subject to a horizontal wind stress vector τ_s with components τ_{xs} and τ_{ys} acting in the plane of the free surface.[18] The pressure at the free surface is constant, corresponding to atmospheric pressure (zero gage pressure). The free surface is assumed to be smooth, so that the wind transfers stress to the water through viscous shear. Because the terms in the equation of motion involving the mass of the water in the control volume are of higher order in smallness than the stresses themselves, they will vanish in the limit as the dimensions of the control

[18]The free surface is assumed to be sufficiently close to horizontal that the cosines of the vertical angles between the free surface and the *x*- and *y*-axes equal unity.

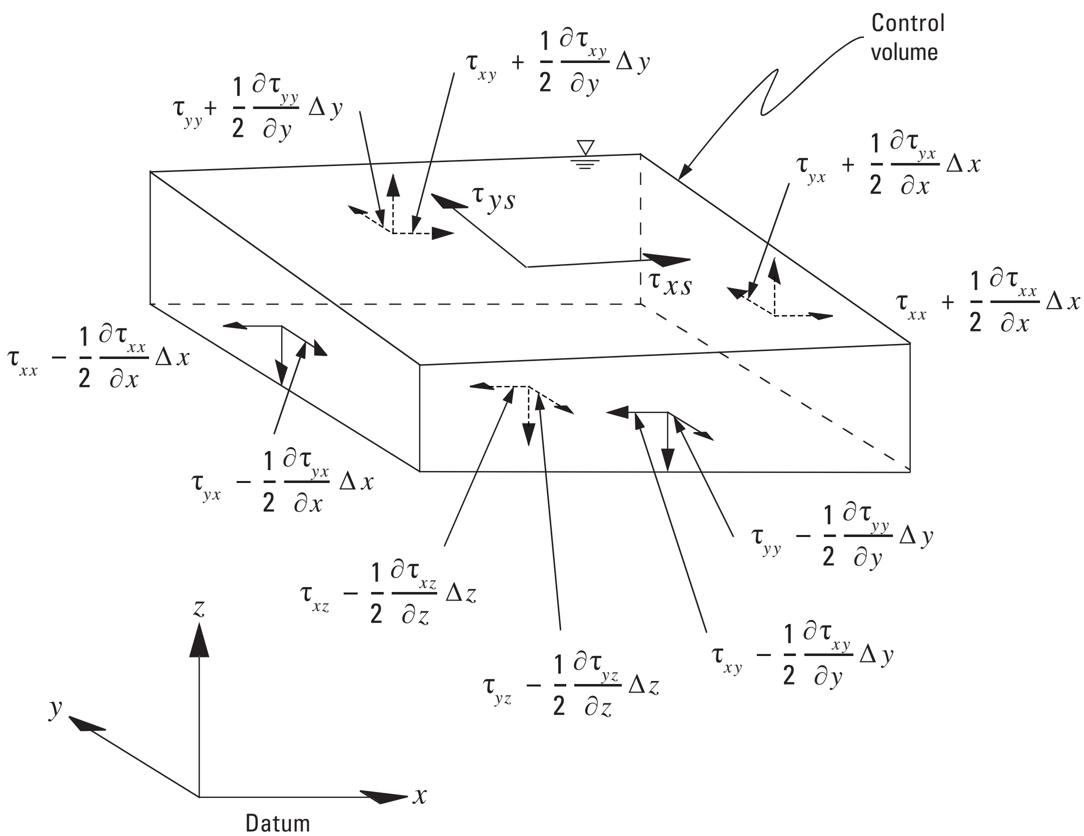

Figure 2.4. Viscous stresses on a surface layer of a water body affected by a wind stress with components τ_{xs} and τ_{ys}.
Expressions in the form $\tau_{xy} + \frac{1}{2}\frac{\partial \tau_{xy}}{\partial y}\Delta y$ represent the viscous stresses on each vertical control volume face.

volume approach zero. The application of the equation of motion then reduces to a stress balance on the control volume. Summing the forces (stress × area) in the *x*-direction from *figure 2.4* gives

$$\begin{aligned}
&\tau_{xs}\Delta x\Delta y + \left(\tau_{xx} + \frac{1}{2}\frac{\partial \tau_{xx}}{\partial x}\Delta x\right)\left(\Delta z + \frac{1}{2}\frac{\partial \zeta}{\partial x}\Delta x\right)\Delta y - \left(\tau_{xx} - \frac{1}{2}\frac{\partial \tau_{xx}}{\partial x}\Delta x\right)\left(\Delta z - \frac{1}{2}\frac{\partial \zeta}{\partial x}\Delta x\right)\Delta y \\
&+ \left(\tau_{xy} + \frac{1}{2}\frac{\partial \tau_{xy}}{\partial y}\Delta y\right)\left(\Delta z + \frac{1}{2}\frac{\partial \zeta}{\partial y}\Delta y\right)\Delta x - \left(\tau_{xy} - \frac{1}{2}\frac{\partial \tau_{xy}}{\partial y}\Delta y\right)\left(\Delta z - \frac{1}{2}\frac{\partial \zeta}{\partial y}\Delta y\right)\Delta x \\
&- \left(\tau_{xz} - \frac{1}{2}\frac{\partial \tau_{xz}}{\partial z}\Delta z\right)\Delta x\Delta y \;=\; 0.
\end{aligned} \tag{2.53}$$

Solving this equation for τ_{xs}, then cancelling terms and eliminating the terms which vanish as $\Delta z \to 0$, yields

$$\tau_{xs} \;=\; -\tau_{xx}\frac{\partial \zeta}{\partial x} - \tau_{xy}\frac{\partial \zeta}{\partial y} + \tau_{xz}\,. \tag{2.54}$$

For the *y*-direction, the corresponding relation is

$$\tau_{ys} \;=\; -\tau_{yx}\frac{\partial \zeta}{\partial x} - \tau_{yy}\frac{\partial \zeta}{\partial y} + \tau_{yz}\,. \tag{2.55}$$

The above expressions are generally simplified one step further to facilitate the formulation of a numerical boundary condition. By neglecting the slope of the free surface, the first two terms on the right sides of equations 2.54 and 2.55 are eliminated. Then the dynamic condition equations become

$$\tau_{xs} = \tau_{xz} \quad \text{and} \quad \tau_{ys} = \tau_{yz} , \tag{2.56}$$

which is the form used in most estuarine models. If the atmospheric pressure-gradient terms in equations 2.47 and 2.48 are included in a model application, the dynamic condition must also include the specification of atmospheric pressure, $p = p_a(x, y, t)$, at the free surface. When a wind is blowing over a large water body, it should also be understood that the free surface will quickly change from smooth conditions, as assumed above, to rough conditions as a result of wave generation. The wind will create pressure differences across the waves that impart stresses to the water column as form drag rather than viscous shear stress alone. Because the net effect of the wind on the water body during either smooth or rough surface conditions is a momentum transfer (flux) from the air to the water flow, it is not really important how the transfer occurs physically except to understand the processes involved.

The fluid stresses (τ_{xz}, τ_{yz}) in equations 2.56 can be defined using the eddy viscosity concept (eq. 2.18) as

$$\tau_{xz} = \rho_0 A_V \frac{\partial u}{\partial z} \quad \text{and} \quad \tau_{yz} = \rho_0 A_V \frac{\partial v}{\partial z} , \tag{2.57}$$

where it has been assumed that the horizontal gradients of vertical velocity can be neglected. The wind stresses (τ_{xs}, τ_{ys}) customarily are defined using a quadratic stress law

$$\tau_{xs} = c_w \rho_a W_a^2 \sin\phi \quad \text{and} \quad \tau_{ys} = c_w \rho_a W_a^2 \cos\phi , \tag{2.58}$$

where

ρ_a is the atmospheric density (~1.2 kg/m^3),

c_w is a dimensionless drag coefficient,

W_a is the wind speed 10 m above the water surface, and

Φ is the angle between the direction of the wind and the positive y-axis (measured positive in the clockwise direction from the y-axis to the wind vector).

The value for the drag coefficient c_w is influenced by several factors, including wind speed, wave height, the stability of the meteorological boundary layer over the water surface, and the degree of variability of the wind speed and direction. Much research has been done on determining the value of c_w. Blake (1991) discusses well the dependence of c_w on wind speed and wave height and includes a reference list of previous work. Estimates of the drag coefficient range between 1.0×10^{-3} and 1.5×10^{-3} for wind speeds between about 4 and 15 m/s. For light winds over a smooth water surface or high winds over a rough water surface, higher values may be required.

2.4.2 Bottom

At a solid boundary of an estuarine flow, the formal hydrodynamic condition is zero velocity. However, for numerical modeling of real estuaries, this boundary condition, known as no-slip, generally is not appropriate. The bottom boundary of an estuary is composed of roughness elements of varying sizes, as represented in *figure 2.5*. The roughness elements can be due to individual sediment grains, bedforms, vegetation, or mounds and burrows related to biological activity. The bottom of most estuaries is classified as hydraulically rough in the sense used in hydraulic engineering to imply the boundary elements protrude above the thickness of the viscous sublayer (Tennekes and Lumley, 1972, p. 158-160). The no-slip condition is satisfied only at the exact boundary surface itself, while along an average boundary, defined as $z = 0$ in *figure 2.5*, the mean velocity obtained by integrating along an arbitrary segment of the x-axis will usually not be zero. The roughness elements at the boundary generate turbulent wakes that are responsible for form drag on the bottom that by far is the largest part of the resistance to flow (the other part is caused by the viscous shearing stresses that act locally on the actual boundary surface in the tangential direction). The no-slip condition applied at $z = 0$ does not account for the influence of the form drag or its possible variations in space. Moreover, implementing the no-slip condition exactly at the boundary surface, even for a smooth boundary, is only meaningful if the very steep velocity gradients that prevail in the viscous sublayer are captured by the numerical model. In the viscous sublayer, the effect of fluid viscosity is important, so the viscous stress terms in the momentum equations must be included. Resolving the viscous sublayer requires a numerical grid size smaller than 1 millimeter, which is expensive in terms of computer resources. Because the flow in the immediate vicinity of the bottom boundary is important only insofar as it determines the overall stress exerted on the boundary, it is preferable to base the bottom boundary condition on the specification of the stress directly as a function of a velocity at some point away from the boundary (normally at the lowest model grid point, but well outside the viscous sublayer). This concept is used in formulating the dynamic boundary condition introduced below.

A kinematic condition at the bottom must also be satisfied, similar to that at the surface. The boundary condition at the bottom for the salt transport equation is zero salt flux.

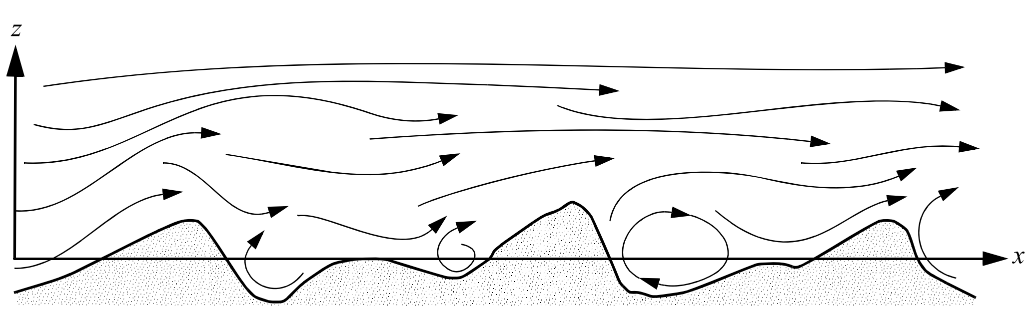

Figure 2.5. Flow over the bottom boundary of an estuary with roughness elements of varying sizes.

2.4.2.1 Kinematic Bottom Condition

The kinematic bottom condition is derived by balancing mass fluxes on a thin fluid layer immediately above the bottom of the estuary (*fig. 2.6*). The result is

$$u\frac{\partial h}{\partial x} + v\frac{\partial h}{\partial y} + w = 0 \qquad \text{on} \quad z = -h(x, y)\,, \tag{2.59}$$

which is similar to the result at the surface except that the location of the bottom $z = -h\ (x,\ y)$, unlike the free surface, is not a function of time and therefore $\partial h/\partial t = 0$. In this case, h represents a vertical distance measured positive downward from a datum (such as a mean sea level height) above the bottom. Equation 2.59 is sometimes referred to as the tangential flow condition because it requires the flow on the boundary to be tangent to the boundary and not to separate from it.

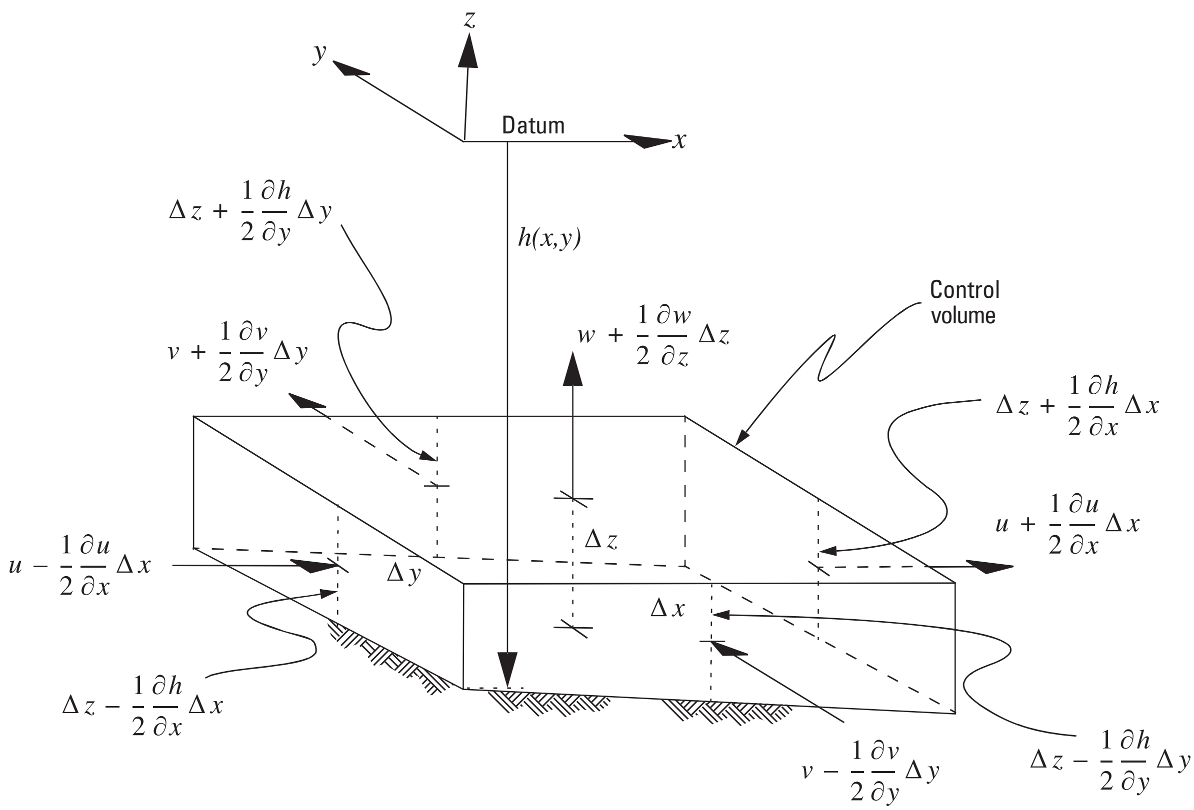

Figure 2.6. Sketch showing velocities for mass flux balance on a bottom control volume in three dimensions. Expressions in the form $u + \frac{1}{2}\frac{\partial u}{\partial x}\Delta x$ represent the velocities on each control volume face. Expressions in the form $\Delta z + \frac{1}{2}\frac{\partial h}{\partial x}\Delta x$ represent the heights of each vertical control volume face.

2.4.2.2 Dynamic Bottom Condition

The dynamic bottom condition is derived by applying the equation of motion to the thin fluid layer on the bottom (*fig. 2.7*). The equation of motion reduces to a balance between the stresses exerted by the boundary on the fluid and the stresses in the fluid exerted on the boundary. The stress vector exerted by the boundary is τ_b and has components τ_{xb} and τ_{yb} acting along the boundary. The boundary slope in any direction is assumed sufficiently small so that the cosine of the vertical angle with the horizontal plane is unity. The balance of stresses results in

$$\tau_{xb} = -\tau_{xx}\frac{\partial h}{\partial x} - \tau_{xy}\frac{\partial h}{\partial y} + \tau_{xz} \tag{2.60}$$

and

$$\tau_{yb} = -\tau_{yx}\frac{\partial h}{\partial x} - \tau_{yy}\frac{\partial h}{\partial y} + \tau_{yz} \tag{2.61}$$

for the *x*- and *y*-directions, respectively. It is common practice to neglect entirely the slopes of the bottom boundary, $\partial h/\partial x$ and $\partial h/\partial y$, so the first two terms on the right sides of the above equations can be eliminated. Then the dynamic equations become

$$\tau_{xb} = \tau_{xz} \qquad \text{and} \qquad \tau_{yb} = \tau_{yz}\ , \tag{2.62}$$

which are the counterparts to equations 2.56 used at the surface. To evaluate equations 2.62, the fluid stresses (τ_{xz}, τ_{yz}) can be defined using equations 2.57 applied at the bottom of the estuary. It remains then to define the boundary stresses (τ_{xb}, τ_{yb}).

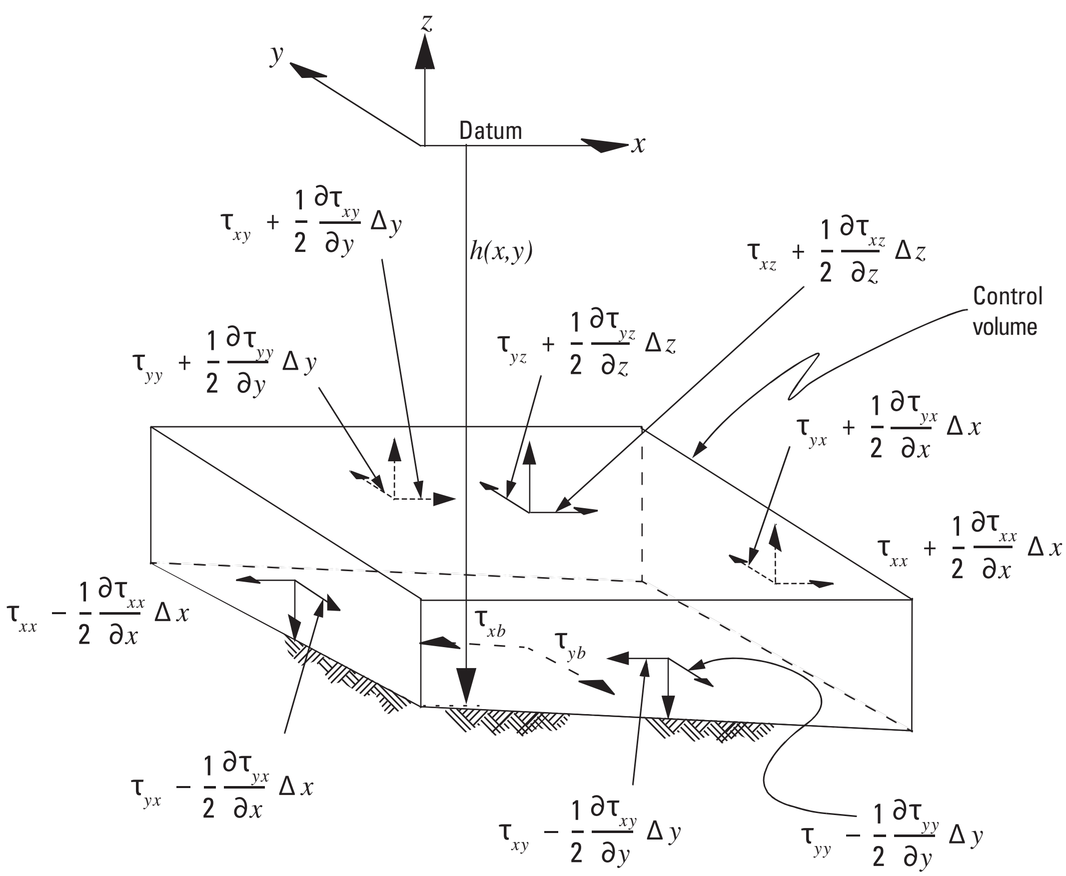

Figure 2.7. Viscous stresses on a bottom layer of a water body with boundary stress components τ_{xb} and τ_{yb}. Expressions in the form $\tau_{yz} + \frac{1}{2}\frac{\partial \tau_{yz}}{\partial z}\Delta z$ represent the viscous stresses on each control volume face.

As noted previously, the strategy in defining the boundary stresses is to relate them to the velocity at a point above the boundary. For this purpose, the well-known logarithmic velocity law generally is adequate so long as the bottom topography is not highly nonuniform and the boundary layer is not stratified.[19] It is assumed that the boundary layer is unaffected by wave-generated currents. Gross and Nowell (1983) found that the dynamic effects from temporal variability (unsteadiness) in a tidal boundary layer did not measurably affect the accuracy of predictions with the logarithmic law in the near-bed region. The appropriate logarithmic law for rough boundary flow is (Tennekes and Lumley, 1972, p. 165, eq. 5.2.49)

$$\frac{u_{res}}{u_*} = \frac{1}{\kappa}\ln\frac{z'}{z_0}\,, \tag{2.63}$$

where

- z' is a vertical distance measured outward from an average position among the roughness elements,
- u_{res} is the resultant velocity parallel to the boundary at a height z',
- u_* is the resultant shear velocity defined as $\sqrt{\tau_b/\rho_0}$,
- z_0 is a characteristic length scale related to the height of the roughness elements and corresponding with the point of zero velocity ($u_{res} = 0$ at $z' = z_0$), and
- κ is von Kármán's constant (~ 0.41).

Equation 2.63 is theoretically valid outside the region of boundary roughness and within a layer of constant (Reynolds) stress. Although a "constant stress layer" exists in channel flow only in the immediate neighborhood of the boundary, the logarithmic profile typically represents the flow well outside this layer. In fact, for steady, uniform channel flow, the logarithmic law traditionally has been used to describe the velocity profile over the entire depth of flow (Keulegan, 1938). Under many ordinary conditions of tidal flow in estuaries, the logarithmic law is a reasonable representation of the velocity profile for the first few meters above the bed.

Equation 2.63 can be solved for the boundary shear stress to obtain a quadratic stress law of the form

$$\tau_b = \rho_0 C_d u_{res}|u_{res}|\,, \tag{2.64}$$

where C_d is a dimensionless drag coefficient. The quadratic term in 2.64 involving the velocity is written with an absolute value sign so the frictional stress always will oppose the flow. In practice, equation 2.64 is rearranged to represent the two components of shear stress with

$$\tau_{xb} = \rho_0 C_d\left(u_b^2 + v_b^2\right)^{1/2} u_b \quad \text{and} \quad \tau_{yb} = \rho_0 C_d\left(u_b^2 + v_b^2\right)^{1/2} v_b\,, \tag{2.65}$$

where u_b, v_b are the horizontal velocity components at a point z'_b above the bottom, and

$$C_d = \kappa^2\left(\ln\frac{z'_b}{z_0}\right)^{-2}\,. \tag{2.66}$$

[19]Refinements of the logarithmic law that incorporate the effect of density stratification are available (Turner, 1973, Chapter 5; Adams and Weatherly, 1981).

Equations 2.65 allow the shear stress components (τ_{xb}, τ_{yb}) to be estimated from the velocities (u_b, v_b) determined by the model and an estimate of either z_0 or C_d.

The value of z_0 depends greatly on the grain size, bottom shape, and near-bed sediment transport (Grant and Madsen, 1982) and can vary widely. Pritchard (1956) suggested the values

z_0 = 0.02 cm for a mud bottom,

z_0 = 0.13 cm for a sand-gravel bottom, and

z_0 = 0.16 cm for a sand-mud bottom.

The higher value suggested for the sand-mud bottom was attributed to the possible presence of ripples. In the presence of high sediment bedload transport, much higher values of z_0 are often used, such as 1 cm (Adams and Weatherly, 1981).

Some modelers prefer to specify the drag coefficient C_d instead of z_0 because it does not vary as widely as z_0. Values of C_d derived from fitting the logarithmic law to field data are usually reported using $z'_b = 100$ cm. In 3-D model studies, the vertical location of the lowest model grid point above the boundary normally defines the value for z'_b. In 2-D model studies, C_d values are sometimes reported that are based on the use of depth-averaged velocity components in equations 2.65. In cases where the bed roughness z_0 is uniform, C_d should not remain constant if the value of z'_b is varying significantly. In general, the use of C_d in the range 0.0025 to 0.004 is fairly typical among 3-D coastal and estuarine modelers; this range of C_d corresponds to a range in z_0, for $z'_b = 100$ cm, of 0.027 to 0.15 cm. Walters (1992), however, required values for C_d in excess of 0.03 when modeling the tides in the upper Delaware Estuary where channel constrictions and bars are prevalent.

2.4.3 Shoreline

Along a shoreline boundary, in theory, either a no-slip or quadratic-stress-law boundary condition can be applied. When modeling large water bodies, however, the typical horizontal grid spacing is so large (>0.25 km) that these boundary conditions yield a distorted horizontal velocity distribution near the boundary. Instead, a “perfect-slip” boundary condition is normally applied that permits the flow to move parallel to the boundary without any boundary frictional resistance. The perfect-slip condition is a reasonable choice so long as the shoreline boundary layer has little influence on horizontal velocity distributions, which is true in most estuaries. The perfect-slip condition can be implemented by adding a line of model nodes outside the boundary and defining the velocity at those outside nodes to be equal to the velocity at the interior nodes adjacent to the boundary.

The mass flux of salt at a shoreline boundary must be set to zero. This is normally achieved by letting no flow cross the boundary, although care must be exercised so that the numerical method does not inadvertently transport salt across the boundary by diffusion.

2.5 Scaling Analysis

It is useful to recast the governing equations in a dimensionless form so that the magnitude of various terms or groups of terms can be estimated for a typical estuary (in this case San Francisco Bay). Cheng and others (1976) and Lynch (1986) have presented similar dimensionless analyses of the 3-D equations, but they selected scaling parameters representative of large lakes. Sheng (1983) presents a 3-D coastal ocean model where the governing equations are solved in a dimensionless form.

The dimensionless variables, denoted by an asterisk (*), are chosen as follows:

$$x^* = \frac{x}{L}, \quad y^* = \frac{y}{L}, \quad z^* = \frac{z}{H}, \quad t^* = \omega t,$$

$$u^* = \frac{u}{u_r}, \quad v^* = \frac{v}{u_r}, \quad w^* = \frac{wL}{u_r H},$$

$$\zeta^* = \frac{\zeta}{D}, \quad \rho^* = \frac{\rho - \rho_1}{\rho_2 - \rho_1}, \text{ and } s^* = \frac{s - s_1}{s_2 - s_1}, \tag{2.67}$$

where

L is a horizontal length scale,

H is a vertical length scale representing the water depth,

D is a vertical length scale representing the tidal amplitude,

u_r is a horizontal reference velocity,

ρ_1 is a minimum density,

ρ_2 is a maximum density,

s_1 is a minimum salinity,

s_2 is a maximum salinity, and

ω is a frequency of the tidal forcing.

Introducing the dimensionless variables into equations 2.38, 2.49, 2.50, and 2.42 transforms the 3-D equations into the following dimensionless forms:

Continuity equation,

$$\frac{\partial u^*}{\partial x^*} + \frac{\partial v^*}{\partial y^*} + \frac{\partial w^*}{\partial z^*} = 0\,; \tag{2.68}$$

Horizontal momentum equations,

$$\beta\frac{\partial u^*}{\partial t^*} + Ro\left[\frac{\partial u^* u^*}{\partial x^*} + \frac{\partial u^* v^*}{\partial y^*} + \frac{\partial u^* w^*}{\partial z^*}\right] - v^* = -\frac{Ro}{Fr^2}\frac{D}{H}\frac{\partial \zeta^*}{\partial x^*} \tag{2.69}$$

$$-\frac{Ro}{Fr_i^2}\int_{z^*}^{\frac{D}{H}\zeta^*}\frac{\partial \rho^*}{\partial x^*}dz^* + E_H\left[\frac{\partial}{\partial x^*}\left(\frac{\partial u^*}{\partial x^*}\right) + \frac{\partial}{\partial y^*}\left(\frac{\partial u^*}{\partial y^*}\right)\right] + E_V\frac{\partial}{\partial z^*}\left(\frac{\partial u^*}{\partial z^*}\right)$$

and

$$\beta\frac{\partial v^*}{\partial t^*} + Ro\left[\frac{\partial u^* v^*}{\partial x^*} + \frac{\partial v^* v^*}{\partial y^*} + \frac{\partial v^* w^*}{\partial z^*}\right] + u^* = -\frac{Ro}{Fr^2}\frac{D}{H}\frac{\partial \zeta^*}{\partial y^*} \tag{2.70}$$

$$-\frac{Ro}{Fr_i^2}\int_{z^*}^{\frac{D}{H}\zeta^*}\frac{\partial \rho^*}{\partial y^*}dz^* + E_H\left[\frac{\partial}{\partial x^*}\left(\frac{\partial v^*}{\partial x^*}\right) + \frac{\partial}{\partial y^*}\left(\frac{\partial v^*}{\partial y^*}\right)\right] + E_V\frac{\partial}{\partial z^*}\left(\frac{\partial w^*}{\partial z^*}\right);$$

Salt transport equation,

$$\frac{\beta}{Ro}\frac{\partial s^*}{\partial t^*} + \left[\frac{\partial u^* s^*}{\partial x^*} + \frac{\partial v^* s^*}{\partial y^*} + \frac{\partial w^* s^*}{\partial z^*}\right] =$$

$$\frac{1}{Pe_H}\left[\frac{\partial}{\partial x^*}\left(\frac{\partial s^*}{\partial x^*}\right) + \frac{\partial}{\partial y^*}\left(\frac{\partial s^*}{\partial y^*}\right)\right] + \frac{1}{Pe_V}\frac{\partial}{\partial z^*}\left(\frac{\partial s^*}{\partial z^*}\right). \tag{2.71}$$

The coefficients of most terms now form recognizable dimensionless numbers that are identified in *table 2.1*. In arriving at the two horizontal momentum equations (2.69 and 2.70), the eddy coefficients were assumed to be constant. Also, the coefficients of the Coriolis terms were arranged to be unity in these two equations. The salt transport equation (2.71) was arranged so that the coefficient of the advection terms was unity.

Estimates of the scaling parameters and coefficients that are typical of the northern reach of San Francisco Bay are

L	=	100 km	H	=	10 m
D	=	1 m	u_r	=	0.25 m/sec
f	=	10^{-4} sec^{-1}	ω	=	5×10^{-5} sec^{-1}
ρ_1	=	10^3 kg/m^3	ρ_2	=	1.025×10^3 kg/m^3
s_1	=	1	s_2	=	34
ρ_0	=	10^3 kg/m	g	=	10 m/sec^2
A_H	=	10^2 m^2/sec	A_V	=	10^{-2} m^2/sec
D_H	=	10^2 m^2/sec	D_V	=	10^{-2} m^2/sec

Table 2.1. Dimensionless numbers in 3-D equations.

Name	Symbol	Definition	Ratio between	Estimate
Rossby number	Ro	$\frac{u_r}{fL}$	$\frac{\text{fluid acceleration}}{\text{Coriolis acceleration}}$	2.5×10^{-2}
Froude number	Fr	$\frac{u_r}{(gH)^{1/2}}$	$\frac{\text{fluid velocity}}{\text{surface wave speed}}$	2.5×10^{-2}
Internal Froude number	Fr_i	$\frac{u_r}{\left(gH\frac{\rho_2 - \rho_1}{\rho_0}\right)^{1/2}}$	$\frac{\text{fluid velocity}}{\text{internal wave speed}}$	0.5
Unsteadiness number	β	$\frac{\omega}{f}$	$\frac{\text{inertial period}}{\text{tidal period}}$	0.5
Depth ratio	—	$\frac{D}{H}$	$\frac{\text{tidal amplitude}}{\text{depth}}$	10^{-1}
Horizontal Ekman number	E_H	$\frac{A_H}{fL^2}$	$\frac{\text{horizontal momentum diffusion}}{\text{Coriolis acceleration}}$	10^{-4}
Vertical Ekman number	E_V	$\frac{A_V}{fH^2}$	$\frac{\text{vertical momentum diffusion}}{\text{Coriolis acceleration}}$	1
Horizontal Péclet number	Pe_H	$\frac{u_r L}{D_H}$	$\frac{\text{mass advection}}{\text{horizontal mass diffusion}}$	2.5×10^2
Vertical Péclet number	Pe_V	$\frac{u_r H}{D_V}$	$\frac{\text{mass advection}}{\text{vertical mass diffusion}}$	2.5×10^2

Because the northern reach of San Francisco Bay is influenced by freshwater inflow from the Sacramento–San Joaquin River Delta, significant density gradients can occur there. The forcing period (1/ω) was chosen to be approximately six hours, or one-quarter of the diurnal tidal cycle in San Francisco Bay, and corresponds with roughly the full range of local velocity change (from flood to ebb tide).

For the above set of parameters, the corresponding magnitudes of the dimensionless numbers are shown in *table 2.1*. In the dimensionless equations, the chosen parameters scale each partial derivative term to approximately equal size and of order unity. The coefficients for each term then provide an order-of-magnitude estimate of the relative importance of the terms and groups of terms with respect to others. The relative magnitude of the terms in the momentum balance equation are shown in *table 2.2* and in the salt balance equation in *table 2.3*.

Owing to the strong tidal forcing in San Francisco Bay, the water surface slope terms are the largest in the momentum equation (*table 2.2*). The baroclinic, Coriolis, vertical momentum diffusion, and temporal acceleration terms also are very significant. The advective acceleration and horizontal momentum diffusion terms are the smallest terms in the estuarine momentum equation and generally are not of major significance. It is not recommended, however, that these terms be neglected. The need for some amount of horizontal momentum diffusion to reproduce horizontal circulation in side bays was discussed in section 2.3.1.1. The scaling analysis here also does not consider changes in the estuarine bathymetry or lateral geometry. Bathymetric and (or) geometric changes can induce significant horizontal velocity shear that may cause the advective acceleration and horizontal momentum diffusion terms to become locally significant. In San Francisco Bay, regions of high velocity gradients occur near the sharp bathymetric gradients at the edges of the deepwater navigation channels, near flow constrictions, and behind islands and headlands where eddies form.

Table 2.2. Relative magnitude of the terms in the momentum equation.

Term	Coefficient	Relative magnitude
Water surface slope	$\frac{Ro\ D}{Fr^2 H}$	4
Baroclinic	$\frac{Ro}{Fr_i^{\ 2}}$	1
Coriolis acceleration	1.0	1
Vertical momentum diffusion	E_V	1
Temporal acceleration	β	0.5
Advective acceleration	R_o	0.025
Horizontal momentum diffusion	E_H	0.0001

Table 2.3. Relative magnitude of the terms in the salt equation.

Term	Coefficient	Relative magnitude
Advective transport	1.0	1
Vertical salt diffusion	$1/Pe_V$	0.004
Horizontal salt diffusion	$1/Pe_H$	0.004

In contrast to the momentum equation, the advective transport terms in the salt equation are very significant (*table 2.3)* and should be evaluated carefully in a numerical model to avoid artificial diffusion or spurious oscillations of the salt concentration field. Péclet numbers as large as those in *table 2.1* indicate that estuarine flows are “advection dominated,” meaning that the transport of salt (and generally other solutes) is mostly by advection by the water currents and not by turbulent diffusion. The diffusion terms in the salt transport equation, however, should not be neglected. The accurate modeling of the vertical diffusion of salt is essential in a stratified estuary if the vertical profile of salinity is to be reproduced accurately. The modeling of horizontal salt diffusion may be less highly refined than the vertical diffusion in most estuaries, but it is still required to determine the proper horizontal distribution of salt. Quite often the size of the horizontal numerical grid used in estuarine modeling is large. All the horizontal advective motions acting over smaller scales than the grid are not resolved directly by the model but are considered to be mixing, and they must be represented by the horizontal diffusion terms. For this reason, the horizontal eddy diffusion coefficient, D_H, is partly based on the size of the smallest eddies that are resolved by a model.

2.6 Coordinate Transformations

The 3-D equations presented so far are written in standard Cartesian or rectangular coordinates.[20] Thus, the equations have a relatively simple form. When using the finite-difference method, the Cartesian equations generally are solved on a square or rectangular grid. The calculations can be very efficient because the simple form of the equations and the uniform grid system are convenient for the implementation of most numerical schemes. Over the last two decades, however, it has become increasingly common to transform the governing equations into other coordinate systems that allow variable or curvilinear grids to be used with greater flexibility in representing curved shoreline and bottom boundaries smoothly, or for resolving interior regions of interest using a higher density of grid points. The transformations can involve the horizontal coordinates or the vertical coordinate or both. Horizontal coordinate transformations are used almost exclusively in transforming the governing equations for finite-difference solution methods. Finite-element and finite-volume methods allow one to work with irregular grid systems without transforming the coordinates of the governing equations. It is also possible to use irregular (usually triangular) grids with finite-difference methods (see, for example, Thacker, 1977), but coordinate transformations are more commonly used. A brief review of the horizontal and vertical coordinate transformations in use today [1997] for estuarine and coastal modeling follows.

[20] If a circulation model is to be applied to regions of the ocean having substantial variations in latitude (generally greater than a few tens of degrees), then the governing equations in rectangular coordinates are not appropriate. Spherical coordinates must be used to consider the curvature of the earth’s surface. For the relatively small horizontal scale of most estuaries, the use of rectangular coordinates introduces negligible errors.

2.6.1 Horizontal Coordinate Transformations

The simplest of horizontal coordinate transformations are those that stretch coordinates to form a numerical grid that is rectangular but not uniform. The transformation used by Butler (1978, 1980), and also implemented in the 3-D model by Sheng (1983), takes the form

$$x = a_x + b_x \hat{x}^{c_x}, \quad y = a_y + b_y \hat{y}^{c_y}, \tag{2.72}$$

where a_x, b_x, c_x, a_y, b_y, and c_y are arbitrarily chosen stretching coefficients. The governing equations are usually solved on a rectangular grid with square grid boxes after being transformed into the new coordinates $\hat{x}$, $\hat{y}$. Several regions within the entire computational domain can be defined by using different sets of stretching coefficients for each region (*fig. 2.8*); the grid at the transition between regions should vary smoothly to prevent computational problems. When the stretching coefficients are constants within each region, the transformation by equations 2.72 does not add any extra terms to the transformed governing equations; the transformation does introduce the stretching coefficients into the horizontal derivative terms, however.

Boericke and Hall (1974) used a form of equations 2.72 with $a_x = 0$, $b_x = c_x = c_y = 1$, and a_y and b_y as geometric (width) variables to map the shoreline of an irregular estuary to a rectangular computational space (*fig. 2.9*). The grid system is one form of a so-called boundary-fitted grid in which the boundaries of the water body are transformed to coincide with the coordinate lines of the grid system. The transformation positions the y-coordinate grid points uniformly across the width of the estuary along each x-coordinate grid line. The y grid spacing then varies with the changing width of the estuary along the longitudinal (x) direction. Different transformations can be applied to different regions to have greater flexibility in positioning points.

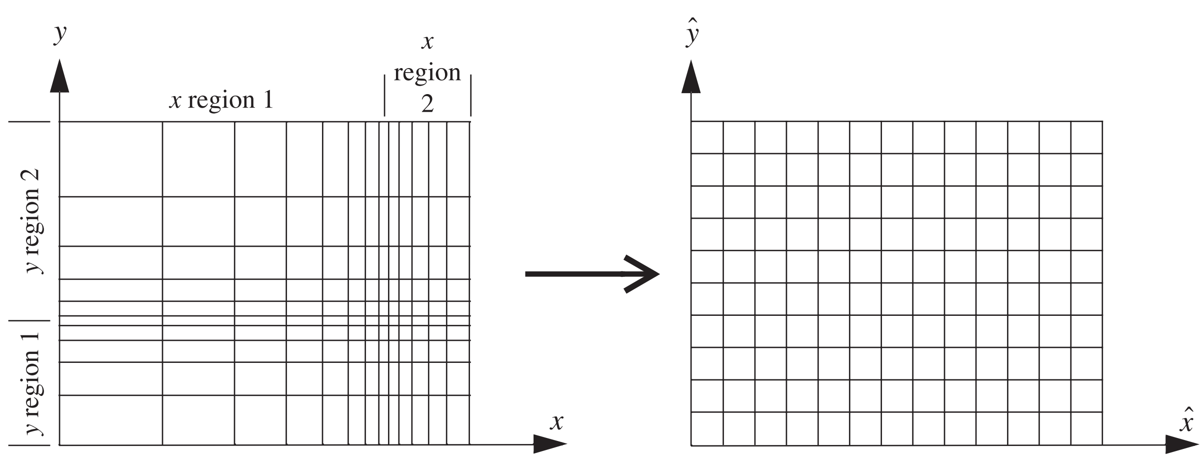

Figure 2.8. Horizontal stretching of coordinates using two regions in both the *x* and *y* directions. (Modified from Sheng, 1983, fig. 2.2.)

Noye and Stevens (1987) used the same horizontal transformation as Boericke and Hall but solved the transformed governing equations by using a nonuniform grid spacing in order to increase the grid resolution in regions of interest within the original coordinate system. The nonuniform grid spacing in the computational space must be chosen according to certain criteria presented by Noye and Stevens to retain the accuracy of the numerical approximations that are achievable for uniformly spaced grids. Because the stretching coefficients are not constant in the method of Boericke and Hall, an additional term is introduced into the expression for the transformed x-derivative.

To achieve even greater flexibility for the horizontal grid point placement than with stretched-coordinate models, curvilinear coordinate models can be used. These models solve forms of the governing equations that are transformed into curvilinear coordinates. The transformed equations can be solved on a rectangular grid, which is then transformed into a curvilinear grid in the original coordinate system. The curvilinear grid is generally fitted to the physical boundary to avoid the stair-step patterns that appear when curved boundaries are represented by conventional rectangular grids. Clustering grid points is possible in regions where increased grid resolution is needed, such as navigation channels (Thompson and Johnson, 1986).

Curvilinear coordinate models have been developed that are based on horizontal grid transformations that are conformal (Reid and others, 1977), generalized orthogonal (Willemse and others, 1985; Blumberg and Herring, 1987), and nonorthogonal (Johnson, 1982; Johnson and others, 1991; Sheng, 1986a; Spaulding, 1984; Spaulding and others, 1990; Muin and Spaulding, 1996). Conformal transformations are fully defined by analytic functions of a complex variable by using the techniques of conformal mapping (Vallentine, 1967). Except at relatively few singular points, conformal grids are orthogonal: families of grid lines intersect perpendicularly to one another. By the definition of a conformal transformation, the angles of the rectangular grid in computational space are preserved in magnitude and sense under the transformation, which assures the orthogonality of the grid in the physical space. For estuarine modeling, a generalized orthogonal curvilinear grid is usually preferred over a conformal grid because it allows a more flexible spacing of grid lines; thus, for example, it is easy with a generalized orthogonal grid to choose grid lines that are

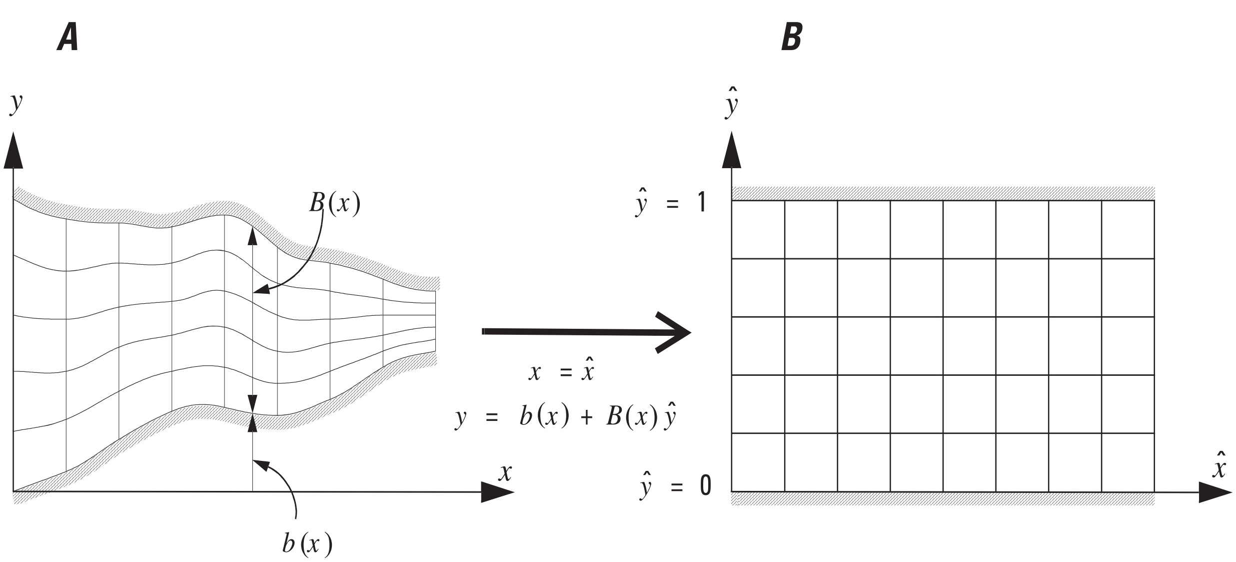

Figure 2.9. Plan view of an estuary shown in (*A*) physical space and (*B*) computational space using the transformation of Boericke and Hall (1974).

more closely spaced near a shoreline (*fig. 2.10*). The determination of a suitable mapping function for a conformal transformation can be a difficult task even for some relatively simple transformations. Nonorthogonal curvilinear grids are the most general of the curvilinear grids because they relax the strict requirement of orthogonality.[21] An accurate fitting of a grid to the boundary of an irregularly shaped estuary often requires a nonorthogonal grid; conformal or generalized orthogonal grids generally must represent an irregular shoreline by some form of smoothed mean boundary profile. An example of a nonorthogonal curvilinear grid, used by Johnson and others (1991, 1993) for hydrodynamic modeling of Chesapeake Bay, is shown in *figure 2.11*.

The price for the greater flexibility of using curvilinear grids is that the form of the curvilinear governing equations is much more complicated than the Cartesian form, particularly the form in nonorthogonal curvilinear coordinates. The nonorthogonal curvilinear equations presented by Johnson and others (1991)[22] list thirty additional terms appearing in each horizontal momentum equation resulting only from the transformation of the two Cartesian terms representing horizontal momentum diffusion; approximately double the number of original terms is also the result of transforming from the Cartesian form of the advection, pressure

[21]Nonorthogonal grids generally should not deviate far from being orthogonal if numerical errors for the equations to be solved on the grid are to be kept under control.

[22]The equations presented by Johnson and others (1991) are in a form in which the velocity components are transformed to be everywhere perpendicular to the local curvilinear coordinate lines. This velocity component transformation is referred to as contravariant.

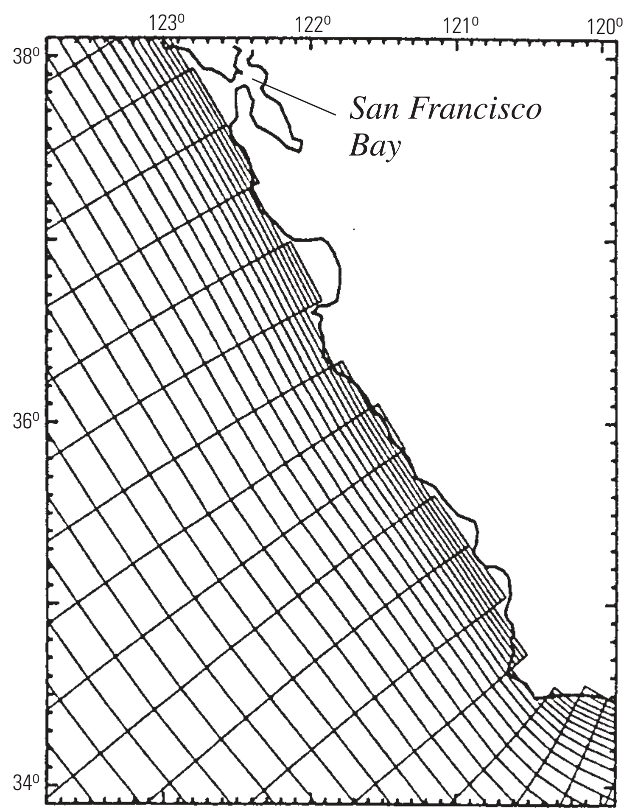

Figure 2.10. Orthogonal curvilinear grid used by Blumberg and Herring (1987) to model a portion of the California coast.
The grid spacing in the offshore direction varies from ~4 kilometers near the coast to ~25 kilometers on the west. (Modified from Blumberg and Herring, 1987, fig. 11B.)

gradient, and Coriolis terms. The governing equations for use with orthogonal grids are significantly less complex that those for nonorthogonal grids, but they still include extra terms that represent the curvature of the coordinate system. Owing to the extra terms, the computational time that is required in solving the nonorthogonal curvilinear equations is approximately double that required for solving the Cartesian equations (Spaulding, 1984). Solving the orthogonal curvilinear equations requires approximately 25 percent greater computational time than the Cartesian equations (A.F. Blumberg, oral commun., 1995). Ideally the savings from any reduction in the number of grid points that is made possible by using a curvilinear model should be sufficient to compensate for the greater cost of the calculations for individual grid points. For a nonorthogonal curvilinear model in particular, that is not always possible. In these instances, the benefits from the greater flexibility in the placement of grid points using a nonorthogonal curvilinear model must outweigh the greater computational cost of the model, or a Cartesian or orthogonal-curvilinear model should be used.

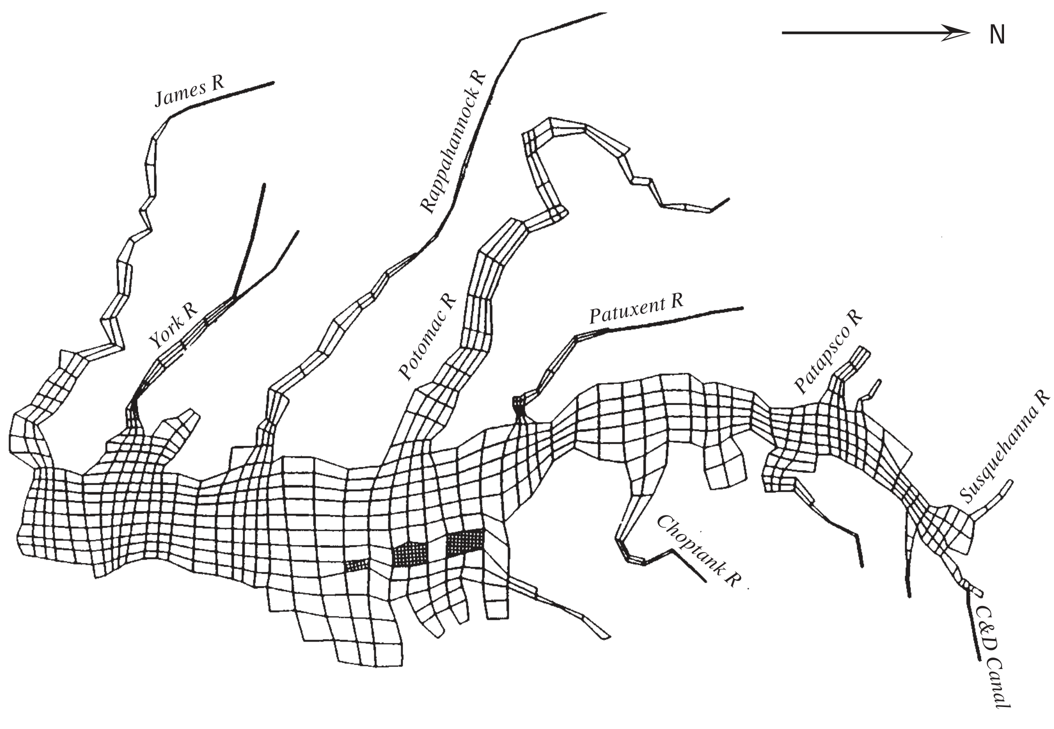

Figure 2.11. Nonorthogonal curvilinear grid used by Johnson and others (1991, 1993) to model Chesapeake Bay. (Modified from Johnson and others, 1991, fig. 2.)

Besides the increased complexity of the governing equations, the following additional drawbacks of models that are based on the curvilinear forms of the governing equations should be considered:

1. Considerable effort must be expended in defining the curvilinear grid transformation from computational to physical space. Generally, a numerical grid generator like the computer program EAGLE (Thompson and others, 1985) is needed to assign the spatial locations of the curvilinear grid points. For an orthogonal grid, the grid generation process is often iterative, continuing until a grid is found that reasonably approximates all boundaries of the domain while also satisfying the constraint equations for the orthogonality of intersecting grid lines. Reviews of grid generation techniques for fluid mechanics computations are given by Eiseman (1985) and Hoffmann (1989).

2. Curvilinear models are not ideally suited for situations when the wetting and drying of boundary grid points occurs, as is common in estuarine tidal flats. In these situations, the estuarine boundary is in motion, and there is little likelihood that the boundary will be represented smoothly through all phases of the wetting and drying cycle.

3. When using curvilinear grids (especially strongly nonorthogonal ones), one must ensure that numerical dispersion errors are not introduced as waves propagate through regions of varying grid size and aspect ratio. Further studies of these errors are needed.

4. According to Wang (1992), a guaranteed conservative form of the advection terms does not exist for the horizontal momentum equations expressed with contravariant velocity components in a curvilinear, orthogonal or nonorthogonal, coordinate system. Although using a conservative form of the momentum advection terms in an estuarine model formulation is not always essential, it is usually desirable for the best possible behavior of the numerical model.

The model described in this report will use Cartesian horizontal coordinates only. As can be concluded from this discussion, for cases in which a reasonably uniform grid resolution is appropriate and when precise boundary fitting is not important (because, for example, boundary areas have very low velocities or are subject to wetting and drying cycles), Cartesian models are preferred for their efficiency, convenience, and generally superior numerical behavior. In any case, solving the Cartesian form of equations should always be the first step in developing and testing a new model, as is the case herein.

2.6.2 Vertical Coordinate Transformations

Three-dimensional models that are based upon a layered or grid-box approach in the vertical direction generally use one of three types of vertical coordinate systems. The first is a standard z-coordinate, or level-plane, system that has been used in the equations derived so far. Using z-coordinates, the governing equations are solved on a vertical grid system that is composed of horizontal layers with exchanges of mass, momentum, and salt taking place between the layers. The position of the layers is fixed vertically. The details of schematizing the governing equations using a z-coordinate layering system are presented in Chapters 3 and 4.

The second type of vertical coordinate system uses density to replace depth (z) as the vertical coordinate, making density an independent variable in the transformed system (x, y, ρ, t). The coordinate z becomes a dependent variable that identifies the depth at which the density is defined for a given x, y location and time t. The governing equations are schematized by using stacked layers of uniform density separated by moving, impermeable interfaces. The locations of the interfaces are defined as $z_k = \zeta_k(x, y, t)$, $k = 1$, km for a system of km layers, as illustrated in *figure 2.12*. In the general case, the layers are coupled at the interfaces through internal friction (momentum transfer), although layered models of seiching in lakes and ocean flows having small vertical Ekman numbers are often used without friction and give satisfactory results. In layered models, a new function P is a substitute for the hydrostatic pressure p. It is called the Montgomery potential, defined as (Cushman-Roisin, 1994, p. 171)

$$P = p + \rho g z .$$

The horizontal pressure gradients $\partial p/\partial x$ and $\partial p/\partial y$, evaluated at constant z, become $\partial P/\partial x$ and $\partial P/\partial y$ when evaluated at constant ρ.

The density-coordinate models are generally referred to as multilayer models (for example, Laevastu, 1975; Liu and Leendertse, 1978) or isopycnic models (for example, Bleck and Boudra, 1981, 1986; Boudra and others, 1987). They are appealing for their relatively simplified mathematics and conceptually realistic approach. They are not, however, well suited to estuarine modeling, which includes a density structure and estuarine geometry that are typically very complicated. In estuaries, the pycnoclines (constant density surfaces) deviate considerably from the horizontal and tend to converge toward one another and to intersect regularly with the surface and bottom boundaries. Upwelling and downwelling flows can also occur. These situations cause severe numerical difficulties for multilayer models, as the layers must then be permitted to converge, collapse, and reappear. Bleck and Boudra (1986) have made progress in dealing with the impediments of multilayer modeling by developing an isopycnic model

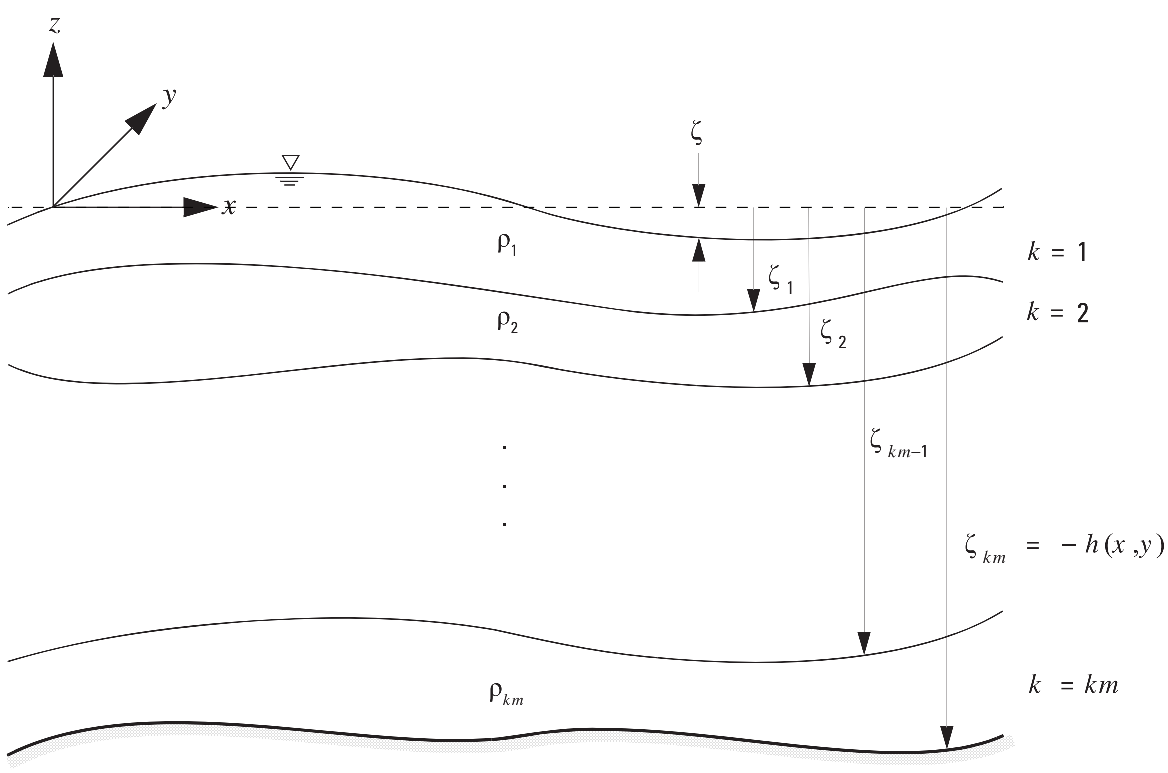

Figure 2.12. Sketch of a multilayered system.

with a special flux-corrected-transport (Zalesak, 1979) algorithm to prevent the collapsing of coordinate layers, but their approach is still not tractable for application to most estuaries. In a few instances, multilayer models have been used with some success in studies of estuarine density fronts.

The third type of coordinate system is based on a vertically “normalized” or “stretched” coordinate that is derived by transforming the *z*-coordinate to create a constant depth flow domain. This coordinate system is called the σ-coordinate system; its use generally requires a constant number of grid boxes in the vertical at all horizontal grid points in a model, independent of the water depth. This type of transformation was first proposed by Phillips (1957) for use in numerical meteorological forecasting and was later introduced for lake modeling by Freeman and others (1972) and Haq and others (1974). Several years later, applications to ocean modeling (Durance, 1976; Davies, 1980; Owen, 1980) and bay modeling (Sen Gupta and others, 1981) first appeared. Because the σ-coordinate system is so widely used in 3-D models of water bodies having variable topography, the details for the transformation of the governing equations are included in Appendix C.

The chief advantage of the σ-coordinate system is that it maps the surface and bottom into horizontal coordinate surfaces.[23] The σ numerical grid is not fixed in space but actually moves up and down with any oscillation of the free surface; in this way, it treats the dynamic free surface in a fairly straightforward manner. Its use also eliminates the need to add layers of small vertical extent to correctly resolve the currents in shallow areas. It is particularly convenient, therefore, to use this system for coastal ocean modeling when it is desirable for the vertical grid spacing to be small in the shallow waters of the continental shelf and large in the deep waters of the ocean. It is possible to use coordinate stretching within the σ-coordinate system to vary the spacing of grid points to achieve higher resolution at some point in the water column such as near the free surface or bottom (Noye and Stevens, 1987; Huang and Spaulding, 1995). Some authors (Spall and Robinson, 1990; Gerdes, 1993) have developed models using hybrid coordinate systems between the σ-coordinate and *z*-coordinate systems, which attempt to draw upon the best features of each.

In estuaries, σ-coordinate models are not always desirable because the large number of vertical grid layers needed to resolve the flow in a deep water estuarine channel may not be warranted in adjacent shallow zones which are often well-mixed vertically; in these cases, the σ grid may lead to “over-resolution” in the shallow zones (*fig. 2.13*) and significantly increase the computational cost of running a σ-coordinate model over a *z*-coordinate model.

Another drawback of the σ-transformation is that the transformation can lead to severe numerical errors in regions of rapidly changing depth such as are common in estuaries. Haney (1991) gives examples of numerical errors that a σ-coordinate ocean model produces when computing the pressure gradient force near steep topography and inadequate vertical and horizontal grid resolution. The errors are due to spatial truncation errors and a problem of “hydrostatic inconsistency” discussed by Janjic (1977). Evaluating the pressure gradients near steep slopes in σ-coordinate models involves taking a difference between two relatively large terms that often are nearly equal. The truncation errors from the approximation of each term can become greatly magnified after the terms

[23]King (1985) presented a modified σ-transformation scheme that maps only the free surface onto a horizontal surface and preserves the bottom profile. The modified transformation, although giving up some of the mathematical elegance of the original transformation, was recommended for cases where the slope of the bottom profile varies sharply.

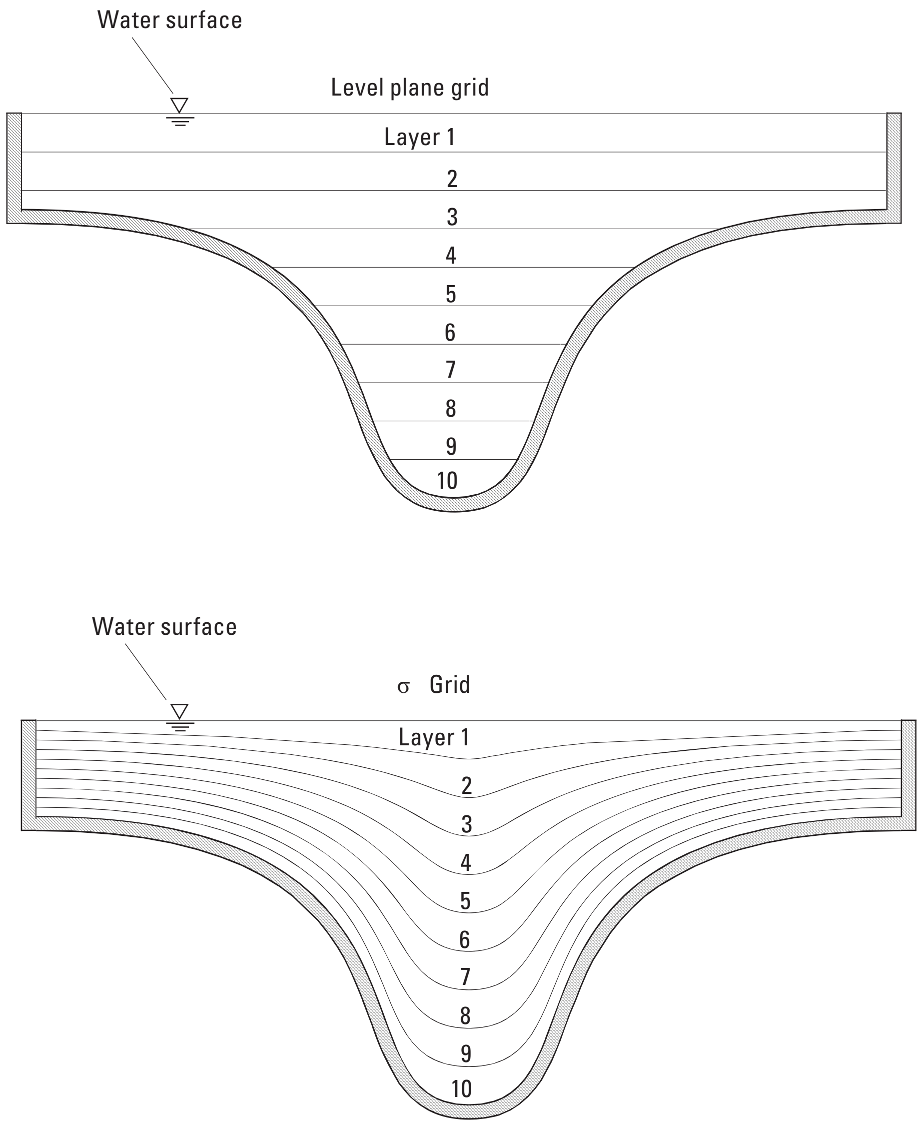

Figure 2.13. Three-dimensional model layering schemes using 10 layers to resolve the deep water channel. The σ grid has more layers than are needed in the shallow water, which generally is well mixed.

are combined. Deleersnijder and Beckers (1992) noted that truncation errors in σ models apply to the space derivatives of any variable in the 3-D equations, not just pressure. If the full approximation of the horizontal diffusive fluxes is included in a σ-coordinate model, truncation errors of the numerical approximation of these terms also can become large. Several studies have shown that a σ-coordinate model must have a high level of grid refinement to produce accurate results near irregular topography. Walters and Foreman (1992) were unable to choose a grid fine enough to obtain acceptable results using a finite-element σ-coordinate model of the Vancouver Island continental shelf. Johnson and others (1989) were forced to convert from using a σ to a z coordinate in their 3-D model of Chesapeake Bay after finding the grid resolution using the σ-coordinate model was inadequate to maintain the proper amount of salt stratification in the deep channels of the bay during lengthy model simulations. In estuaries, therefore, a z-coordinate model may be better suited for hydrodynamic modeling for reasons of both accuracy and efficiency.

3. Layer Averaging the Governing Equations

3.1 Introduction

The present model is based on a z-coordinate system, as discussed in section 2.6.2. The grid system that is used in solving the model equations is composed of layers, as is illustrated in *figure 3.1*. Because the interfaces between the layers are level planes, this kind of model is sometimes called a multilevel model (Liu and Leendertse, 1978) to distinguish it from a multilayer model which is more commonly used to identify a density-coordinate model. Because both multilevel and multilayer models are based on the concept of layers, Cheng and others (1976) referred to both types of models as multilayer models but labeled them as Type I and Type II models, respectively.

The hydrodynamic variables usually change considerably over the depth of an estuarine flow. In order to base the model computations on mass and momentum fluxes in the different layers, it is necessary to prepare the governing equations for the finite-difference method by integrating them over the height of each layer. By choosing the layer-integrated, volumetric transports as dependent variables, this approach will insure that the model equations are in a conservative form. One advantage of this form is that the depth-integrated continuity equation is linear. If primitive variables were used, terms involving products of the layer thicknesses and the horizontal velocity components would appear in the discrete form of the depth-integrated continuity equation; when the time-varying surface layer thickness and the surface velocity components are out of phase (as is typical of a standing wave), the calculations for these terms are susceptible to phase errors and amplitude errors. Another benefit of integrating the governing equations over layers is that the equations for a single-layer system reduce to a conservative form of the 2-D vertically averaged equations; thus in an area of shallow water where only one layer is required, the 3-D model becomes automatically a 2-D model without any modifications to the model coding.

The procedure for layer averaging the 3-D governing equations of Chapter 2 is defined in some detail in Chapter 3. Very few approximations are made; the set of model equations for a layered system that is the result is fully three-dimensional. The form of the layer-averaged equations is similar to that first presented by Leendertse and others (1973).

The starting point is the 3-D equations in approximately the form of equations 2.38 to 2.42 with the turbulent stresses represented by $\tau_{xx} = -\rho_0\overline{u'u'}$, $\tau_{xy} = -\rho_0\overline{u'v'}$, $\tau_{xz} = -\rho_0\overline{u'w'}$, $\tau_{yx} = -\rho_0\overline{v'u'}$, $\tau_{yy} = -\rho_0\overline{v'v'}$, and $\tau_{yz} = -\rho_0\overline{v'w'}$, and the turbulent salt fluxes represented by $J_x = -\rho_0\overline{u's'}$, $J_y = -\rho_0\overline{v's'}$, and $J_z = -\rho_0\overline{w's'}$. The introduction of the eddy viscosity and eddy diffusivity will come in a later step. The 3-D equations in the appropriate form are

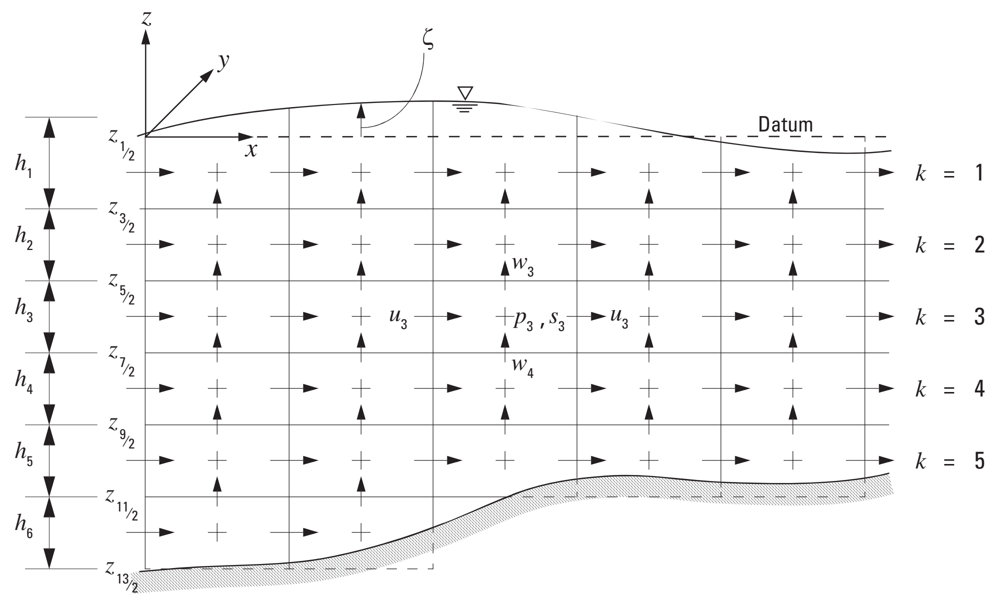

Figure 3.1. Multilevel model computational grid showing the stacked layers and the location of variables.

$$\frac{\partial u}{\partial x} + \frac{\partial v}{\partial y} + \frac{\partial w}{\partial z} = 0 \tag{3.1}$$

$$\frac{\partial u}{\partial t} + \frac{\partial uu}{\partial x} + \frac{\partial uv}{\partial y} + \frac{\partial uw}{\partial z} - fv = -\frac{1}{\rho_0}\frac{\partial p}{\partial x} + \frac{1}{\rho_0}\left(\frac{\partial \tau_{xx}}{\partial x} + \frac{\partial \tau_{xy}}{\partial y} + \frac{\partial \tau_{xz}}{\partial z}\right) \tag{3.2}$$

$$\frac{\partial v}{\partial t} + \frac{\partial uv}{\partial x} + \frac{\partial vv}{\partial y} + \frac{\partial vw}{\partial z} + fu = -\frac{1}{\rho_0}\frac{\partial p}{\partial y} + \frac{1}{\rho_0}\left(\frac{\partial \tau_{yx}}{\partial x} + \frac{\partial \tau_{yy}}{\partial y} + \frac{\partial \tau_{yz}}{\partial z}\right) \tag{3.3}$$

$$0 = -\frac{1}{\rho_0}\frac{\partial p}{\partial z} - \frac{g\rho}{\rho_0} \tag{3.4}$$

$$\frac{\partial s}{\partial t} + \frac{\partial us}{\partial x} + \frac{\partial vs}{\partial y} + \frac{\partial ws}{\partial z} = \frac{1}{\rho_0}\left(\frac{\partial J_x}{\partial x} + \frac{\partial J_y}{\partial y} + \frac{\partial J_z}{\partial z}\right) . \tag{3.5}$$

Figure 3.1 illustrates a multilevel grid for a specific case where the number of layers at each vertical location is either five or six. The layers are counted downward from the surface and are of height h_k. In general, the height of each layer is constant; the exceptions are those at the surface and the bottom. The surface layer height $h_1$varies as a function of both time and space because of the propagation of the tides and other waves. The bottom layer height varies with the changing bathymetry as a function of space only.[24] The layer types are designated as either surface, middle, or bottom. In the special case of a single layer representing the entire depth of flow, the layer will be classified as a surface layer, but the position of the bottom of this layer will vary. In the general case, the number of layers at each horizontal location is *km*. Because no wetting and drying of nodal points is considered, it is assumed that the free surface never drops below the bottom of the first layer.

[24]Because the test case included in Chapter 5 of this report is for a constant-depth basin, the number of layers (*km*) does not vary with horizontal location and the bottom layer is a constant height.

For present purposes, the heights of all middle layers are equal, although this is not a requirement; for generality, the designation of a height (h_k) that could vary from layer to layer will be retained for these layers. The use of equal layer heights permits a convenient implementation of a vertical finite-difference approximation that is second-order accurate in space. If uneven layer heights are chosen, the vertical numerical approximation will become only first-order accurate. The changing heights of the surface and bottom layers will actually introduce some first-order error into the approximation of the vertical mixing terms, but the error in most cases is minor.

The average of any 3-D variable over a layer k will be indicated by a subscript k. The layer averages for the model variables of horizontal velocity, pressure, density, and salinity are defined as

$$u_k = \frac{1}{h_k}\int_{z_{k+1/2}}^{z_{k-1/2}} u\ dz \ , \qquad v_k = \frac{1}{h_k}\int_{z_{k+1/2}}^{z_{k-1/2}} v\ dz \ , \qquad p_k = \frac{1}{h_k}\int_{z_{k+1/2}}^{z_{k-1/2}} p\ dz \ ,$$

$$\rho_k = \frac{1}{h_k}\int_{z_{k+1/2}}^{z_{k-1/2}} \rho\ dz \ , \qquad \text{and} \qquad s_k = \frac{1}{h_k}\int_{z_{k+1/2}}^{z_{k-1/2}} s\ dz \ , \tag{3.6}$$

where the integration limits $z_{k-1/2}$ and $z_{k+1/2}$ define the z coordinates of the layer interfaces. The coordinate $z_{1/2} = \zeta$ represents the free surface elevation, and $z_{km+1/2} = z_b$ represents the bottom elevation measured from the datum.

Over the height of each layer, the 3-D variable can be represented as the sum of the average value for that layer and a deviation from that average at the point (x, y, z) (*fig. 3.2*):

$$\begin{aligned}
u(x, y, z, t) &= u_k(x, y, t) + u''_k(x, y, z, t)\ , \\
v(x, y, z, t) &= v_k(x, y, t) + v''_k(x, y, z, t)\ , \\
p(x, y, z, t) &= p_k(x, y, t) + p''_k(x, y, z, t), \\
\rho(x, y, z, t) &= \rho_k(x, y, t) + \rho''_k(x, y, z, t)\ , \text{ and} \\
s(x, y, z, t) &= s_k(x, y, t) + s''_k(x, y, z, t)\ .
\end{aligned} \tag{3.7}$$

The integral of the deviation term over a layer will by definition equal zero; for example, $\int_{z_{k+1/2}}^{z_{k-1/2}} u''_k\ dz = 0$. The integral of a variable that already is a layer average yields a product of the layer-average variable and the layer thickness; for example, $\int_{z_{k+1/2}}^{z_{k-1/2}} u_k\ dz = u_k h_k$. The quantities $u_k h_k$ and $v_k h_k$ are volumetric transports and are represented by the symbols U_k and V_k, respectively. The volumetric transports are dependent variables in the model; the velocities u_k and v_k are computed from the volumetric transports by dividing by h_k.

Leibnitz' rule relates the derivative of a 3-D variable to its layer average. For a generic variable $F(x, y, t)$, the Leibnitz rule, applied to an integral over a layer, produces

$$\frac{\partial}{\partial x}\int_{z_{k+1/2}}^{z_{k-1/2}} F\,dz = \int_{z_{k+1/2}}^{z_{k-1/2}} \frac{\partial F}{\partial x}\,dz + F_{k-1/2}\frac{\partial z_{k-1/2}}{\partial x} - F_{k+1/2}\frac{\partial z_{k+1/2}}{\partial x} \tag{3.8}$$

or, after rearranging and inserting F_k,

$$\int_{z_{k+1/2}}^{z_{k-1/2}} \frac{\partial F}{\partial x}\,dz = \frac{\partial}{\partial x}(h_k F_k) - F_{k-1/2}\frac{\partial z_{k-1/2}}{\partial x} + F_{k+1/2}\frac{\partial z_{k+1/2}}{\partial x}\ . \tag{3.9}$$

The integral over a layer for a product of two variables, F and G, is related to the product of the two layer-averaged variables as follows:

$$\begin{aligned} \langle FG\rangle &= \langle (F_k + F_k'')(G_k + G_k'')\rangle \\ &= \langle F_k G_k\rangle + \langle F_k G_k''\rangle + \langle F_k'' G_k\rangle + \langle F_k'' G_k''\rangle \\ &= h_k F_k G_k + \langle F_k'' G_k''\rangle \quad . \end{aligned} \tag{3.10}$$

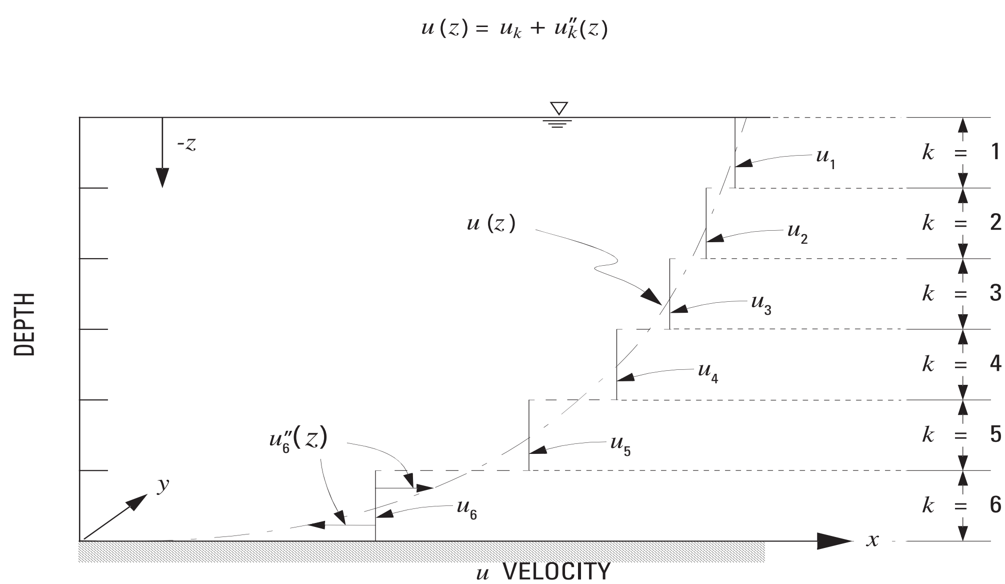

Figure 3.2. Diagram of a 3-dimensional horizontal velocity profile $u(z)$ approximated by layer-averaged values u_k (eq. 3.6). The deviation of u_k from u is u_k''.

Here < > is shorthand notation for the layer integral $\int_{z_{k+½}}^{z_{k-½}} (\ )\, dz$. The integral of a term involving a derivative of z can be simplified by using the fundamental theorem of calculus. Thus

$$\int_{z_{k+½}}^{z_{k-½}} \frac{\partial F}{\partial z}\, dz = F_{k-½} - F_{k+½}\,, \tag{3.11}$$

where the fractional subscripts $k-½$ and $k+½$ indicate that the variable F is evaluated at the interface between two layers. Formally, an interface value is defined by $F_{k+½} = [F(x, y, z, t)]_{z = z_{k+½}}$. For computational purposes, the interface values can be evaluated as the simple average of the adjacent layer-averages of the same variables, such as

$$F_{k+½} = \frac{1}{2}(F_k + F_{k+1}) \tag{3.12}$$

or, if unequal layer heights are used, the formula

$$F_{k+½} = \theta F_{k+1} + (1-\theta)F_k \tag{3.13}$$

can be applied with $\theta = h_k/(h_k + h_{k+1})$ to improve the accuracy of interpolations.

3.2 Continuity Equation

Integration of the continuity equation over a layer yields

$$\int_{z_{k+½}}^{z_{k-½}} \frac{\partial u}{\partial x}\, dz + \int_{z_{k+½}}^{z_{k-½}} \frac{\partial v}{\partial y}\, dz + \int_{z_{k+½}}^{z_{k-½}} \frac{\partial w}{\partial z}\, dz = 0 \tag{3.14}$$

or, after substitution of equations 3.9 and 3.11,

$$\frac{\partial U_k}{\partial x} + \frac{\partial V_k}{\partial y} - \left[u_{k-½}\frac{\partial z_{k-½}}{\partial x} + v_{k-½}\frac{\partial z_{k-½}}{\partial y} - w_{k-½}\right]$$
$$+ \left[u_{k+½}\frac{\partial z_{k+½}}{\partial x} + v_{k+½}\frac{\partial z_{k+½}}{\partial y} - w_{k+½}\right] = 0\,. \tag{3.15}$$

The bracketed terms in equation 3.15 are simplified by applying the boundary conditions for each layer. With the exception of the free surface and the bottom of the estuary, the layer interfaces are horizontal; thus,

$$\frac{\partial z_{k\pm½}}{\partial x} = 0\,. \tag{3.16}$$

At the free surface and the bottom, the kinematic boundary conditions presented in Chapter 2 (eqs. 2.52 and 2.59) are applicable. These conditions, written in the present notation, are

$$\frac{\partial z_{½}}{\partial t} + u_{½}\frac{\partial z_{½}}{\partial x} + v_{½}\frac{\partial z_{½}}{\partial y} - w_{½} = 0 \tag{3.17}$$

and

$$u_{km+½}\frac{\partial z_{km+½}}{\partial x} + v_{km+½}\frac{\partial z_{km+½}}{\partial y} - w_{km+½} = 0\,, \tag{3.18}$$

where the subscripts $½$ and $km+½$ refer to the free surface and the bottom, respectively. Applying the boundary conditions to equation 3.15 results in the following forms of the continuity equations for surface, middle, and bottom layers:
Surface layer,

$$\frac{\partial\zeta}{\partial t} - w_{3/2} + \frac{\partial U_1}{\partial x} + \frac{\partial V_1}{\partial y} = 0\ ; \tag{3.19}$$

Middle layers,

$$w_{k-½} - w_{k+½} + \frac{\partial U_k}{\partial x} + \frac{\partial V_k}{\partial y} = 0 \qquad k = 2, 3, \ldots, km-1\,; \tag{3.20}$$

Bottom layer,

$$w_{km-½} + \frac{\partial U_{km}}{\partial x} + \frac{\partial V_{km}}{\partial y} = 0\ . \tag{3.21}$$

In equation 3.19, the substitution $\zeta = z_{1/2}$ has been made to use conventional notation. By combining equations 3.20 and 3.21, it is possible to write an expression for the vertical velocity component at an interface $k - 1/2$ as

$$w_{k-½} = -\sum_{k=2}^{km}\left\{\frac{\partial U_k}{\partial x} + \frac{\partial V_k}{\partial y}\right\}. \tag{3.22}$$

This expression can be evaluated for $w_{3/2}$ and substituted into equation 3.19 to yield this expression for the water surface elevation:

$$\frac{\partial\zeta}{\partial t} + \sum_{k=1}^{km}\left\{\frac{\partial U_k}{\partial x} + \frac{\partial V_k}{\partial y}\right\} = 0\,. \tag{3.23}$$

A variation of equation 3.23 is obtained by integrating the continuity equation over the entire depth of flow. This is written

$$\frac{\partial\zeta}{\partial t} + \frac{\partial}{\partial x}\left(\sum_{k=1}^{km} U_k\right) + \frac{\partial}{\partial y}\left(\sum_{k=1}^{km} V_k\right) = 0\,, \tag{3.24}$$

where the quantities $\sum_{k=1}^{km} U_k$ and $\sum_{k=1}^{km} V_k$ represent the vertically-integrated components of the volume-transport velocity. Equation 3.24 is the actual form of the continuity equation that is used in the model in determining the water surface elevation.

3.3 Momentum Equations

In developing the layer-averaged form for the horizontal momentum equations, consider first integrating the acceleration terms over a layer for the *x*-component equation:

$$\int_{z_{k+½}}^{z_{k-½}} \frac{\partial u}{\partial t}\,dz + \int_{z_{k+½}}^{z_{k-½}} \frac{\partial uu}{\partial x}\,dz + \int_{z_{k+½}}^{z_{k-½}} \frac{\partial uv}{\partial y}\,dz + \int_{z_{k+½}}^{z_{k-½}} \frac{\partial uw}{\partial z}\,dz \quad . \tag{3.25}$$

Applying equations 3.9 and 3.11 gives

$$\frac{\partial U_k}{\partial t} + \frac{\partial}{\partial x}\int_{z_{k+½}}^{z_{k-½}} uu\,dz + \frac{\partial}{\partial y}\int_{z_{k+½}}^{z_{k-½}} uv\,dz - u_{k-½}\left[\frac{\partial z_{k-½}}{\partial t} + u_{k-½}\frac{\partial z_{k-½}}{\partial x} + v_{k-½}\frac{\partial z_{k-½}}{\partial y} - w_{k-½}\right]$$

$$+ u_{k+½}\left[\;0\; + u_{k+½}\frac{\partial z_{k+½}}{\partial x} + v_{k+½}\frac{\partial z_{k+½}}{\partial y} - w_{k+½}\right] . \tag{3.26}$$

At the free surface and bottom, the bracketed terms disappear because of the kinematic boundary conditions. At all other layer interfaces, the derivatives of $z_{k-½}$ and $z_{k+½}$ equal zero. Thus, the simplified form of 3.26 applicable to all layers is

$$\frac{\partial U_k}{\partial t} + \frac{\partial}{\partial x}\int_{z_{k+½}}^{z_{k-½}} uu\,dz + \frac{\partial}{\partial y}\int_{z_{k+½}}^{z_{k-½}} uv\,dz + (uw)_{k-½} - (uw)_{k+½} \;, \tag{3.27}$$

subject to[25] $(uw)_{½} = (uw)_{km+½} = 0$. Substituting equation 3.10 for the integral expressions in 3.27 and noting that $u''_k = u - u_k$ and $v''_k = v - v_k$ (see eq. 3.2) gives

$$\frac{\partial U_k}{\partial t} + \frac{\partial (Uu)_k}{\partial x} + \frac{\partial (Vu)_k}{\partial y} + (uw)_{k-½} - (uw)_{k+½}$$

$$+ \frac{\partial}{\partial x}\int_{z_{k+½}}^{z_{k-½}} (u-u_k)^2\,dz + \frac{\partial}{\partial y}\int_{z_{k+½}}^{z_{k-½}} (u-u_k)(v-v_k)\,dz \;, \tag{3.28}$$

[25]The quantities $(uw)_{½}$ and $(uw)_{km+½}$ are not literally zero for the general case of a sloping free surface and bottom boundary (with slip allowed). These quantities are set to zero in equation 3.27 to force the bracketed terms in expression 3.26 to vanish at the free surface and bottom as required by the kinematic boundary conditions.

which is the desired form for the x-component, layer-averaged advection terms. The corresponding expression for the y-momentum equation is

$$\frac{\partial V_k}{\partial t} + \frac{\partial (Uv)_k}{\partial x} + \frac{\partial (Vv)_k}{\partial y} + (vw)_{k-1/2} - (vw)_{k+1/2}$$

$$+ \frac{\partial}{\partial x} \int_{z_{k+1/2}}^{z_{k-1/2}} (u - u_k)(v - v_k)\, dz + \frac{\partial}{\partial y} \int_{z_{k+1/2}}^{z_{k-1/2}} (v - v_k)^2\, dz \,. \tag{3.29}$$

The two integral expressions in each of 3.28 and 3.29 account for the variation of the 3-D velocity over a layer and sometimes are referred to as momentum dispersion terms. These terms, although typically quite small, are theoretically zero only if the velocity does not vary with z over a layer. These terms can be formally represented by introducing momentum correction coefficients into the advection terms in a way which is similar to the coefficients introduced into a two-dimensional model by Pritchard (1971b, p. 31). Because little information is available to estimate momentum coefficients for a layered model, this approach is not followed here and the terms will be dropped. If necessary, one could add these terms into the horizontal stresses and adjust the value assigned to the horizontal eddy viscosity.

The integration of the Coriolis term in the x- and y-momentum equations over a layer is straightforward and results in

$$-f \int_{z_{k+1/2}}^{z_{k-1/2}} v\, dz = -f V_k \tag{3.30}$$

and

$$+f \int_{z_{k+1/2}}^{z_{k-1/2}} u\, dz = +f U_k \,. \tag{3.31}$$

Integration of the pressure-gradient term over the depth of a layer proceeds as follows. Considering the x-direction gradient, after integration and application of Leibnitz' rule, the result is

$$\frac{1}{\rho_0} \int_{z_{k+1/2}}^{z_{k-1/2}} \frac{\partial p}{\partial x}\, dz = \frac{1}{\rho_0}\left[\frac{\partial h_k p_k}{\partial x} - p_{k-1/2}\frac{\partial z_{k-1/2}}{\partial x} + p_{k+1/2}\frac{\partial z_{k+1/2}}{\partial x}\right] . \tag{3.32}$$

At the free surface, it is assumed that the atmospheric pressure is a zero gage pressure so $p_{1/2} = 0$. After again recalling that $\partial z_{k \pm 1/2}/\partial x = 0$ at layer interfaces, the right-side expression for the surface and middle layers reduces to

$$\frac{1}{\rho_0} \frac{\partial h_k p_k}{\partial x} \,, \tag{3.33}$$

and for the bottom layer to

$$\frac{1}{\rho_0}\frac{\partial h_{km}p_{km}}{\partial x} + \frac{p_{km+½}}{\rho_0}\frac{\partial z_{km+½}}{\partial x} , \qquad (3.34)$$

where $p_{km+½}$ represents the pressure at the bottom of the bottom layer. Whenever h_k is a constant, it can be moved outside the differentiation sign. Thus, for a middle layer the term can be rewritten as

$$\frac{h_k}{\rho_0}\frac{\partial p_k}{\partial x} \qquad k = 2, 3, \ldots, km-1 . \qquad (3.35)$$

For a surface layer, h_k is not constant, so the expression for 3.33 expands into

$$\frac{1}{\rho_0}\frac{\partial h_1 p_1}{\partial x} = \frac{h_1}{\rho_0}\frac{\partial p_1}{\partial x} + \frac{p_1}{\rho_0}\frac{\partial \zeta}{\partial x} ,$$

which, after substitution for p_1 in the second term on the right side, becomes[26]

$$\frac{1}{\rho_0}\frac{\partial h_1 p_1}{\partial x} = \frac{h_1}{\rho_0}\frac{\partial p_1}{\partial x} + \frac{h_1}{\rho_0}\frac{g\rho_1}{2}\frac{\partial \zeta}{\partial x} + \frac{g}{\rho_0 h_1}\frac{\partial \zeta}{\partial x}\int_{z_{3/2}}^{\zeta}\int_{z}^{\zeta}(\rho - \rho_1)\, dz'dz . \qquad (3.36)$$

[26]The average pressure p_1 for the surface layer is defined by integrating the hydrostatic pressure $p = g\int_z^{\zeta}\rho\, dz'$ over the surface layer as follows:

$$p_1 = \frac{1}{h_1}\int_{z_{3/2}}^{\zeta} p\, dz = \frac{g}{h_1}\int_{z_{3/2}}^{\zeta}\int_{z}^{\zeta}\rho\, dz'dz ,$$

then $\rho = \rho_1 + \rho''_1$ is substituted to obtain

$$p_1 = \frac{g\rho_1}{h_1}\int_{z_{3/2}}^{\zeta}\int_{z}^{\zeta} dz'dz + \frac{g}{h_1}\int_{z_{3/2}}^{\zeta}\int_{z}^{\zeta}\rho'' dz'dz$$

$$= \frac{1}{2}g\rho_1 h_1 + \frac{g}{h_1}\int_{z_{3/2}}^{\zeta}\int_{z}^{\zeta}(\rho - \rho_1)dz'dz .$$

For a bottom layer, the expression using 3.34 can be shown to be

$$\frac{1}{\rho_0}\frac{\partial h_{km}p_{km}}{\partial x} + \frac{p_{km+1/2}}{\rho_0}\frac{\partial z_{km+1/2}}{\partial x} = \frac{h_{km}}{\rho_0}\frac{\partial p_{km}}{\partial x} - \frac{h_{km}}{\rho_0}\frac{g\rho_{km}}{2}\frac{\partial h_{km}}{\partial x} + \frac{g}{\rho_0 h_{km}}\frac{\partial h_{km}}{\partial x}\int_{z_{km+1/2}}^{z_{km-1/2}}\int_{z}^{z_{km-1/2}}(\rho - \rho_{km})dz'\,dz. \tag{3.37}$$

The two double integral terms in equations 3.36 and 3.37, containing the three-dimensional density ρ, are zero if the density is assumed to be uniform vertically across the surface and bottom layers. An approximation is introduced if these terms are neglected when the vertical density varies continuously within the surface and bottom layers. The error from the approximation is small if the surface and bottom layer heights are small enough to avoid a large change in density across the layers. If the near-surface and bottom waters of an estuary are vertically mixed by surface wind and bottom friction, respectively, the error of the approximation is eliminated. These terms are neglected here, as is customary. In summary, the x-momentum pressure gradient term for the surface, middle, and bottom layers is approximated by the following expressions:

Surface layer,

$$\frac{1}{\rho_0}\int_{z_{3/2}}^{\zeta}\frac{\partial p}{\partial x}\,dz = \frac{h_1}{\rho_0}\left(\frac{\partial p_1}{\partial x} + \frac{g\rho_1}{2}\frac{\partial \zeta}{\partial x}\right); \tag{3.38}$$

Middle layers,

$$\frac{1}{\rho_0}\int_{z_{k+1/2}}^{z_{k-1/2}}\frac{\partial p}{\partial x}\,dz = \frac{h_k}{\rho_0}\frac{\partial p_k}{\partial x} \qquad k = 2, 3, \ldots, km-1\,; \tag{3.39}$$

Bottom layer,

$$\frac{1}{\rho_0}\int_{z_{km+1/2}}^{z_{km-1/2}}\frac{\partial p}{\partial x}\,dz = \frac{h_{km}}{\rho_0}\left(\frac{\partial p_{km}}{\partial x} - \frac{g\rho_{km}}{2}\frac{\partial h_{km}}{\partial x}\right). \tag{3.40}$$

For the special case of a single layer representing the entire depth of flow, the result is

$$\frac{1}{\rho_0}\int_{z_{3/2}}^{\zeta}\frac{\partial p}{\partial x}\,dz = \frac{h_1}{\rho_0}\left(\frac{\partial p_1}{\partial x} + \frac{g\rho_1}{2}\frac{\partial \zeta}{\partial x} + \frac{g\rho_1}{2}\frac{\partial z_{3/2}}{\partial x}\right), \tag{3.41}$$

where $z_{3/2}$ represents the location of the bottom. Similar expressions are available for the pressure gradient term in the y-momentum equation.

The average pressure in any layer can be related to the average pressure in the layer above through the hydrostatic pressure equation, which is approximated by

$$p_k = p_{k-1} + g\rho_{k-½}h_{k-½}\,.$$

Here $h_{k-½}$ is the average of the heights for layers k - 1 and k and represents the vertical distance between the centers of the two layers. By differentiating this equation with respect to x and y, the pressure gradients for one layer can be determined from the layer above. For the x-direction pressure gradient, the result is

$$\begin{aligned}\frac{\partial p_k}{\partial x} &= \frac{\partial p_{k-1}}{\partial x} + g\frac{\partial h_{k-½}\rho_{k-½}}{\partial x} \\ &= \frac{\partial p_{k-1}}{\partial x} + gh_{k-½}\frac{\partial \rho_{k-½}}{\partial x} + g\rho_{k-½}\frac{\partial h_{k-½}}{\partial x} \\ &= \frac{\partial p_{k-1}}{\partial x} + \frac{gh_{k-1}}{2}\frac{\partial \rho_{k-1}}{\partial x} + \frac{gh_k}{2}\frac{\partial \rho_k}{\partial x} + \frac{g\rho_{k-1}}{2}\frac{\partial h_{k-1}}{\partial x} + \frac{g\rho_k}{2}\frac{\partial h_k}{\partial x}\,.\end{aligned} \tag{3.42}$$

In the surface layer, the x pressure gradient is approximated by

$$\frac{\partial p_1}{\partial x} = \frac{g\rho_1}{2}\frac{\partial \zeta}{\partial x} + \frac{gh_1}{2}\frac{\partial \rho_1}{\partial x}\,. \tag{3.43}$$

Successively substituting equations 3.43 and 3.42 into equations 3.38 to 3.40, a general formula for the x pressure gradient term can be seen by induction to be

$$\frac{1}{\rho_0}\int_{z_{k+½}}^{z_{k-½}} \frac{\partial p}{\partial x}\,dz = \frac{h_k}{\rho_0}\left[g\rho_1\frac{\partial \zeta}{\partial x} + \frac{gh_1}{2}\frac{\partial \rho_1}{\partial x} + \sum_{m=2}^{k}\left(\frac{gh_{m-1}}{2}\frac{\partial \rho_{m-1}}{\partial x} + \frac{gh_m}{2}\frac{\partial \rho_m}{\partial x}\right)\right] \tag{3.44}$$

where the summation is omitted for $k = 1$. The corresponding formula for the y pressure gradient term is

$$\frac{1}{\rho_0}\int_{z_{k+½}}^{z_{k-½}} \frac{\partial p}{\partial y}\,dz = \frac{h_k}{\rho_0}\left[g\rho_1\frac{\partial \zeta}{\partial y} + \frac{gh_1}{2}\frac{\partial \rho_1}{\partial y} + \sum_{m=2}^{k}\left(\frac{gh_{m-1}}{2}\frac{\partial \rho_{m-1}}{\partial y} + \frac{gh_m}{2}\frac{\partial \rho_m}{\partial y}\right)\right]\,. \tag{3.45}$$

Now consider the integration of the stress terms in equations 3.2 and 3.3 over a layer. After integration and application of equations 3.9 and 3.11 to the x-component terms, the result is

$$\begin{aligned}&\frac{1}{\rho_0}\int_{z_{k+½}}^{z_{k-½}} \frac{\partial \tau_{xx}}{\partial x}\,dz + \frac{1}{\rho_0}\int_{z_{k+½}}^{z_{k-½}} \frac{\partial \tau_{xy}}{\partial x}\,dz + \frac{1}{\rho_0}\int_{z_{k+½}}^{z_{k-½}} \frac{\partial \tau_{xz}}{\partial x}\,dz = \\ &\frac{1}{\rho_0}\left(\frac{\partial (h\tau_{xx})_k}{\partial x} + \frac{\partial (h\tau_{xy})_k}{\partial y} + \left[-(\tau_{xx})_{k-½}\frac{\partial z_{k-½}}{\partial x} - (\tau_{xy})_{k-½}\frac{\partial z_{k-½}}{\partial y} + (\tau_{xz})_{k-½}\right]\right. \\ &\qquad\left. - \left[-(\tau_{xx})_{k+½}\frac{\partial z_{k+½}}{\partial x} - (\tau_{xy})_{k+½}\frac{\partial z_{k+½}}{\partial y} + (\tau_{xz})_{k+½}\right]\right)\,.\end{aligned} \tag{3.46}$$

At the free surface and bottom, the dynamic boundary conditions from Chapter 2 (eqs. 2.54 and 2.60) can be applied to equation 3.46 in the form

$$\tau_{xs} = -(\tau_{xx})_{½}\frac{\partial z_{½}}{\partial x} - (\tau_{xy})_{½}\frac{\partial z_{½}}{\partial y} + (\tau_{xz})_{½} \tag{3.47}$$

and

$$\tau_{xb} = -(\tau_{xx})_{km+½}\frac{\partial z_{km+½}}{\partial x} - (\tau_{xy})_{km+½}\frac{\partial z_{km+½}}{\partial y} + (\tau_{xz})_{km+½} \quad . \tag{3.48}$$

At all other layer interfaces, equation 3.16 again applies so that the right side of 3.46 reduces to

$$\frac{1}{\rho_0}\left(\frac{\partial(h\tau_{xx})_k}{\partial x} + \frac{\partial(h\tau_{xy})_k}{\partial y} + (\tau_{xz})_{k-½} - (\tau_{xz})_{k+½}\right), \tag{3.49}$$

subject to the redefinition that $(\tau_{xz})_{½} = \tau_{xs}$ and $(\tau_{xz})_{km+½} = \tau_{xb}$. It is now convenient to introduce the concept of the horizontal eddy viscosity in the form

$$(\tau_{xx})_k = \rho_0\left(A_H\frac{\partial u}{\partial x}\right)_k \qquad (\tau_{xy})_k = \rho_0\left(A_H\frac{\partial u}{\partial y}\right)_k , \tag{3.50}$$

so that equation 3.49 becomes

$$\frac{\partial}{\partial x}\left(A_H h\frac{\partial u}{\partial x}\right)_k + \frac{\partial}{\partial y}\left(A_H h\frac{\partial u}{\partial y}\right)_k + \frac{(\tau_{xz})_{k-½}}{\rho_0} - \frac{(\tau_{xz})_{k+½}}{\rho_0} , \tag{3.51}$$

which is the final form of the layer-averaged stress terms. The expression for the *y*-momentum stress terms is

$$\frac{\partial}{\partial x}\left(A_H h\frac{\partial v}{\partial x}\right)_k + \frac{\partial}{\partial y}\left(A_H h\frac{\partial v}{\partial y}\right)_k + \frac{(\tau_{yz})_{k-½}}{\rho_0} - \frac{(\tau_{yz})_{k+½}}{\rho_0} \tag{3.52}$$

subject to $(\tau_{yz})_{½} = \tau_{ys}$ and $(\tau_{yz})_{km+½} = \tau_{yb}$.

3.4 Salt Transport Equation

The steps in deriving the layer-averaged salt transport equation are similar to those used on the momentum equations. Integration of the advection terms in equation 3.5 results in

$$\int_{z_{k+½}}^{z_{k-½}} \frac{\partial s}{\partial t}\,dz + \int_{z_{k+½}}^{z_{k-½}} \frac{\partial us}{\partial x}\,dz + \int_{z_{k+½}}^{z_{k-½}} \frac{\partial vs}{\partial y}\,dz + \int_{z_{k+½}}^{z_{k-½}} \frac{\partial ws}{\partial z}\,dz =$$

$$\frac{\partial(hs)_k}{\partial t} + \frac{\partial(uhs)_k}{\partial x} + \frac{\partial(vhs)_k}{\partial y} + (ws)_{k-½} - (ws)_{k+½}$$

$$+ \frac{\partial}{\partial x}\int_{z_{k+½}}^{z_{k-½}} (u-u_k)(s-s_k)\,dz + \frac{\partial}{\partial y}\int_{z_{k+½}}^{z_{k-½}} (v-v_k)(s-s_k)dz \quad , \tag{3.53}$$

which is very similar in form to the momentum acceleration terms expressed by 3.28 and 3.29. Equation 3.53 is valid for all layers subject to the boundary conditions of $(ws)_{½} = (ws)_{km+½} = 0$, which cause the kinematic conditions at the free surface and the bottom of the water column to be satisfied; the kinematic conditions prevent the advective flux of salt through the boundaries. Integration of the turbulent diffusion terms in equation 3.5 results in

$$\frac{1}{\rho_0}\left(\frac{\partial(hJ_x)_k}{\partial x} + \frac{\partial(hJ_y)_k}{\partial y} + (J_z)_{k-½} - (J_z)_{k+½}\right), \tag{3.54}$$

which is subject to the boundary conditions of no turbulent salt flux at the water column free surface and bottom; this condition is enforced by setting[27] $(J_z)_{½} = (J_z)_{km+½} = 0$. Substituting the concept of a horizontal eddy diffusivity in the form

$$(J_x)_k = \rho_0\left(D_H\frac{\partial s}{\partial x}\right)_k \qquad (J_y)_k = \rho_0\left(D_H\frac{\partial s}{\partial y}\right)_k \tag{3.55}$$

into 3.54 results in

$$\frac{\partial}{\partial x}\left(D_H h\frac{\partial s}{\partial x}\right)_k + \frac{\partial}{\partial y}\left(D_H h\frac{\partial s}{\partial y}\right)_k + \frac{(J_z)_{k-½}}{\rho_0} - \frac{(J_z)_{k+½}}{\rho_0} \tag{3.56}$$

which is the final form of the layer-averaged turbulent salt flux terms. The form of 3.56 is close to that of the layer-averaged turbulent stress terms in the momentum equations expressed by 3.51 and 3.52.

The two integral terms in equation 3.53 are salt dispersion terms representing advective fluxes of salt in the x- and y-directions caused by vertical non-uniformities of the velocity and salinity over a layer. If the 3-D velocity and salt concentration do not vary with z over a layer, these terms will vanish. In general, if layer heights are small enough to avoid a large change in velocity and salinity across the layers, these terms will be small. Here these terms will be dropped. If for a certain application these terms are significant, the magnitude of D_H can be adjusted.

---

[27]The conditions of no turbulent flux of salt at the water column free surface and bottom are formally represented by

$$0 = -(J_x)_{½}\frac{\partial z_{½}}{\partial x} - (J_y)_{½}\frac{\partial z_{½}}{\partial y} + (J_z)_{½}$$

and

$$0 = -(J_x)_{km+½}\frac{\partial z_{km+½}}{\partial x} - (J_y)_{km+½}\frac{\partial z_{km+½}}{\partial y} + (J_z)_{km+½}.$$

Because the terms involving the boundary slopes are already eliminated in 3.54, the conditions are satisfied simply by requiring that $(J_z)_{½} = (J_z)_{km+½} = 0$ in 3.56.

3.5 Equation Summary

A recapitulation of the layer-averaged form of the governing equations follows:

Continuity equations,

$$\frac{\partial \zeta}{\partial t} + \frac{\partial}{\partial x}\left(\sum_{k=1}^{km} U_k\right) + \frac{\partial}{\partial y}\left(\sum_{k=1}^{km} V_k\right) = 0 \text{ and} \tag{3.57}$$

$$(w)\Big|_{k+1/2}^{k-1/2} = -\frac{\partial U_k}{\partial x} - \frac{\partial V_k}{\partial y} \qquad k = 2, 3, \ldots, km\ ; \tag{3.58}$$

Momentum equations,

$$\begin{aligned}&\frac{\partial U_k}{\partial t} + \frac{\partial (Uu)_k}{\partial x} + \frac{\partial (Vu)_k}{\partial y} + (uw)\Big|_{k+1/2}^{k-1/2} - fV_k + \frac{h_k}{\rho_k} g \rho_1 \frac{\partial \zeta}{\partial x} = \\ &-\frac{h_k}{\rho_k}\left[\frac{gh_1}{2}\frac{\partial \rho_1}{\partial x} + \sum_{m=2}^{k}\left(\frac{gh_{m-1}}{2}\frac{\partial \rho_{m-1}}{\partial x} + \frac{gh_m}{2}\frac{\partial \rho_m}{\partial x}\right)\right] + \frac{\partial}{\partial x}\left(A_H h \frac{\partial u}{\partial x}\right)_k + \frac{\partial}{\partial y}\left(A_H h \frac{\partial u}{\partial y}\right)_k + \left(\frac{\tau_{xz}}{\rho}\right)\Bigg|_{k+1/2}^{k-1/2}\end{aligned} \tag{3.59}$$

and

$$\begin{aligned}&\frac{\partial V_k}{\partial t} + \frac{\partial (Uv)_k}{\partial x} + \frac{\partial (Vv)_k}{\partial y} + (vw)\Big|_{k+1/2}^{k-1/2} + fU_k + \frac{h_k}{\rho_k} g \rho_1 \frac{\partial \zeta}{\partial y} = \\ &-\frac{h_k}{\rho_k}\left[\frac{gh_1}{2}\frac{\partial \rho_1}{\partial y} + \sum_{m=2}^{k}\left(\frac{gh_{m-1}}{2}\frac{\partial \rho_{m-1}}{\partial y} + \frac{gh_m}{2}\frac{\partial \rho_m}{\partial y}\right)\right] + \frac{\partial}{\partial x}\left(A_H h \frac{\partial v}{\partial x}\right)_k + \frac{\partial}{\partial y}\left(A_H h \frac{\partial v}{\partial y}\right)_k + \left(\frac{\tau_{yz}}{\rho}\right)\Bigg|_{k+1/2}^{k-1/2};\end{aligned} \tag{3.60}$$

Salt transport equation,

$$\frac{\partial (hs)_k}{\partial t} + \frac{\partial (uhs)_k}{\partial x} + \frac{\partial (vhs)_k}{\partial y} + (ws)\Big|_{k+1/2}^{k-1/2} = \frac{\partial}{\partial x}\left(D_H h \frac{\partial s}{\partial x}\right)_k + \frac{\partial}{\partial y}\left(D_H h \frac{\partial s}{\partial y}\right)_k + \left(\frac{J_z}{\rho}\right)\Bigg|_{k+1/2}^{k-1/2}. \tag{3.61}$$

The notation $(\ )\big|_{k+1/2}^{k-1/2}$ represents the difference between interface values for a layer. The layer-averaged density ρ_k has been substituted for ρ_0 in the denominator of the pressure, vertical stress, and vertical salt flux terms; this substitution requires little effort to implement in the numerical model and reduces any error caused by the Boussinesq approximation. Except as noted for equation 3.58, this set of equations applies for all layers; the free surface and the bottom boundary conditions are satisfied by defining $w_{km+1/2} = 0$, $(uw)_{1/2} = (uw)_{km+1/2} = 0$, $(vw)_{1/2} = (vw)_{km+1/2} = 0$, $(\tau_{xz}, \tau_{yz})_{1/2} = (\tau_{xs}, \tau_{ys})$, $(\tau_{xz}, \tau_{yz})_{km+1/2} = (\tau_{xb}, \tau_{yb})$, $(ws)_{1/2} = (ws)_{km+1/2} = 0$, and $(J_z)_{1/2} = (J_z)_{km+1/2} = 0$. As noted, the summation term in equations 3.59 and 3.60 is omitted for a surface layer ($k = 1$). Equations 3.57 to 3.61 are the 3-D equations that are discretized by using a finite-difference method in the next chapter.

4. Finite-difference Formulation

4.1 Introduction

This chapter describes the semi-implicit finite-difference formulation used on the 3-D governing equations of Chapter 3. The details of the 3-D formulation begin in section 4.3.

The semi-implicit method is a general time-integration technique that can be implemented by various choices for a finite-difference scheme. One of the fundamental choices is between schemes involving either two or three time levels in the finite-difference equations. There are 3-D, semi-implicit, estuarine and coastal ocean models based on both two-level (Backhaus, 1985; Casulli and Cheng, 1992) and three-level (Hamrick, 1992; Muin and Spaulding, 1997a) finite-difference schemes. The three-level models use the semi-implicit approach in the 2-D, external-mode portion of a mode-splitting scheme. Three-level schemes sometimes are not favored for use in hydrodynamic codes owing to the extra storage they require and the extra difficulty they entail by requiring more than one initial condition to start the computation. Yet three-level schemes have the advantage of being easily centered in time to achieve second-order accuracy for the time integration.

In the research leading to this report, both a two-level scheme and a three-level scheme were investigated to implement the semi-implicit method in three dimensions. The two schemes were first coded using the 1-D equations for open channel flow and tested on a few nonlinear cases of flows in a rectangular channel with homogeneous density. On the basis of this testing, the three-level scheme was chosen for extension to three dimensions.

The details of the two 1-D schemes are given in the next section of this chapter before proceeding with the details of the 3-D scheme. The presentation of the 1-D schemes is a useful basis for comparing the two- and three-level approaches, and it also demonstrates the straightforward implementation of the semi-implicit method in one dimension before becoming involved with the greater mathematical complexity of implementing the method in three dimensions. The testing of the 1-D schemes is included in Chapter 5.

4.2 Semi-Implicit One-Dimensional Schemes

The 1-D equations to be solved are the equations of continuity and x-momentum for a rectangular channel with friction. Because the water density is considered to be homogeneous, no salt transport equation is needed and no longitudinal density-gradient term is in the x-momentum equation. The equations are the following:[28]

[28]The 1-D equations for unsteady open-channel flow are derived in numerous references such as Liggett (1975) and Cunge and others (1980). Yen (1973) presents a derivation by integrating the full 3-D governing equations. The form of equations 4.1 and 4.2 are taken from equations 2.28 in Cunge and others (1980, p.16) after simplifying them by assuming a constant channel width.

Continuity,

$$\frac{\partial \zeta}{\partial t} + \frac{\partial U}{\partial x} = 0\,; \tag{4.1}$$

x-Momentum,

$$\frac{\partial U}{\partial t} + \frac{\partial u U}{\partial x} + gH\frac{\partial \zeta}{\partial x} = -gHS_f\,. \tag{4.2}$$

Here, $U = uH$ is the discharge per unit width (or volumetric transport); u is the average channel velocity; $H = h + \zeta$ is the total depth of flow, where h is the location of the channel bottom measured positive downward from a datum (*fig. 4.1*); ζ is the water surface elevation measured positive upward from a datum; and x and t are the independent variables. The variable S_f is a friction slope defined by[29]

$$S_f = \frac{n^2 U|U|}{H^2 R^{4/3}} = \gamma U|U|\,, \tag{4.3}$$

where n is Manning's resistance coefficient and the hydraulic radius of the channel is $R = BH/(B + 2H)$ where B is the width of the channel. For a wide channel $(B \gg H)$, the hydraulic radius in equation 4.3 can be replaced by the total depth H.

The two-level and the three-level schemes use a Crank-Nicolson time-averaging approach (Crank and Nicolson, 1947) for the implicit treatment of the pressure gradient term $gH(\partial\zeta/\partial x)$ in the 1-D x-momentum equation and for the volumetric transport gradient term $\partial U/\partial x$ in the 1-D continuity equation. The two-level scheme is sometimes referred to as a trapezoidal scheme because the Crank-Nicolson averaging is centered between the values at the beginning and end of a time step, similar to the well-known trapezoidal rule for numerical integration. Friction is treated implicitly in both 1-D models, and the advection term $\partial(uU)/\partial x$ in the x-momentum equation is treated explicitly. By this choice of implicit terms the finite-difference equations are free from the time step limitation due to the Courant-Friedrich-Lewy (CFL) criterion[30] based on the gravity-wave speed (Casulli and Cheng,

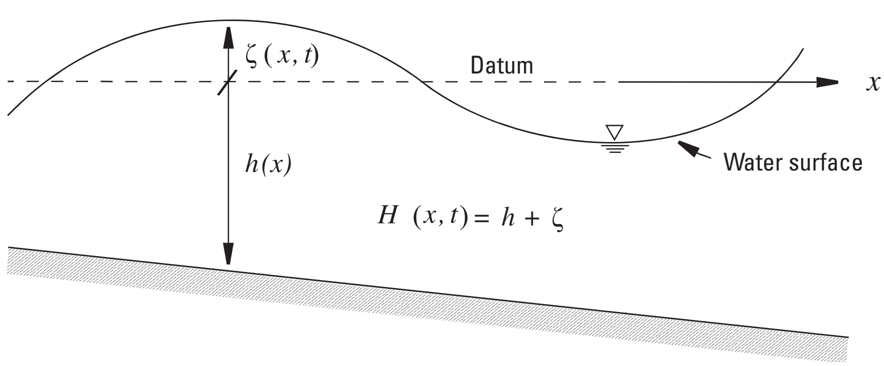

Figure 4.1. Definition sketch for 1-dimensional channel.

[29]The form of the friction slope defined by Manning's formula in equation 4.3 assumes metric units are used. For English units an additional coefficient of 2.208 would appear in the denominator.

[30]The Courant-Friedrich-Lewy stability criterion can be expressed as

$$Cr \le 1$$

in which Cr is known as a Courant (or CFL) number. The Courant number definition is based either on the speed of surface gravity waves or the advective velocity u. These two Courant numbers are referred to herein as the gravity-wave Courant number and the advection Courant number and in one dimension are defined by $Cr_g = (u + \sqrt{gH}) \cdot \Delta t/\Delta x$ and $Cr_a = u \cdot \Delta t/\Delta x$, respectively.

1990). If no iteration process is used, the equations are still subject to a CFL stability limitation on Δt based on the velocity u if, for example, upwind differencing is used for the explicit treatment of the advection term (Casulli and Cheng, 1990); however, because velocity generally is an order of magnitude smaller than the surface wave speed in a typical estuary, potentially there can be a ten-fold increase in the time step for the semi-implicit scheme beyond that required for a fully explicit scheme. For accuracy considerations it is usually desirable to time-center the nonlinear coefficients in the two-level scheme by introducing an iteration process. The iteration also guarantees the unconditional linear stability of the scheme if centered differences for the advection term are updated with new-time-level information within the iteration process. The three-level scheme is already centered in time without iteration, but it includes an option for inserting one or more iterations of a two-level (trapezoidal) scheme to stabilize the three-level scheme and suppress any high frequency oscillations that may appear in solutions due to strong nonlinearities or steep gradients.

In both the two-level and the three-level schemes, the two dependent variables (in this case U and ζ) are computed at different points on a staggered grid; the two-time-level grid, involving time levels $t = n\Delta t$ and $t = (n + 1)\Delta t$, is shown in *figure 4.2*. The grid is uniform in space, so there are IM-1 equal space intervals Δx with IM being the number of U or ζ grid points. The discretization in time is defined by the set of points $t_n = n\Delta t$, $n = 0, 1, 2, \ldots$ where $\Delta t =$ constant. The computation starts from a known condition at time $t = 0$, and subsequent time step solutions advance from the previously known solution at time t_n to the new time t_{n+1}. A specification of known upstream and downstream boundary conditions is required for a problem to be solved when the flow conditions are subcritical.

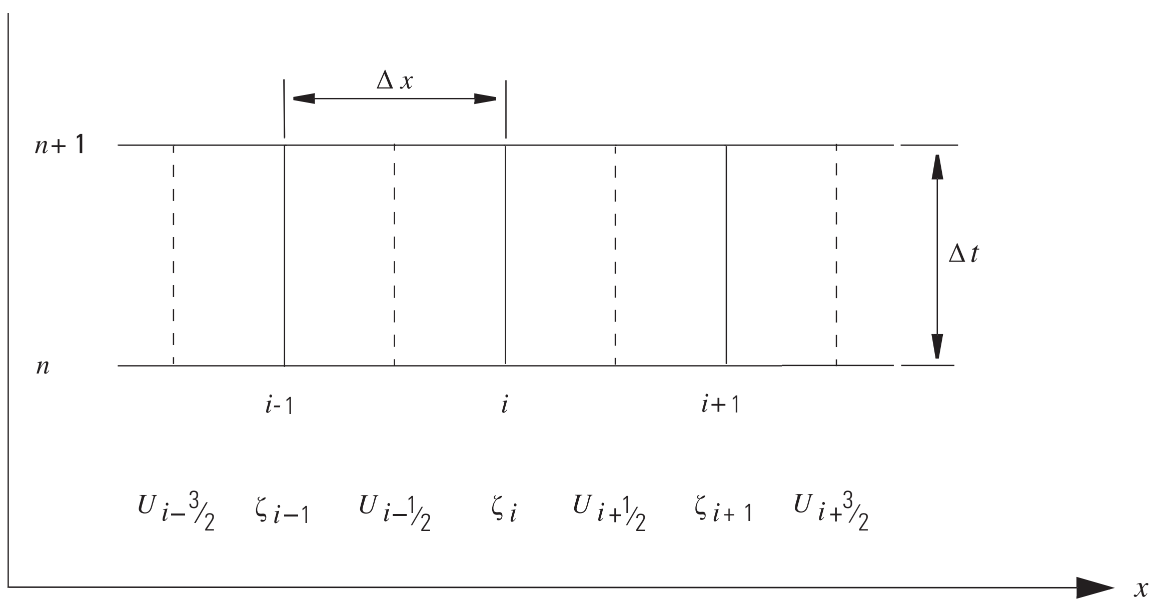

Figure 4.2. Two-time-level staggered grid for the 1-dimensional model.

4.2.1 Two-Level Semi-Implicit Scheme

The two-level semi-implicit scheme closely resembles the iterative scheme first published by Abbott and Ionescu (1967) and later used by Verwey (1971) in a model for the Danish Hydraulic Institute. The scheme here is most similar to the version of the Abbott-Ionescu scheme described by Cunge and others (1980, p. 97–98). One change in the scheme here is in the manner in which the system of finite-difference equations are formed for each time step. The momentum equations are substituted into the continuity equations so that a linear system of equations is formed involving only the unknown water surface elevations $\{\zeta_i\}$. This reduces the size of the matrix to be solved to half the size of one involving both dependent variables. For typical 1-D problems the savings in storage space for the reduced matrix generally is not important, but the savings for 3-D problems can be significant.

The equations are solved by using separate explicit and implicit stages to keep the computer code modular. In a solution for one dimensional flow with homogeneous density, only the advection term in the momentum equation is treated explicitly. Owing to the staggered grid, the continuity and momentum equations are applied to different control volumes shifted one-half cell relative to one another. Continuity is applied at the ζ-points and momentum is applied at the U-points.

The equation for the explicit (or advection) stage is

$$\frac{\hat{U}_{i-1/2} - U^n_{i-1/2}}{\Delta t} + \frac{(uU)^{n+1/2}_i - (uU)^{n+1/2}_{i-1}}{\Delta x} = 0 \qquad (4.4)$$

which is solved directly for $\hat{U}_{i-1/2}$ to give

$$\hat{U}_{i-1/2} = U^n_{i-1/2} - \frac{\Delta t}{\Delta x}((uU)^{n+1/2}_i - (uU)^{n+1/2}_{i-1}) \; . \qquad (4.5)$$

$\hat{U}_{i-1/2}$ is a temporary variable that represents a partial value for $U^{n+1}_{i-1/2}$ after application of the advection operator. The equations for the implicit (or wave-propagation) stage are as follows:
Continuity,

$$\frac{\zeta^{n+1}_i - \zeta^n_i}{\Delta t} + \frac{1}{2}\left(\frac{U^{n+1}_{i+1/2} - U^{n+1}_{i-1/2}}{\Delta x} + \frac{U^n_{i+1/2} - U^n_{i-1/2}}{\Delta x}\right) = 0\,; \qquad (4.6)$$

Momentum,

$$\frac{U^{n+1}_{i-1/2} - \hat{U}_{i-1/2}}{\Delta t} + \frac{g}{2}H^{n+1/2}_{i-1/2}\left(\frac{\zeta^{n+1}_i - \zeta^{n+1}_{i-1}}{\Delta x} + \frac{\zeta^n_i - \zeta^n_{i-1}}{\Delta x}\right) = -gH^{n+1/2}_{i-1/2}\gamma^{n+1/2}_{i-1/2}(\chi_{i-1/2}\left|U^n_{i-1/2}\right|U^{n+1}_{i-1/2} + (1-\chi_{i-1/2})\left|U^n_{i-1/2}\right|U^n_{i-1/2}) \; . \qquad (4.7)$$

Here $\chi_{i-1/2}$ is a weighting coefficient for the frictional resistance term. The use of time level $n + 1/2$ for the variables in equations 4.5 and 4.7 is symbolic since no such time level exists; it means that the variables are evaluated mid-way between time levels $n\Delta t$ and $(n+1)\Delta t$; for example,

$$U^{n+1/2}_{i+1/2} = \frac{1}{2}(\tilde{U}^{n+1}_{i+1/2} + U^n_{i+1/2}) \; . \qquad (4.8)$$

The solution scheme involves iteration; the symbol (~) in equation 4.8 denotes an approximate solution at time $t = (n+1)\Delta t$ taken from the preceding iteration. For the first (starting) iteration, it is assumed that $\tilde{U}^{n+1}_{i+½} = U^{n}_{i+½}$, $\tilde{u}^{n+1}_{i+½} = u^{n}_{i+½}$, and $\tilde{H}^{n+1}_{i+½} = H^{n}_{i+½}$; in this way, the variables superscripted with $n + ½$ are always known. One should use caution if this scheme is used with only one iteration each time step; then the scheme is only first-order accurate because the coefficients $H^{n+½}_{i-½}$ and $\gamma^{n+½}_{i-½}$ in equation 4.7 and the advection term $((uU)^{n+½}_{i} - (uU)^{n+½}_{i-1})/\Delta x$ in equation 4.4 are evaluated backward-in-time at the $n\Delta t$ time level instead of being centered at the $(n + ½)\Delta t$ time level. In Chapter 5 it will be demonstrated that a significant loss of accuracy can result if the scheme is used with only one iteration.

The weighting coefficient χ was suggested by Cunge and others (1980) to improve accuracy in evaluating the friction term when a rapid variation and reversal of the discharge can occur; in the first iteration, $\chi_{i-½}$ is equal to 1.0, and in each subsequent iteration, it is defined by

$$\chi_{i-½} = \frac{U^{n+½}_{i-½}\,U^{n+½}_{i-½} - U^{n}_{i-½}U^{n}_{i-½}}{U^{n}_{i-½}(U^{n+1}_{i-½} - U^{n}_{i-½})} \quad . \tag{4.9}$$

Because the water surface elevation ζ_i and the volumetric transport $U_{i-½}$ are computed at different nodal points, the values for $(uU)_i$, $(uU)_{i-1}$ and $H_{i-½}$ in equations 4.5 and 4.7 must be obtained by some form of interpolation. The usual procedure is to calculate the average of the two adjacent values on the grid. For improved accuracy here, a center-weighted average of the four adjacent values is used. Thus, the total depth H at the point $i + ½$ is

$$H_{i+½} = \frac{9}{16}(H_{i+1} + H_i) - \frac{1}{16}(H_{i+2} + H_{i-1}) \,, \tag{4.10}$$

which applies at all points except those immediately adjacent to the boundary, where a two-point average is used.

Before actually solving the implicit stage of the two-level scheme, the momentum equation (eq. 4.7) is first rewritten in the form

$$U^{n+1}_{i-½} = R^{n+½}_{i-½}\Big(\hat{U}_{i-½} - \frac{g}{2}(\Delta t/\Delta x)H^{n+½}_{i-½}(\zeta^{n+1}_{i} - \zeta^{n+1}_{i-1} + \zeta^{n}_{i} - \zeta^{n}_{i-1}) \;\; - g\Delta x(1 - \chi_{i-½})H^{n+½}_{i-½}\gamma^{n+½}_{i-½}\left|U^{n}_{i-½}\right|U^{n}_{i-½}\Big) \tag{4.11}$$

where $R^{n+½}_{i-½} = (1 + g\Delta t\,\chi_{i-½}H^{n+½}_{i-½}\,\gamma^{n+½}_{i-½}\left|U^{n}_{i-½}\right|)^{-1}$. After substituting equation and a similar expression for $U^{n+1}_{i+½}$ into the continuity equation (eq. 4.6), $U^{n+1}_{i+½}$ and $U^{n+1}_{i-½}$ are eliminated, and an equation of the following form is obtained:

$$A_i\zeta^{n+1}_{i-1} + B_i\zeta^{n+1}_{i} + C_i\zeta^{n+1}_{i+1} = D_i \;, \tag{4.12}$$

where the coefficients A_i, B_i, C_i, and D_i, are known functions of the flow variables defined by

$$A_i = -\frac{g}{4}(\Delta t/\Delta x)^2 R^{n+1/2}_{i-1/2} H^{n+1/2}_{i-1/2},$$

$$B_i = 1 + \frac{g}{4}(\Delta t/\Delta x)^2 \left(R^{n+1/2}_{i+1/2} H^{n+1/2}_{i+1/2} + R^{n+1/2}_{i-1/2} H^{n+1/2}_{i-1/2}\right),$$

$$C_i = -\frac{g}{4}(\Delta t/\Delta x)^2 R^{n+1/2}_{i+1/2} H^{n+1/2}_{i+1/2}, \text{ and}$$

$$\begin{aligned} D_i = {} & \zeta^n_i + \frac{g}{4}(\Delta t/\Delta x)^2 \left(R^{n+1/2}_{i+1/2} H^{n+1/2}_{i+1/2}(\zeta^n_{i+1} - \zeta^n_i) + R^{n+1/2}_{i-1/2} H^{n+1/2}_{i-1/2}(\zeta^n_i - \zeta^n_{i-1}\right) \\ & -\frac{1}{2}(\Delta t/\Delta x) R^{n+1/2}_{i+1/2} \hat{U}_{i+1/2} - R^{n+1/2}_{i-1/2} \hat{U}_{i-1/2} \\ & -\frac{1}{2}(\Delta t/\Delta x)(U^n_{i+1/2} - U^n_{i-1/2}) \\ & +\frac{g}{2}((\Delta t)^2/\Delta x)((1-\chi_{i+1/2}) R^{n+1/2}_{i+1/2} H^{n+1/2}_{i+1/2} \gamma^{n+1/2}_{i+1/2} \left|U^n_{i+1/2}\right| U^n_{i+1/2} \\ & -(1-\chi_{i-1/2}) R^{n+1/2}_{i-1/2} H^{n+1/2}_{i-1/2} \gamma^{n+1/2}_{i-1/2} \left|U^n_{i-1/2}\right| U^n_{i-1/2}) \ . \end{aligned} \quad (4.13)$$

Applying equation 4.12 to each of the interior points of the computational grid results in a system of IM-2 linear algebraic equations involving IM unknown values of ζ^{n+1}_i. The matrix form of the equations is tridiagonal (elements occur only on the main diagonal and on the first subdiagonals above and below). After adding two boundary conditions to complete the equation set, the tridiagonal system can be rapidly solved using the double-sweep method (Cunge and others, 1980, p. 106–108).[31] Once the water surface elevations are known, the volumetric transports are found explicitly through the momentum equation in the form of equation 4.11. The scheme generally gives satisfactory results while using no more than two iterations per time step (that is, two solutions of the tridiagonal system of equations).

A linear analysis of stability for the two-level, semi-implicit scheme without an iteration procedure is discussed by Casulli and Cheng (1990). They considered three choices for the explicit approximation of the advection term: space-centered differencing, upwind differencing, and an Eulerian-Lagrangian method (ELM) using linear interpolation. Only the ELM method was found to be unconditionally linearly stable. The linear stability of the upwind differencing formulation requires that the Courant number based on the material velocity u not exceed unity. The linear stability of the centered differencing formulation requires the flow to be strictly subcritical and the time step to satisfy the inequality

$$k_1 \Delta t < \frac{1}{Fr^2} - 1,$$

where $Fr = u/\sqrt{gH}$ is the Froude number and $k_1 = gS_f/u$ is a friction parameter taken as constant. Without using any iteration, the centered differencing of the advection term must be evaluated at the backward ($n\Delta t$) time level; the resulting advection scheme is only first-order accurate in time. Using iteration, the advection term in equation 4.4 is centered in both space and time, thus gaining full second-order accuracy. The centering in time is achieved in the context of an explicit calculation by weighting the forward time level solution from the previous iteration with the backward time level solution (eq. 4.8). This equal weighting was originally shown to be unconditionally linearly stable by Abbott and Ionescu (1967). Here the centered differencing approach (with iteration) is preferred over the ELM approach of Casulli and Cheng (1990) because it is more efficiently implemented and generally will result in greater accuracy for most typical choices of the grid parameters Δt and Δx. The ELM approach also is not easily implemented for the strictly conservative form of the governing equations used here.

[31]In the mathematics literature the double-sweep method is sometimes called the Thomas algorithm (Ames, 1977, p. 52).

Of course a proof of unconditional or conditional stability for the linear (constant coefficient) shallow water equations will not necessarily apply to the full nonlinear equations. The existence of a phenomenon called nonlinear instability (Phillips, 1959) is well known in the field of computational fluid dynamics. As will be demonstrated in Chapter 5, nonlinear instabilities seem to arise in the semi-implicit model, most likely because of the lack of a built-in damping mechanism in the scheme. When these instabilities occurred in test runs using either one or two iterations, they were in all cases suppressed and eliminated by additional iterations (usually one), resulting in a smooth solution. This stabilizing effect from the iteration procedure ought to be useful for real modeling situations. Duwe and others (1983) recognized this effect and added a second step (iteration) to their 2-D semi-implicit model to remove nonlinear instabilities.

4.2.2 Three-Level Semi-Implicit Scheme

The three-level scheme uses the same staggered spatial grid as the two-level scheme, but it involves an additional time level at $t = (n-1)\Delta t$ (*fig. 4.3*). The scheme is based on the well-known explicit leapfrog differencing method (*fig. 4.4A*) and uses an implicit (Crank-Nicolson type) modification to leapfrog differencing for the discretization of implicit terms (*fig. 4.4B*).

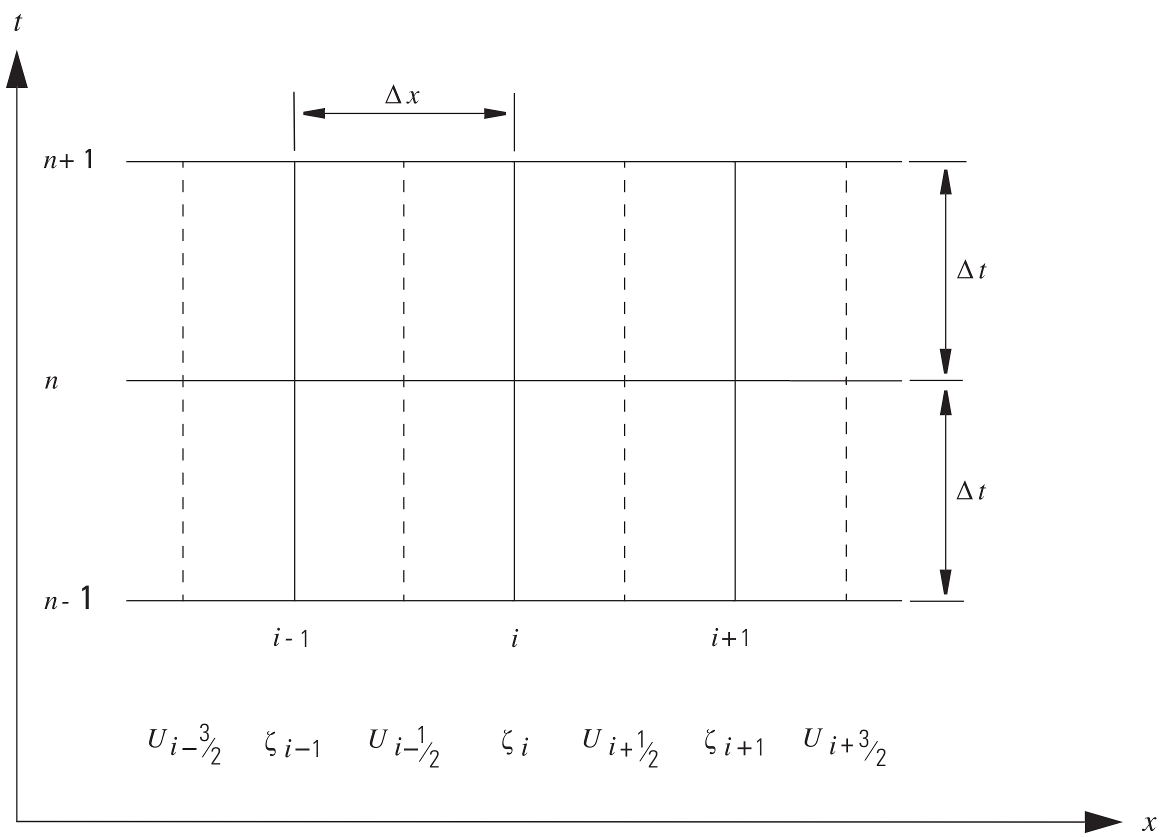

Figure 4.3. Three-time-level staggered grid for the 1-dimensional model.

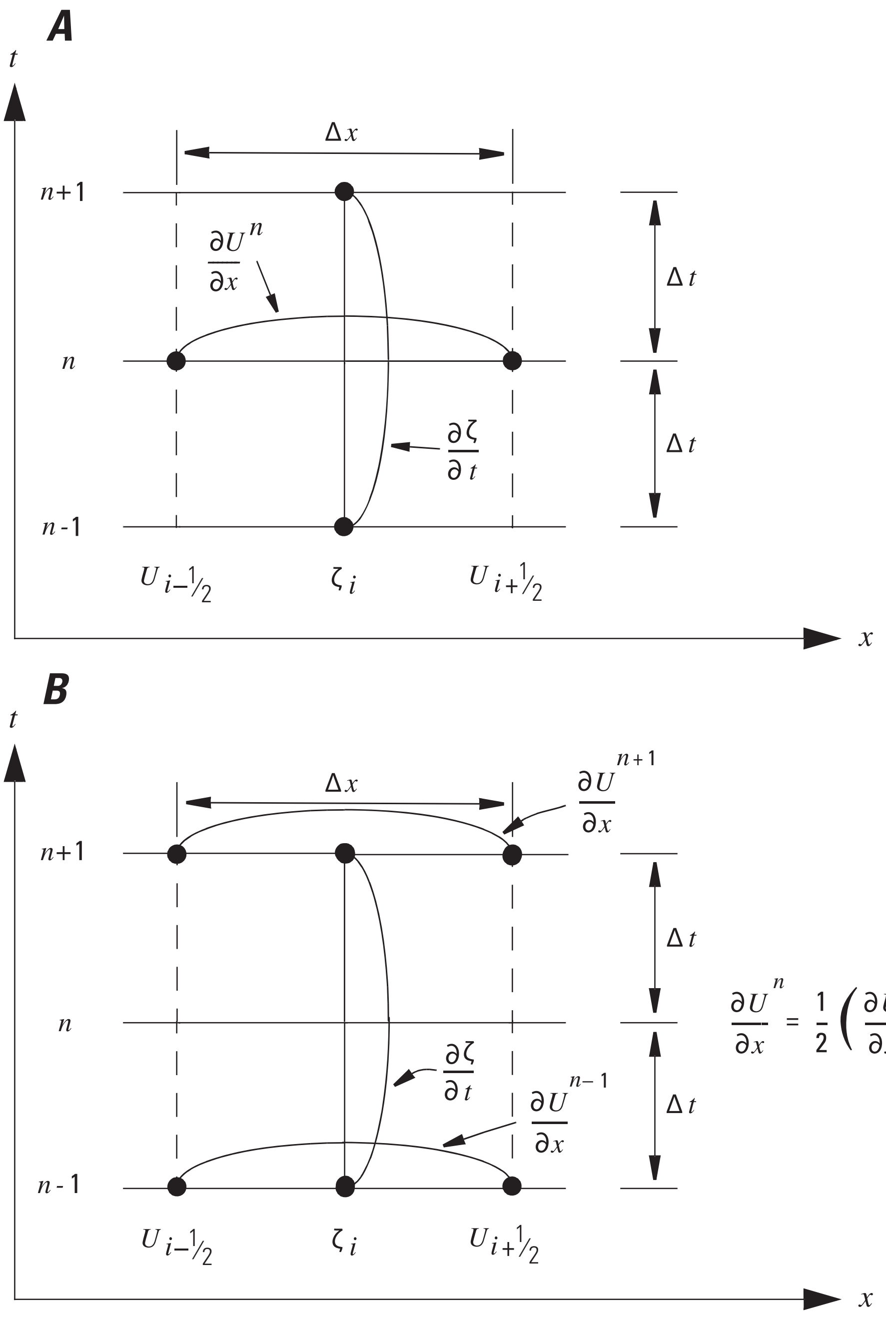

$$\frac{\partial U}{\partial x}^{n} = \frac{1}{2}\left(\frac{\partial U}{\partial x}^{n+1} + \frac{\partial U}{\partial x}^{n-1}\right)$$

Figure 4.4. Computational stencils for (*A*) explicit leapfrog differencing method and (*B*) implicit (Crank-Nicolson type) leapfrog differencing method used in the three-time-level 1-dimensional scheme.

The equation for the explicit stage is

$$\frac{\hat{U}_{i-1/2} - U^{n-1}_{i+1/2}}{2\Delta t} + \frac{(uU)^n_i - (uU)^n_{i-1}}{\Delta x} = 0\,, \tag{4.14}$$

which is solved directly for $\hat{U}_{i-1/2}$ to give

$$\hat{U}_{i-1/2} = U^{n-1}_{i+1/2} - \frac{2\Delta t}{\Delta x}\left((uU)^n_i - (uU)^n_{i-1}\right)\quad , \tag{4.15}$$

where $\hat{U}_{i-1/2}$, again, is a temporary variable. The equations for the implicit stage are the following:

Continuity,

$$\frac{\zeta^{n+1}_i - \zeta^{n-1}_i}{2\Delta t} + \frac{1}{2}\left(\frac{(U^{n+1}_{i+1/2} - U^{n+1}_{i-1/2})}{\Delta x} + \frac{(U^{n-1}_{i+1/2} - U^{n-1}_{i-1/2})}{\Delta x}\right) = 0 \quad ; \tag{4.16}$$

Momentum,

$$\frac{U^{n+1}_{i-1/2} - \hat{U}_{i-1/2}}{2\Delta t} + \frac{g}{2}H^n_{i-1/2}\left(\frac{\zeta^{n+1}_i - \zeta^{n+1}_{i-1}}{\Delta x} + \frac{\zeta^{n-1}_i - \zeta^{n-1}_{i-1}}{\Delta x}\right) = -gH^n_{i-1/2}\gamma^n_{i-1/2}\left|U^{n-1}_{i-1/2}\right|U^{n+1}_{i-1/2}\;. \tag{4.17}$$

In this scheme, the nonlinear coefficients $H^n_{i-1/2}$ and $\gamma^n_{i-1/2}$ in the momentum equation and the advection term in equation 4.15 are easily centered in time by evaluating them at time level *n*. Therefore, no iteration is required to achieve second-order accuracy in the time integration, in contrast to the two-level scheme. Spatial interpolations in the form of equation 4.10 also can be used in the three-level scheme.

The solution of the implicit stage requires rewriting the momentum equation in the form

$$U^{n+1}_{i-1/2} = R^n_{i-1/2}(\hat{U}_{i-1/2} - g(\Delta t/\Delta x)H^n_{i-1/2}(\zeta^{n+1}_i - \zeta^{n+1}_{i-1} + \zeta^{n-1}_i - \zeta^{n-1}_{i-1}))\;\;, \tag{4.18}$$

where $R^n_{i-1/2} = (1 + 2g\Delta t H^n_{i-1/2}\gamma^n_{i-1/2}\left|U^{n-1}_{i-1/2}\right|)^{-1}$. Then the substitution of equation 4.18 and a similar expression for $U^{n+1}_{i+1/2}$ into the continuity equation (eq. 4.16) results in an equation identical in form to equation 4.12,

$$A_i\zeta^{n+1}_{i-1} + B_i\zeta^{n+1}_i + C_i\zeta^{n+1}_{i+1} = D_i\;, \tag{4.19}$$

but with the coefficients A_i, B_i, C_i, and D_i, defined as follows:

$$\begin{aligned}
A_i &= -g(\Delta t/\Delta x)^2\, R^n_{i-1/2}H^n_{i-1/2}\;,\\
B_i &= 1 + g(\Delta t/\Delta x)^2(R^n_{i+1/2}H^n_{i+1/2} + R^n_{i-1/2}H^n_{i-1/2}),\\
C_i &= -g(\Delta t/\Delta x)^2\, R^n_{i+1/2}H^n_{i+1/2}\;,\quad \text{and}\\
D_i &= \zeta^{n-1}_i + g(\Delta t/\Delta x)^2\,(R^n_{i+1/2}H^n_{i+1/2}(\zeta^{n-1}_{i+1} - \zeta^{n-1}_i) - R^n_{i-1/2}H^n_{i-1/2}(\zeta^{n-1}_i - \zeta^{n-1}_{i-1}))\\
&\quad - (\Delta t/\Delta x)(R^n_{i+1/2}\hat{U}_{i+1/2} - R^n_{i-1/2}\hat{U}_{i-1/2})\\
&\quad - (\Delta t/\Delta x)(U^{n-1}_{i+1/2} - U^{n-1}_{i-1/2})
\end{aligned} \tag{4.20}$$

The system of equations that results from applying equation 4.19 to each of the computational grid points is solved for $\left\{\zeta^{n+1}_i\right\}$ using the double-sweep method. Equation 4.18 is then used to calculate the volumetric transports $\left\{U^{n+1}_{i-1/2}\right\}$ explicitly.

As noted previously, it is sometimes helpful to follow the time-step solution of the semi-implicit leapfrog scheme with one or (occasionally) more iterations of a two-level semi-implicit scheme to stabilize the solution and suppress any two-grid-interval oscillations in time. The two-level scheme from section 4.2.1 can be used, but with the variables superscripted with $n + \frac{1}{2}$ defined by

$$H_{i-\frac{1}{2}}^{n+\frac{1}{2}} = \frac{1}{2}\left(\tilde{H}_{i-\frac{1}{2}}^{n+1} + H_{i-\frac{1}{2}}^{n}\right),$$

$$U_{i-\frac{1}{2}}^{n+\frac{1}{2}} = \frac{1}{2}\left(\tilde{U}_{i-\frac{1}{2}}^{n+1} + U_{i-\frac{1}{2}}^{n}\right), \text{ and}$$

$$u_{i-\frac{1}{2}}^{n+\frac{1}{2}} = \frac{1}{2}\left(\tilde{u}_{i-\frac{1}{2}}^{n+1} + u_{i-\frac{1}{2}}^{n}\right) \quad .$$

In this case, the symbol (~) denotes the estimates of the unknowns from the semi-implicit leapfrog solution. The two-level scheme also is convenient for starting the computations of the three-level scheme from the initial condition at $t = 0$. The combination of a three-level scheme followed by a two-level scheme is referred to here as a semi-implicit, leapfrog-trapezoidal scheme. Explicit leapfrog-trapezoidal schemes commonly are used in atmospheric modeling (Mesinger and Arakawa, 1976) and other areas of computational physics (Zalesak, 1979, p. 361–362).

The semi-implicit three-level scheme can easily be converted to a standard explicit leapfrog scheme with relatively minor changes to the coding. The explicit leapfrog scheme executes more rapidly[32] than the semi-implicit scheme if identical time and space step sizes are used in both schemes; therefore, when accuracy considerations restrict the time step so that the CFL criterion for surface waves does not exceed unity, the explicit scheme is preferred. Using the explicit scheme, each nodal value of the water surface elevation at the $(n + 1)\Delta t$ time level is computed directly from the continuity equation by

$$\zeta_i^{n+1} = \zeta_i^{n-1} - 2\Delta t\left(U_{i+\frac{1}{2}}^{n} - U_{i-\frac{1}{2}}^{n}\right)/\Delta x \quad . \tag{4.21}$$

The volumetric transport is obtained directly from the momentum equation written in the form

$$U_{i-\frac{1}{2}}^{n+1} = R_{i-\frac{1}{2}}^{n}\left(\hat{U}_{i-\frac{1}{2}} - 2g\Delta t H_{i-\frac{1}{2}}^{n}\left(\zeta_i^n - \zeta_{i-1}^n\right)/\Delta x\right), \tag{4.22}$$

where $\hat{U}_{i-\frac{1}{2}}$ is still defined in equation 4.15, and $R_{i-\frac{1}{2}}^{n}$ is defined in equation 4.18. It also is easy to include a step with an explicit trapezoidal scheme after applying the explicit leapfrog scheme.

4.3 Semi-Implicit Three-dimensional Scheme

The 3-D finite-difference scheme is applied to the layer-averaged governing equations derived in Chapter 3 (eqs. 3.57–3.61). The semi-implicit, leapfrog-trapezoidal scheme just presented in one dimension can be extended to three dimensions. The finite-difference equations are described in detail below.

[32]The speed-up from using the explicit versus the semi-implicit leapfrog scheme (with identical time and space steps) is not really significant in one dimension. In three dimensions the speed-up is indeed significant.

The premise of the semi-implicit method in three-dimensions is identical to that in one dimension: certain key terms in the governing equations are treated implicitly to ensure that the stability of the scheme does not depend on the CFL criterion for the surface-wave celerity. The terms treated implicitly are the two horizontal divergence terms involving the summation of layer volumetric transports in the continuity equation (eq. 3.57), and the barotropic pressure gradient terms in the *x*- and *y*-momentum equations (eqs. 3.59 and 3.60). In addition to these terms, the vertical stress (or vertical momentum diffusion) terms in the momentum equations are treated implicitly to avoid a time-step limitation in shallow water, as discussed in Davies (1985).[33] The remaining terms in the momentum equations (advection, Coriolis, horizontal momentum diffusion, and the baroclinic pressure gradient) are treated explicitly. In the salt transport equation (eq. 3.61), only the vertical salt diffusion term is treated implicitly.

The choice for the horizontal location of variables on the numerical grid is the staggered arrangement known as a C-grid (Mesinger and Arakawa, 1976) (*fig. 4.5*). The C-grid has the advantage that difference quotients are easily centered in space to obtain second-order accuracy. The horizontal dimensions of each cell are Δx and Δy, considered to be constant and equal here. The vertical locations of variables are pictured in *figure 4.6* for the multilevel grid (also refer to *fig. 3.1*). The center of each 3-D cell is numbered with indices i, j, k. Pressure ($p_{i,\,j,\,k}$), salinity ($s_{i,\,j,\,k}$), and density ($\rho_{i,\,j,\,k}$) are defined at the center. The *x*-direction velocity component ($u_{i+\frac{1}{2},j,k}$) and volumetric transport ($U_{i+\frac{1}{2},j,k}$) are located at half-integers of i and whole integers of j and k; the *y*-direction velocity component ($v_{i,j+\frac{1}{2},k}$) and volumetric transport ($V_{i,j+\frac{1}{2},k}$) are located at half-integers of j and whole integers of i and k; the vertical velocity component ($w_{i,j,k-\frac{1}{2}}$) is located at each layer interface between cell centers. The water surface elevation ($\zeta_{i,j}$) is a two-dimensional variable defined at the center of each horizontal grid cell with integer values of i and j. As discussed in Chapter 3, the height of a surface or bottom layer in the present model can vary in space; in the surface layer, the height can vary with both space and time. For generality here, the layer height variable is designated with a subscript including all three spatial indices and a superscript indicating the time step (for example, $h^n_{i,j,k}$); the height is defined at each cell center. The computer code has been developed with the layer height variable as a 3-D, time-dependent array so that arbitrary geometries and wetting and drying of nodal points can eventually be easily incorporated. For the development here, the indices on h which pertain to layers of constant height are superfluous.

The overall shape of the horizontal grid is rectangular with dimensions (*imax*, *jmax*). The grid boxes that fall within the boundaries of a water body are labeled as "wet cells" and are indexed, by row, between the values of $i = i1$, *im,* and, by column, between the values of $j = j1$, *jm*. For a rectangular water body, $i1$, $j1$, *im,* and *jm* are constants that are independent of the row or column. For a water body of arbitrary shape, the indices $i1$ and *im* vary between rows and the indices $j1$ and *jm* vary between columns; these indices are used to define the boundaries of the water body. Points exterior to the boundary are dry cells. In order to simplify the computer code, at least one dry cell must always be adjacent to the boundary. Thus for a rectangular domain of wet cells, it is typical that $i1 = j1 = 2$ and $im = imax - 1$ and $jm = jmax - 1$.

[33]The implicit treatment of the vertical stress terms in the 3-D formulation is roughly analogous to treating the friction term implicitly in the 1-D formulation.

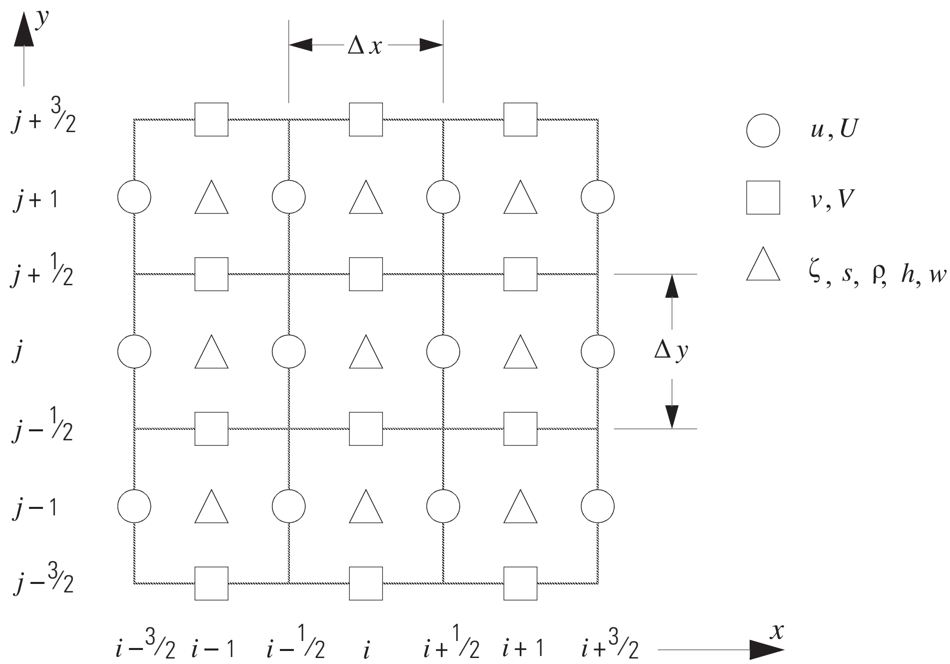

Figure 4.5. The space-staggered horizontal grid (C-grid) used in the 3-dimensional model showing the location of variables.

In describing the computations, it is assumed that the integration process has progressed to a time level n and that all model variables are defined for that time and also for the previous time level $n - 1$. The computations advance the solution variables one time step to time level $n + 1$. Thereafter, the computation cycle is repeated for time level $n + 2$ and again for each subsequent time level until a simulation is completed. To start a computation, the information needed at the $n - 1$ time level usually is not available. For this case, the trapezoidal scheme is used by itself to obtain the solution at the second time level; because the trapezoidal scheme involves only two time levels, it does not require starting information at the $n - 1$ time level. In starting the computation, the coefficients of the trapezoidal scheme, which are normally defined at time level $n + \frac{1}{2}$, are evaluated backward-in-time at time level n.

4.3.1 Semi-Implicit Leapfrog Scheme

In this section, the finite-difference forms of the equations of momentum, continuity, and salt transport are introduced using the semi-implicit leapfrog scheme. The steps in the numerical integration procedure are outlined. The discretization of the momentum equations is discussed first, followed by the continuity equation and the salt transport equation.

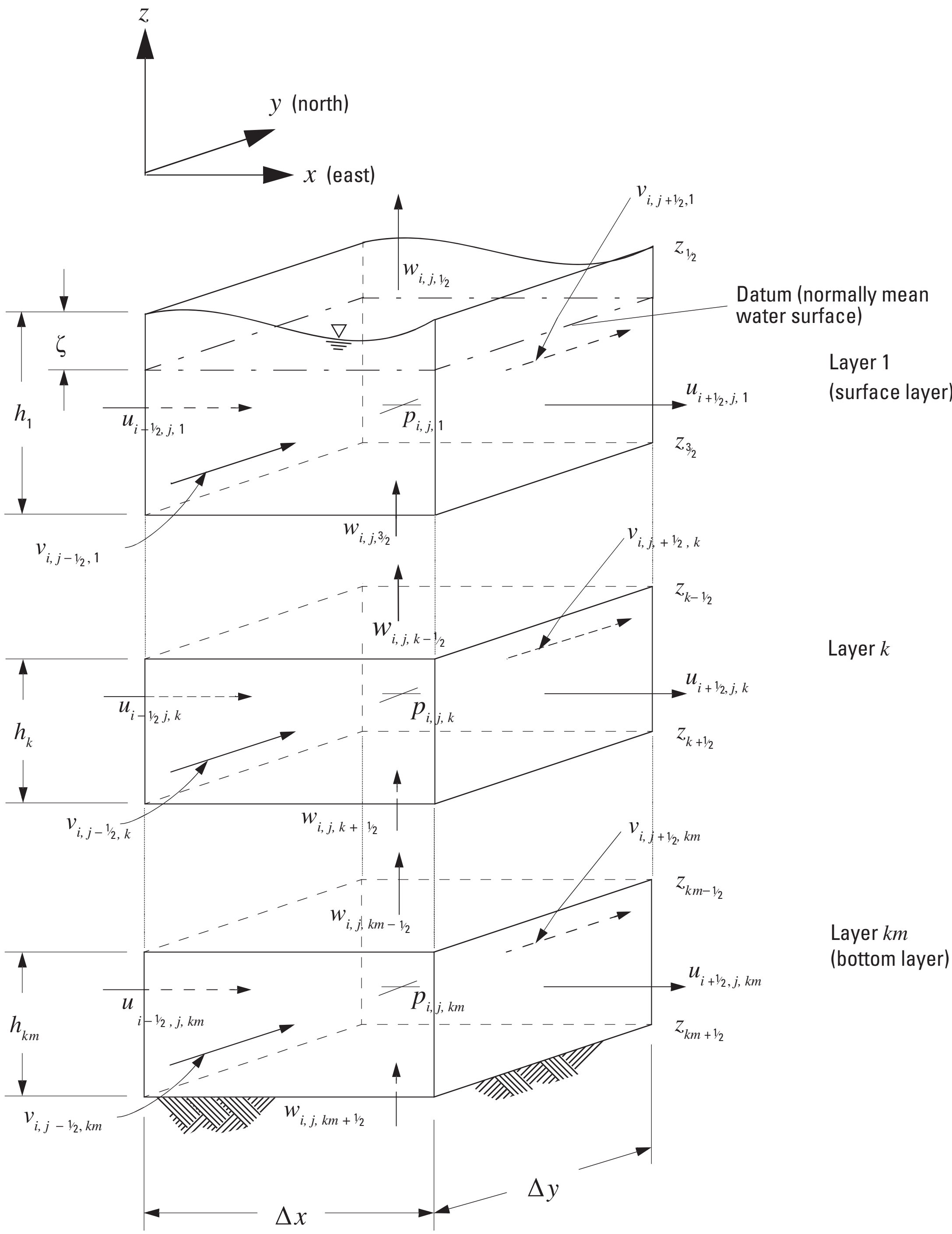

Figure 4.6. Multilevel staggered grid for the 3-dimensional model.

4.3.1.1 Momentum equations

The solution of the momentum equations is separated into two stages in which first the explicit terms and then the implicit terms are evaluated. The separation is not a form of time-splitting but simply a grouping of terms for convenience in making the computer program modular and facilitating the presentation of equations. The finite-difference equation for the *x*-direction momentum equation is written so it is centered within layer *k* at the horizontal point $(i+\frac{1}{2})\Delta x,\ j\Delta y$; the explicit stage is represented by

$$\hat{U}_{i+\frac{1}{2},j,k} = U^{n-1}_{i+\frac{1}{2},j,k} + 2\Delta t[-(ADV_x)^n + (COR_x)^n - (BCLINIC_x)^n + (HDIFF_x)^{n-1}]_{i+\frac{1}{2},j,k}\,, \tag{4.23}$$

where the terms in brackets refer to the discretized form of the corresponding groupings of terms in equation 3.59. The bracketed terms are expanded fully using the leapfrog scheme and displayed in Appendix D (eqs. D.1–D.4). The symbol $(\hat{\ })$ in equation 4.23 denotes a solution for the layer volumetric transport which includes only the contribution from the explicit terms. The corresponding finite-difference equation for the explicit stage of the *y*-direction momentum equation is centered within layer *k* at the point $i\Delta x$, $(j+\frac{1}{2})\Delta y$ and is represented by

$$\hat{U}_{i,j+\frac{1}{2},k} = U^{n-1}_{i,j+\frac{1}{2},k} + 2\Delta t[-(ADV_y)^n - (COR_y)^n - (BCLINIC_y)^n + (HDIFF_y)^{n-1}]_{i,j+\frac{1}{2},k}\,. \tag{4.24}$$

Here the bracketed terms refer to groupings of terms in equation 3.60, and they are expanded fully in Appendix D (eqs. D.5–D.8). All terms in equations 4.23 and 4.24, except horizontal diffusion (*HDIFF*), are centered in time at time level *n* to achieve second-order numerical accuracy. The horizontal diffusion is written backward-in-time at time level $n-1$ because the centering of that term can result in a weak instability; although formally this uncentered treatment of the horizontal diffusion introduces first-order truncation error, the actual size of the error should be miniscule. Presently in the model, the horizontal momentum exchange (or eddy viscosity) coefficient A_H is defined at the center of each cell with whole integers of the indices *i*, *j*, *k*.

The shear stress terms in equations 3.59 and 3.60 can be replaced by introducing the concept of the vertical momentum exchange (or eddy viscosity) coefficient:[34]

$$\frac{\tau_{xz}}{\rho} = A_V\frac{\partial u}{\partial z}\,, \qquad \frac{\tau_{yz}}{\rho} = A_V\frac{\partial v}{\partial z}\,. \tag{4.25}$$

Then the finite-difference equation for the implicit stage of the *x*-momentum equation is written as

$$\begin{aligned} U^{n+1}_{i+\frac{1}{2},j,k} = {} & \hat{U}_{i+\frac{1}{2},j,k} - g\frac{\Delta t}{\Delta x}\bar{h}^n_{i+\frac{1}{2},j,k}\left(\frac{\bar{\rho}^n_{i+\frac{1}{2},j,1}}{\bar{\rho}^n_{i+\frac{1}{2},j,k}}\right)\cdot(\zeta^{n+1}_{i+1,j} - \zeta^{n+1}_{i,j} + \zeta^{n-1}_{i+1,j} - \zeta^{n-1}_{i,j}) \\ & + \Delta t\left(A^n_{V\,i+\frac{1}{2},j,k-\frac{1}{2}}\cdot\left(\frac{(U/\bar{h})^{n+1}_{i+\frac{1}{2},j,k-1} - (U/\bar{h})^{n+1}_{i+\frac{1}{2},j,k}}{\bar{\bar{h}}^{n+1}_{i+\frac{1}{2},j,k-\frac{1}{2}}} + \frac{u^{n-1}_{i+\frac{1}{2},j,k-1} - u^{n-1}_{i+\frac{1}{2},j,k}}{\bar{\bar{h}}^{n-1}_{i+\frac{1}{2},j,k-\frac{1}{2}}}\right)\right. \\ & \left. - A^n_{V\,i+\frac{1}{2},j,k+\frac{1}{2}}\cdot\left(\frac{(U/\bar{h})^{n+1}_{i+\frac{1}{2},j,k} - (U/\bar{h})^{n+1}_{i+\frac{1}{2},j,k+1}}{\bar{\bar{h}}^{n+1}_{i+\frac{1}{2},j,k+\frac{1}{2}}} + \frac{u^{n-1}_{i+\frac{1}{2},j,k} - u^{n-1}_{i+\frac{1}{2},j,k+1}}{\bar{\bar{h}}^{n-1}_{i+\frac{1}{2},j,k+\frac{1}{2}}}\right)\right)\,, \end{aligned} \tag{4.26}$$

[34]The *z*-derivatives of *u* and *v* in equations 4.25 are mathematically undefined at the layer interfaces because the layer-averaged velocities are discontinuous there. A *z*-derivative at an interface is therefore understood to imply a finite-difference quotient involving the layer variables above and below the interface.

where the overbar ($^-$) on a layer height or density variable is used to represent a spatial average in the x-direction between adjacent values; for example, $\bar{h}_{i+1/2,j,k} = (h_{i,j,k} + h_{i+1,j,k})/2$. Also, $\bar{\bar{h}}_{i+1/2,j,k-1/2}$ is defined to be the average of layer heights $\bar{h}_{i+1/2,j,k-1}$ and $\bar{h}_{i+1/2,j,k}$. The average values of the layer heights only are needed in the computations involving the surface and bottom layers where the heights are permitted to vary horizontally. The substitution $u^{n+1}_{i+1/2,j,k} = (U/\bar{h})^{n+1}_{i+1/2,j,k}$ has been made in the vertical diffusion term because the dependent variable used in the model is the layer volumetric transport U^{n+1}_k rather than the average layer velocity u^{n+1}_k. The layer velocity u_k is available in the computer code at time level $n-1$ and therefore is used directly in the diffusion term.

The finite-difference equation similar to 4.26 for y-momentum is

$$
\begin{aligned}
V^{n+1}_{i,j+1/2,k} = {} & \hat{V}_{i,j+1/2,k} - g\frac{\Delta t}{\Delta y}\bar{h}^n_{i,j+1/2,k}\left(\frac{\bar{\rho}^n_{i,j+1/2,1}}{\bar{\rho}^n_{i,j+1/2,k}}\right)\cdot(\zeta^{n+1}_{i,j+1} - \zeta^{n+1}_{i,j} + \zeta^{n-1}_{i,j+1} - \zeta^{n-1}_{i,j}) \\
& + \Delta t\left(A^n_{V_{i,j+1/2,k-1/2}}\cdot\left(\frac{(V/\bar{h})^{n+1}_{i,j+1/2,k-1} - (V/\bar{h})^{n+1}_{i,j+1/2,k}}{\bar{\bar{h}}^{n+1}_{i,j+1/2,k-1/2}} + \frac{v^{n-1}_{i,j+1/2,k-1} - v^{n-1}_{i,j+1/2,k}}{\bar{\bar{h}}^{n-1}_{i,j+1/2,k-1/2}}\right)\right. \\
& \left. - \quad A^n_{V_{i,j+1/2,k+1/2}}\cdot\left(\frac{(V/\bar{h})^{n+1}_{i,j+1/2,k} - (V/\bar{h})^{n+1}_{i,j+1/2,k+1}}{\bar{\bar{h}}^{n+1}_{i,j+1/2,k+1/2}} + \frac{v^{n-1}_{i,j+1/2,k} - v^{n-1}_{i,j+1/2,k+1}}{\bar{\bar{h}}^{n-1}_{i,j+1/2,k+1/2}}\right)\right) .
\end{aligned}
\tag{4.27}
$$

Here the overbar represents a spatial average in the y-direction between adjacent values; for example, $\bar{h}_{i,j+1/2,k} = (h_{i,j,k} + h_{i,j+1,k})/2$; also $\bar{\bar{h}}_{i,j+1/2,k-1/2} = (\bar{h}_{i,j+1/2,k-1} + \bar{h}_{i,j+1/2,k})/2$. Hereinafter the use of overbars is dropped for convenience, and a layer height or density variable possessing a half-integer subscript in any one of the three spatial indices is considered to be an average of the nearest adjacent values.[35]

Because the surface layer height is time dependent, $h^{n+1}_{i,j,1}$ is unknown for the evaluation of equations 4.26 and 4.27. This value is estimated in the computations by extrapolating in time using the second-order formula

$$
\hat{h}^{n+1}_{i,j,1} = 3(h^n_{i,j,1} - h^{n-1}_{i,j,1}) + h^{n-2}_{i,j,1} . \tag{4.28}
$$

Using this estimate of $h^{n+1}_{i,j,1}$ in equations 4.26 and 4.27 has worked well in numerical testing of the model and is more accurate than, say, choosing $h^{n+1}_{i,j,1} \approx h^n_{i,j,1}$. The estimate of $\hat{h}^{n+1}_{i,j,1}$ is made first during each time step calculation immediately before the array that stores values of $h^{n-2}_{i,j,1}$ is rewritten; therefore, the storage of an extra 3-D array is not required to evaluate equation 4.28.

In equations 4.26 and 4.27, the boundary shear stress terms for the wind and bottom friction are boundary conditions for the surface and bottom layers. The wind stress is specified as a forcing function at the free surface by substituting

$$
A^n_{V_{i+1/2,j,1/2}}\cdot\frac{1}{2}\left(\frac{(U/h)^{n+1}_{i+1/2,j,0} - (U/h)^{n+1}_{i+1/2,j,1}}{h^{n+1}_{i+1/2,j,1/2}} + \frac{u^{n-1}_{i+1/2,j,0} - u^{n-1}_{i+1/2,j,1}}{h^{n-1}_{i+1/2,j,1/2}}\right) = \frac{(\tau_{xs})^n_{i+1/2,j,1/2}}{\rho^n_{i+1/2,j,1}}
$$

and

[35] In the 3-D model, higher order averages such as the one in equation 4.10 in the 1-D model are not used.

$$A^{n}_{V_{i,j+1/2,1/2}} \cdot \frac{1}{2}\left(\frac{(V/h)^{n+1}_{i,j+1/2,0} - (V/h)^{n+1}_{i,j+1/2,1}}{h^{n+1}_{i,j+1/2,1/2}} + \frac{v^{n-1}_{i,j+1/2,0} - v^{n-1}_{i,j+1/2,1}}{h^{n-1}_{i,j+1/2,1/2}}\right) = \frac{(\tau_{ys})^{n}_{i,j+1/2,1/2}}{\rho^{n}_{i,j+1/2,1}},$$

where τ_{xs} and τ_{ys} are defined by equations 2.58. The use of the zero subscript refers to a fictitious layer that does not enter into the computations. The frictional stress at the bottom is specified by substituting

$$A^{n}_{V_{i+1/2,j,km+1/2}} \cdot \frac{1}{2}\left(\frac{(U/h)^{n+1}_{i+1/2,j,km} - (U/h)^{n+1}_{i+1/2,j,km+1}}{h^{n+1}_{i+1/2,j,km+1/2}} + \frac{u^{n-1}_{i+1/2,j,km} - u^{n-1}_{i+1/2,j,km+1}}{h^{n-1}_{i+1/2,j,km+1/2}}\right) = \frac{(\tau_{xb})^{n}_{i+1/2,j,km+1/2}}{\rho^{n}_{i+1/2,j,km}}$$

and

$$A^{n}_{V_{i,j+1/2,km+1/2}} \cdot \frac{1}{2}\left(\frac{(V/h)^{n+1}_{i,j+1/2,km} - (V/h)^{n+1}_{i,j+1/2,km+1}}{h^{n+1}_{i,j+1/2,km+1/2}} + \frac{v^{n-1}_{i,j+1/2,km} - v^{n-1}_{i,j+1/2,km+1}}{h^{n-1}_{i,j+1/2,km+1/2}}\right) = \frac{(\tau_{yb})^{n}_{i,j+1/2,km+1/2}}{\rho^{n}_{i,j+1/2,km}},$$

where the subscript $km + 1$ refers to a fictitious layer. The frictional stresses τ_{xb} and τ_{yb} are determined using equations 2.65 written in terms of the horizontal volumetric transports computed in the bottom layer. Thus

$$\frac{(\tau_{xb})^{n}_{i+1/2,j,km+1/2}}{\rho^{n}_{i+1/2,j,km}} = C^{n}_{\mathrm{d}_{i+1/2,j}} \frac{\sqrt{(U^{n-1}_{i+1/2,j,km})^2 + (\overline{V}^{n-1}_{i+1/2,j,km})^2}}{(h^{n}_{i+1/2,j,km})^2} U^{n+1}_{i+1/2,j,km} \tag{4.29}$$

and

$$\frac{(\tau_{yb})^{n}_{i,j+1/2,km+1/2}}{\rho^{n}_{i,j+1/2,km}} = C^{n}_{\mathrm{d}_{i,j+1/2}} \frac{\sqrt{(\overline{U}^{n-1}_{i,j+1/2,km})^2 + (V^{n-1}_{i,j+1/2,km})^2}}{(h^{n}_{i,j+1/2,km})^2} V^{n+1}_{i,j+1/2,km}, \tag{4.30}$$

where

$$\overline{V}^{n-1}_{i+1/2,j,km} = (V^{n-1}_{i+1,j+1/2,km} + V^{n-1}_{i,j+1/2,km} + V^{n-1}_{i,j-1/2,km} + V^{n-1}_{i+1,j-1/2,km})/4,$$

$$\overline{U}^{n-1}_{i,j+1/2,km} = (U^{n-1}_{i+1/2,j,km} + U^{n-1}_{i+1/2,j+1,km} + U^{n-1}_{i-1/2,j,km} + U^{n-1}_{i+1/2,j+1,km})/4, \text{ and}$$

$$C^{n}_{\mathrm{d}_{i,j+1/2}} = \kappa^2[\ln((h^{n}_{i,j+1/2,km}/2)/(z_0)_{i,j+1/2})]^{-2}.$$

The use of an overbar to represent a four-point spatial average for a volumetric transport variable will be retained in subsequent equations.

The vertical momentum exchange (or eddy viscosity) coefficient A_V in equations 4.26 and 4.27 is a variable that must be computed as the flow field evolves. First the eddy viscosity under neutral (unstratified) conditions is computed using the Prandtl mixing length model in the form of equation 2.31; then the neutral value is adjusted for the effect of stratification by the stability function represented by equation 2.27. The individual values of A_V are computed at the layer interfaces lying vertically between pressure points (in the same location as the vertical component of velocity w in *figure 4.6*); they are then interpolated horizontally to the layer interfaces lying vertically between the velocity components where they are required to evaluate equations 4.26 and 4.27. The discretized equations for the computation of the vertical distribution of A_V are given in Appendix E. In the equations hereafter, A_V is considered known.

Because the x- and y-momentum equation treatments are similar, only the x-momentum equation is discussed. From this point, the strategy of Casulli and Cheng (1992) is followed by rewriting the system of momentum equations for node $(i + 1/2, j)$ in the compact matrix form[36]

$$\boldsymbol{A}_{i+1/2,j}\boldsymbol{U}^{n+1}_{i+1/2,j} = \boldsymbol{G}_{i+1/2,j} - g\frac{\Delta t}{\Delta x}\rho^{n}_{i+1/2,j,1}(\zeta^{n+1}_{i+1,j} - \zeta^{n+1}_{i,j})\boldsymbol{R}_{i+1/2,j}\,, \tag{4.31}$$

where $\boldsymbol{U}$, $\boldsymbol{R}$, $\boldsymbol{G}$, and $\boldsymbol{A}$ are

$$\boldsymbol{U}^{n+1}_{i+1/2,j} = [U^{n+1}_1, U^{n+1}_2, \ldots, U^{n+1}_{km}]^T_{i+1/2,j}\,, \qquad \boldsymbol{R}_{i+1/2,j} = \left[\frac{h^n_1}{\rho^n_1}, \frac{h^n_2}{\rho^n_2}, \ldots, \frac{h^n_{km}}{\rho^n_{km}}\right]^T_{i+1/2,j}\,,$$

$$\boldsymbol{G}_{i+1/2,j} =$$

$$\begin{bmatrix} \hat{U}_1 - g\frac{\Delta t}{\Delta x}h^n_1\left(\frac{\rho^n_1}{\rho^n_1}\right)(\zeta^{n-1}_{i+1,j} - \zeta^{n-1}_{i,j}) + 0 - \Delta t A^n_{V3/2}\frac{(u^{n-1}_1 - u^{n-1}_2)}{h^{n-1}_{3/2}} + 2\Delta t\frac{(\tau_{xs})^n_{1/2}}{\rho^n_1} \\ \hat{U}_2 - g\frac{\Delta t}{\Delta x}h^n_2\left(\frac{\rho^n_1}{\rho^n_2}\right)(\zeta^{n-1}_{i+1,j} - \zeta^{n-1}_{i,j}) + \Delta t A^n_{V3/2}\frac{(u^{n-1}_1 - u^{n-1}_2)}{h^{n-1}_{3/2}} - \Delta t A^n_{V5/2}\frac{(u^{n-1}_2 - u^{n-1}_3)}{h^{n-1}_{5/2}} \\ \vdots \\ \hat{U}_{km} - g\frac{\Delta t}{\Delta x}h^n_{km}\left(\frac{\rho^n_1}{\rho^n_{km}}\right)(\zeta^{n-1}_{i+1,j} - \zeta^{n-1}_{i,j}) + \Delta t A^n_{V\,km-1/2}\frac{(u^{n-1}_{km-1} - u^{n-1}_{km})}{h^{n-1}_{km-1/2}} + 0 \end{bmatrix}_{i+1/2,j}, \text{ and}$$

[36]Bold-faced variables are matrices.

$$A_{i+½,j} = \begin{bmatrix} 1+\dfrac{\Delta t A^n_{V3/2}}{h^{n+1}_1 \cdot h^{n+1}_{3/2}} & -\dfrac{\Delta t A^n_{V3/2}}{h^{n+1}_2 \cdot h^{n+1}_{3/2}} & & & 0 \\ -\dfrac{\Delta t A^n_{V3/2}}{h^{n+1}_1 \cdot h^{n+1}_{3/2}} & 1+\dfrac{\Delta t A^n_{V3/2}}{h^{n+1}_2 \cdot h^{n+1}_{3/2}}+\dfrac{\Delta t A^n_{V5/2}}{h^{n+1}_2 \cdot h^{n+1}_{5/2}} & -\dfrac{\Delta t A^n_{V5/2}}{h^{n+1}_3 \cdot h^{n+1}_{5/2}} & & \\ & -\dfrac{\Delta t A^n_{V5/2}}{h^{n+1}_2 \cdot h^{n+1}_{5/2}} & \ddots & \ddots & \\ & & \ddots & \ddots & -\dfrac{\Delta t A^n_{Vkm-1/2}}{h^{n+1}_{km} \cdot h^{n+1}_{km-1/2}} \\ 0 & & & -\dfrac{\Delta t A^n_{Vkm-1/2}}{h^{n+1}_{km-1} \cdot h^{n+1}_{km-1/2}} & 1+\dfrac{\Delta t A^n_{Vkm-1/2}}{h^{n+1}_{km} \cdot h^{n+1}_{km-1/2}}+\dfrac{2\Delta t C^n_{d}\sqrt{(U^2)^{n-1}_{km}+(\bar{V}^2)^{n-1}_{km}}}{(h^2)^n_{km}} \end{bmatrix}_{i+½,j} .$$

The matrix A is tridiagonal and clearly has all positive elements on the main diagonal and all nonpositive elements on the off-diagonals; it has the properties referred to in mathematics as those of an M-matrix.[37] In general, A is non-symmetric[38] but diagonally dominant.[39] Since the system of equations 4.31 also should be irreducible,[40] it can be uniquely transformed with a double-sweep algorithm to the form

$$U^{n+1}_{i+½,j} = [A^{-1}G]_{i+½,j} - g\frac{\Delta t}{\Delta x}\rho^n_{i+½,j,1}(\zeta^{n+1}_{i+1,j} - \zeta^{n+1}_{i,j})[A^{-1}R]_{i+½,j} \quad . \tag{4.32}$$

In executing the double-sweep algorithm, the results actually sought are only the two matrix products $A^{-1}G$ and $A^{-1}R$, which are column vectors equal in order to the number of model layers; the inverse of A is never computed by itself. Equation 4.32 is useful because it is an expression that can be formally substituted into the continuity equation.

[37] A matrix $A = (\alpha_{ij})$ is an M-matrix if $(\alpha_{ij} \le 0)$ for $i \ne j$, A is nonsingular (determinant $A \ne 0$), and $A^{-1} \ge 0$. (Meijerink and van der Vorst, 1977)

[38] A matrix $A = (\alpha_{ij})$ is symmetric if $\alpha_{ij} = \alpha_{ji}$ and non-symmetric otherwise. In the two-level model formulated by Casulli and Cheng (1992), the matrix A is symmetric because the model is formulated with the dependent variable of velocity rather than volumetric transport. Here the matrix A is symmetric only when the layer heights are all equal. This rarely occurs because the surface layer height generally varies with time. There is, however, very little computational penalty for executing the double sweep algorithm on the non-symmetric rather than symmetric system.

[39] A $km \times km$ matrix, $A = (\alpha_{ij})$, is diagonally dominant if $|\alpha_{ii}| \ge \sum_{j=1,\, i\ne j}^{km} |\alpha_{ij}|$ and for some i strict inequality holds.

[40] An irreducible system of km equations means that the equations cannot be rearranged so that some of the unknown variables can be found by solving fewer than km equations.

4.3.1.2 Continuity Equation

The finite-difference analog of the continuity equation is

$$\zeta_{i,j}^{n+1} = \zeta_{i,j}^{n-1} - \frac{\Delta t}{\Delta x}\left[\sum_{k=1}^{km}(U_{i+½,j,k}^{n+1} - U_{i-½,j,k}^{n+1} + U_{i+½,j,k}^{n-1} - U_{i-½,j,k}^{n-1})\right]$$

$$- \frac{\Delta t}{\Delta y}\left[\sum_{k=1}^{km}(V_{i,j+½,k}^{n+1} - V_{i,j+½,k}^{n+1} + V_{i,j+½,k}^{n-1} - V_{i,j-½,k}^{n-1})\right] \quad . \tag{4.33}$$

By defining a row matrix $\Xi = [1, 1, \ldots , 1]$ with km elements equal to unity, equation 4.33 can be rewritten in matrix notation as

$$\zeta_{i,j}^{n+1} = \zeta_{i,j}^{n-1} - \frac{\Delta t}{\Delta x}\left[\Xi \boldsymbol{U}_{i+½,j}^{n+1} - \Xi \boldsymbol{U}_{i-½,j}^{n+1}\right] - \frac{\Delta t}{\Delta y}\left[\Xi \boldsymbol{V}_{i,j+½}^{n+1} - \Xi \boldsymbol{V}_{i,j-½}^{n+1}\right] - d_{i,j}^{n-1} \quad , \tag{4.34}$$

where

$$d_{i,j}^{n-1} = \frac{\Delta t}{\Delta x}\left[\sum_{k=1}^{km} U_{i+½,j,k}^{n-1} - \sum_{k=1}^{km} U_{i-½,j,k}^{n-1}\right] + \frac{\Delta t}{\Delta y}\left[\sum_{k=1}^{km} V_{i,j+½,k}^{n-1} - \sum_{k=1}^{km} V_{i,j+½,k}^{n-1}\right].$$

After substituting equation 4.32 for $\boldsymbol{U}$ and a similar equation for $\boldsymbol{V}$ into equation 4.34, an equation involving only the unknown surface elevation is obtained:

$$\begin{aligned}
\zeta_{i,j}^{n+1} &- g\left(\frac{\Delta t}{\Delta x}\right)^2 \{ \rho_{i+½,j,1}^{n} [\Xi \boldsymbol{A}^{-1}\boldsymbol{R}]_{i+½,j} (\zeta_{i+1,j}^{n+1} - \zeta_{i,j}^{n+1}) \\
&\qquad - \rho_{i-½,j,1}^{n} [\Xi \boldsymbol{A}^{-1}\boldsymbol{R}]_{i-½,j} (\zeta_{i,j}^{n+1} - \zeta_{i,j-1}^{n+1}) \} \\
&- g\left(\frac{\Delta t}{\Delta x}\right)^2 \{ \rho_{i,j+½,1}^{n} [\Xi \boldsymbol{A}^{-1}\boldsymbol{R}]_{i,j+½} (\zeta_{i,j+1}^{n+1} - \zeta_{i,j}^{n+1}) \\
&\qquad - \rho_{i,j-½,1}^{n} [\Xi \boldsymbol{A}^{-1}\boldsymbol{R}]_{i,j-½} (\zeta_{i,j}^{n+1} - \zeta_{i,j-1}^{n+1}) \} \\
&= \zeta_{i,j}^{n-1} - \frac{\Delta t}{\Delta x}\left\{ \left[\Xi \boldsymbol{A}^{-1}\boldsymbol{G}\right]_{i+½,j} - \left[\Xi \boldsymbol{A}^{-1}\boldsymbol{G}\right]_{i-½,j} \right\} \\
&\qquad - \frac{\Delta t}{\Delta y}\left\{ \left[\Xi \boldsymbol{A}^{-1}\boldsymbol{G}\right]_{i,j+½} - \left[\Xi \boldsymbol{A}^{-1}\boldsymbol{G}\right]_{i,j-½} \right\} - d_{i,j}^{n-1} \ .
\end{aligned} \tag{4.35}$$

Because the matrix $\boldsymbol{A}$ is an M-matrix, its matrix inverse $\boldsymbol{A}^{-1}$ has all non-negative elements (for proof see Lancaster and Tismenetsky, 1985). Therefore, the matrix products $\Xi\boldsymbol{A}^{-1}\boldsymbol{R}$ and $\Xi\boldsymbol{A}^{-1}\boldsymbol{G}$ in equation 4.35 are each a single non-negative number. Rearranging equation 4.35, the following form can be obtained:

$$-sx_{i-\frac{1}{2},j}\zeta^{n+1}_{i-1,j} - sy_{i,j-\frac{1}{2}}\zeta^{n+1}_{i,j-1} + r_{i,j}\zeta^{n+1}_{i,j} - sy_{i,j+\frac{1}{2}}\zeta^{n+1}_{i,j+1} - sx_{i+\frac{1}{2},j}\zeta^{n+1}_{i+1,j} = q_{i,j} \tag{4.36}$$

where

$$sx_{i\pm\frac{1}{2},j} = g\left(\frac{\Delta t}{\Delta x}\right)^2 \rho^n_{i\pm\frac{1}{2},j,1}\left[\Xi\boldsymbol{A}^{-1}\boldsymbol{R}\right]_{i\pm\frac{1}{2},j} ,$$

$$sy_{i,j\pm\frac{1}{2}} = g\left(\frac{\Delta t}{\Delta x}\right)^2 \rho^n_{i,j\pm\frac{1}{2},1}\left[\Xi\boldsymbol{A}^{-1}\boldsymbol{R}\right]_{i,j\pm\frac{1}{2}} ,$$

$$r_{i,j} = 1 + sx_{i+\frac{1}{2},j} + sx_{i-\frac{1}{2},j} + sy_{i,j+\frac{1}{2}} + sy_{i,j-\frac{1}{2}} ,$$

$$q_{i,j} = \zeta^{n-1}_{i,j} - \frac{\Delta t}{\Delta x}\left(\left[\Xi\boldsymbol{A}^{-1}\boldsymbol{G}\right]_{i+\frac{1}{2},j} - \left[\Xi\boldsymbol{A}^{-1}\boldsymbol{G}\right]_{i-\frac{1}{2},j}\right)$$
$$- \frac{\Delta t}{\Delta y}\left(\left[\Xi\boldsymbol{A}^{-1}\boldsymbol{G}\right]_{i,j+\frac{1}{2}} - \left[\Xi\boldsymbol{A}^{-1}\boldsymbol{G}\right]_{i,j-\frac{1}{2}}\right) - d^{n-1}_{i,j} ,$$

and $d^{n-1}_{i,j}$ is as defined for equation 4.34. Equation 4.36 can be written at each of the interior nodal points of the rectangular grid (excluding the fictitious row and column along each boundary) to form N = (*imax* – 2) × (*jmax* – 2) simultaneous linear equations in the unknowns $\{\zeta_{i,j}\}$. If the set of equations is written in matrix form, the coefficient matrix is five-diagonal with a tridiagonal band along the main diagonal and two additional diagonals displaced an equal amount above and below the main diagonal (*fig.4.7*); the amount the outer diagonals are displaced is referred to as the matrix bandwidth and is dependent on the dimensions of the grid and the ordering of the unknowns. Here the most common "natural" ordering is used in which the numbering is done along the smallest dimension of the finite-difference grid. For example, if the smallest dimension is the *y* (north-south) direction, the natural ordering scheme numbers from bottom to top (south to north) on a column starting with the first (westernmost) column that is not fictitious (*fig. 4.8*). Other orderings such as the "ordering along the diagonals" and the "red-black" ordering also are mathematically consistent (see Young, 1971, p. 159). For problems involving irregularly shaped regions, the form of the coefficient matrix does not change. Dry point equations are represented with a value of 1.0 on the main diagonal and zeros for the other elements of the equation row; the continuity equation for a dry point therefore is reduced to $\zeta^{n+1}_{i,j} = \zeta^n_{i,j}$ where the assigned water surface elevation is artificial. Because all the dry point equations can be made identical, only one must be stored.

The coefficient matrix for the system of water surface elevation equations 4.36 is both symmetric and positive definite,[41] a fortuitous circumstance. Therefore, the equations can be solved efficiently by iteration using the preconditioned conjugate-gradient method discussed in the next section. Once the $\zeta^{n+1}_{i,j}$ are determined, equation 4.32 and the corresponding equation for $\boldsymbol{V}^{n+1}_{i,j+\frac{1}{2}}$ can be solved explicitly for the new layer volumetric transports.

[41]For a formal discussion of positive definite equation systems, see Golub and Van Loan (1989, p. 139ff). In general terms, if $\boldsymbol{A}$ is symmetric with non-negative diagonal elements and diagonally dominant, $\boldsymbol{A}$ is positive definite.

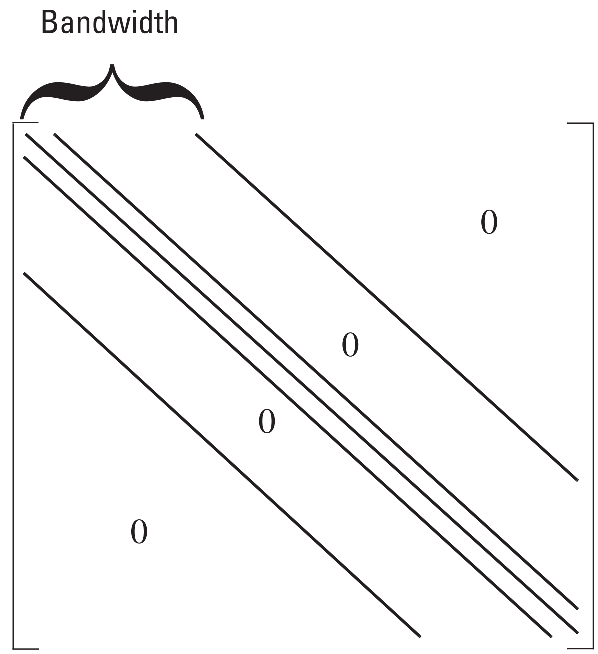

Figure 4.7. Representation of five-diagonal coefficient matrix.

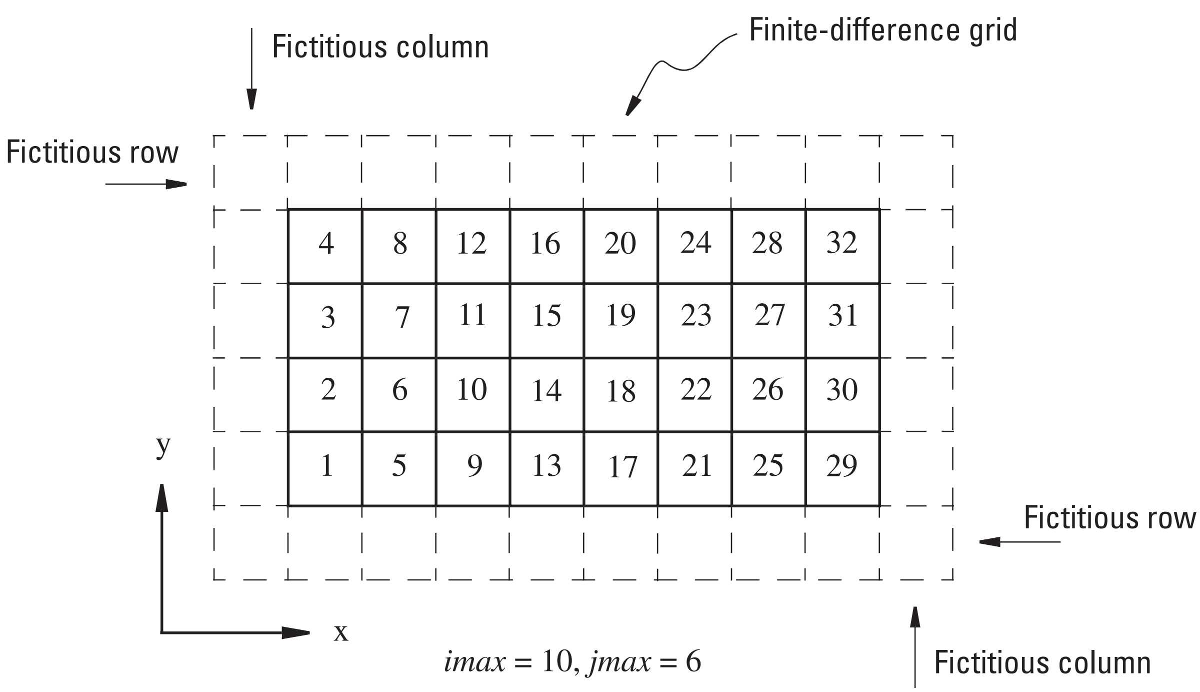

Figure 4.8. Illustration of the "natural" ordering scheme used in forming the matrix system of equations for the free-surface elevation.
In the above example, the bandwidth would be five. *imax* is the total number of columns in the finite-difference grid (including fictitious columns). *jmax* is the total number of rows in the finite-difference grid (including fictitious rows).

Finally, the vertical velocity w in the water column can be derived from the continuity equation as

$$w^{n+1}_{i,j,k-\frac{1}{2}} = w^{n+1}_{i,j,k+\frac{1}{2}} - \left(U^{n+1}_{i+\frac{1}{2},j,k} - U^{n+1}_{i-\frac{1}{2},j,k}\right)/\Delta x - \left(V^{n+1}_{i,j+\frac{1}{2},k} - V^{n+1}_{i,j-\frac{1}{2},k}\right)/\Delta y \tag{4.37}$$

$$(k = 2, 3, 4, \ldots, km).$$

This equation is solved explicitly, starting from the bottom layer in which $w_{i,j,km+\frac{1}{2}}$ is assigned a zero value.

4.3.1.3 Matrix Solution

The matrix $\{\zeta^{n+1}_{i,j}\}$ can be solved by either direct (noniterative) or iterative techniques. The primary difference is that direct techniques (such as Gaussian elimination and its variants) produce a solution after a predetermined number of arithmetic operations, whereas iterative methods produce a sequence of approximate solutions which converge to the correct value. For large systems of linear equations where the coefficient matrix is sparsely populated (few nonzero elements), iterative techniques generally represent the best approach since they require less storage[42] and are less susceptible to round off errors. If a good first estimate for the unknowns in an iterative solution is available, it can also require less computer time to obtain a solution of comparable accuracy to a direct solution. The preconditioned conjugate-gradient method (PCGM) (Meijerink and van der Vorst, 1977) is an especially attractive iterative technique that is ideally suited for matrix solutions that have symmetric and positive definite coefficient matrices; convergence of the iterative process in those solutions is generally rapid. Various forms of the PCGM have been tested and compare favorably with other iterative methods when applied to ground-water flow modeling problems where the matrix system of equations is similar in form to that solved here (see for example, Kuiper, 1981, 1987; Meyer and others, 1989; Hill, 1990).

The preference for direct or iterative solution techniques may well depend on the size of the problem being solved. Estuarine and coastal modeling problems can easily involve large matrix solutions with 100,000 or more unknowns. Because iterative techniques can efficiently solve these large systems with considerably lower storage requirements than direct techniques, they are usually the best choice. However, there is a trend toward solving larger and larger systems by direct methods, so further research directly comparing the two approaches for a variety of actual 3-D estuarine modeling problems is still needed. Here the PCGM was adopted without doing any comparison with a direct technique. For the small problem tested in this report, a direct solution technique certainly could have been chosen.

The matrix solution for $\{\zeta^{n+1}_{i,j}\}$ is implemented by using the non-symmetric preconditioned conjugate-gradient (NSPCG) software package developed at the Center for Numerical Analysis at the University of Texas at Austin (Kincaid and others, 1989). This package provides many preconditioning and acceleration methods to aid in selecting an iterative technique that is optimal for a particular matrix structure, computer architecture (vector or scalar), and computer storage limitations. The reader is referred to Oppe and others (1988) for the preconditioners and acceleration methods that are available. Without testing the 3-D estuarine model on actual large scale field problems, it is not possible to judge fairly the iterative techniques available in the NSPCG package. A few comparisons of techniques were made for the simple problem in this report, and the conjugate-gradient accelerator clearly was more efficient than the next best choice, which was successive over relaxation. The best preconditioner was modified incomplete Cholesky (see Axelsson and Lindskog, 1986), which was used for all test runs in this report. Also promising, however, was using a red-black (or odd-even) reduction scheme on the matrix system and then solving the reduced matrix system using the

[42]In direct solution techniques, many of the elements of a sparse coefficient matrix that are originally zero will become nonzero in the course of the computation, and they will require storage space. In computations with iterative techniques, no new nonzero elements are introduced in the coefficient matrix.

modified incomplete Cholesky conjugate-gradient (MICCG) scheme; this approach demands greater storage than using MICCG alone because the reduced system matrix must be stored. All comparisons were made on a scalar workstation. The NSPCG package is coded specifically for comparing iterative techniques, but it may not be ideal for achieving maximum efficiency in an operational code. Once further experience is gained with iterative matrix schemes for the model, an efficient coding of the best overall scheme will be implemented in the model.

In order to speed convergence of the iterative solution at each time step, the initial estimates for the unknown array of $\zeta_{i,j}^{n+1}$ are taken from the surface layer heights $\hat{h}_{i,j,1}^{n+1}$ that are estimated by extrapolation using equation 4.28 (ζ is obtained from the surface layer height by subtracting the depth of the layer below the model datum). Using these initial estimates (which are usually quite accurate), the iterative solution typically required no more than one or two iterations to converge to a solution within a strict tolerance. It is likely that larger and more complex problems will require more iterations.

4.3.1.4 Salt Transport Equation

The salt transport equation is solved after the hydrodynamic variables are determined. The vertical salt flux term in equation 3.61 is replaced by introducing the vertical salt exchange (or eddy diffusion) coefficient:

$$\frac{J_z}{\rho} = D_V \frac{\partial s}{\partial z}. \tag{4.38}$$

In the finite-difference equation, the vertical diffusion of salt is treated implicitly, and the advection and horizontal diffusion terms are treated explicitly. The finite-difference equation is centered within a layer k at the horizontal point $i\Delta x$, $j\Delta y$:

$$\frac{h_{i,j,k}^{n+1} s_{i,j,k}^{n+1} - h_{i,j,k}^{n-1} s_{i,j,k}^{n-1}}{2\Delta t} + D_{Vi,j,k+1/2}^{n} \frac{(s_{i,j,k}^{n+1} - s_{i,j,k+1}^{n+1} + s_{i,j,k}^{n-1} - s_{i,j,k+1}^{n-1})}{(h_{i,j,k}^{n} + h_{i,j,k+1}^{n})}$$

$$- D_{Vi,j,k-1/2}^{n} \frac{(s_{i,j,k-1}^{n+1} - s_{i,j,k}^{n+1} + s_{i,j,k-1}^{n-1} - s_{i,j,k}^{n-1})}{(h_{i,j,k-1}^{n} + h_{i,j,k}^{n})} = F_{i,j,k}^{n}, \tag{4.39}$$

where $F_{i,j,k}^{n}$ represents the explicit terms and is defined by

$$F_{i,j,k}^{n} = -(ADV_s)_{i,j,k}^{n} + (HDIFF_s)_{i,j,k}^{n-1} \quad . \tag{4.40}$$

The expanded form of the two terms in $F_{i,j,k}^{n}$ is included in Appendix D (eqs. D.9 and D.10). Equation 4.39 can be rearranged into the following form

$$A_{i,j,k} s_{i,j,k-1}^{n+1} + B_{i,j,k} s_{i,j,k}^{n+1} + C_{i,j,k} s_{i,j,k+1}^{n+1} = D_{i,j,k} \tag{4.41}$$

where

$$A_{i,j,k} = -D^n_{V_{i,j,k-\frac{1}{2}}}/(h^n_{i,j,k-1} + h^n_{i,j,k}),$$

$$B_{i,j,k} = h^{n+1}_{i,j,k}/(2\Delta t) + D^n_{V_{i,j,k+\frac{1}{2}}}/(h^n_{i,j,k} + h^n_{i,j,k+1}) + D^n_{V_{i,j,k-\frac{1}{2}}}/(h^n_{i,j,k-1} + h^n_{i,j,k}),$$

$$C_{i,j,k} = -D^n_{V_{i,j,k+\frac{1}{2}}}/(h^n_{i,j,k} + h^n_{i,j,k+1}), \quad \text{and}$$

$$\begin{aligned} D_{i,j,k} = {} & F^n_{i,j,k} + (h^{n-1}_{i,j,k} s^{n-1}_{i,j,k})/(2\Delta t) \\ & - D^n_{V_{i,j,k+\frac{1}{2}}}(s^{n-1}_{i,j,k} - s^{n-1}_{i,j,k+1})/(h^n_{i,j,k} + h^n_{i,j,k+1}) \\ & + D^n_{V_{i,j,k-\frac{1}{2}}}(s^{n-1}_{i,j,k-1} - s^{n-1}_{i,j,k})/(h^n_{i,j,k-1} + h^n_{i,j,k}) \end{aligned} \tag{4.42}$$

Applying equation 4.41 to each of the layers at a computational point $i\Delta x$, $j\Delta y$ results in a system of km equations involving km unknown values of $s^{n+1}_{i,j,k}$. The boundary conditions are satisfied by choosing $A_{i,j,1} = 0$, $C_{i,j,km} = 0$ and setting the diffusion coefficients to zero at the free surface and bottom. The matrix form of the equations is tridiagonal, which can be efficiently solved with the double sweep algorithm. Once the new salinities are computed, they are used to update the density field using the equation of state presented in Appendix B.

4.3.2 Semi-Implicit Trapezoidal Scheme

The finite-difference equations for the semi-implicit trapezoidal scheme are nearly identical to those of the semi-implicit leapfrog scheme, except the time interval over which the scheme is applied is halved to Δt from $2\Delta t$. The integration procedure is centered at the time level $(n + \frac{1}{2})\Delta t$ and no longer involves the time level $(n - 1)\Delta t$. The scheme, as used here, involves three time levels (n, $n + \frac{1}{2}$, $n + 1$) but is referred to as a two-level scheme since it is executed over a single time step. The variables needed in the scheme at the $(n + \frac{1}{2})\Delta t$ time level are determined by averaging; for example,

$$U^{n+\frac{1}{2}}_{i+\frac{1}{2},j,k} = \frac{1}{2}\left(\tilde{U}^{n+1}_{i+\frac{1}{2},j,k} + U^n_{i+\frac{1}{2},j,k}\right),$$

where the symbol (˜) denotes the estimate of the unknown from the semi-implicit leapfrog solution. The form of the explicit stage for the x-momentum finite-difference equation is

$$\hat{U}_{i+\frac{1}{2},j,k} = U^n_{i+\frac{1}{2},j,k} + \Delta t[-(ADV_x)^{n+\frac{1}{2}} + (COR_x)^{n+\frac{1}{2}} - (BCLINIC_x)^{n+\frac{1}{2}} + (HDIFF_x)^n]_{i+\frac{1}{2},j,k}, \tag{4.43}$$

which is very similar to equation 4.23 for the leapfrog scheme. The bracketed terms are identical to those expanded in Appendix D but are evaluated at the time level indicated. The finite-difference equation for the implicit stage of the x-momentum equation is

$$
\begin{aligned}
U^{n+1}_{i+\frac{1}{2},j,k} = {} & \hat{U}_{i+\frac{1}{2},j,k} - \frac{g}{2}\frac{\Delta t}{\Delta x} h^{n+\frac{1}{2}}_{i+\frac{1}{2},j,k}\left(\frac{\rho^{n+\frac{1}{2}}_{i+\frac{1}{2},j,1}}{\rho^{n+\frac{1}{2}}_{i+\frac{1}{2},j,k}}\right)\cdot\left(\zeta^{n+1}_{i+1,j} - \zeta^{n+1}_{i,j} + \zeta^{n}_{i+1,j} - \zeta^{n}_{i,j}\right) \\
& + \frac{\Delta t}{2}\left(A_{V\,i+\frac{1}{2},j,k-\frac{1}{2}}^{\;n+\frac{1}{2}}\cdot\left(\frac{(U/h)^{n+1}_{i+\frac{1}{2},j,k-1} - (U/h)^{n+1}_{i+\frac{1}{2},j,k}}{h^{n+1}_{i+\frac{1}{2},j,k-\frac{1}{2}}} + \frac{u^{n}_{i+\frac{1}{2},j,k-1} - u^{n}_{i+\frac{1}{2},j,k}}{h^{n}_{i+\frac{1}{2},j,k-\frac{1}{2}}}\right)\right. \\
& \left. - A_{V\,i+\frac{1}{2},j,k+\frac{1}{2}}^{\;n+\frac{1}{2}}\cdot\left(\frac{(U/h)^{n+1}_{i+\frac{1}{2},j,k} - (U/h)^{n+1}_{i+\frac{1}{2},j,k+1}}{h^{n+1}_{i+\frac{1}{2},j,k+\frac{1}{2}}} + \frac{u^{n}_{i+\frac{1}{2},j,k} - u^{n}_{i+\frac{1}{2},j,k+1}}{h^{n}_{i+\frac{1}{2},j,k+\frac{1}{2}}}\right)\right) ,
\end{aligned} \tag{4.44}
$$

which is analogous to the leapfrog equation 4.26. The continuity equation for the trapezoidal scheme is

$$
\begin{aligned}
\zeta^{n+1}_{i,j} = {} & \zeta^{n}_{i,j} - \frac{1}{2}\frac{\Delta t}{\Delta x}\left[\sum_{k=1}^{km}\left(U^{n+1}_{i+\frac{1}{2},j,k} - U^{n+1}_{i-\frac{1}{2},j,k} + U^{n}_{i+\frac{1}{2},j,k} - U^{n}_{i-\frac{1}{2},j,k}\right)\right] \\
& - \frac{1}{2}\frac{\Delta t}{\Delta x}\left[\sum_{k=1}^{km}\left(V^{n+1}_{i,j+\frac{1}{2},k} - V^{n+1}_{i,j+\frac{1}{2},k} + V^{n}_{i,j+\frac{1}{2},k} - V^{n}_{i,j-\frac{1}{2},k}\right)\right] .
\end{aligned} \tag{4.45}
$$

It is straightforward to develop all the equations for the trapezoidal step from those already presented in section 4.3.1.

The iteration for the matrix solution in the trapezoidal step is started with the earlier estimates for $\left\{\zeta^{n+1}_{i,j}\right\}$ from the leapfrog step. The accuracy of these estimates causes the iterative convergence to be rapid.

Experience with the 3-D model has shown that the trapezoidal step is not always needed. For example, the 3-D test case in this report could be solved accurately with just the leapfrog step. The trapezoidal step is needed mostly to stabilize the solution for markedly nonlinear problems and to improve the accuracy of the time integration when large time steps are used. If necessary to stabilize a solution, more than one iteration of the trapezoidal step can also be used; a sparing use of additional iterations is advisable, however, to keep the computer run time of the model from becoming excessively long.

5. Numerical Experiments

5.1 Introduction

Numerical experiments are useful in first verifying that the computer coding of a computational scheme can accurately solve the governing equations under at least some combinations of computational grid intervals and wave conditions. For this purpose, the test problems used in experiments must have solutions that are available either analytically or from another independently developed and verified computer model. Once the computer code is verified, numerical experiments are then useful in studying the stability and convergence properties of a numerical scheme by comparing solutions that are computed by using varying time and space steps and wave conditions.

The von Neumann (or Fourier) method (O'Brien and others, 1950) is a widely used tool for studying the stability of numerical schemes that are used in solving linear differential equations. It is based on representing the solution of a difference equation as a finite Fourier series and studying the decay or amplification of each mode individually to determine stability or instability. By introducing the concept of a complex propagation factor, Leendertse (1967) extended the von Neumann method for use in analyzing the convergence of linear numerical schemes. Using two-time-level, finite-difference discretizations of the linear shallow water equations, Casulli and Cheng (1990) and Casulli and Cattani (1994) used the von Neumann method to study the stability of 1-D and 3-D semi-implicit methods, respectively. Cunge and others (1980) present a von Neumann convergence analysis in the form of amplitude and phase error portraits for the 1-D semi-implicit scheme of Abbott-Ionescu. Using a finite-element discretization of the 1-D linear shallow-water equations, Gray and Lynch (1977) applied the von Neumann method to analyze the convergence of both two- and three-time-level semi-implicit schemes. Although the von Neumann method is indeed useful, it is fundamentally incomplete as it does not take into account the full effects of nonlinearity, iteration schemes, and interpolations on the properties of stability and convergence.

In this chapter, numerical experiments are used to investigate the stability and convergence of the full nonlinear form of the 1-D and 3-D semi-implicit schemes presented in Chapter 4. An emphasis is placed on studying the effect of iteration.[43] Instances of nonlinear instability are shown to occur in the 1-D experiments that are not revealed by the linear von Neumann analysis. Iteration is shown to be effective in suppressing the instabilities and obtaining a smooth solution. Because adding iterations does increase the computer run time of a model simulation, finding the minimum number of iterations that are needed to achieve a stable and accurate solution is an important goal.

5.2 One-Dimensional Experiments

The two-level and three-level semi-implicit schemes for one dimension are tested below using two numerical experiments. The first experiment routes a hydrograph down a rectangular channel with an initially shallow depth of flow. The experiment represents an inland river modeling problem that is strongly nonlinear and has high frictional resistance. The second experiment simulates the propagation of a repeating semidiurnal tide into a closed basin of constant depth. The tidal flow experiment is influenced only a little by frictional resistance but is affected by nonlinear advection and the rapidly changing bidirectional flow that is typical in estuaries.

5.2.1 Hydrograph Routing

This experiment was first designed by the U.S. Geological Survey (USGS) in the early 1980s to test and compare three different 1-D finite-difference flow models, including the two widely used models developed by the National Weather Service (Fread, 1978) and the U.S. Geological Survey (Schaffranek and others, 1981).[44] The experiment has since been used by USGS researchers (for example, DeLong, 1993, fig. 2) to test other flow models that are based on numerical schemes of varying accuracies. The

[43] In the case of the three-time-level scheme, iteration is used here to mean the addition during each time step of one or more trapezoidal-scheme steps after the leapfrog- scheme step.

[44] The 1-D models by Fread (1978) and Schaffranek and others (1981) are based on the fully implicit four-point scheme by Preissmann (1961); there are a few differences between the two models in the details of how the four-point scheme is implemented.

solution to the fully nonlinear test problem is well known from these past model applications; the convergence characteristics of these previously tested models vary widely, depending on their numerical accuracy.

The channel characteristics and initial flow conditions for the hydrograph experiment are given in *figure 5.1*. The channel is rectangular; top width B = 100 ft (30.5 m),[45] bed slope $S_0 = 0.001$, and length L = 150,000 ft (45,720 m). The Manning resistance coefficient for the channel is 0.045. The initial steady flow is $Q_0 = 250$ ft^3/s (7.1 m^3/s), and the initial flow depth according to Manning's formula is $H_0 = 1.688$ ft (0.51 m). The channel is considered wide enough so that the hydraulic radius in equation 4.3 can be approximated by the flow depth.

For the test problem, the discharge at the upstream boundary of the channel ($x = 0$) is described by

$$Q(t) = 250 + \frac{750}{\pi}\left(1 - \cos\frac{\pi t}{75}\right) \qquad 0 < t < 150$$

and

$$Q(t) = 250 \qquad t \geq 150,$$

where the time t is expressed in minutes from the start of the simulation and discharge is in cubic feet per second (ft^3/s). At the downstream boundary of the channel (x = 150,000), the depth of flow is constant at H_0. The simulation is run for 500 minutes. The results of the hydrograph routing are examined at x = 50,000 ft (15,240 m) to avoid any effect from the downstream boundary condition on the computed hydrograph. (The water level at the downstream boundary does not rise until the hydrograph passes 50,000 ft.)

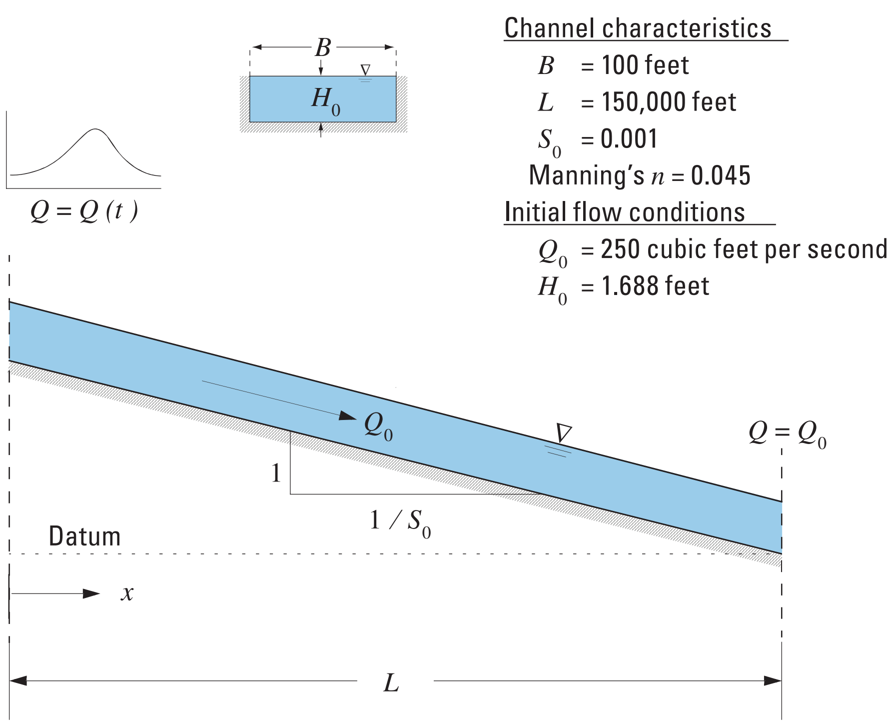

Figure 5.1. Channel characteristics and initial flow conditions for the 1-dimensional hydrograph test problem.

[45]The 1-D numerical experiments, as originally designed, were posed in English units; these units are adopted here for consistency. The metric unit conversions are shown in parentheses following the English units.

5.2.1.1 Two-Level Scheme

Figure 5.2 shows three computed hydrographs using the two-level, semi-implicit scheme described in section 4.2.1. Two of the solutions are based on computations using a coarse numerical grid size of Δx = 5,000 ft (1,524 m) and Δt = 5 minutes; the third solution is considered a "base solution" and is computed using an extremely small grid size that keeps the numerical error in the solution negligible. The base solution agrees to a high degree of accuracy with the solutions to this problem obtained using the other flow models tested by the USGS. All three solutions were computed with the number of iterations (*niter*) of the numerical scheme fixed throughout the simulation; the coarse grid solutions used values of *niter* = 1 and *niter* = 2, the base solution used *niter* = 5.

Figure 5.2 indicates that a significant improvement in accuracy is gained by solving the coarse grid case using two iterations rather than one. The root mean square error (RMS_e in table 5.1) of the solution measured against the base solution improved from 7.6 percent using *niter* = 1 to 2.7 percent using *niter* = 2. The improvement is due to a centering in time of the nonlinear coefficients of the finite-difference momentum equation by the iteration process, as discussed in section 4.2.1. Because the frictional attenuation of the routed hydrograph is significant, the backward-in-time evaluation of the frictional coefficient γ in equation 4.7 is mostly responsible for the large underestimation of the wave attenuation in the solution using *niter* = 1; also affecting the accuracy, but to a lesser degree, is the backward-in-time evaluation of the coefficient H in the pressure (water surface slope) and friction terms in equation 4.7. The centering in time of both γ and H by the iteration process raises the accuracy of the time integration scheme from first to second order.

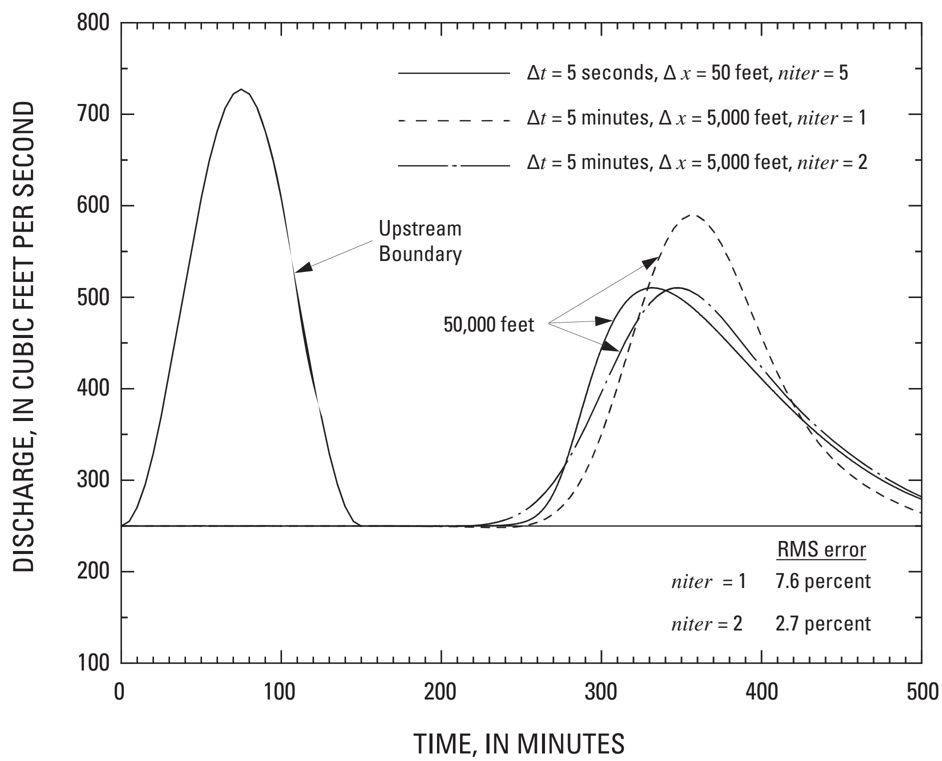

Figure 5.2. Hydrographs computed with the two-level, semi-implicit scheme using a large spatial step size of Δx = 5,000 feet (1,524 meters) and a time step size of Δt = 5 minutes.
Solutions using one iteration (*niter* = 1) and two iterations (*niter* = 2) are compared against a base solution using a very small time and space step and five iterations (*niter* = 5). The hydrograph at the upstream boundary is also plotted. RMS, root mean square.

Table 5.1. Definition of error measures (expressed as percentages) for the hydrograph test problem.

Description	Definition
Root mean square error: Root mean square error of the computed hydrograph, normalized on the peak discharge of the base solution hydrograph	$RMS_e = \left. \dfrac{100\left[\sum_{n=1}^{nts} (Q^n(x) - Q_b^n(x))^2\right]^{1/2}}{(nts)^{1/2}\, Q_b^{max}(x)} \right\rvert_{x = 50{,}000 \text{ feet}}$
Amplitude error: Error in the peak discharge of the computed hydrograph, normalized on the peak discharge of the base solution hydrograph	$A_e = \left. \dfrac{100(Q^{max}(x) - Q_b^{max}(x))}{Q_b^{max}(x)} \right\rvert_{x = 50{,}000 \text{ feet}}$
Phase error: Error in the time associated with the center of gravity of the computed hydrograph, normalized on the time associated with the center of gravity of the base solution hydrograph	$P_e = \left. \dfrac{100(T(x) - T_b(x))}{T_b(x)} \right\rvert_{x = 50{,}000 \text{ feet}}$ where $T(x) = \dfrac{\int_0^{TL} t(Q(x,t) - Q_0)dt}{\int_0^{TL} (Q(x,t) - Q_0)dt}$
Mass preservation error: Error in mass preservation for the computed solution, normalized on the total mass from the base solution	$M_e = \left. 100\left(1 - \dfrac{\int_0^{L} (H(x,t) - H_0)dx}{\int_0^{L} (H_b(x,t) - H_0)dx}\right) \right\rvert_{t = 500 \text{ minutes}}$

nts	= number of time steps in 500 minute simulation
$Q_b^n(x)$	= discharge for the base solution at location x and time $t = n\Delta t$
$Q_b^{max}(x)$	= peak discharge for the base solution at location x (= 510.25 cubic feet per second at x = 50,000 feet)
$T_b(x)$	= time associated with center of gravity of base solution at location x (= 362.85 minutes for x = 50,000 feet)
$H_b(x, t)$	= depth of flow for the base solution at location x and time t
Q_0	= initial steady discharge (= 250 cubic feet per second)
H_0	= initial water depth determined by Manning's formula for a wide rectangular channel (= 1.688464 feet)
TL	= time of simulation (= 500 minutes)
L	= length of channel (= 150,000 feet)

Integrations were computed numerically using Simpson's Rule.

The solution shown in *figure 5.2* using two iterations is only slightly improved if additional iterations are included in the simulation. The error that remains in the solution when two (or more) iterations are used is attributable to the coarse Δx space step chosen. In *figure 5.3*, the base solution for discharge is plotted at 125-minute intervals against distance along the channel to indicate the spatial scale of the wave as it propagates down the channel. A space step of 5,000 ft (1,524 m) represents the upstream wave over only six or seven grid points. The coarse spatial resolution causes a decrease in the speed of the solution gravity waves, which manifests itself as a time lag between the center of gravity of the computed hydrograph and the base solution. This tendency for coarsely resolved wave components of a numerical solution to be delayed (or accelerated) compared to nature is known as phase error.

The effect of space step size on the solution convergence and stability is evaluated systematically by testing the two-level scheme using increasing values for Δx, starting with a small value of 100 ft (30.5 m); the time step is fixed at 5 minutes. The errors in each computed solution relative to the base solution are quantified in various ways by computing the root mean square error (RMS_e), amplitude error (A_e), phase error (P_e), and mass preservation error (M_e) that are summarized in *table 5.1*. The first three of these error measures are based on a comparison between the computed hydrograph and the base solution hydrograph at x = 50,000 ft (15,240 m). The mass preservation error is computed from the error (relative to the base solution) in total mass of water simulated within the channel at the termination of the simulation (t = 500 minutes). Each of the error measures are expressed as a percentage. The parameters of the base solution and the definitions of the variables used in defining the error measures are listed at the bottom of *table 5.1*.

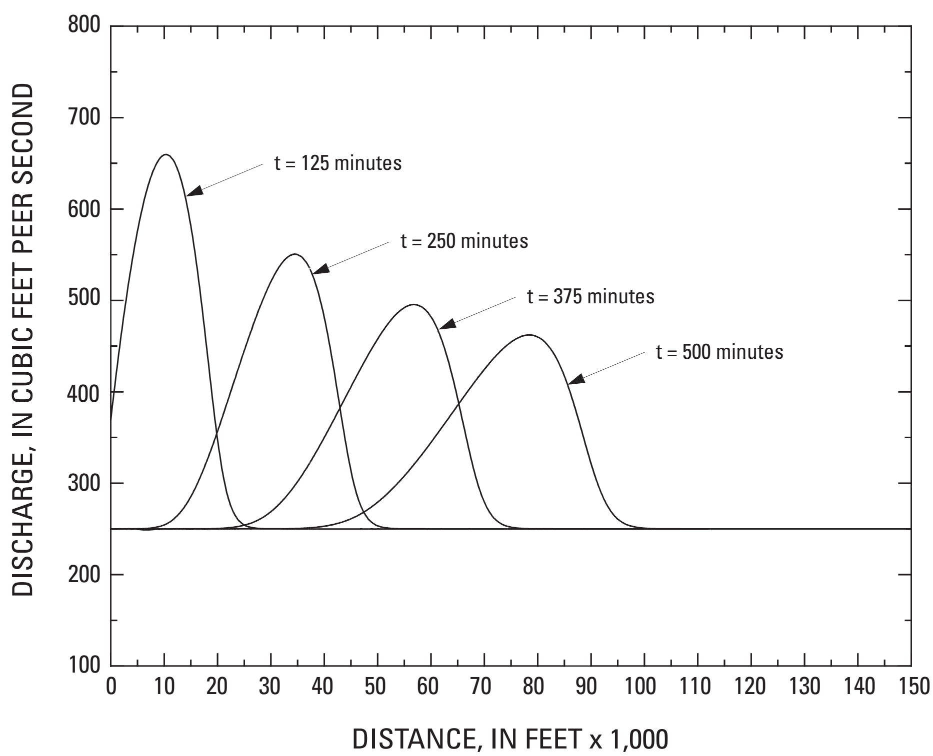

Figure 5.3. Base solution of the hydrograph problem shown at 125-minute intervals during the simulation.

Table 5.2 lists the values of Δx used in the numerical experiment and the ranges of the Courant numbers occurring during each simulation. Both the gravity-wave (Cr_g) and the advection (Cr_a) Courant numbers are listed because both are relevant to the stability and accuracy of the semi-implicit schemes.

The four error measures that are computed from solutions using the two-level model are graphed in *figure 5.4* using three curves that each represent a solution for a different value of *niter*. The results clearly show an improvement in the solution accuracy when the number of iterations are increased from one to two. There is no choice for Δx that yields a solution with acceptable accuracy when only one iteration is used and the time step is 5 minutes. The solutions using two iterations converge to the base solution within acceptable error tolerances for spatial step sizes of 2,500 ft (762 m) or less.

The solutions with the three largest values of Δx (= 2,500, 5,000, and 10,000) and *niter* = 2 are plotted in *figure 5.5* to illustrate the improvement in accuracy with decreasing Δx. It is apparent that the spatial step sizes of 5,000 ft (1,524 m) and 10,000 ft (3,048 m) are much larger than should ever be employed in practice; these solutions show that the magnitude of errors can be large, even when iteration is used if Δx is not chosen properly.

The error measures plotted in *figure 5.4* for solutions using five iterations are not significantly different from those using two iterations and in fact are mostly larger. *Table 5.3* lists the error measures computed for ten solutions using increasing values of *niter* when Δx = 2,500 ft (762 m) and Δx = 5 minutes; the iterative process of convergence to a solution actually “overshoots” on the second iteration, and the solution using two iterations does indeed have smaller error measures overall than the solutions using additional iterations. While this will not be true in general, it is significant that for this difficult test problem, the addition of only a second iteration to the scheme is sufficient to raise the accuracy to an acceptable level.

Table 5.2. Ranges of Courant numbers for hydrograph problem simulations using 5 minutes as a time step (Δt).

[Δx, size of the computational space interval]

Δx, in feet	Cr_g	Cr_a
100	26.7–37.5	4.4-6.8
500	5.3–7.5	0.89-1.4
1,000	2.7–3.8	0.44-0.68
2,000	1.3–1.9	0.22-0.34
2,500	1.1–1.5	0.18-0.27
5,000	0.53–0.75	0.09-0.14
10,000	0.27–0.38	0.04-0.07

Cr_g = gravity-wave Courant number = $(u + \sqrt{gH}) \cdot \Delta t / \Delta x$

Cr_a = advection Courant number = $u \cdot \Delta t / \Delta x$

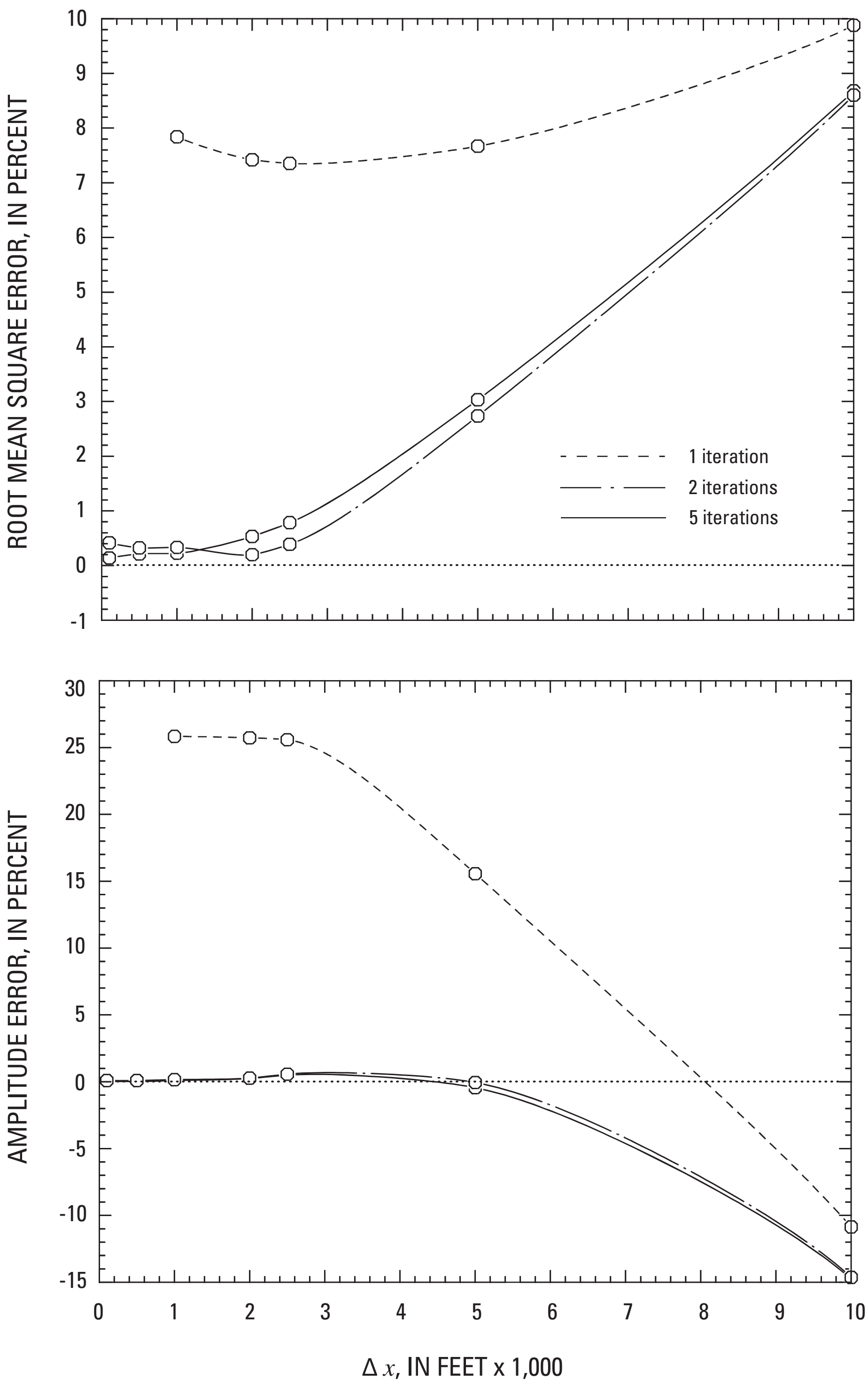

Figure 5.4. Error measures using the two-level semi-implicit scheme on the hydrograph test problem. Δt = 5 minutes for all simulations. Δt is the size of the computational time interval. Δx is the size of the computational space interval.

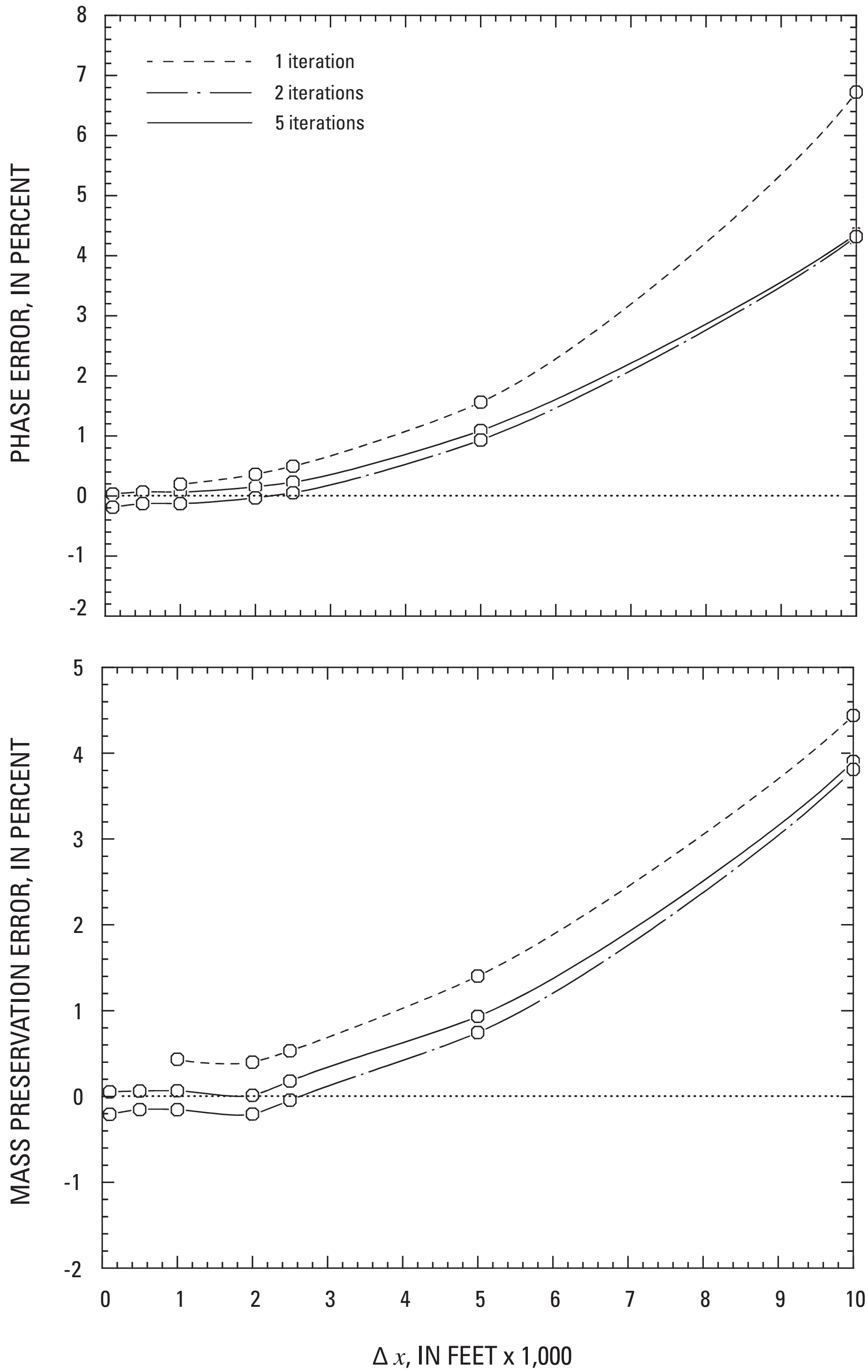

Figure 5.4. Continued.

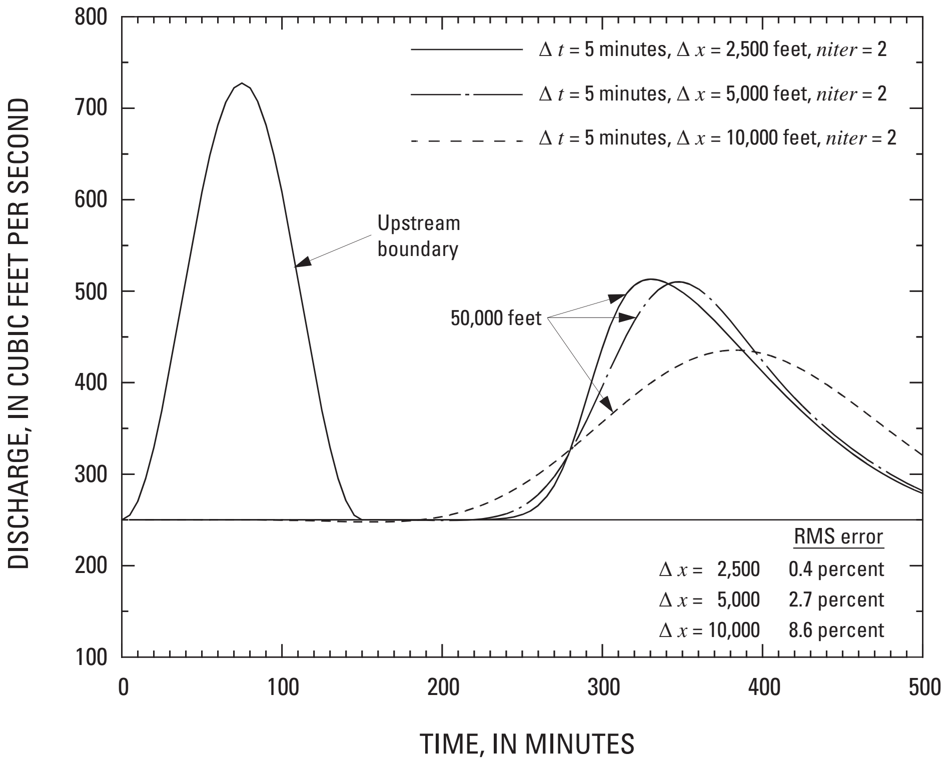

Figure 5.5. Two-level scheme solutions for the hydrograph problem using three different values for space steps (Δx) and a time step (Δt) of 5 minutes. RMS, root mean square.

Table 5.3. Error measures using the two-level semi-implicit scheme on the hydrograph problem with the number of iterations (*niter*) ranging from 1 to 10.

[Note: the error measures are expressed in percent. All simulations used Δx = 2,500 feet and Δt = 5 minutes]

Number of iterations	Root mean square error	Amplitude error	Phase error	Mass preservation error
1	7.37	25.6	0.53	0.50
2	0.41	0.56	0.05	– 0.04
3	0.79	0.37	0.19	0.23
4	0.81	0.50	0.19	0.23
5	0.81	0.49	0.18	0.23
6	0.81	0.49	0.18	0.23
7	0.81	0.49	0.18	0.23
8	0.81	0.49	0.18	0.23
9	0.81	0.49	0.18	0.23
10	0.81	0.49	0.18	0.23

The iteration process has a definite effect on the stability of the two-level scheme. The solutions attempted using a single iteration (with Δx = 5 minutes) remained stable and free of significant oscillations only for values of Δx greater than or equal to 1,000 ft (305 m). The solution using Δx = 1,000 ft (305 m) corresponds to a maximum gravity-wave Courant number of 3.8 and an advection Courant number of 0.68 (*table 5.2*). For smaller values of Δx and increasing Courant numbers, the solutions using one iteration exhibited either severe oscillations or complete instability. *Figure 5.2* shows the solution using a single iteration with Δx = 500 ft (152 m) and Δt = 5 minutes. The solution has severe oscillations and is on the verge of going completely unstable at the termination of the 500 minute simulation. The addition of a second iteration stabilizes the solution and removes most of the error. For the space-centered differencing of the advection term used here, Casulli and Cheng (1990) found, using the von Neumann analysis, the requirement that the flow be subcritical to ensure linear stability of the two-level scheme without implementing iterations. Because the flow in the test problem remains subcritical throughout the simulation, the instabilities that occur for high Courant numbers are a form of nonlinear instability. No instabilities were encountered in any of the solutions attempted using two or five iterations for Courant numbers as high as Cr_g = 37.5 and Cr_a = 6.8.

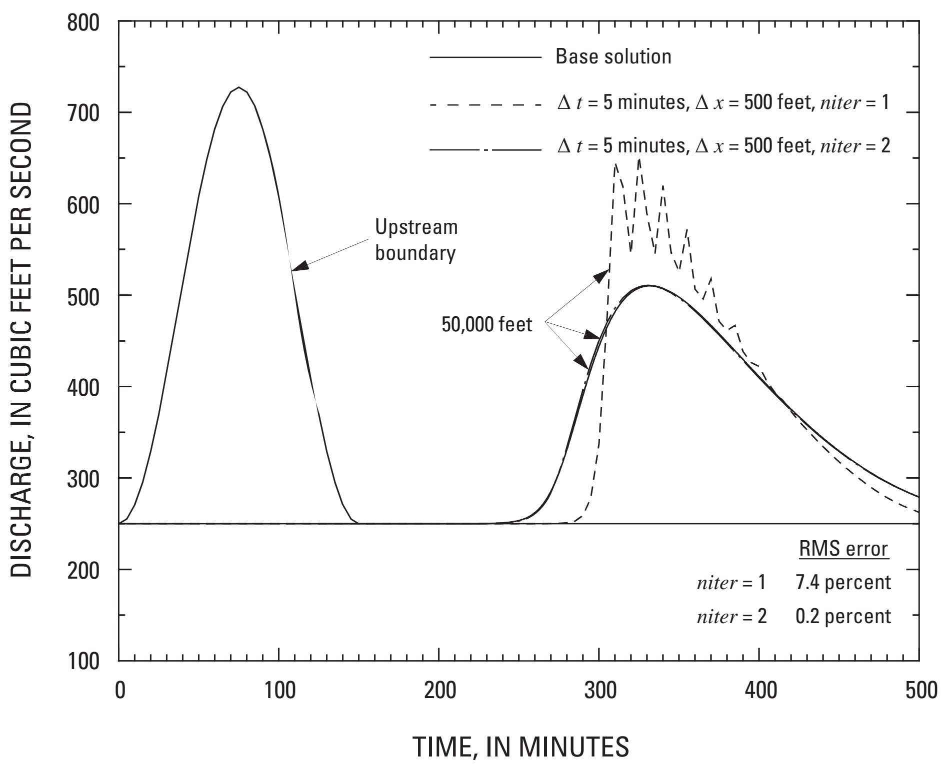

Figure 5.6. Solution using the two-level scheme on the verge of going unstable when using only one iteration (*niter* = 1). A second iteration (*niter* = 2) stabilizes the solution and removes most of the error. The solution using two iterations is almost indistinguishable from the base solution. Δx is the size of the computational space interval. Δt is the size of the computational time interval. RMS, root mean square

All of the error measures presented in *figure 5.4* for solutions with $\Delta x \geq$ 1,000 ft (305 m) were obtained using the four-point interpolation scheme given by equation 4.10. For solutions with $\Delta x <$ 1,000 ft (305 m), two-point interpolation was used because it gave results identical to those from the higher-order interpolation. Only the solutions using the two largest values of Δx (5,000 and 10,000) were affected significantly when the low-order interpolation was used; for these solutions there was additional attenuation in the routed hydrograph.

The two-level model was tested again to determine the behavior of errors as the time step Δt was varied over a wide range while keeping the space step fixed at 2,000 ft (610 m). The list of time steps and the ranges of Courant numbers for the test runs are given in *table 5.4*. The graphs of the four error measures from *table 5.1* are presented in *figure 5.7* using three curves that are labeled by the number of iterations used in the solutions (similar to *fig. 5.4*). Because the time base of the input hydrograph is 150 minutes, a time step of 15 minutes corresponds to ten points in time to resolve the hydrograph.

An inspection of the graphs in *figure 5.7* reveal the following information regarding the numerical errors:

1. The magnitude of the errors generally increases with Δt.
2. There is much less error in the solutions using two iterations than in those using one iteration. The time step must be reduced to 1 minute or less to keep the errors for solutions using one iteration to a reasonable level; a time step of 10 minutes or less is acceptable if two or more iterations are used.
3. Mass preservation and phase errors are reasonably small ($< \pm$ 1.4 percent) for all runs using Δx = 2,000 ft (610 m). Mass preservation errors are negative (indicating a loss of mass) for the solutions using two iterations, but positive otherwise; phase errors generally are positive (lagging) except for the three solutions using two iterations and $\Delta t \geq$ 5 minutes, which have negative (leading) phase errors. In general, mass preservation and phase errors are affected more by a large Δx than by a large Δt, as suggested by comparing results in *figure 5.7* with those in *figure 5.4.*

Regarding stability, the following information was found in preparing the test simulations for *figure 5.7*:

1. No stable solutions were obtained using one iteration with a time step greater than 5 minutes and gravity-wave and advection Courant numbers greater than 1.9 and 0.34, respectively.
2. The solutions using two iterations were stable up to a time step of 15 minutes, but the solution for Δt = 15 minutes was spoiled with severe oscillations (see *fig. 5.8*).
3. The solutions using five iterations were stable up to a time step of 20 minutes, the largest attempted.

Table 5.4. Ranges of Courant numbers for hydrograph problem simulations using a space step (Δx) of 2,000 feet.

Δt, in minutes	Cr_g	Cr_a
0.5	0.13–0.19	0.02–0.03
1	0.27–0.38	0.04–0.07
2.5	0.67–0.95	0.11–0.18
5	1.3–1.9	0.22–0.34
10	2.7–3.8	0.44–0.68
15	4.0–5.6	0.67–1.0
20	5.3–7.5	0.89–1.4

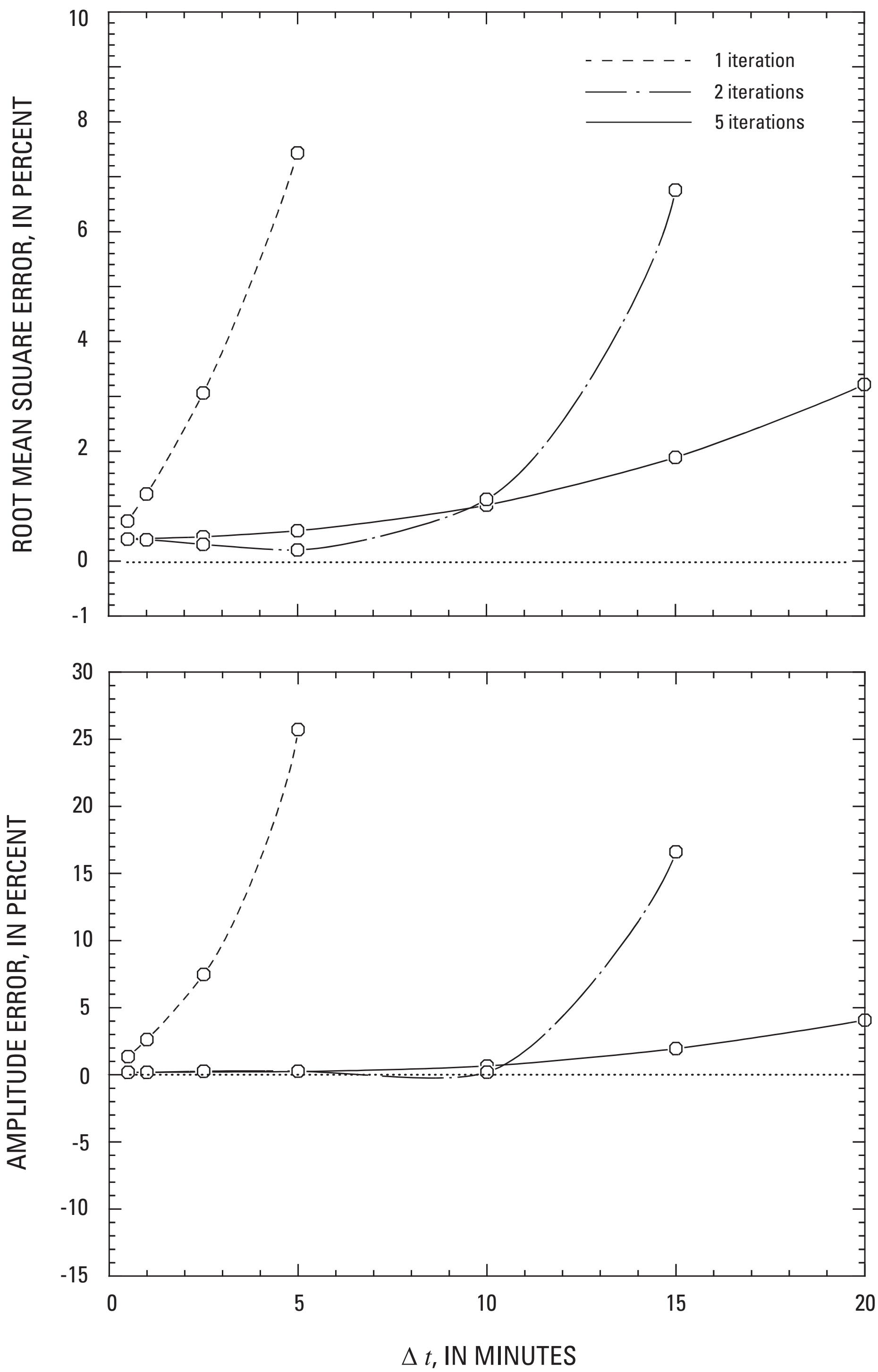

Figure 5.7. Error measures using the two-level, semi-implicit scheme on the hydrograph test problem. Δx is the size of the computational space interval; Δx = 2,000 feet for all simulations. Δt is the size of the computational time interval.

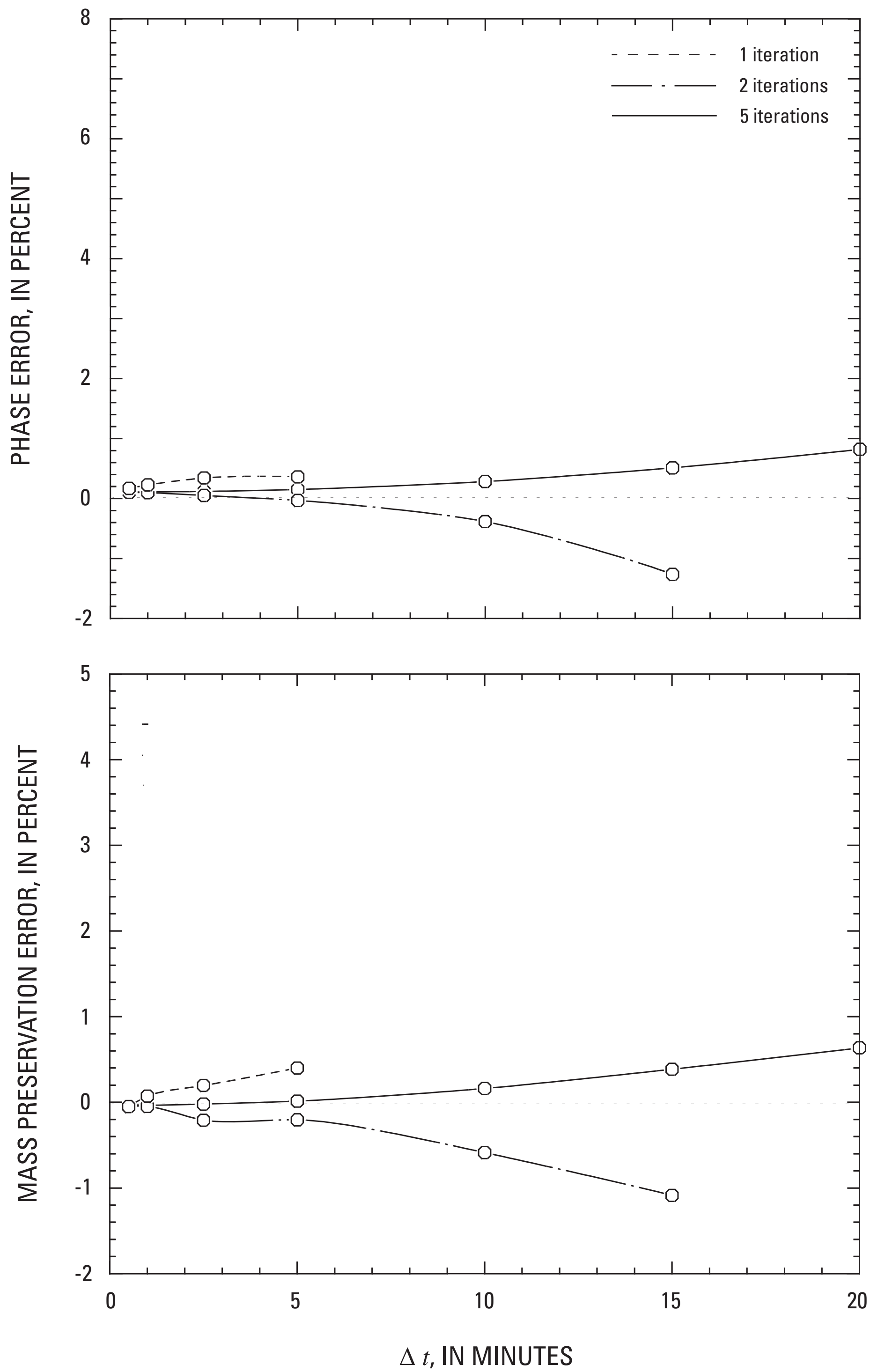

Figure 5.7. Continued.

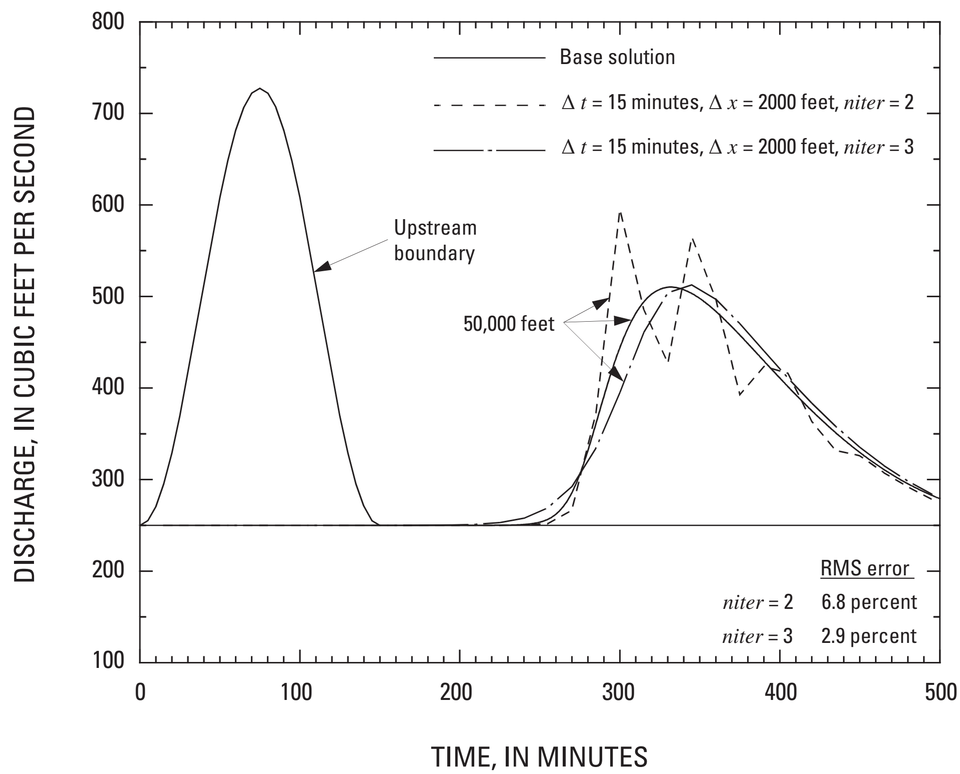

Figure 5. 8. Solution using two iterations (*niter* = 2) with the two-level scheme that is stabilized, and greatly improved, with an additional iteration (*niter* = 3).
Δx is the size of the computational space interval. Δt is the size of the computational time interval. RMS, root mean square

Overall the results for this numerical experiment indicate the two-level scheme benefits in terms of both accuracy and stability from the use of iterations. The improvements gained by a second iteration outweigh the costs associated with the increase (by nearly twofold) in the computer run time. Use of more than two iterations may not be cost effective unless the extra iterations are needed to stabilize a particular solution for which reducing the size of the time step is not desirable. It is common in iterative solution schemes to control the number of iterations internally in the computer code by allowing the iterations to continue until some predefined error tolerance is satisfied, on the basis of the change in solution variables between iterations. This process is not recommended here as it would typically require a minimum of three iterations, which often will be more than are needed.

5.2.1.2 Three-Level Scheme

The graphs of error measures for solutions to the hydrograph problem using the three-level scheme are plotted in *figures 5.9* and *5.10.* The four error measures are plotted against Δx in *figure 5.9* and against Δt in *figure 5.10*. The grid sizes used for the solutions in these figures correspond exactly with those for the two-level solutions in *figures 5.4* and *5.7* and are listed in *tables 5.2* and *5.4*. The three curves plotted in each graph of *figures 5.9* and *5.10* correspond to solutions using (1) the semi-implicit leapfrog scheme, without a trapezoidal step; (2) the semi-implicit leapfrog-trapezoidal scheme, with one iteration of the trapezoidal step; and (3) the semi-implicit leapfrog-trapezoidal scheme, with four iterations of the trapezoidal step. These three solution methods are similar in terms of computational effort to the two-level solutions using one, two, and five iterations, respectively. This similarity allows the two- and three-level schemes to be compared directly.

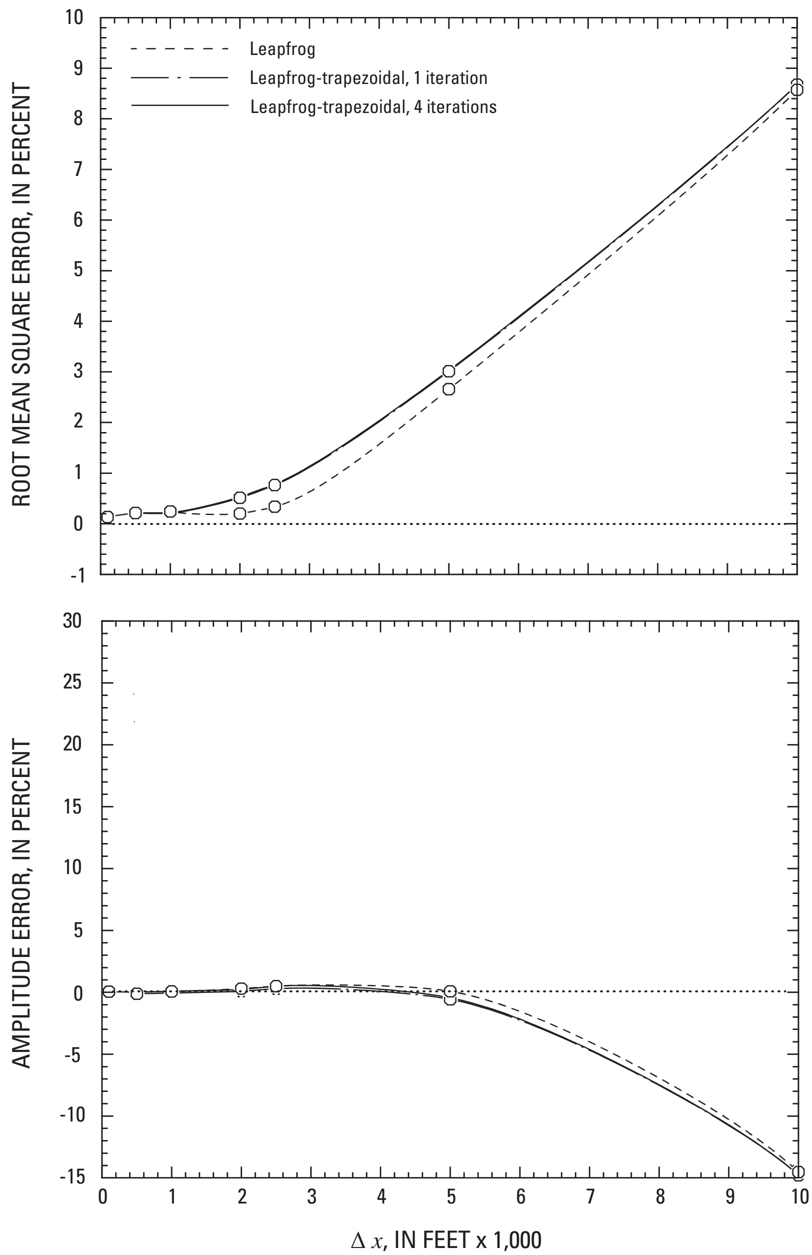

Figure 5.9. Error measures using the three-level semi-implicit scheme on the hydrograph test problem for different values of the computational space interval (Δx). Δt = 5 minutes for all simulations. Δt is the size of the computational time interval. On each of these graphs, the error measures plotted for the leapfrog-trapezoidal solutions using 1 and 4 iterations are virtually indistinguishable.

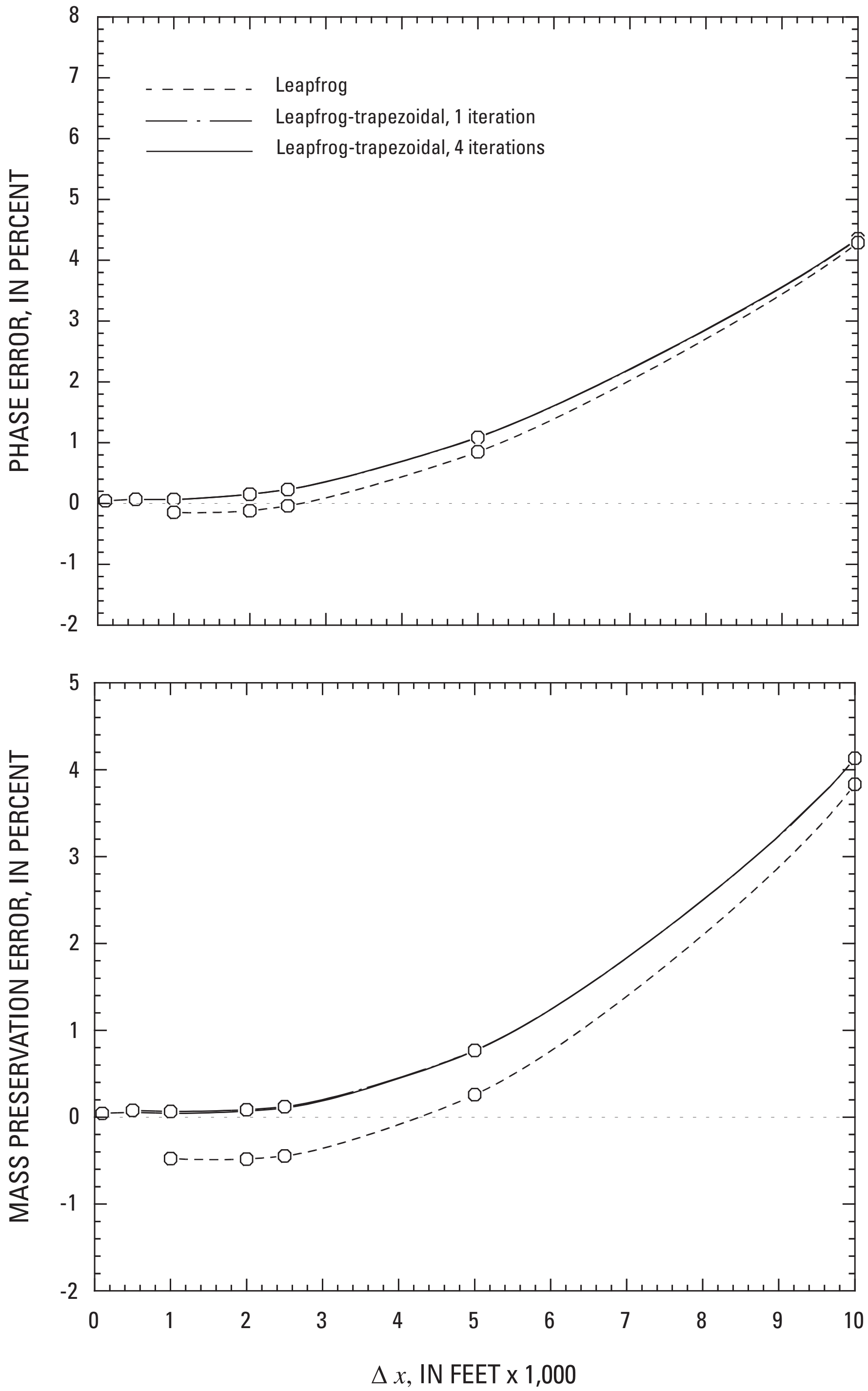

Figure 5.9. Continued.

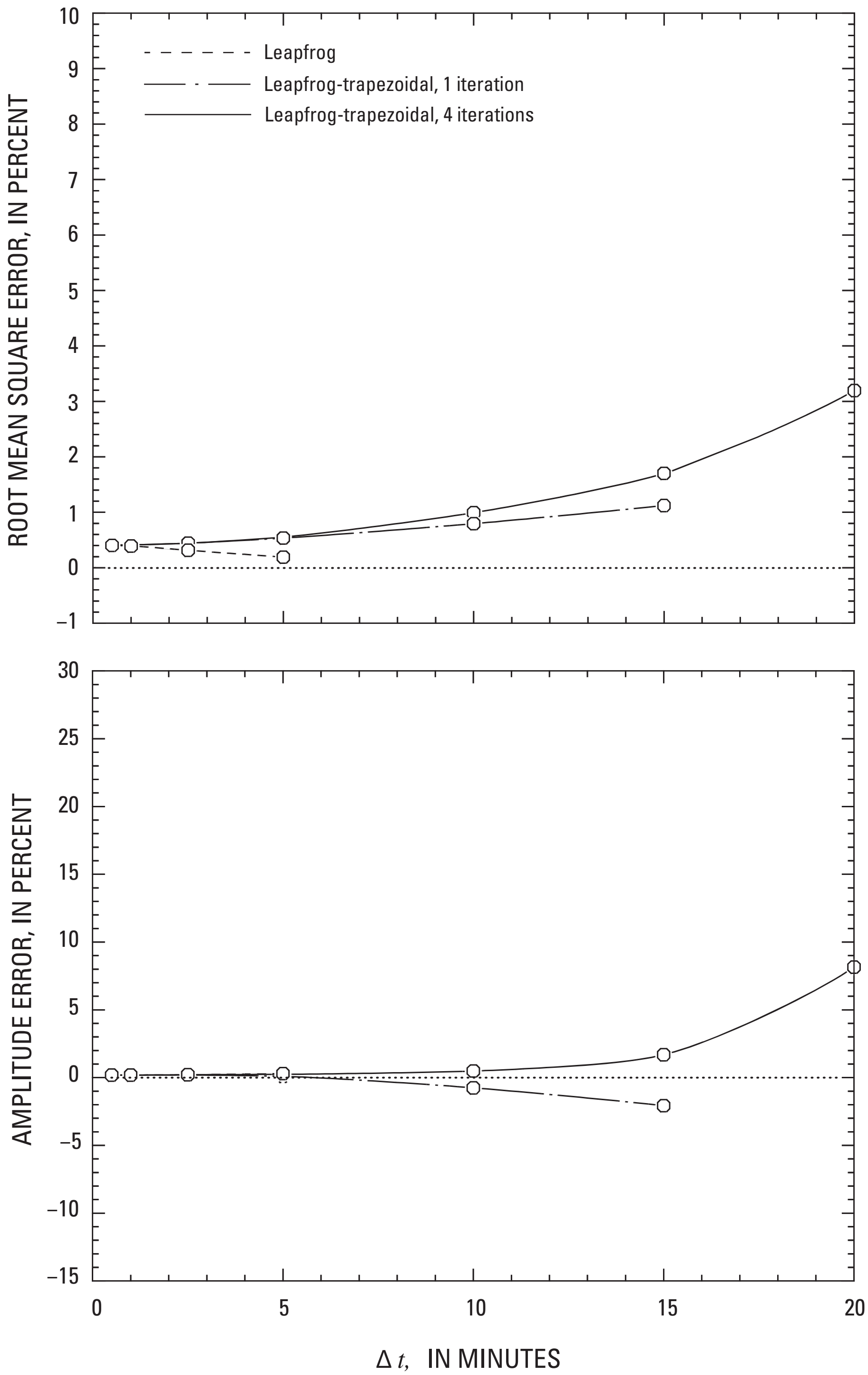

Figure 5.10. Error measures using the three-level semi-implicit scheme on the hydrograph test problem for different values of the computational time interval (Δt). Δx = 2,000 feet for all simulations. Δx is the size of the computational space interval.

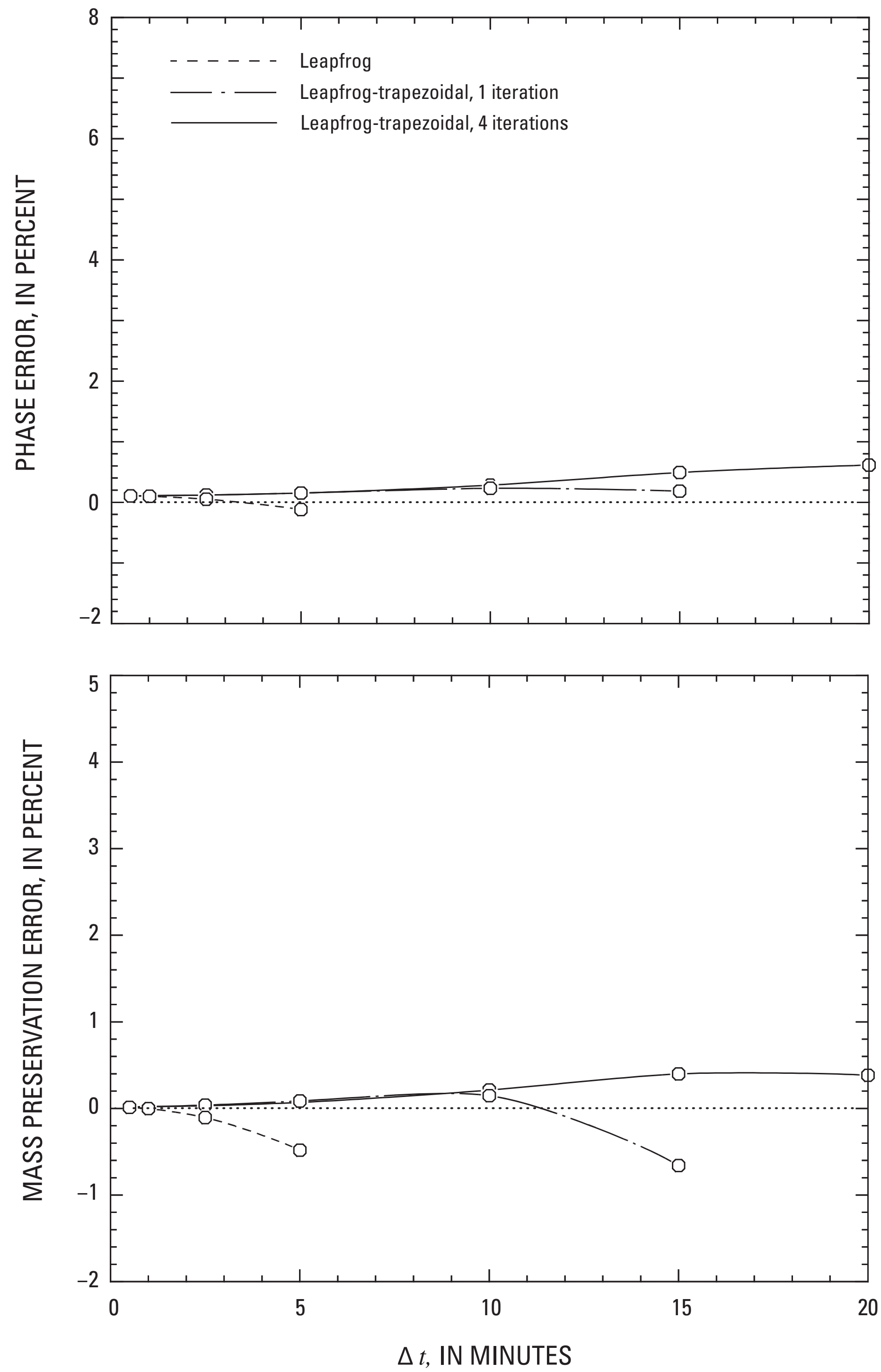

Figure 5.10. Continued.

As seen in *figures 5.9* and *5.10,* the leapfrog scheme[46] solution to the hydrograph problem produces errors much smaller than those produced by the two-level scheme without iteration (*niter* = 1) shown in *figures 5.4* and *5.7*. By involving three time levels in the finite-difference equations, the leapfrog scheme achieves second-order accuracy in the time integration by evaluating the nonlinear coefficients γ and *H* in equation and the advection term in equation 4.14, at the time level *n,* which is centered between levels $n + 1$ and $n - 1$ (*fig.4.3*). As pointed out previously, the solutions to this test problem are particularly sensitive to the evaluation of the frictional coefficient γ. A direct comparison of computed hydrographs using the leapfrog and two-level (*niter* = 1) schemes is shown in *figure 5.11* for a grid size of Δx = 2,500 ft (762 m) and Δt = 5 minutes. The results show that the leapfrog scheme gives a much better estimation of the frictional attenuation in the hydrograph.

The error measures for the leapfrog scheme solutions plotted in *figures 5.9* and *5.10* are mostly smaller[47] than those for the leapfrog-trapezoidal solutions, although only slightly. As the next 1-D numerical experiment will demonstrate, this is not always true; in some instances, the addition of a trapezoidal scheme step will improve the accuracy of the leapfrog scheme significantly. For the hydrograph test problem, however, the primary benefit of the trapezoidal step is not to improve accuracy but to extend the range of stability of the scheme. The improvement in stability is the same as that gained through the addition of iterations to the

[46]As used here, the phrase leapfrog scheme is meant to imply the semi-implicit version of the scheme rather than the explicit version.

[47]The mass preservation errors, however, are mostly larger in the leapfrog solutions than in the leapfrog-trapezoidal solutions.

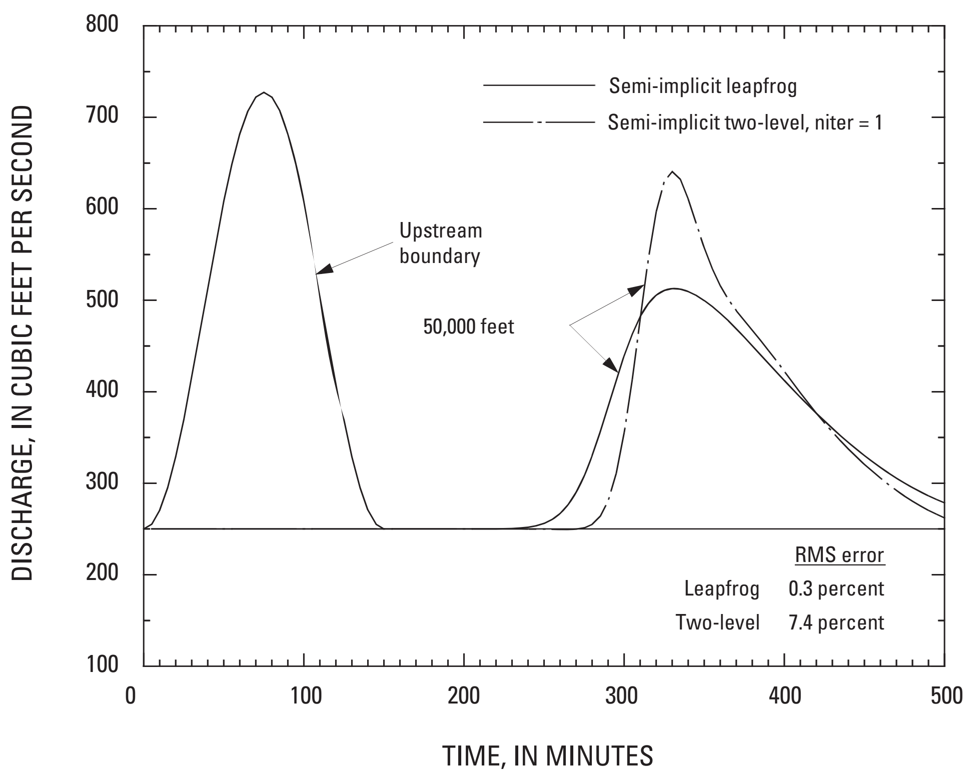

Figure 5.11. Comparison of computed hydrographs with the leapfrog semi-implicit scheme and the two-level semi-implicit scheme (*niter* = 1).
The leapfrog solution has very little error. For both runs, Δx = 2,500 feet, Δt = 5 minutes.
Δx is the size of the computational space interval. Δt is the size of the computational time interval. RMS, root mean square.

two-level scheme. In the simulations for *figure 5.9*, the basic leapfrog scheme yielded stable solutions using a Δt of 5 minutes only for spatial step sizes that are greater than or equal to 1,000 ft (305 m). In *figure 5.10,* the leapfrog solutions were stable only up to a time step of 5 minutes for the space step of 2, 000 ft (610 m). The leapfrog-trapezoidal solutions in *figure 5.10* with one iteration of the trapezoidal step were stable up to a time step of 15 minutes; with four iterations, the solutions were stable up to a time step of 20 minutes.

In comparing the error measures in *figure 5.10* with those in *figure 5.7*, it is significant that the addition of the trapezoidal step to the leapfrog scheme gave solutions that generally have equal or smaller errors than solutions using two iterations of the two-level scheme. In particular, for the large time steps of 10 and 15 minutes, the error measures are noticeably smaller in *figure 5.10* for the solutions using the leapfrog-trapezoidal scheme (1 iteration) than in *figure 5.7* for the solutions using the two-level scheme (*niter* = 2). The leapfrog-trapezoidal scheme solution for Δt = 15 minutes and Δx = 2,000 ft (610 m) also did not exhibit the oscillations shown in *figure 5.8* for the solution using the two-level scheme (*niter* = 2).

5.2.1.3 Remarks

Based on the results of the hydrograph numerical experiment, the three-level scheme is more accurate than the two-level scheme. The two-level scheme without using iterations is only first-order accurate and requires an extremely small numerical grid size to reduce the error in the hydrograph solutions to an acceptable level. Using two iterations, it is possible to raise the accuracy of the two-level scheme to second order, but the same order of accuracy can be achieved at approximately half the computational cost by using the three-level, leapfrog scheme. The use of iteration in the solutions for either scheme extends the range of computational intervals and Courant numbers for which the solutions are stable. If a single iteration of the trapezoidal step is used in the three-level scheme (so that, for example, a stable solution is obtained for a large time step), generally the scheme still is more accurate than the comparable two-level scheme using two iterations. The use of more than one iteration of the trapezoidal step in the three-level scheme, or more than two iterations in the two-level scheme, was not worthwhile for the hydrograph problem, considering the extra computational cost incurred for the minimal improvement in accuracy that is gained; if the extra iterations are needed to stabilize a particular solution, then the time step and Courant numbers may be too large on the basis of accuracy considerations anyway.

As noted previously, the hydrograph routing problem has been used by the USGS to test three 1-D models (Fread, 1978; Schaffranek and others, 1981; and Delong, 1993) that are based on the popular four-point finite-difference scheme. A few comments can be made regarding how the semi-implicit, three-level scheme presented here compares with the four-point scheme. The four-point scheme, first introduced by Preissmann (1961), is a fully implicit scheme in which both of the independent variables are computed at the same grid points rather than at different ones as in the case of a staggered grid. The scheme is nearly second-order accurate in the space and time integration methods so long as a finite-difference weighting factor θ is chosen close to 0.5 (for unconditional linear stability, θ must be greater than or equal to 0.5). The overall accuracy (convergence characteristics) of the four-point and semi-implicit schemes are similar for solutions with gravity-wave Courant numbers greater than one (see Fread, 1974, for a detailed report on the convergence characteristics of the four-point scheme). For gravity-wave Courant numbers less than one, the high frequency solution components of the four-point scheme have leading phase errors; these errors are the cause of the $2\Delta x$-wavelength oscillation in the four-point solution shown in *figure 5.12* using the model of Schaffranek and others (1981). Solutions obtained using the two other four-point models included oscillations similar to those in *figure 5.12*. No oscillations, either leading or lagging, are present in the semi-implicit, leapfrog solution using the staggered grid. Solution oscillations are a common problem in modeling estuaries of complex bathymetry, so a numerical scheme is usually sought in which the $2\Delta x$ waves are damped.

The semi-implicit, leapfrog scheme is considerably more computationally efficient than the four-point scheme when both use the same values for Δt and Δx. Because the four-point scheme is fully implicit, it involves the solution of a system of nonlinear algebraic equations at each time step for the unknown water surface elevations and volumetric transports using a functional iterative procedure such as the Newton-Raphson method (Amein and Fang, 1970). The semi-implicit leapfrog scheme only involves the solution of a tridiagonal system of linear equations at each time step for the water surface elevation using the double-sweep method; the volumetric transports are computed explicitly. When a trapezoidal step is added to the leapfrog scheme, the computational time is still significantly lower than that for the four-point scheme.[48] Because in one dimension the computational time for

[48]A carefully controlled comparison of the computer run times for the leapfrog-trapezoidal and four-point schemes was not done because the four-point computer codes are only a part of complete modeling systems for natural rivers that have many features and options that affect model run time; the leapfrog-trapezoidal scheme was programmed only as a test code for rectangular channels exclusively.

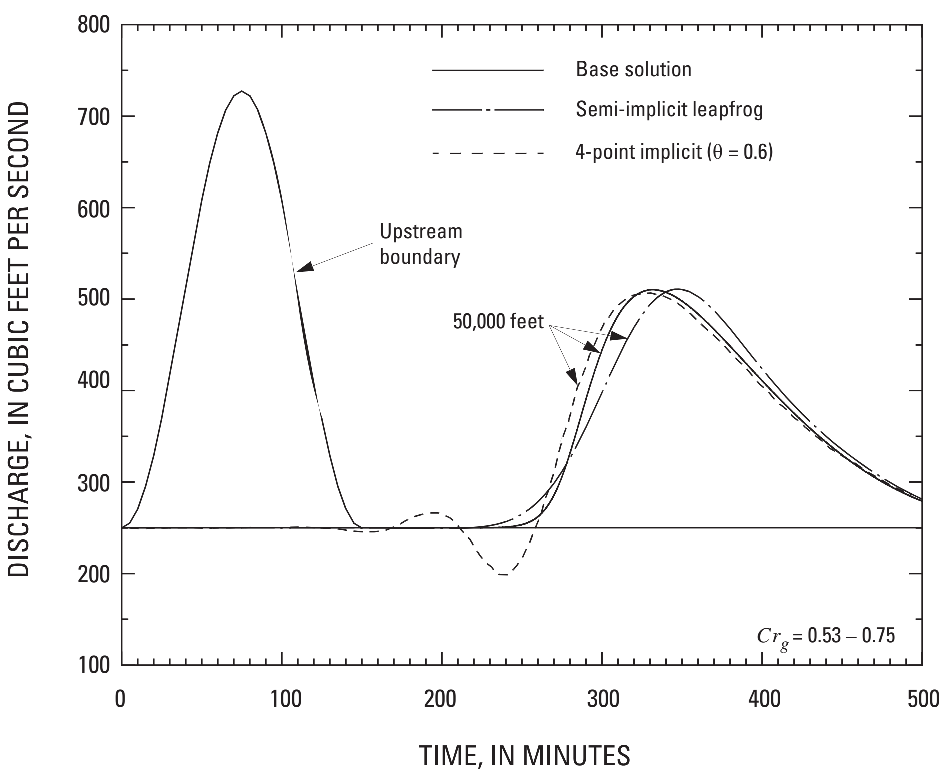

Figure 5.12. Comparison of solutions to the hydrograph problem with the leapfrog semi-implicit scheme and the four-point model of Schaffranek and others (1981) using a space step (Δx) of 5,000 feet and a time step (Δt) Of 5 minutes for all simulations. Cr_g is the gravity-wave Courant number.

a numerical scheme generally is not too important in choosing a scheme, the four-point scheme is sometimes preferred over other schemes for the convenience of the fully dense grid and the ease with which the compact four-point computational stencil allows the space interval Δx to be varied between node points without affecting the accuracy of the approximation. In one dimension, staggered grid schemes are in general not as well suited to irregular Δx distance intervals as the four-point scheme. In three dimensions, however, the computational run time of a multidimensional four-point scheme would be prohibitively long for most real applications, and the semi-implicit scheme clearly is a better choice for reasons of computational efficiency. Flexibility in the horizontal grid point placement in a 3-D model can be achieved using a coordinate transformation, which is easily accommodated with a semi-implicit scheme, as demonstrated in the 3-D, curvilinear-coordinate model of Muin and Spaulding (1997a).

5.2.2 Tidal Flow in a Closed Channel

The second 1-D numerical experiment uses a variation of a problem suggested by Alan F. Blumberg (written commun., 1992) to test the numerical damping characteristics of a hydrodynamic model. It is the propagation of a tidal wave from the sea into a wide rectangular channel that is closed at the landward boundary (*fig. 5.13*). The channel is 315,000 ft (96 km) long and filled with water initially at rest ($Q_0 = 0$) to a uniform depth $H_0 = 33$ ft (10 m). The channel is wide in comparison with the depth of water, so the simulations are based on a unit width. The Manning resistance coefficient for the channel is $n = 0.020$.

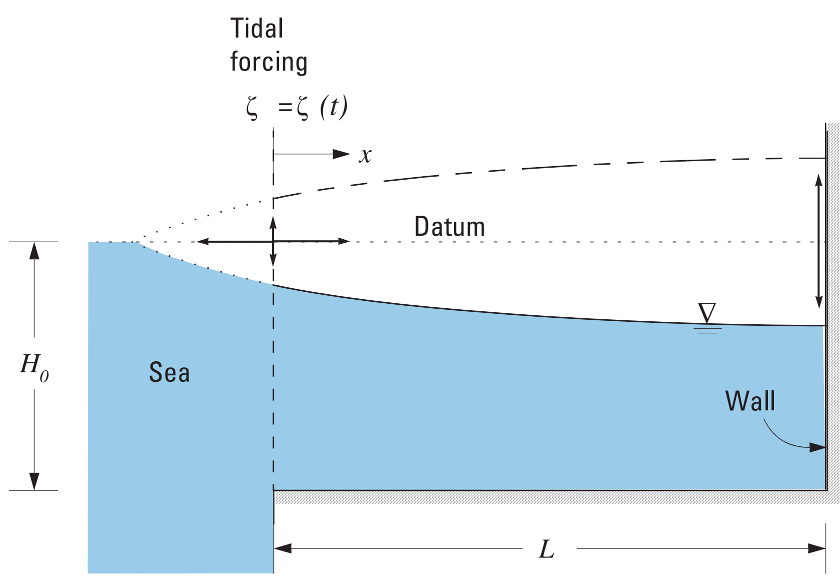

EXPLANATION

Channel characteristics

B = 1 foot (unit width channel)
L = 315,000 feet
S_0 = 0.00
Manning's n = 0.020

Initial flow conditions

Q_0 = 0.0
H_0 = 33 feet

Figure 5.13. Channel characteristics and initial flow conditions for the 1-dimensional tidal test problem. The water in the channel is initially at rest at a uniform depth of H_0. Tidal forcing is introduced at the seaward boundary causing the water surface to oscillate. Two successive positions of the water surface are shown. At the seaward boundary, water moves up and down and horizontally. At the wall boundary, water moves up and down only.

The driving force for this problem is the variation in water surface elevation ζ at the seaward boundary that is caused by a simple harmonic tide

$$\zeta(t) = A \sin\left(\frac{2\pi t}{t_p}\right), \tag{5.1}$$

where the time t is expressed in hours from the start of the simulation. The tidal amplitude is A = 3 ft (0.9 m) and the tidal period is t_p = 12.4 hours. A period of 12.4 hours corresponds with the principal lunar constituent of the astronomical tide known as the M_2 tide.

The dimensions of the channel length and depth were chosen so that the wavelength[49] of the M_2 tide is close to four times the length L of the tidal channel. Under these conditions, the traveling wave entering the channel interferes constructively (adds together) with the wave reflected from the wall boundary, thereby setting up a resonant oscillation in the channel. The result is a tidal range of water surface elevation that is greater at the closed boundary than at the open boundary. This effect is illustrated in *figure 5.14* by using a solution to the problem showing water surface elevation at six locations along the channel against time.

[49]The wavelength of the tide can be estimated as $L_w = t_p \cdot \sqrt{gH_0}$ with t_p expressed in seconds.

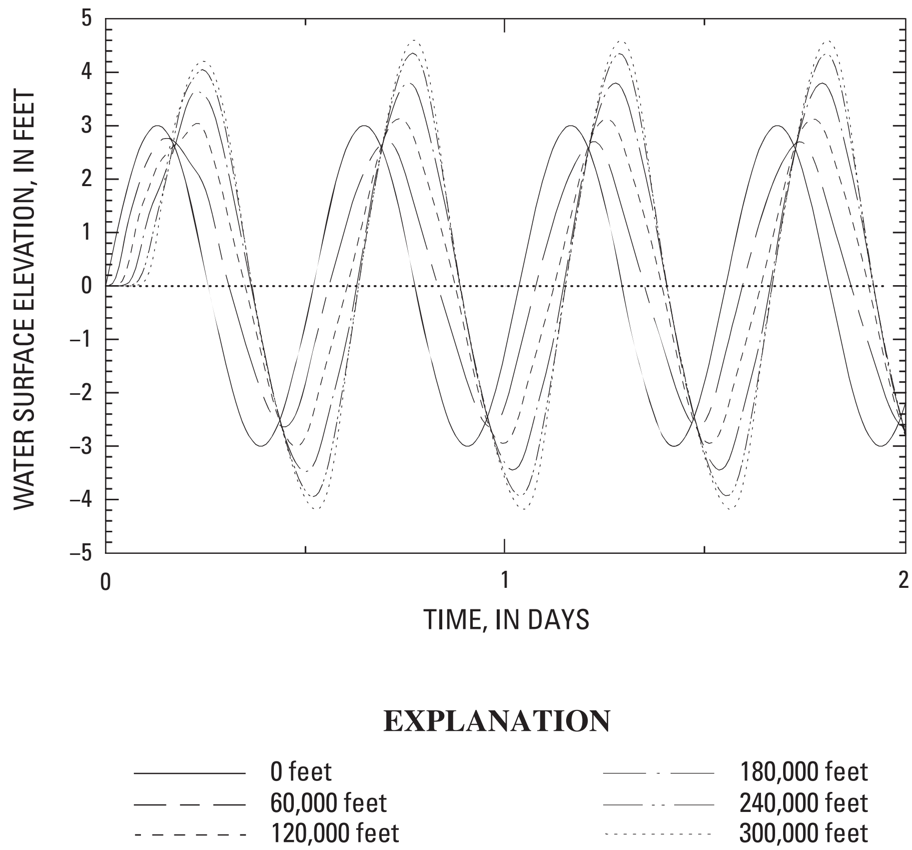

Figure 5.14. Water surface elevations at six locations along the tidal channel. The distances are measured landward from the seaward boundary.

Each test simulation for the tidal problem is run for a total of six days (144 hours). This allows sufficient time for any solution instabilities to appear. The results of each simulation are presented at the location x = 180,000 ft (55 km) from the seaward boundary of the tidal channel. A solution for water surface elevation and velocity is shown in *figure 5.15*. After simulating ten cycles of the M_2 tide, results from the 11th cycle are examined in detail and used in the computation of error measures.

5.2.2.1 Two-Level Scheme

Figure 5.16 shows three solutions of the tidal problem using the two-level scheme; one is the base solution included in both graphs. The solid lines present the base solution obtained by using the two-level scheme with a very small grid size of Δt = 0.5 minutes, Δx = 400 ft (122m) and with five iterations (*niter* = 5). The base solution is assumed to be free of numerical error for the purposes of computing error measures for the solutions with coarser grid sizes. The two solutions indicated by the dashed curves in *figure 5.16* are computed using large time steps of 60 minutes (*fig. 5.16A*) and 30 minutes (*fig. 5.16B*.); both solutions use a space step (Δx) of 6,000 ft (1,828 m) and two iterations (*niter* = 2). *Figure 5.17* shows a plot of the volumetric transport ($U = uh$) from the solution using Δt = 60 minutes compared with the volumetric transport of the base solution. The root mean square error (RMS_e) of the solution is computed relative to the base solution using the volumetric transport variable defined in *table 5.5.* The RMS_e is 8.7 percent for the 60-minute solution and 2.3 percent for the 30-minute solution. The other error measures defined in are computed as A_e = 5.2 percent, P_e = 0.35 percent, and M_e = 4.7 percent for the solution using Δt = 60 minutes, and A_e = – 0.8 percent, P_e = 0.16 percent, and M_e = 1.0 percent for the solution using Δt = 30 minutes.

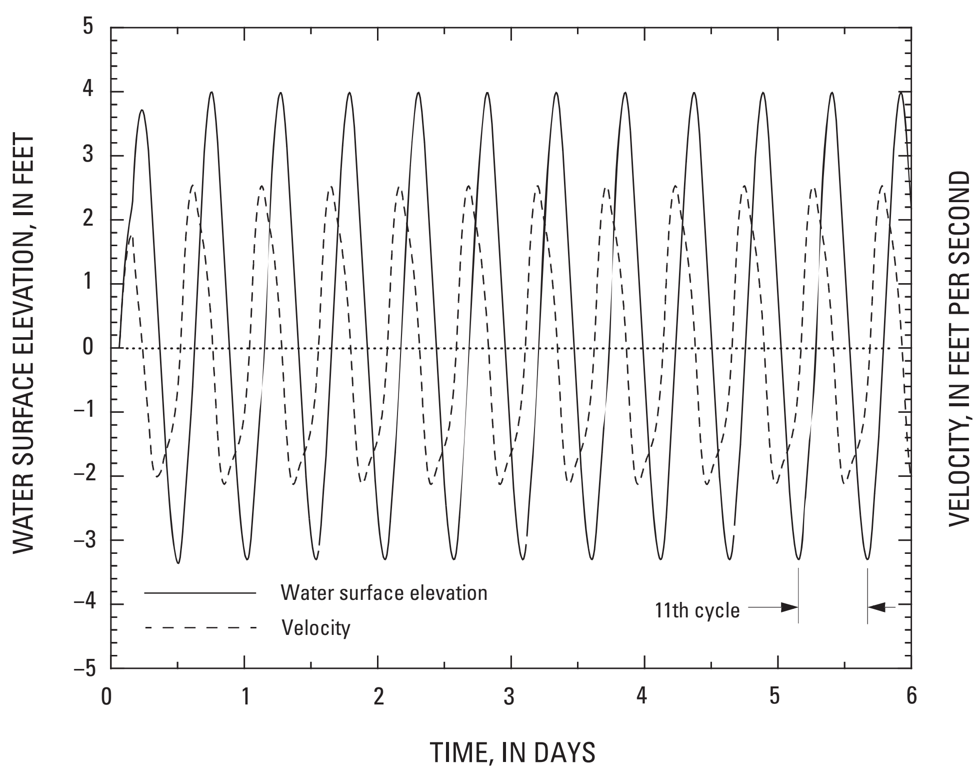

Figure 5.15. Solution of the tidal problem for water surface elevation and velocity at the location x = 180,000 feet. The results of simulations for the 11th cycle of the M_2 tide are examined in detail in figure 5.16.

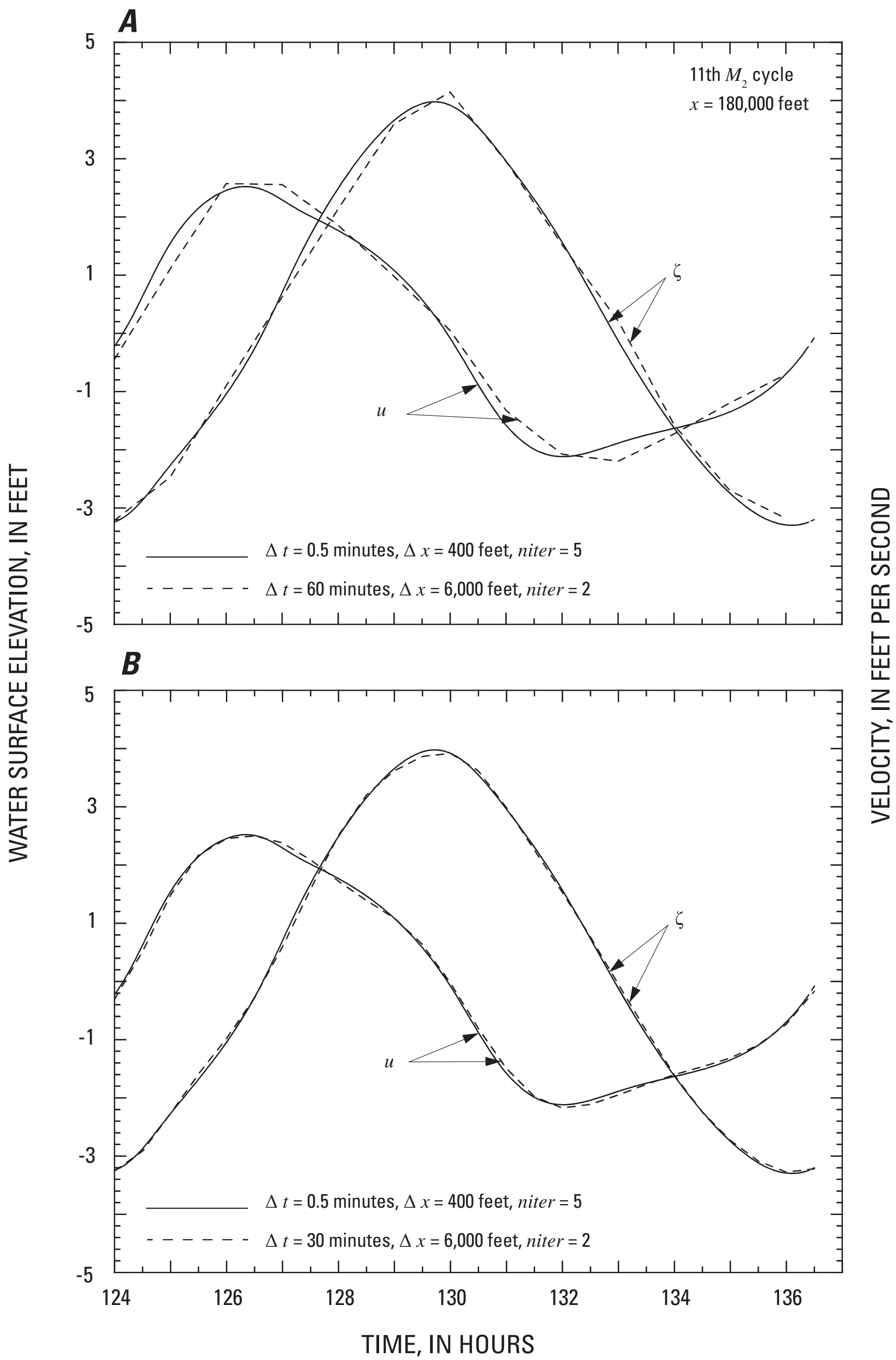

Figure 5.16. Solutions for water surface elevation (ζ) and velocity (u) computed with the two-level semi-implicit scheme using a space step (Δx) of 6,000 feet and a time step (Δt) of (*A*) 60 minutes and (*B*) 30 minutes. The solutions using two iterations ($niter = 2$) are compared against a base solution that used small time and space steps and five iterations ($niter = 5$). The solutions are shown for the 11th M_2 cycle at a location 18,000 feet from the seaward boundary of the tidal channel.

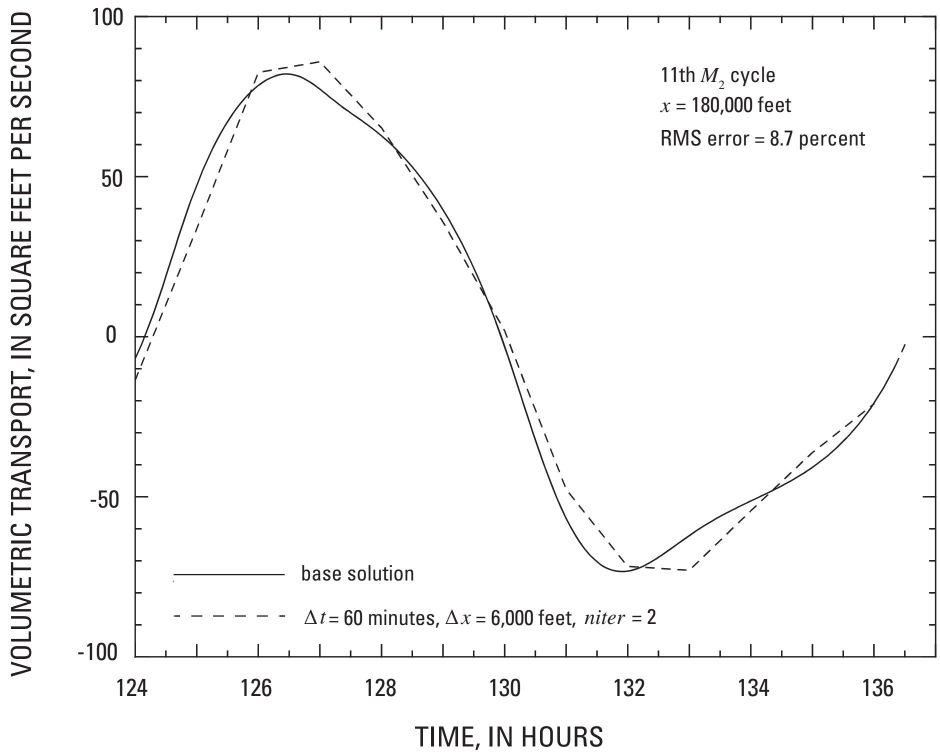

Figure 5.17. Solution for volumetric transport ($U = uh$) using the two-level semi-implicit scheme. The solution for time step Δt = 60 minutes and space step Δx = 6,000 feet is compared with the base solution. RMS, root mean square.

Considering that time steps of 60 minutes and 30 minutes are quite large relative to the 12.4 hour period of the tidal forcing, the solutions in *figure 5.16* are reasonably good. Simulations using these two time steps were made using the two-level scheme, trying both larger and smaller values of Δx, and the results generally were only slightly changed. Because of the long tidal wavelength, Δx, up to the largest value of Δx = 30,000 ft (9,144 m), had relatively little effect on the solutions.

The two-level scheme was tested further by keeping Δx constant at 6,000 ft (1,828 m) and varying Δt over a wide range. The values of Δt and the corresponding Courant numbers are given in *table 5.6*. The test simulations revealed that only for the smallest choice, Δt = 1 minute, is a stable solution obtained when the two-level scheme is used with one iteration (*niter* = 1); the 1 minute solution had very little error (RMS_e = 0.05 percent). Each simulation using *niter* = 1 and $\Delta t \geq 5$ minutes ran for only several tidal cycles before oscillations developed that eventually grew to destroy the solutions entirely. The oscillations could be traced back to the nonlinear advection term in the momentum equation and appeared first in the solutions at the times just prior to the high and low water points in the tidal cycle. As a consequence of the standing wave character of the solution, at the times just before high and low water, the volumetric transport and water surface elevation are changing in opposite directions and the magnitude of the advection term is oscillating near zero.

Table 5.5. Definition of error measures (expressed as percentages) for the tidal test problem.

[The first three error measures are based on comparisons between the computed solution and the base solution during the 11th tidal cycle at x =180,000 feet. The mass preservation error is computed as the maximum error (relative to the base solution) in total mass of water within the channel during each simulated time step]

Description	Definition
Root mean square error: Root mean square error of the computed volumetric transport, normalized on the maximum volumetric transport of the base solution	$RMS_e = \left.\dfrac{100\left[\sum_{n=n1}^{nts11}(U^n(x)-U_b^n(x))^2\right]^{1/2}}{(nts11)^{1/2}\,U_b^{max}(x)}\right\rvert_{x=180,000}$
Amplitude error: Error in the maximum water surface elevation, normalized on the maximum water surface elevation of the base solution	$A_e = \left.\dfrac{100(\zeta^{max}(x)-\zeta_b^{max}(x))}{\zeta_b^{max}(x)}\right\rvert_{x=180,000}$
Phase error: Error in the time associated with the center of gravity of the computed water surface distribution, normalized on the time associated with the center of gravity of the base solution	$P_e = \left.\dfrac{100(T(x)-T_b(x))}{T_b(x)}\right\rvert_{x=180,000}$ where $T(x) = \dfrac{\int_{t_1}^{t_2} t[H(x,t)-(H_0+\zeta^{min}(x))]dt}{\int_{t_1}^{t_2}[H(x,t)-(H_0+\zeta^{min}(x))]dt}$
Mass preservation error: Maximum error in mass preservation for the computed solution, normalized on the total mass from the base solution	$M_e = \max\lvert E^n\rvert \quad n = 1, 2, ..., nts$ where $E^n = 100\left.\left(1-\dfrac{\int_0^L(H(x,t)-(H_0-5))dx}{\int_0^L(H_b(x,t)-(H_0-5))dx}\right)\right\rvert_{t=n\Delta t}$

t_1	=	7,440 minutes (= 124 hours)
t_2	=	8,190 minutes (= 136.5 hours)
n_1	=	$t_1/\Delta t$
n_2	=	$t_2/\Delta t$
nts11	=	$n_2 - n_1$
nts	=	number of time steps in a 6 day simulation
$U_b^n(x)$	=	volumetric transport for the base solution at location x and time $t = n\Delta t$
$U_b^{max}(x)$	=	maximum volumetric transport for the base solution at location x (= 82.34 square feet per second at 180,000 feet)
$\zeta_b^{max}(x)$	=	maximum water surface elevation for the base solution at location x (= 4.00 feet)
$\zeta^{min}(x)$	=	minimum water surface elevation at location x
H_0	=	initial water depth in tidal channel (= 33.0 feet)
L	=	length of channel (= 315,000 feet)

Integrations were computed numerically with Simpson's Rule.

Table 5.6. Ranges of Courant numbers for tidal problem simulations using Δx = 6000 feet as a space step.

[Δx, size of the computational space interval]

Δt, in minutes	Cr_g	Cr_a
1	0.31–0.38	0.04
5	1.6–1.9	0.21
10	3.1–3.8	0.43
15	4.6–5.7	0.66
30	9.2–11.3	1.33
45	13.8–17.0	2.00
60	18.4–22.6	2.66

Cr_g = gravity-wave Courant number = $(u + \sqrt{gH}) \cdot \Delta t / \Delta x$
Cr_a = advection Courant number = $u \cdot \Delta t / \Delta x$

An example of an unstable solution is shown in *figure 5.18A* using Δt = 10 minutes. The first 1.5 days of the solution are plotted before the solution eventually fails completely. In *figure 5.18B,* the same solution is shown with the advection term "turned off;" a smooth solution is obtained. Because the base solution shown in *figure 5.18B* includes the advection term, the effect of neglecting this term is visible; advection increases the mean (tidally averaged) value of the volumetric transport by a small, but not necessarily insignificant, amount. The solution results for other values of Δt are similar to those in *figure 5.18* although the oscillations tended to occur slightly later in the simulations for larger Δt. In all cases, however, when advection was neglected, the oscillations disappeared. By trial and error it was discovered that stable solutions could be obtained with larger values of Δx. In particular, solutions using Δx = 30,000 ft (9,144 m) gave stable and accurate solutions up to a time step of 15 minutes with *niter* = 1; for time steps larger than 15 minutes, the solutions were stable but overdamped. Of course, by using larger values of Δx, the Courant numbers were decreased, which may have contributed to the improved stability.

It should be noted that no attempt was made to obtain stable results by smoothing the solutions using *niter* = 1. In all cases, however, the solutions were made stable by adding a second iteration (or more) to the scheme. The error measures for these solutions are presented later.

5.2.2.2 Three-Level Scheme

Using a space step of Δx = 6,000 ft (1,829 m), the semi-implicit, leapfrog scheme gave more stable solutions to the tidal problem than the two-level scheme without iteration. Of the time steps listed in *table 5.6,* the two-level scheme (*niter* = 1) gave a stable solution only for Δt = 1 minute; the leapfrog scheme gave stable solutions for Δt = 1, 5, and 10 minutes. All the solutions with the leapfrog scheme using $\Delta t \geq$ 15 minutes developed oscillations and eventually became unstable. Similar to the results observed for the two-level scheme, the unstable leapfrog scheme solutions were stabilized when the advection term was turned off; there was an increasing tendency, however, for the numerical solution to amplify the range of the tidal oscillation as the time step increased.

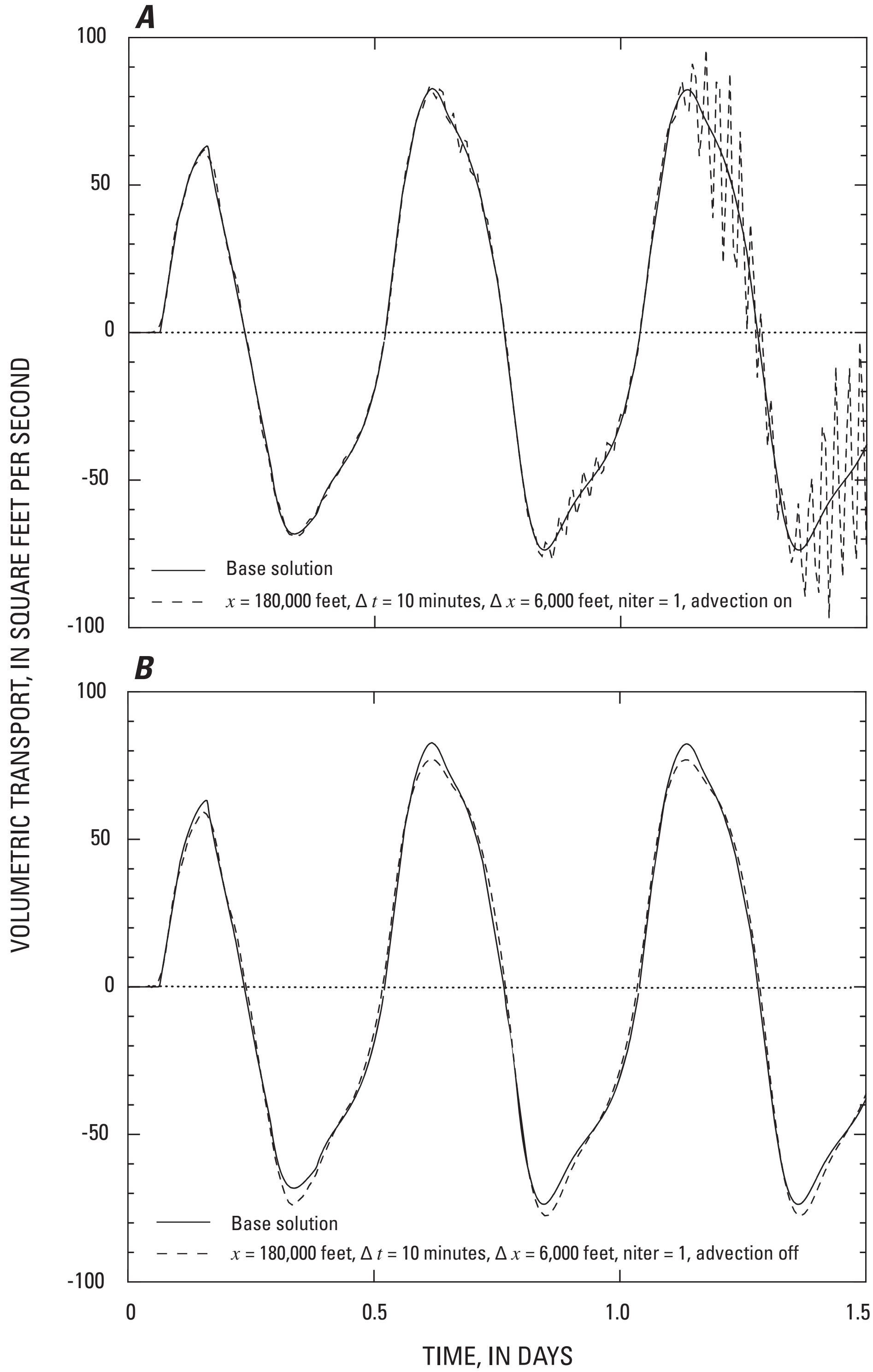

Figure 5.18. Solutions using one iteration (*niter* = 1) of the two-level scheme with (*A*) advection terms turned on and (*B*) advection terms turned off. The instability is a nonlinear one that appears to come from the advection terms. Δt is the size of the computational time interval. Δx is the size of the computational space interval.

To stabilize the leapfrog solutions without neglecting the advection term, a weak time filter proposed by Asselin (1972) was added to the computational scheme. Because this filter requires three consecutive values in time of the function to be filtered, it could be applied only to the three-level scheme. The filter is essentially a smoothing procedure that replaces the center value of the function to be smoothed using the relation

$$\bar{F}^n = F^n + \frac{\beta}{2}(\bar{F}^{n-1} - 2F^n + F^{n+1}) \ , \tag{5.2}$$

where $\bar{F}$ is a smoothed value and β is a smoothing coefficient, usually chosen to be 0.05. Prior to smoothing F^n, the value of $\bar{F}^{n-1}$ in equation 5.2 is already smoothed from the previous time step.

Solutions using the leapfrog scheme with and without the smoothing procedure are shown in *figure 5.19*. The simulation without smoothing becomes unstable during the eighth tidal cycle. With smoothing, the solution is both stable and accurate. A solution with Δt = 30 minutes is similarly stabilized with smoothing by using β = 0.05; stable solutions could not be obtained, however, for the two largest time steps (t = 45 and 60 minutes), even with a larger value for β.

Because very little computer time is required to apply the time filter, using it is better than adding one or more trapezoidal steps to the scheme if it can be used successfully to stabilize a solution. However, the question naturally arises: Does the time filter introduce too much damping (smoothing) into the solution? It was found that the filter damping is minimal so long as the β coefficient is kept small (β ≤ 0.10). In addition, because the unsmoothed leapfrog solutions to the tidal problem tended to be slightly over-amplified, the small amount of damping introduced by the filter when β = 0.05 actually reduced the solution errors slightly.

The four error measures from *table 5.5* are graphed against Δt in *figure 5.20* for solutions using the three-level scheme and Δx = 6,000 ft (1, 829 m). The three curves in each graph again represent the three different levels of iteration in the scheme beginning with leapfrog only (no iteration). The solutions using both the leapfrog scheme and the leapfrog-trapezoidal scheme (one iteration) included smoothing (β = 0.05) for Δt ≥ 10 minutes; the solutions using the leapfrog-trapezoidal scheme (four iterations) included no smoothing. Without smoothing, three of the solutions using one iteration of the trapezoidal step were found to be unstable; these used Δt = 10, 15, and 45 minutes. It was apparent that one iteration of the trapezoidal step was not always sufficient to stabilize a leapfrog solution; in one case, a stable leapfrog solution (using Δx = 6,000 ft, Δt = 10 minutes, no smoothing) became unstable only after a trapezoidal step was added. In general, iteration had a stabilizing effect since all solutions were stable without smoothing when two or more iterations of the trapezoidal step were added to the leapfrog scheme. The error measures for solutions using the leapfrog-trapezoidal scheme with one and four iterations are nearly equal. The effects from the smoothing in the solutions using one iteration are very small; the only noticeable effect of the smoothing is that most of the amplitude errors in *figure 5.20* are more negative (damped) for the solutions in which the smoothing is used.

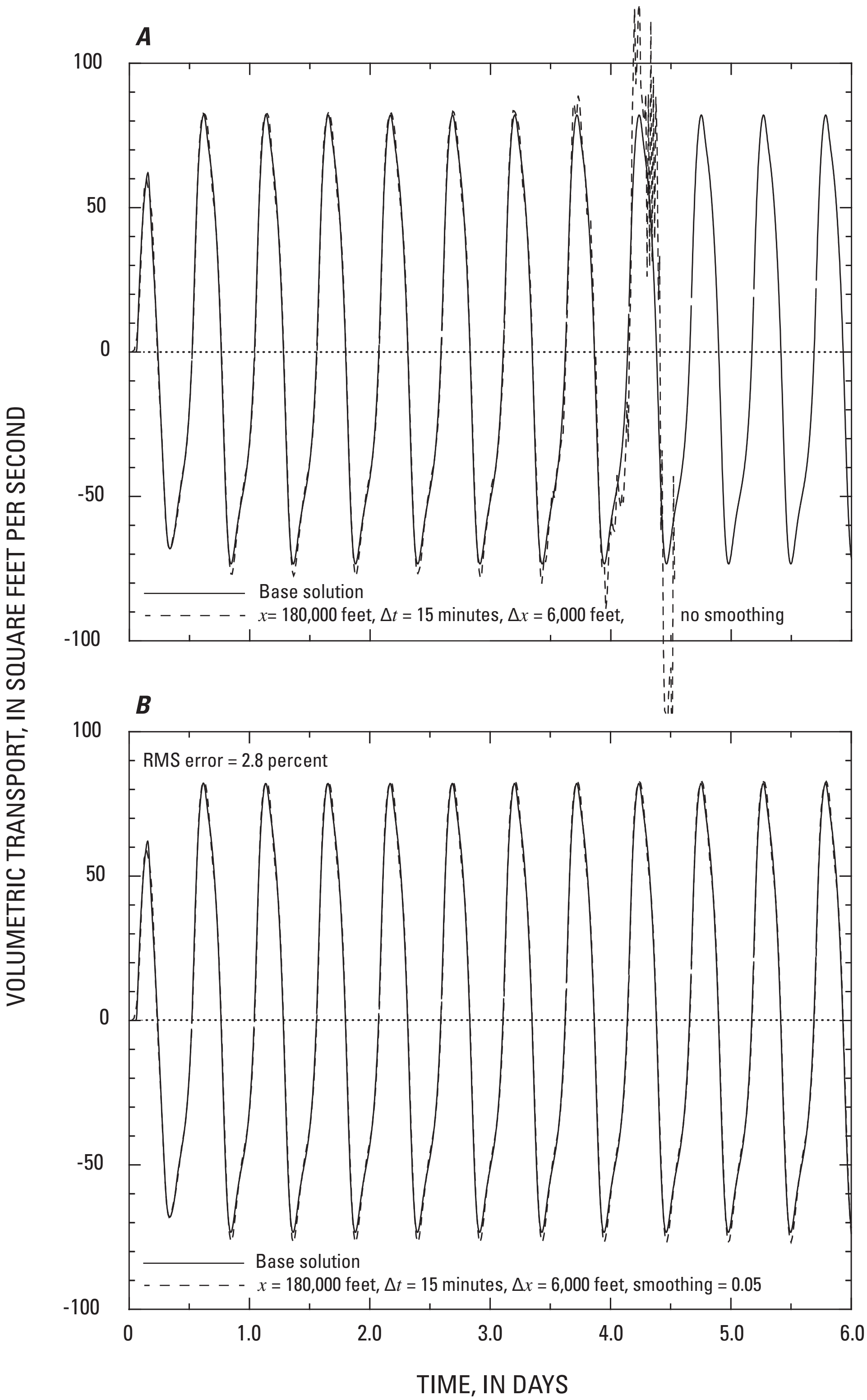

Figure 5.19. Solutions using the three-level semi-implicit, leapfrog scheme (no trapezoidal step) (*A*) with no smoothing and (*B*) with smoothing (β = 0.05).
Without smoothing the run becomes unstable after 4 days. With only minimal smoothing a very good solution is obtained. Δt is the size of the computational time interval. Δx is the size of the computational space interval. RMS, root mean square.

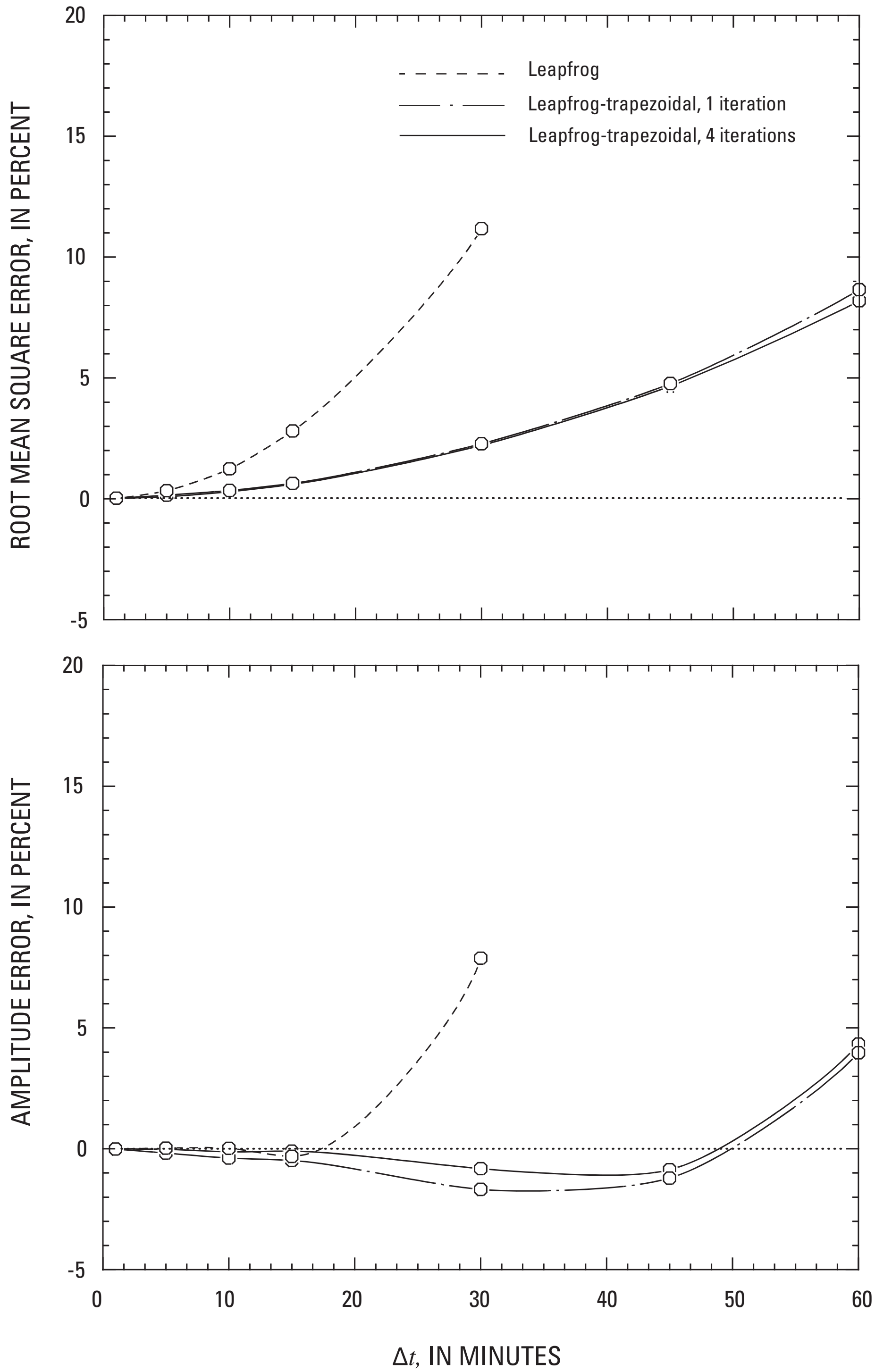

Figure 5.20. Solutions using the three-level semi-implicit scheme for the tidal test problem. All simulations used space step $\Delta x = 6{,}000$ feet. The solutions with the leapfrog scheme and the leapfrog-trapezoidal scheme (1 iteration) used smoothing ($\beta = 0.05$) for time step $\Delta t \geq 10$ minutes.

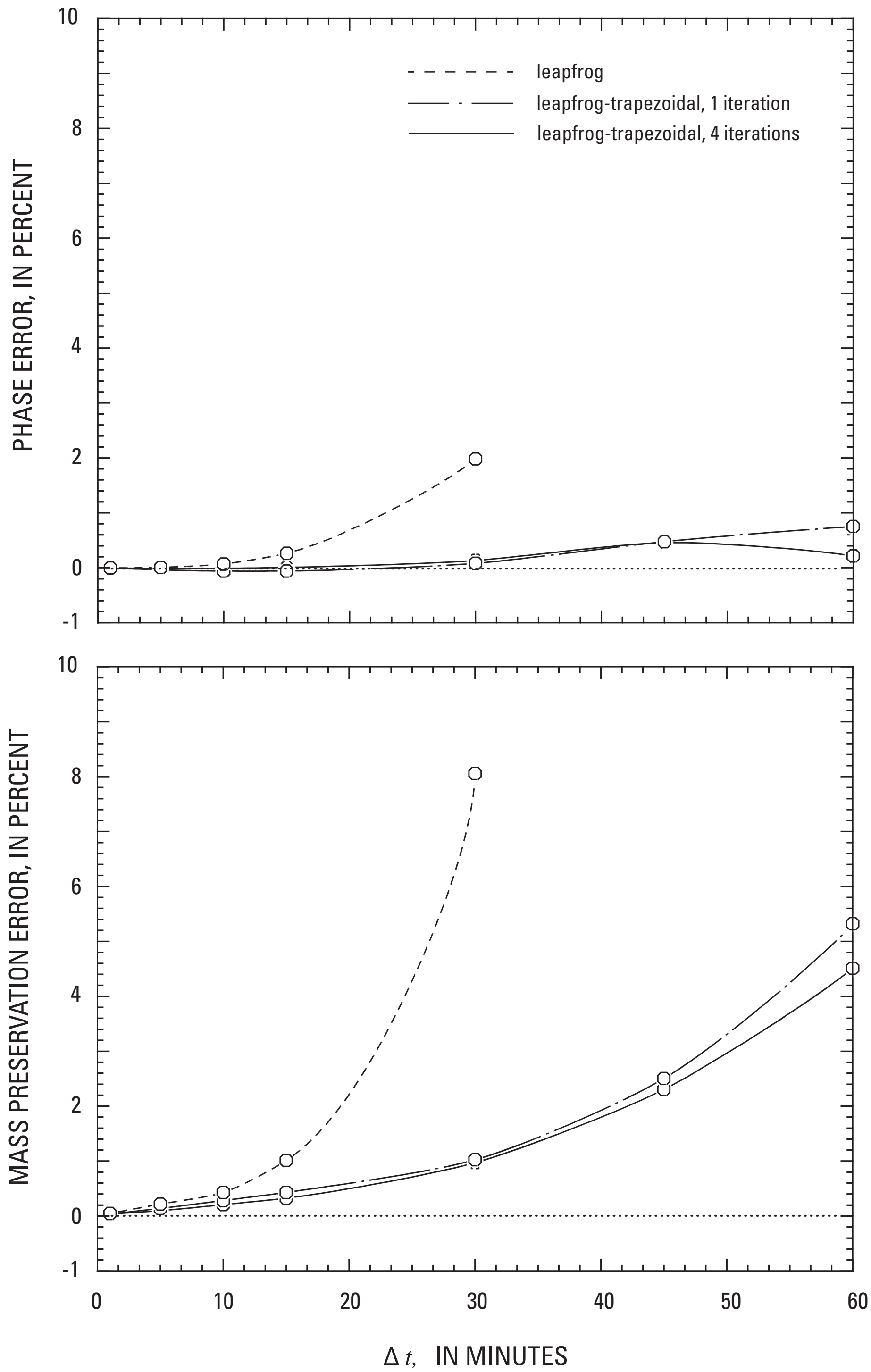

Figure 5.20. Continued.

5.2.2.3 Remarks

The comparison between the error measures for the two-level scheme (*niter* = 2) and the leapfrog-trapezoidal scheme (one iteration of the trapezoidal step) are given in *figure 5.21*. The two schemes are very similar in terms of accuracy. The main difference between the two schemes using this test problem was in the performance of the schemes without iteration. Although both schemes suffered from stability problems when iteration was not used, the problems were less troublesome with the leapfrog scheme. The availability of a time filter is an advantage of the three-level scheme.[50] Two of the simulations attempted using the leapfrog scheme could be made stable with this filter without introducing too much damping into the solution. The leapfrog solutions that were stable without smoothing actually improved slightly (had reduced errors) with smoothing because the unsmoothed leapfrog scheme has a slight tendency to amplify the solution to this tidal problem. Several of the unsmoothed leapfrog-trapezoidal solutions with one iteration were unstable; these solutions could be stablized by the filter. Because the computational time required to use the filter is minimal, and the effects on the solution accuracy generally are minimal (and in some cases are beneficial), there is little reason not to employ it routinely in the three-level solutions.

Based on the results of both 1-D numerical experiments, it was decided to use the three-level scheme in the 3-D model.

5.3 Three-Dimensional Experiment

The 3-D numerical experiment uses a problem presented in a report by Leendertse and Liu (1977) to test the early Rand Corporation 3-D model. It simulates a uninodal standing oscillation or seiche (Wilson, 1972) in a rectangular basin. The simple geometry and boundary conditions of the problem make it a good test case for the basic computational scheme of a 3-D model.

5.3.1 Seiching in a Rectangular Basin

The test basin for the seiching experiment is 46 km long, 14 km wide, and 12 m deep (*fig. 5.22*). Initially the fluid in the basin is at rest but displaced so that the free surface profile is a half-cosine wave. At the moment the free surface is released, the fluid begins an oscillatory motion that continues until the motion is damped out by frictional resistance. The initial amplitude of the seiche is 25 cm displaced vertically upward at the west (left) end of the basin. The horizontal computational grid for the numerical solution is shown in *figure 5.22B*; the grid size is $\Delta x = \Delta y = 2$ km. The vertical grid consists of six layers; each layer is 2 m thick.

[50] The time filter also is easily added to a 3-D, three-level scheme.

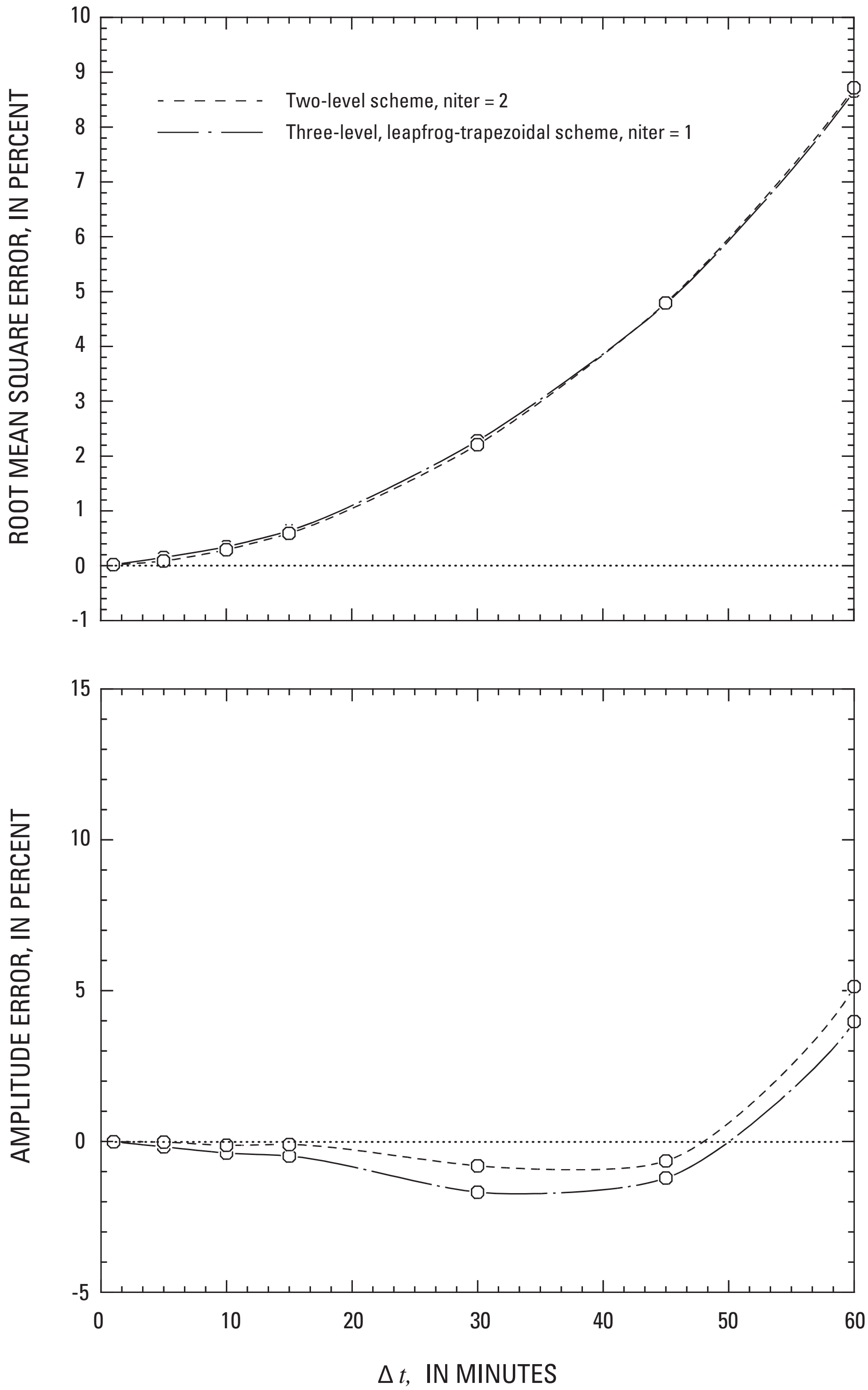

Figure 5.21. Comparison of error measures between the two-level scheme with two iterations (*niter* = 2) and the three-level leapfrog-trapezoidal scheme with one iteration (*niter* = 1) of the trapezoidal step.
All simulations were with space step Δx = 6,000 feet. The leapfrog-trapezoidal solutions were smoothed (β = 0.05) for time step $\Delta t \geq$ 10 minutes.

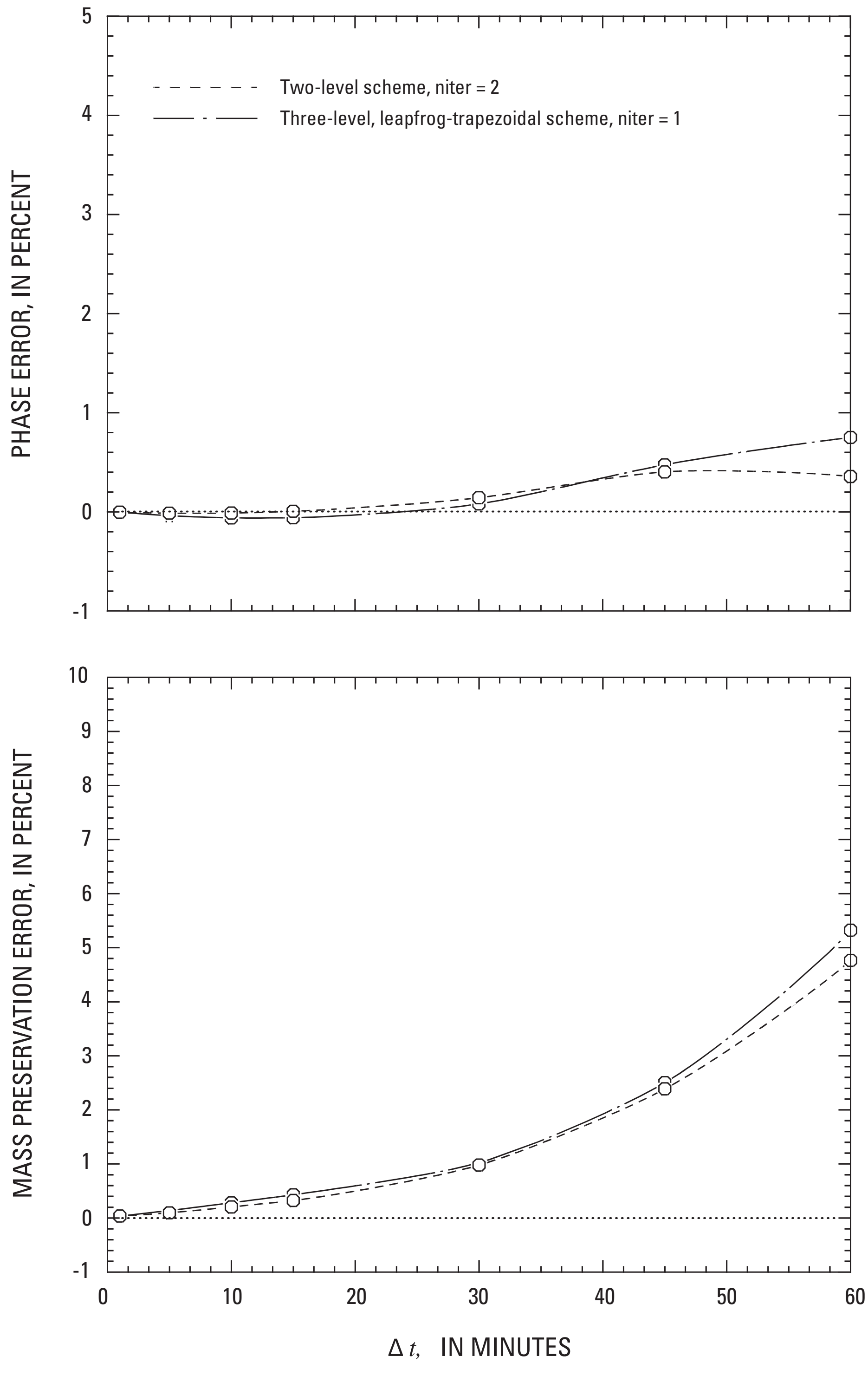

Figure 5.21. Continued.

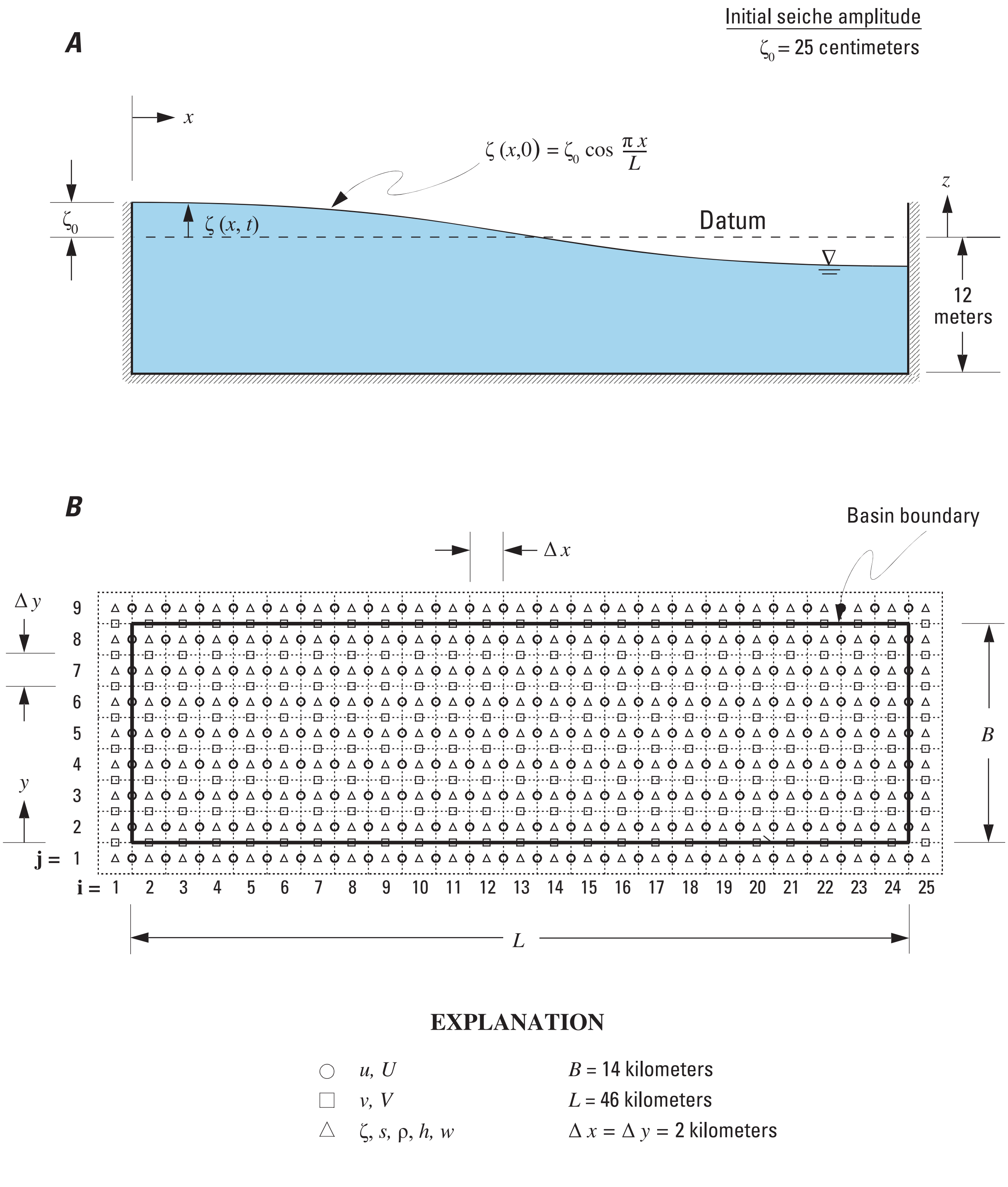

Figure 5.22. Diagram of *(A)* the test problem for an oscillating wave (seiche) in a rectangular basin and *(B)* the horizontal computational grid for the numerical solution.
The vertical grid uses six layers, each 2 meters thick.

An analytical solution to the seiching problem exists if the Coriolis and advection terms in the governing equations are neglected and the fluid in the basin is assumed to be frictionless (see Neumann and Pierson, 1966, p. 291). The first test of the 3-D numerical scheme was the simulation of this ideal fluid motion. The computed and analytical solutions for the initial 0.675 hours of the simulation are shown in *figure 5.23* at the computational nodal points indicated; the computations use the simplest formulation of the leapfrog scheme in which all terms in the finite-difference equations are treated explicitly (explicit leapfrog). For this computation, the time step was restricted to 45 seconds so that the gravity-wave Courant number did not exceed unity. In *figure 5.23A*, the solution for the horizontal velocity component u is plotted for the middle of the basin. Because the internal friction in the fluid is zero, no shear in the velocity profile develops and the solution for u is identical within each vertical layer. In *figures 5.23B and 5.23C,* the solution for the water surface elevation ζ and the vertical velocity component w are plotted for the west end of the basin. The velocity w, which varies with the vertical location in the water column, is plotted only for the third layer from the surface ($k = 3$). The curves representing the computed and analytical solutions in *figure 5.23* are indistinquishable on the graphs, indicating negligible error in the computed results. The computed solution at all other nodes also was in virtually perfect agreement with the analytical solution.

The results shown in *figure 5.24* are identical to those shown in *figure 5.23* except that the numerical solution is computed using the semi-implicit, leapfrog scheme. The numerical results again agree with the analytical solution and in this case provide confidence that the computations for the matrix solution that is a part of the semi-implicit scheme are working correctly in the 3-D computer code.

Figure 5.25 shows the time history of the solutions for u, ζ, and w from *figure 5.24* extended to twenty hours. Owing to the absence of friction, the oscillation continues indefinitely without damping at a period of $T = 2L/(gH)^{1/2}$. The agreement between the computed and analytical solutions is excellent over the entire 20 hours.

To test the semi-implicit, leapfrog scheme under conditions having gravity-wave Courant numbers of one and above, three simulations were conducted using time steps of 3, 5, and 10 minutes. These time steps correspond to Courant numbers (Cr_g) equalling 1.0, 1.6, and 3.3, respectively. The 20-hour computed solutions for the horizontal velocity component u at mid-basin are plotted in *figure 5.26* for the three time steps; the analytical solution also is plotted on each graph. The results indicate that a significant lagging phase error can occur in the numerical solution when the Courant number is increased. This tendency for lagging phase error in the semi-implicit scheme at Courant numbers greater than one is well known (Mesinger and Arakawa, 1976) and was identified earlier in the results of the 1-D hydrograph-routing numerical experiment. In the seiching experiment, the phase error becomes more prevalent as the simulation runs longer because it is cumulative.

The magnitude of the phase error can be reduced, although not eliminated, by the addition of the trapezoidal step to the semi-implicit, leapfrog scheme. *Figure 5.27* presents the same graphs as *figure 5.26* but with numerical computations using the semi-implicit, leapfrog-trapezoidal scheme. The phase error is reduced significantly (by more than half) with the addition of the trapezoidal step. Using more than one iteration of the trapezoidal step failed to make any significant difference in the computed solution results.

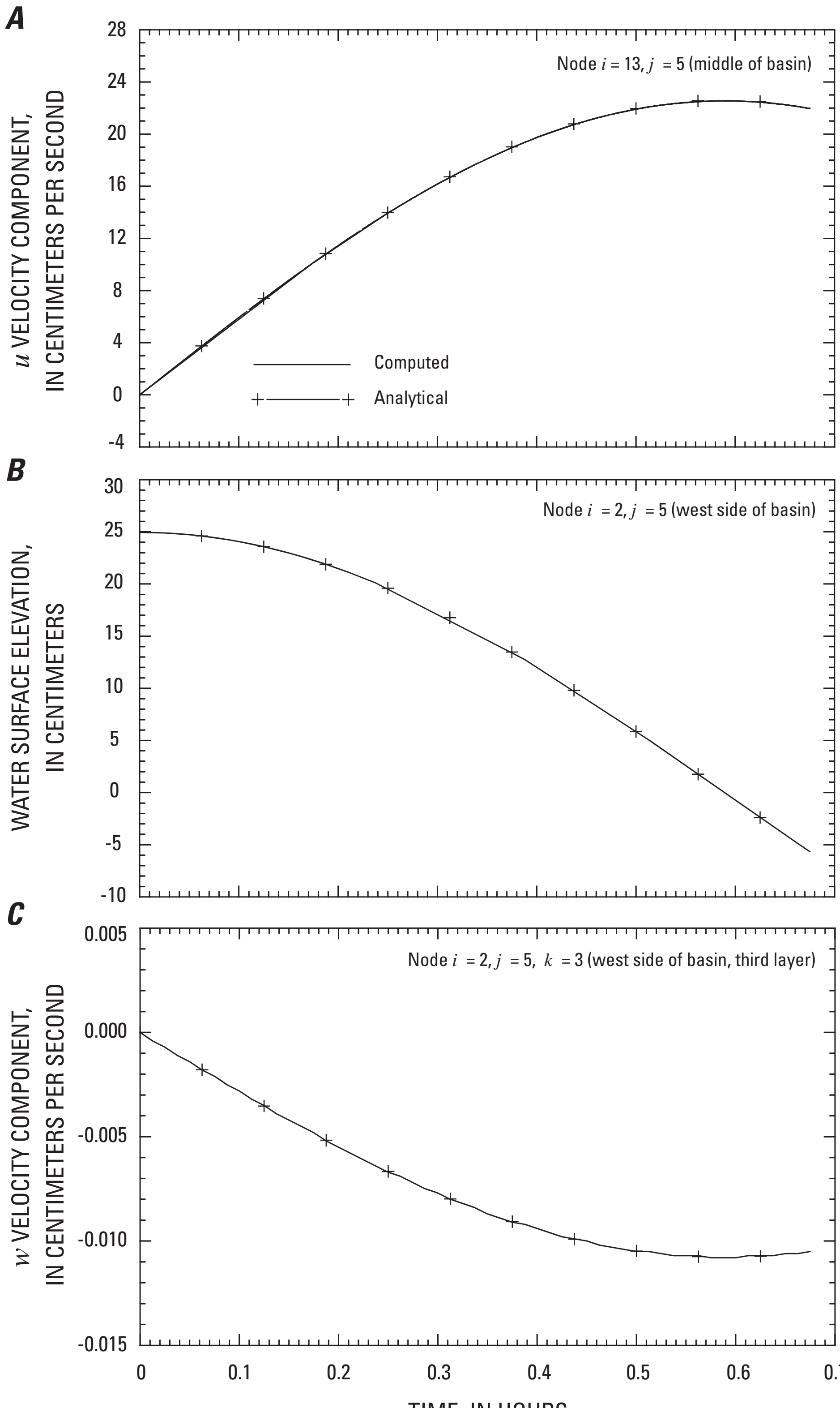

Figure 5.23. Computed and analytical solutions for the 3-dimensional (3-D) seiching test problem assuming an ideal (non-viscous) fluid and using the 3-D, explicit, leapfrog scheme for the numerical solution. A computational time step of 45 seconds was used for the numerical solution.

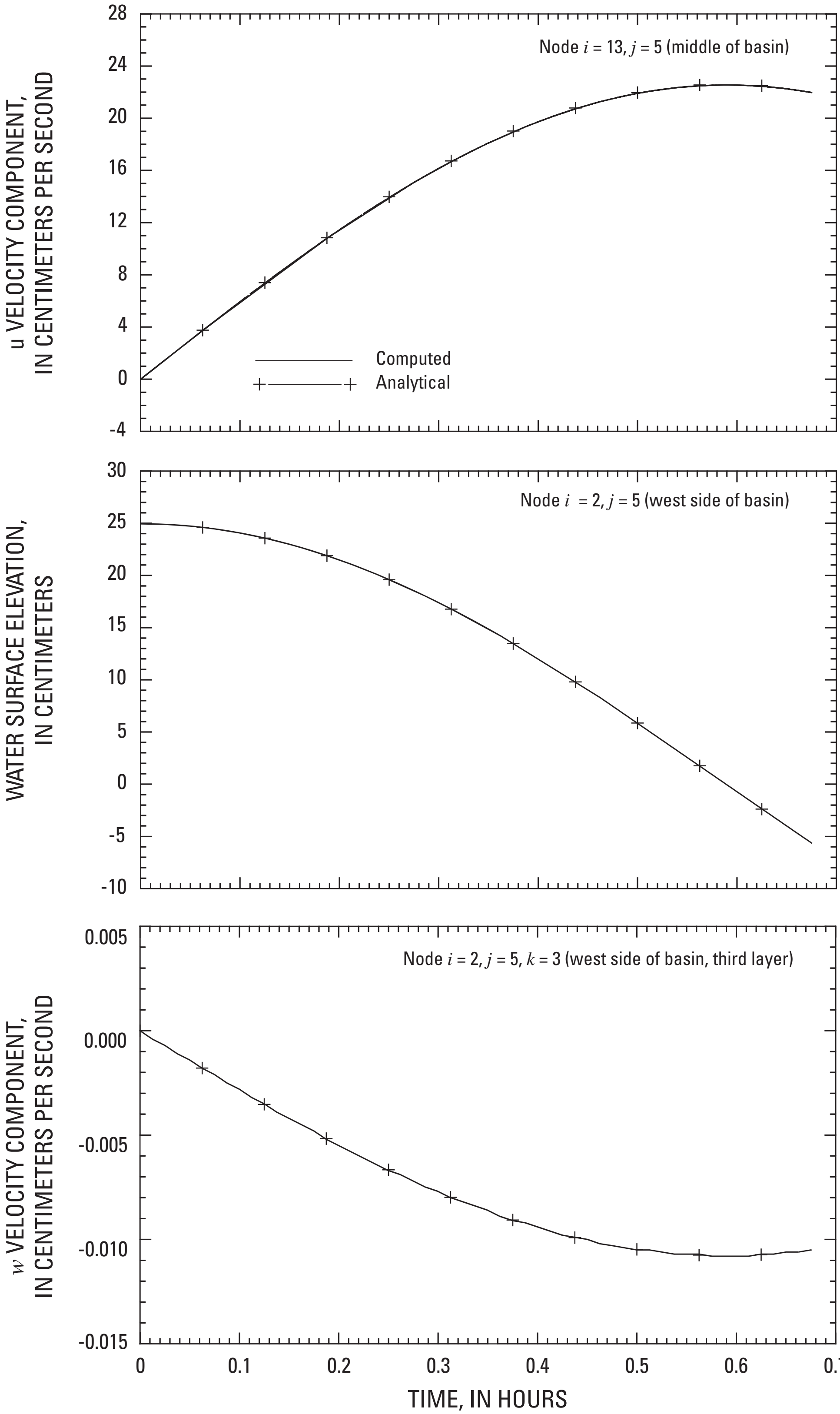

Figure 5.24. Computed and analytical solutions for the 3-dimensional (3-D) seiching test problem assuming an ideal (non-viscous) fluid and using the 3-D, semi-implicit leapfrog scheme for the numerical solution. A computational time step of 45 seconds was used for the numerical solution.

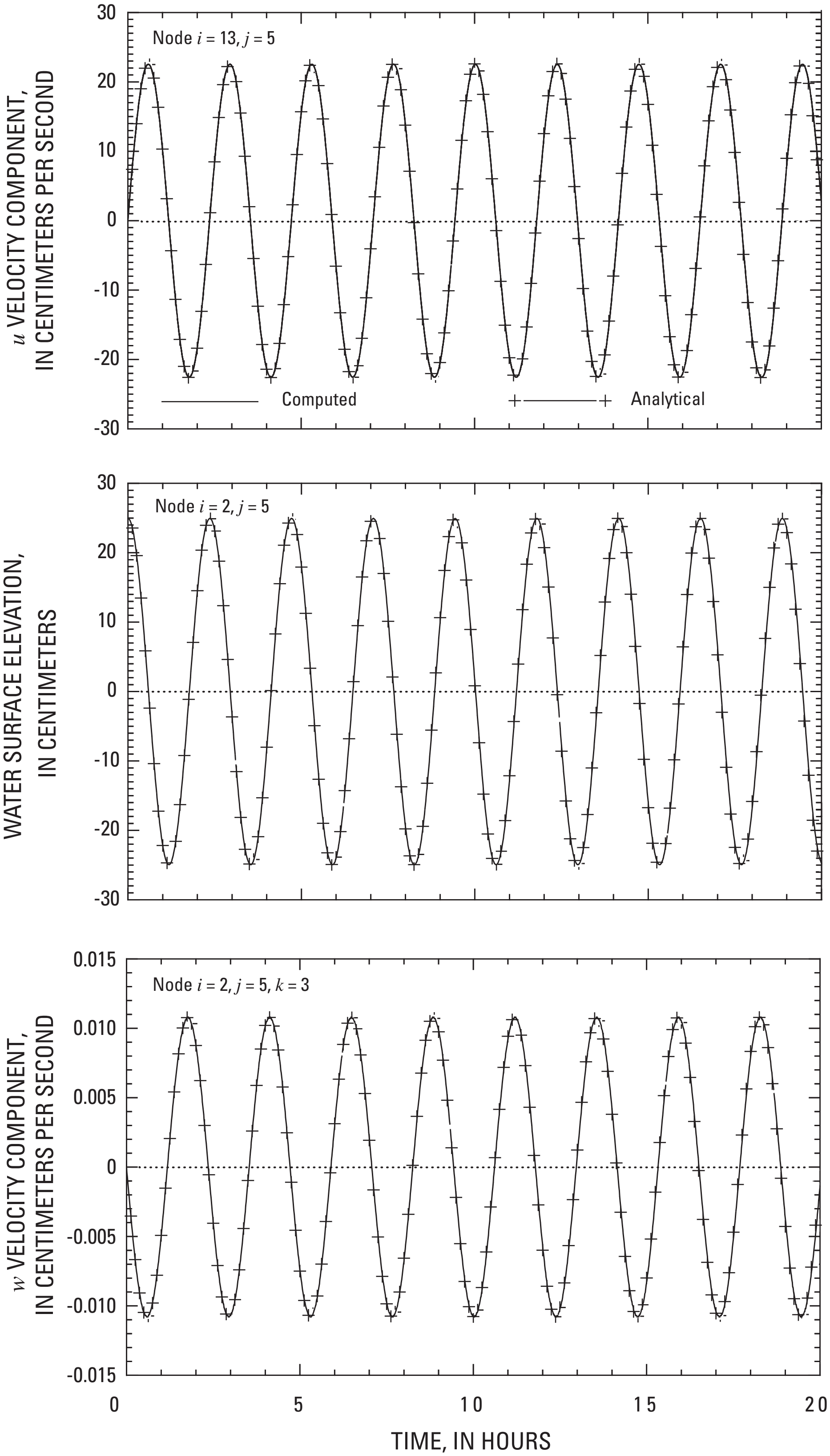

Figure 5.25. Twenty-hour time history of computed and analytical solutions for the seiching of an ideal fluid. The numerical solution is computed using the 3-dimensional semi-implicit leapfrog scheme and a time step of 45 seconds.

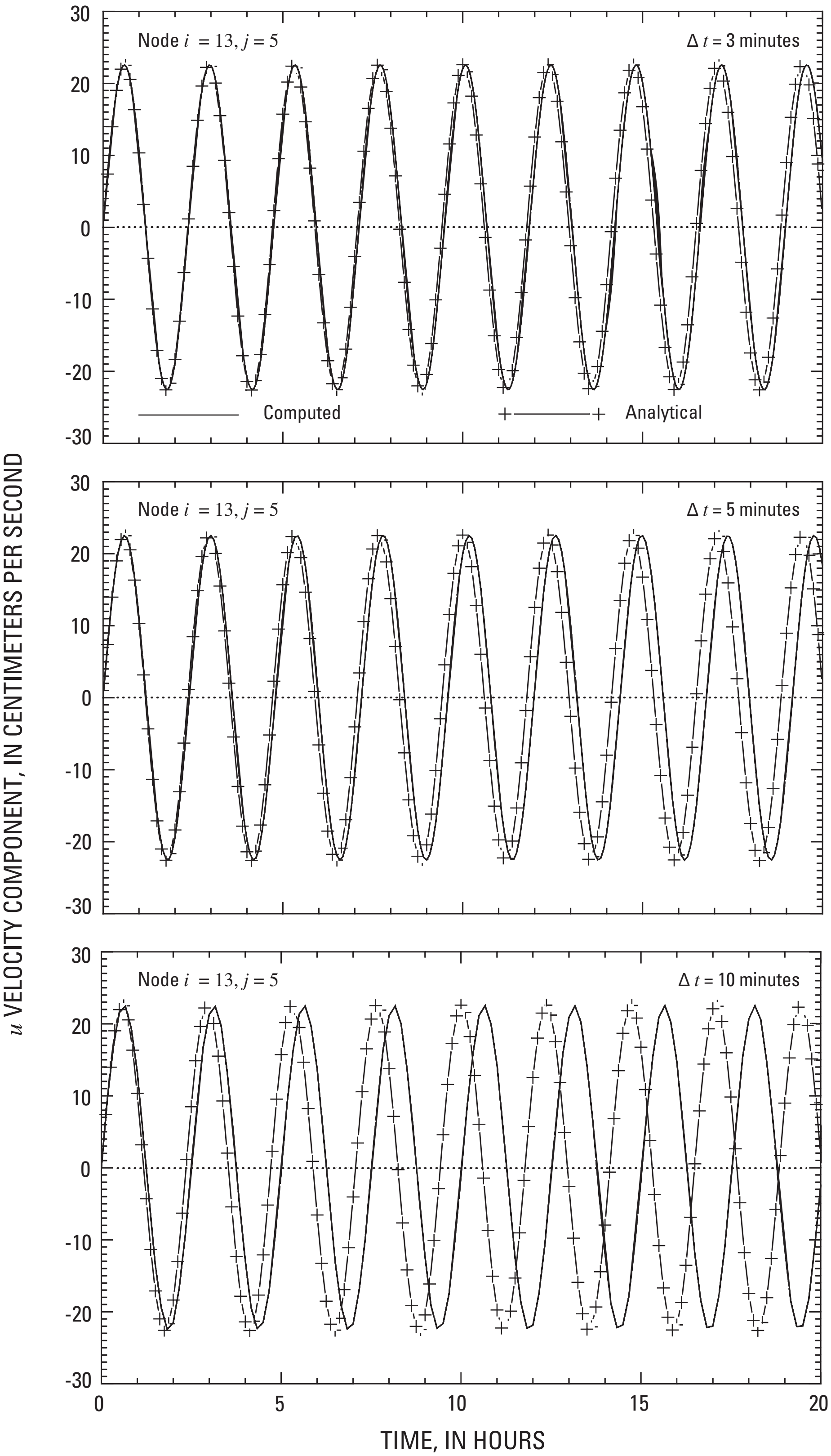

Figure 5.26. Mid-basin solutions for the 3-dimensional seiching problem using an ideal fluid and three different time steps (Δt) for the semi-implicit leapfrog scheme. The analytical solution is shown for comparison.

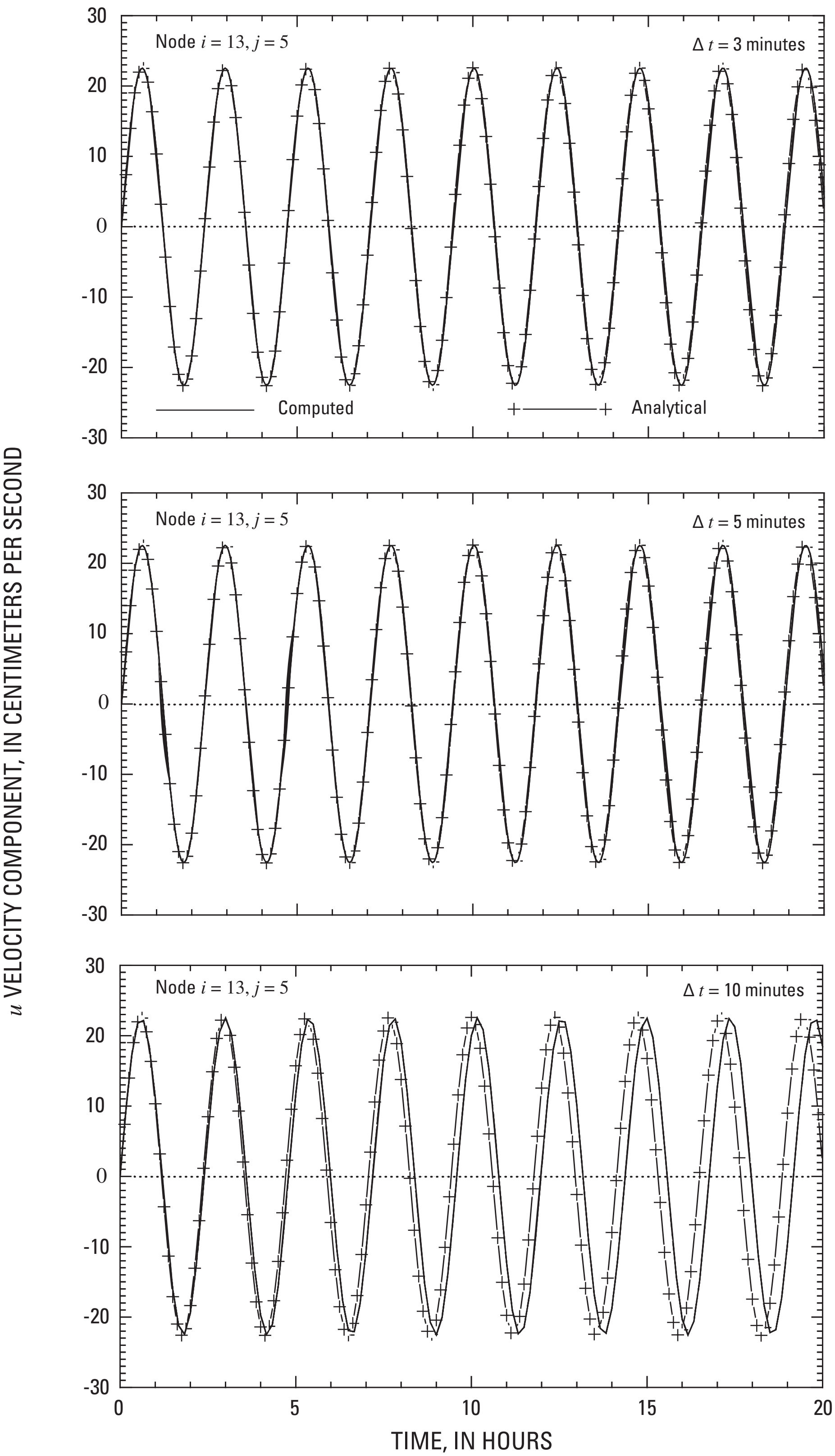

Figure 5.27. Mid-basin solutions for the 3-dimensional seiching problem using an ideal fluid and three different time steps (Δt) for the semi-implicit leapfrog-trapezoidal scheme. The analytical solution is shown for comparison.

After testing the 3-D scheme for the seiching problem using a non-viscous (ideal) fluid, it was tested for a viscous (real) fluid. For the viscous fluid problem, all terms in the finite-difference equations were included except the Coriolis term.[51] The fluid was assumed to be of homogeneous density, and the bottom drag coefficient (used in eq. 2.64) was set to $C_d = 0.008$. The horizontal eddy viscosity A_H was set to zero.[52]

The vertical turbulence parameterization used to simulate the seiching problem by Leendertse and Liu (1977) was based on a one-equation turbulence model (Launder and Spaulding, 1972; Rodi, 1980a). In the one-equation model, a differential transport equation is solved for the distribution of the turbulent kinetic energy per unit mass (K), and a simple empirical relation (such as eq. 2.32) is used to specify the distribution of the turbulent mixing length (Λ); the turbulent eddy viscosity is computed from K and Λ using the Kolmogorov-Prandtl expression:

$$A_V = \Lambda\sqrt{K} \ . \tag{5.3}$$

As an independent check on the full nonlinear calculations of the semi-implicit, 3-D scheme, this code was used to reproduce as nearly as possible the predictions for the viscous seiching problem presented by Leendertse and Liu (1977). For this purpose the mixing length turbulence parameterization of the semi-implicit model was modified to more closely represent the one-equation parameterization used in Leendertse and Liu (1977). As discussed in Rodi (1980a, p. 22), the mixing length parameterization is a special case of the one-equation parameterization if the turbulence is in a state of local equilibrium. Local equilibrium means that the production and dissipation of the turbulence energy are in balance at each point in the flow and that the transport influence, by advection or diffusion, of turbulent kinetic energy from other points in the flow is negligible. By equating the production and dissipation terms used by Leendertse and Liu (1977), the following mixing length formula is obtained:

$$A_{V_0} = 3.16\Lambda^2\left(\frac{\partial u}{\partial z}\right) \ . \tag{5.4}$$

This equation is identical to the form of equation 2.31 in this report (assuming $\partial v / \partial z = 0$), except for the introduction of the coefficient 3.16. Thus, in the simulation of the seiching problem, the coefficient 3.16 was inserted into the turbulence coding of the semi-implicit scheme. The initial value of the turbulent kinetic energy per unit mass was chosen to be 0.4 cm^2/s^2 (Leendertse and Liu, 1977) and was used in equation 5.4 to estimate a background value for the eddy viscosity; the background value was then added to the value calculated by equation 5.4. The value for the horizontal eddy viscosity used by Leendertse and Liu (1977) was zero.

A sample velocity distribution from the seiching problem is shown in *figure 5.28* after 0.6 hour of simulation. The gradual development of the vertical velocity profile at the center of the basin is shown in *figure 5.29A*. The viscous effects in the computed solution cause these velocities to be lower than those in the analytical solution for a non-viscous fluid. The computed water surface elevation for the viscous fluid is shown at the west end of the basin in *figure 5.29B* and is damped slightly from the ideal fluid solution. The computed results in *figure 5.29* are in close agreement with those presented by Leendertse and Liu (1977, figures 7 and 8). The 20-hour time history of the viscous solution is plotted in *figure 5.30*, illustrating the solution damping. The solution was checked for mass preservation in the surface layer of the model and the error was virtually zero.

---

[51]The Coriolis term was set to zero so that there was no *y*-direction variation in the computed velocity field.

[52]Several test simulations were done using increasing values for A_H. No noticeable diffusion appeared in solutions for A_H less than about 100 m^2/s, which is large.

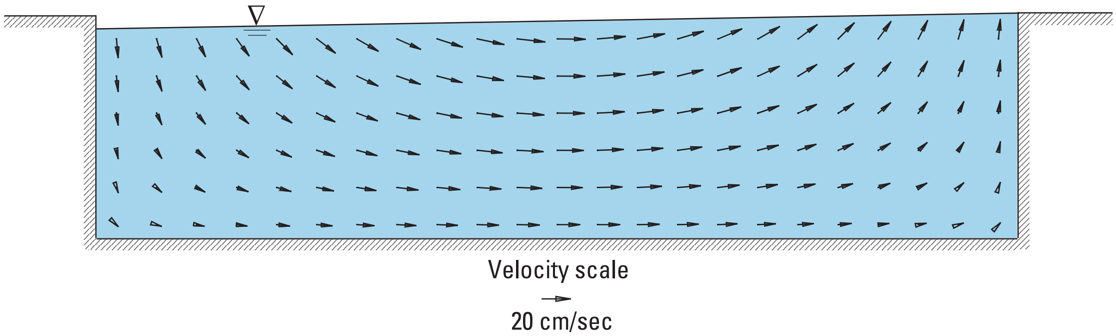

Figure 5.28. Sample velocity distribution after 0.6 hour of simulation for the 3-dimensional seiching problem using a viscous fluid.
cm/sec, centimeter per second.

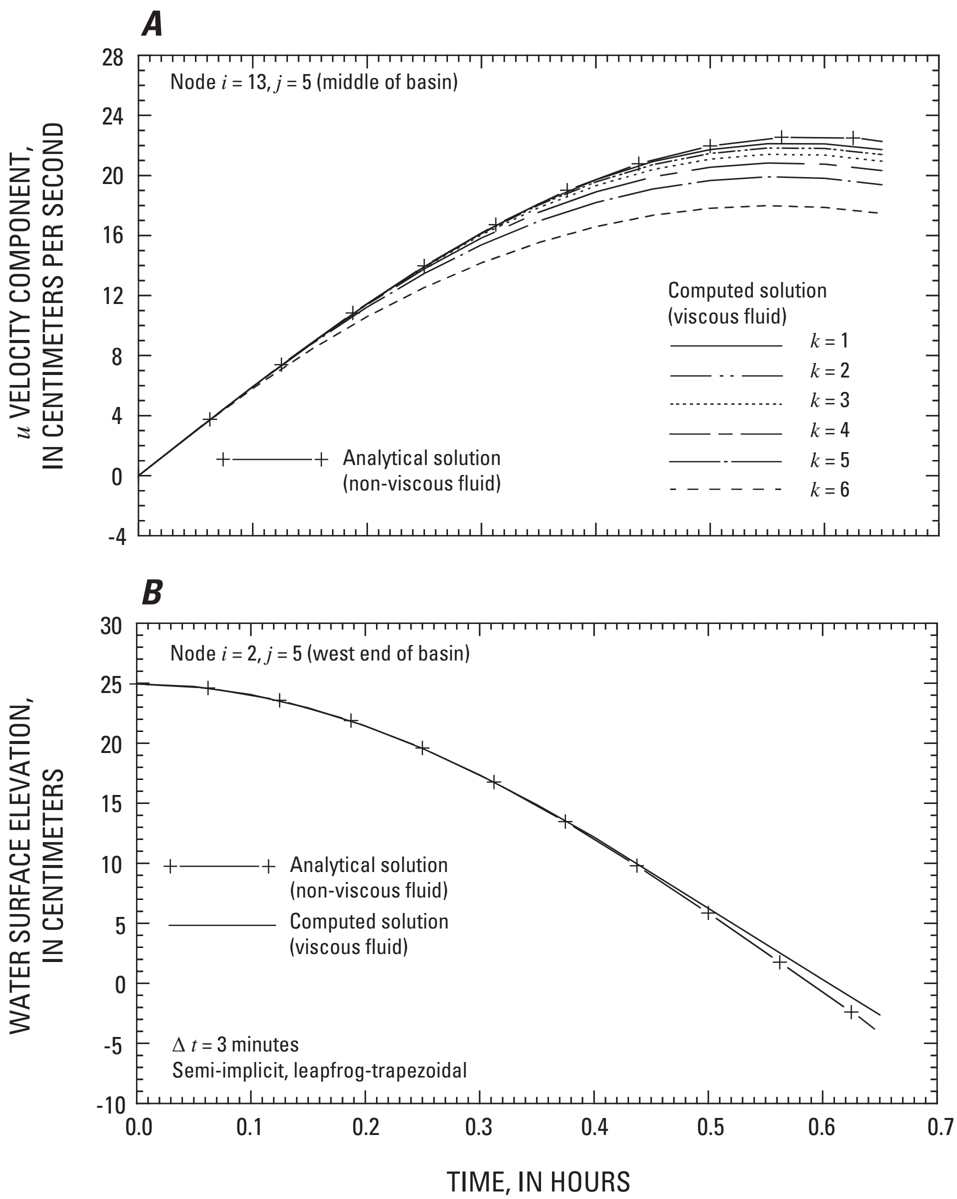

Figure 5.29. Computed solution for the 3-dimensional seiching problem using a viscous, homogeneous fluid. Analytical solution for an ideal (non-viscous) fluid. Δt, time step; k, layer number

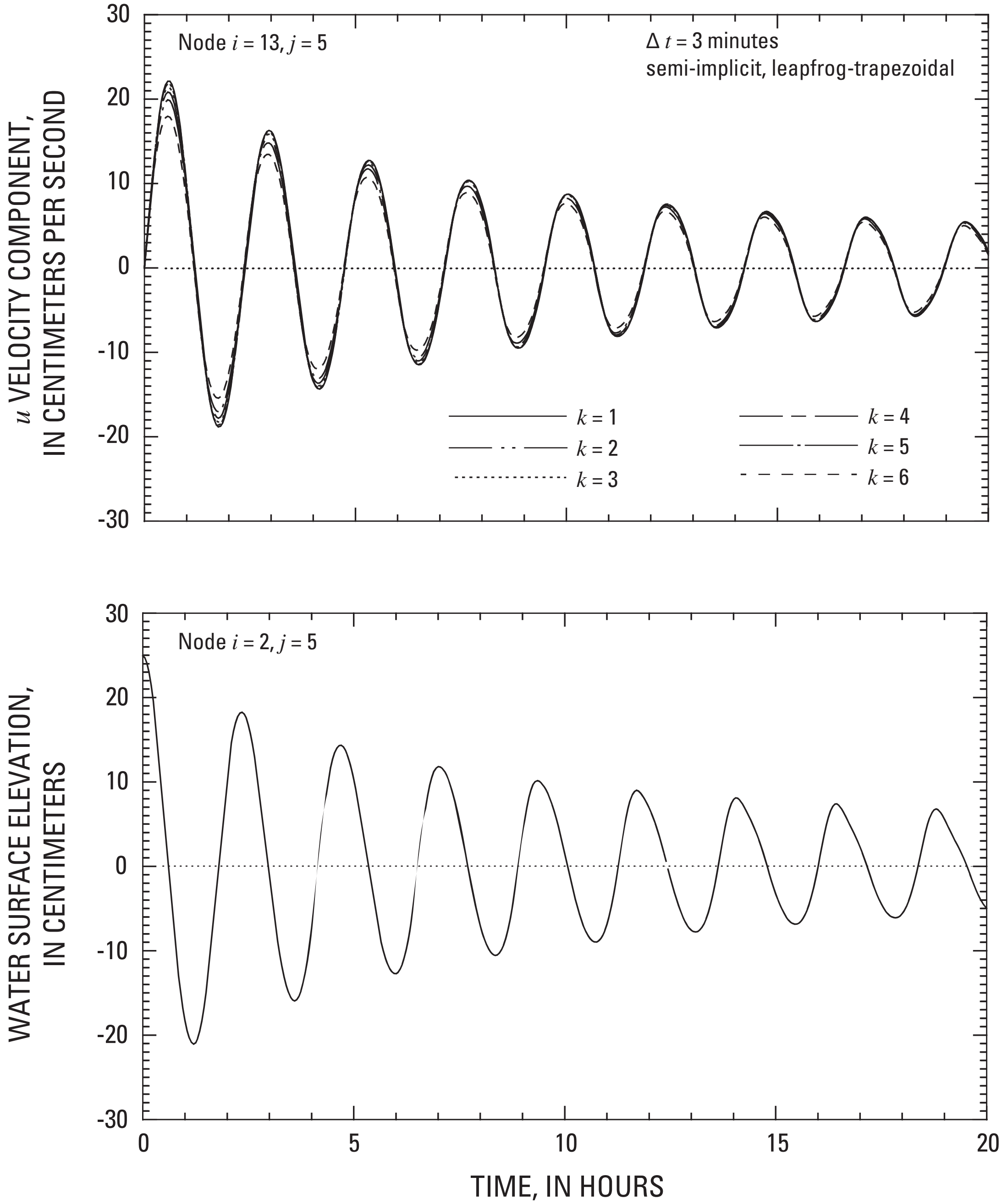

Figure 5.30. Simulated 20-hour time history for seiching of a viscous, homogeneous fluid.

Continuing with comparisons of test simulations with those of Leendertse and Liu (1977), a second simulation of the viscous seiching problem was computed using a slightly shorter basin length of 44 km. The simulation covered 20 hours using the same model parameters as those used to simulate the longer basin. The calculations used the semi-implicit, leapfrog scheme with a time step of 45 seconds. The vertical profiles of the *u* velocity component at mid-basin were saved to a file at a constant time interval of 3.125 hours (250 time steps). A plot of these profiles is shown in *figure 5.31*. The same solution profiles, digitized from the report by Leendertse and Liu (1977, fig. 12), are also shown. Although the two sets of profiles are in reasonably close agreement, the semi-implicit solution predicts larger absolute magnitudes for the velocities in each profile than was computed by Leendertse and Liu. It was suspected that the cause of the difference was that equation 5.4 underestimated the magnitude of the eddy viscosities computed by the turbulence model of Leendertse and Liu. Leendertse and Liu (1977, fig. 6*D*) graphically present a distribution of the magnitudes of the turbulent kinetic energy per unit mass calculated from their turbulence model after 60 time steps of simulation; using equation 5.3 to translate these values into a distribution of the eddy viscosity, a depth-averaged eddy viscosity at mid-basin was calculated as approximately 300 cm^2/s.[53] The depth-averaged eddy viscosity calculated during the semi-implicit simulation after 60 time steps (using eq. 5.4) was only 200 cm^2/s. To decrease the differences between the two sets of velocity profiles in *figure 5.31*, another simulation with the semi-implicit, leapfrog scheme was made using a constant value of 300 cm^2/s for the eddy viscosity. The two sets of profiles are in closer agreement (*fig. 5.32*); some differences still exist but are most likely attributable to the difference in turbulence parameterizations or to inexact digitizing of profiles from the report by Leendertse and Liu. Note that the computed profiles using the constant eddy viscosity exhibit less vertical variation in velocity (shear) than in the previous solution in which the eddy viscosity varied over the depth.

One final simulation of the seiching problem was made to test the semi-implicit scheme for conditions using variable density. A linear vertical density gradient of $\Delta\rho / \Delta z = 0.035$ $kg/m^3/cm$ was introduced with freshwater at the free surface. Equation 5.4 was used to estimate the eddy viscosity under homogeneous density conditions, and the effects of stratification were incorporated using the stability functions (eqs. 2.27 and 2.36) proposed by Munk and Anderson (1948). The longer basin length of 46 km was used. The oscillation in this test showed greater vertical shear in the velocity profile than the test using the homogeneous density because the vertical mixing was reduced by the stratification (*fig. 5.33*). The results were very similar to those of Leendertse and Liu (1977, fig. 9), but they were not identical because of differences in the turbulence parameterizations and stability functions used in the two models.

[53]A depth-averaged eddy viscosity of 300 cm^2/s is quite high for a basin 12 meters deep. A standard estimate for the depth-averaged eddy viscosity in constant density flow in which the turbulence is generated by bottom shear stress is $0.067Hu^*$ (Fischer and others, 1979). This estimate corresponds to a maximum of about $A_{V_0} = 100$ cm^2/s. A simulation using $A_{V_0} = 100$ cm^2/s did not agree well with the solution of Leendertse and Liu (1977).

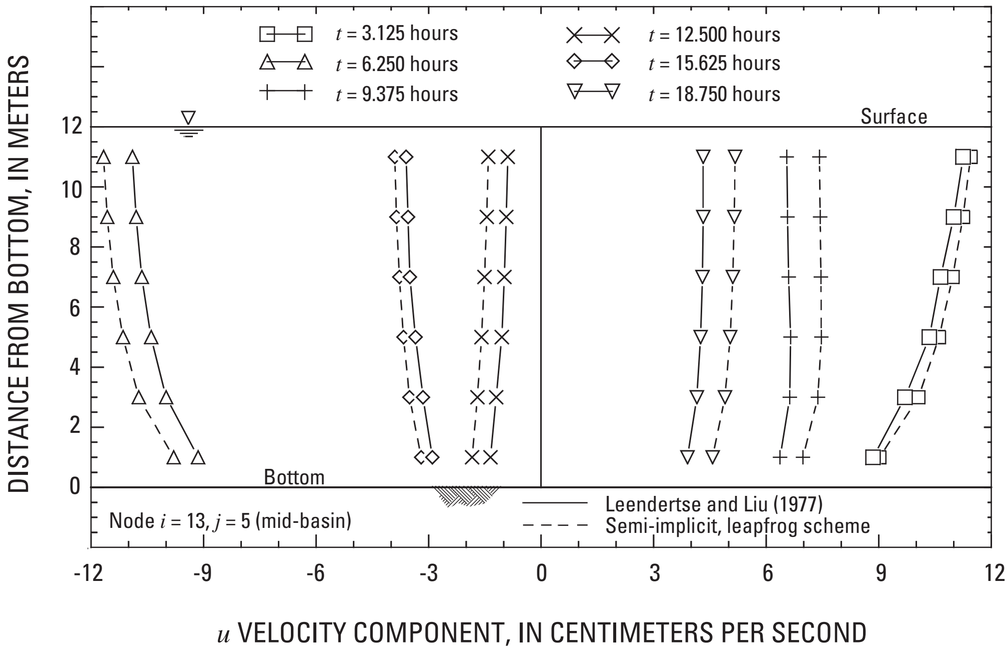

Figure 5.31. Velocity profiles for the 3-dimensional (3-D) seiching problem using a viscous, homogeneous fluid in a 44-kilometer basin and a vertical eddy viscosity defined by a mixing length formula. The profiles were computed using the 3-D, semi-implicit, leapfrog scheme and a vertical eddy viscosity defined by equation 5.4. For comparison, the velocity profiles from the report by Leendertse and Liu (1977, fig. 12) also are shown.

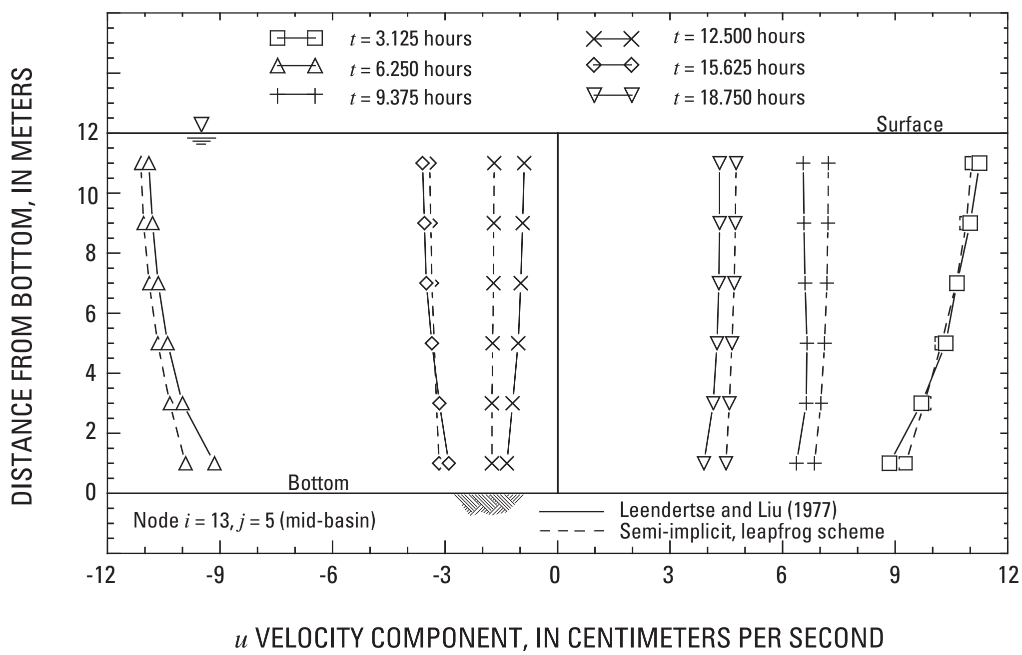

Figure 5.32. Velocity profiles for the 3-dimensional (3-D) seiching problem using a viscous, homogeneous fluid in a 44-kilometer basin and a constant vertical eddy viscosity.
The profiles were computed using the 3-D, semi-implicit, leapfrog scheme and a vertical eddy viscosity of 300 cm^2/sec. For comparison, the velocity profiles from the report by Leendertse and Liu (1977, fig. 12) also are shown.

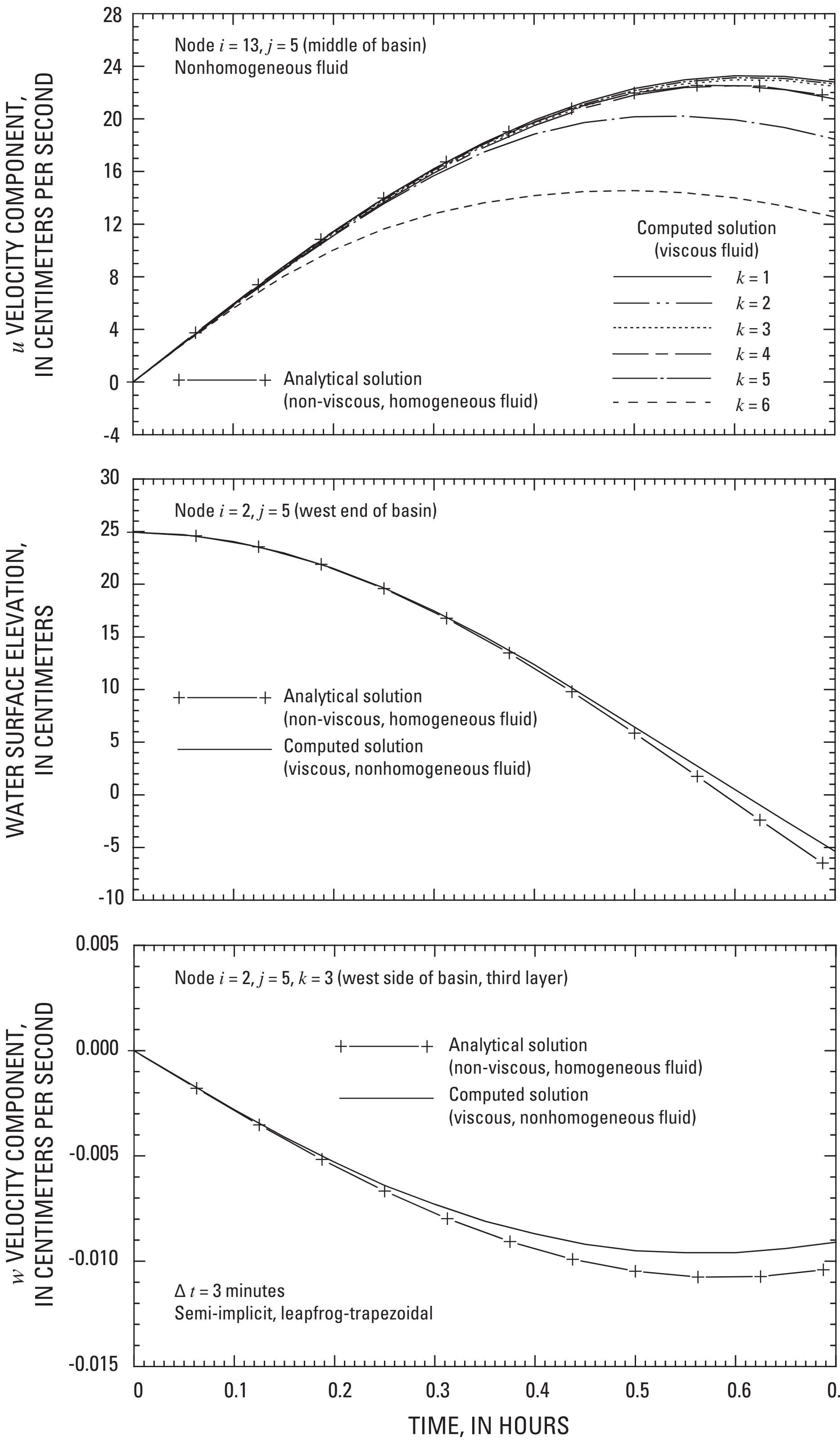

Figure 5.33. Computed solution of the 3-dimensional (3-D) seiching problem using a viscous fluid of nonhomogeneous density. For comparison, the analytical solution for an ideal (non-viscous, homogeneous) fluid is shown. The computed solution is determined using the 3-D, semi-implicit, leapfrog-trapezoidal scheme and a time step of 3 minutes. *k*, layer number; Δt, time step.

5.3.1.1 Remarks

Although more testing is necessary, the 3-D solutions look very good and establish confidence that the computer coding of the numerical scheme is working as expected. Phase error is more apparent in the seiching experiment than in the 1-D test experiments because the phase error is cumulative during the seiching calculation. Phase error is a well known feature of implicit schemes when the time step is relatively large and the CFL condition significantly exceeds unity. The trapezoidal step is a useful device to reduce the phase error, although at additional computational expense. Solutions for the 1-D tidal experiment generally contained very small phase errors, because an open boundary condition in the experiment prevents any accumulation of error. Consequently, in the modeling of real estuaries, it is likely that phase error will not be a problem.

6. Summary and Conclusions

A new 3-D, finite-difference model has been developed and tested. The model uses a semi-implicit, leapfrog-trapezoidal numerical scheme that is efficient and essentially second-order accurate in the spatial and temporal numerical approximations. The numerical scheme is based on treating the gravity-wave and vertical diffusion terms implicitly and other terms in the governing equations explicitly. The model does not rely on any form of vertical/horizontal mode-splitting to incorporate implicit vertical diffusion into the semi-implicit scheme. The governing equations for the multilevel scheme are arranged in conservation form by integrating them over the height of each horizontal layer. The layer-integrated volumetric transports replace velocities as the dependent variables so that the depth-integrated continuity equation used in the solution for the water surface elevation is linear. The advantage of the semi-implicit approach is that the solution for the water surface elevation is uncoupled in the model from the solution for volumetric transport. A five-diagonal system of linear equations is solved at each time step for the water surface elevation using an efficient preconditioned conjugate-gradient method. Volumetric transports are computed explicitly from the momentum equations.

Prior to developing the 3-D model, two 1-D models described in sections 4.2.1 and 4.2.2 were tested to compare two-time-level versus three-time-level approaches for the time integration. On the basis of the 1-D numerical results presented in Chapter 5, the three-time-level (semi-implicit, leapfrog-trapezoidal) scheme was extended to three dimensions. The advantage of leapfrog-trapezoidal integration is the ease with which nonlinear terms can be centered in time to achieve second-order accuracy during both of the leapfrog and trapezoidal steps. The 1-D hydrograph test experiment described in Chapter 5 shows that the centering in time of the coefficient for the nonlinear bottom friction term can be important for the overall accuracy of a numerical solution. Nonlinear terms in the two-level scheme can be centered in time only by averaging the old and new time levels, which makes iteration necessary. The three-level, leapfrog scheme can occasionally be used very efficiently without a trapezoidal step (no iteration) to achieve second-order accuracy. The three-level-scheme solutions to the hydrograph problem that used one trapezoidal step after every leapfrog step generally had smaller errors than the two-level-scheme solutions using two iterations in each time step owing to the benefit of centering in time both steps of the leapfrog-trapezoidal scheme. The 1-D tidal test experiment described in Chapter 5 illustrates that nonlinear advection can cause instabilities in both the two-level and three-level schemes, especially when iteration is not used. The instabilities were less troublesome for the three-level, leapfrog scheme, and in some instances they could be eliminated by adding a simple time filter (Asselin, 1972) that introduced only minimal damping into a solution. The range of stability for both the two-level and three-level schemes can be extended by using iteration, although the number of iterations should be kept to a minimum because iteration in three dimensions is expensive. Using more than one iteration of the trapezoidal step in the three-level scheme or more than two iterations in the two-level scheme was not worthwhile for the 1-D test experiments, considering the extra computational expense incurred for minimal improvement in accuracy; in the few instances when extra iterations were needed to stabilize a particular solution, the values for the time step and Courant numbers were too large anyway to retain needed accuracy.

Although more testing of the 3-D, semi-implicit scheme is necessary, the results from the seiching experiment look promising. Accurate results are obtained for time steps that exceed the CFL condition for the gravity waves. Mass preservation is excellent. Because of the implicit nature of the numerical scheme, some phase errors do appear in solutions having large time steps. However, it is unlikely that this source of error will be prevalent in real tidal simulations of estuaries. If it is, it can at least be minimized by the use of the trapezoidal step in the scheme.

7. References

Abbott, M.B., and Ionescu, F., 1967, On the numerical computation of nearly-horizontal flows: Journal of Hydraulic Research, v. 5, no. 2, p. 97–117.

Abraham, Gerrit, 1988, Turbulence and mixing in stratified tidal flows, *in* Dronkers, J.J., and van Leussen, Wim, eds., Physical processes in estuaries: Berlin, Germany, Springer, p. 149–180.

Adams, C.E., and Weatherly, G.L., 1981, Suspended-sediment transport and benthic boundary-layer dynamics: Marine Geology, v. 42, p. 1–18.

Amein, M.M., and Fang, C.S., 1970, Implicit flood routing in natural channels: American Society of Civil Engineers, Journal of the Hydraulics Division, v. 96, no. 12, p. 2481–2500.

American Society of Civil Engineers, 1988, Turbulence modeling of surface water flow and transport—Part I, Prepared by the Task Committee on Turbulence Models in Hydraulic Computations: American Society of Civil Engineers, Journal of Hydraulic Engineering, v. 114, no. 9, p. 970–991.

Ames, W.F., 1977, Numerical methods for partial differential equations (2nd ed.): New York, Academic Press, 365 p.

Asselin, R., 1972, Frequency filters for time integrations: American Meteorological Society, Monthly Weather Review, v. 100, p. 487–490.

Axelsson, O., and Lindskog, G., 1986, On the eigenvalue distribution of a class of preconditioning methods: Numerical Mathematics, v. 48, p. 479–498.

Backhaus, J.O., 1983, A semi-implicit scheme for the shallow water equations for application to shelf sea modeling: Continental Shelf Research, v. 2, no. 4, p. 243–254.

Backhaus, J.O., 1985, A three-dimensional model for the simulation of shelf sea dynamics: Deutsche Hydrographische Zeitschrift [German Hydrographic Newspaper], v. 38, p. 165–187.

Bedford, K.W., Dingman, J.S., and Yeo, W.K., 1987, Preparation of estuary and marine model equations by generalized filtering methods, *in* Nihoul, J.C.J., and Jamart, B.M., eds., Three-dimensional models of marine and estuarine dynamics: Amsterdam, Netherlands, Elsevier, p. 113–125.

Beer, F.P., and Johnston, E.R., 1962, Vector mechanics for engineers—statics and dynamics: New York, McGraw-Hill, 781 p.

Benqué, J.P., Cunge, J.A., Feuillet, Jacques, Hauguel, Alain, and Holly, F.M., 1982, New method for tidal current computation: American Society of Civil Engineers, Journal of the Waterway, Port, Coastal, and Ocean Division, v. 108, no. 3, p. 396–417.

Berger, R.C., Martin, W.D., McAdory, R.T., and Schmidt, J.H., 1994, Galveston Bay 3D model study, channel deepening, circulation, and salinity results, Proceedings of the Third Estuarine and Coastal Modeling Conference: American Society of Civil Engineers, Oak Brook, Ill., September 8–10, 1993, p. 1–13.

Berger, R.C., McAdory, R.T., Schmidt, J.H., Martin, W.D., and Hauck, L.H., 1995, Houston–Galveston navigation channels, Texas project—Report 4, three-dimensional numerical modeling of hydrodynamics and salinity: U.S. Army Corps of Engineers Waterways Experiment Station, Vicksburg, Miss., Technical Report HL-92-7, 29 p., 425 plus.

Blake, R.A., 1991, The dependence of wind stress on wave height and wind speed: American Geophysical Union, Journal of Geophysical Research (Oceans), v. 96, no. C11, p. 20531–20545.

Bleck, Rainer, and Boudra, D.B., 1981, Initial testing of a numerical ocean circulation model using a hybrid (quasi-isopycnic) vertical coordinate: American Meteorological Society, Journal of Physical Oceanography, v. 11, no. 6, p. 755–770.

Bleck, Rainer, and Boudra, D.B., 1986, Wind-driven spin-up in eddy-resolving ocean models formulated in isopycnic and isobaric coordinates: American Geophysical Union, Journal of Geophysical Research (Oceans), v. 91, no. C6, p. 7,611–7,621.

Blumberg, A.F., 1977, Numerical model of estuarine circulation: American Society of Civil Engineers, Journal of the Hydraulics Division, v. 103, no. 3, p. 295–310.

Blumberg, A.F., 1986, Turbulent mixing processes in lakes, reservoirs, and impoundments; Chapter 4 in Gray, W.G., ed., Physics-based modeling of lakes, reservoirs, and impoundments: American Society of Civil Engineers, p. 79–104.

Blumberg, A.F., 1991, A primer for ECOM-si [Estuarine Coastal and Ocean Model-semi-implicit]: Hydrator, Inc., Mahwah, N.J., Prepared for the U.S. Geological Survey, 68 p.

Blumberg, A.F., and Galperin, Boris, 1990, On the summer circulation in New York Bight and contiguous estuarine waters, *in* Cheng, R.T., ed., Residual currents and long-term transport: New York, Springer, Coastal and Estuarine Studies, v. 38, p. 451–468.

Blumberg, A.F., and Goodrich, D.M., 1990, Modeling of wind induced destratification in Chesapeake Bay: Estuaries, v. 13, p. 1236–1249.

Blumberg, A.F., and Herring, H.J., 1987, Circulation modeling using orthogonal curvilinear coordinates, *in* Nihoul, J.C.J., and Jamart, B.M., eds., Three-dimensional models of marine and estuarine dynamics: Amsterdam, Netherlands, Elsevier, p. 55–88.

Blumberg, A.F., and Mellor, G.L., 1980, A coastal ocean numerical model, *in* Sündermann, Jürgen, and Holz, K.-P., eds., Lecture notes on coastal and estuarine studies—mathematical modelling of estuarine physics: Proceedings of an International Symposium held at the German Hydrographic Institute, Hamburg, August 24–26, 1978, Berlin, Germany, Springer, p. 203–219.

Blumberg, A.F., and Mellor, G.L., 1987, A description of a three-dimensional coastal ocean circulation model, *in* Heaps, N.S., ed., Three-dimensional coastal ocean models: American Geophysical Union, Washington, D.C., Coastal and Estuarine Sciences Monograph Series, v. 4, p. 1–16.

Blumberg, A.F., Signell, R.P., and Jenter, H.L., 1993, Modeling transport processes in the coastal ocean: Journal of Marine Environmental Engineering, v. 1, no. 1, p. 31–52.

Boericke, R.R., and Hall, D.W., 1974, Hydraulics and thermal dispersion in an irregular estuary: American Society of Civil Engineers, Journal of the Hydraulics Division, v. 100, no. 1, p. 85–102.

Boudra, D.B., Bleck, Rainer, and Schott, Friedrich, 1987, Study of transport fluctuations and meandering of the Florida current using an isopycnic coordinate numerical model, *in* Nihoul, J.C.J., and Jamart, B.M., eds., Three-dimensional models of marine and estuarine dynamics: Amsterdam, Netherlands, Elsevier, p. 149–168.

Boussinesq, Joseph, 1877, Essai sur la théorie des eaux courantes: Mémoires présentés par divers savants à l'Académie des Sciences, Paris, v. 23, no. 1, p. 1–680.

Boussinesq, Joseph, 1903, Théorie analytique de la chaleur, vol. 2: Paris, Gathier-Villars.

Bowden, K.F., 1977, Turbulent processes in estuaries, Chapter 5 *in* Studies in geophysics— estuaries, geophysics, and the environment: Washington, D.C., National Academy of Sciences, p. 46–56.

Bryan, Kirk, 1969, A numerical method for the study of the circulation of the world ocean: Journal of Computational Physics, v. 4, p. 347–376.

Burau, J.R., and Cheng, R.T., 1989, A vertically averaged spectral model for tidal circulation in estuaries—-Part 1. Model formulation: U.S. Geological Survey Water-Resources Investigations Report 88-4126, 31 p.

Butler, H.L., 1978, Coastal flood simulation in stretched coordinates, *in* Proceedings of the Sixteenth Coastal Engineering Conference: American Society of Civil Engineers, Hamburg, Germany, August 27–September 3, 1978, p. 1030–1048.

Butler, H.L., 1980, Evolution of a numerical model for simulating long-period wave behavior in ocean-estuarine systems, *in* Hamilton, Peter, and Macdonald, K.B., eds., Estuarine and wetland processes with emphasis on modeling: Marine Science, v. 11, New York, Plenum Press, p. 147–182.

Casulli, Vincenzo, 1990, Semi-implicit finite difference methods for the two-dimensional shallow water equations: Journal of Computational Physics, v. 86, p. 56–74.

Casulli, Vincenzo, and Cattani, Elena, 1994, Stability, accuracy and efficiency of a semi-implicit method for three-dimensional shallow water flow: Computers & Mathematics with Applications, v. 27, no. 4, p. 99–112.

Casulli, Vincenzo, and Cheng, R.T., 1990, Stability analysis of Eulerian-Lagrangian methods for the one-dimensional shallow-water equations: Applied Mathematical Modelling, v. 14, p.122–131.

Casulli, Vincenzo, and Cheng, R.T., 1992, Semi-implicit finite difference methods for three-dimensional shallow water flow: International Journal for Numerical Methods in Fluids, v. 15, p. 629–648.

Casulli, Vincenzo, and Stelling, G.S., 1996, Simulation of three-dimensional, non-hydrostatic free-surface flows for estuaries and coastal seas, *in* Spaulding, M.L., and Cheng, R.T., eds., Proceedings of the Fourth Estuarine and Coastal Modeling Conference: American Society of Civil Engineers, San Diego, Calif., October 26–29, 1995, p.1–12.

Chapman, R.S., Johnson, W.H., Vemulakonda, S.R., 1996, User's guide for the sigma stretched version of CH3D-WES—A three-dimensional numerical hydrodynamic, salinity, and temperature model: U.S. Army Corps of Engineers, Waterways Experiment Station, Technical report HL-96-21, 28 p. plus appendixes.

Cheng, R.T., and Casulli, Vincenzo, 1996, Modeling the periodic stratification and gravitational circulation in San Francisco Bay, California, 1996, *in* Spaulding, M.L., and Cheng, R.T., eds., Proceedings of the Fourth Estuarine and Coastal Modeling Conference: American Society of Civil Engineers, San Diego, Calif., October 26–29, 1995, p. 240–254.

Cheng, R.T., Casulli, Vincenzo, and Gartner, J.W., 1993, Tidal, residual, inter-tidal mud-flat (TRIM) model with applications to San Francisco Bay: Estuarine, Coastal and Shelf Science, v. 36, p. 235–280.

Cheng, R.T., Powell, T.M. and Dillon, T.M., 1976, Numerical models of wind-driven circulation in lakes: Applied Mathematical Modelling, v. 1, p. 141–159.

Cheng, R.T., and Smith, P.E., 1990, A survey of three-dimensional numerical estuarine models, *in* Spaulding, M.L., ed., Proceedings of the First Estuarine and Coastal Modeling Conference: American Society of Civil Engineers, Newport, R. I., November 15–17, 1989, p. 1–15.

Chu, W.-S., Liou, J.-Y, and Flenniken, K.D., 1989, Numerical modeling of tide and current in Central Puget Sound—Comparison of a three-dimensional and a depth-averaged model: American Geophysical Union, Water Resources Research, v. 25, no. 4, p. 721–734.

Crank, J., and Nicolson, P., 1947, A practical method for numerical evaluation of solutions of partial differential equations of the heat-conduction type: Proceedings of the Cambridge Philosophical Society, v. 43, p. 50–67.

Cunge, J.A., Holly, F.M., and Verwey, Adrianus, 1980, Practical aspects of computational river hydraulics: London, Great Britain, Pitman Publishing, 420 p.

Currie, I.G., 1974, Fundamental mechanics of fluids: New York, McGraw-Hill, 441 p.

Cushman-Roisin, Benoit, 1994, Layered models, Chapter 12 *in* Introduction to geophysical fluid dynamics: Englewood Cliffs, N.J., Prentice Hall, p. 169–179.

Davies, A.M., 1980, Application of the Galerkin Method to the formulation of a three-dimensional nonlinear hydrodynamic numerical sea model: Applied Mathematical Modelling, v. 4, p. 245–256.

Davies, A.M., 1985, Application of the Dufort-Frankel and Saul'ev methods with time splitting to the formulation of a three dimensional hydrodynamic sea model: International Journal for Numerical Methods in Fluids, v. 5, no. 5, p. 405–425.

Davies, A.M., 1987, Spectral models in continental shelf sea oceanography, *in* Heaps, N.S., ed., Three-dimensional coastal ocean models: American Geophysical Union, Washington, D.C., Coastal and Estuarine Sciences Monograph Series, v. 4, p. 71–106.

Davies, A.M., 1991, On the finite difference and modal methods for computing tidal and wind wave current profiles: International Journal for Numerical Methods in Fluids, v. 12, no. 2, p. 101–124.

Davies, A.M., Aldridge, John, and Lawrence, John, 1993, Formulation and application of a three dimensional shallow sea model including wave-current interaction, *in* Wang, S.S.Y., ed., Proceedings of the First International Conference on Hydro-Science and Engineering: v. 1, pt. B, Washington, D.C., June 7–11, 1993, p. 1618–1625.

Davies, A.M., Jones, J.E., and Xing, J., 1997a, Review of recent developments in tidal hydrodynamic modeling. I—Spectral models: American Society of Civil Engineers, Journal of Hydraulic Engineering, v. 123, no. 4, p. 278–292.

Davies, A.M., Jones, J.E., and Xing, J., 1997b, Review of recent developments in tidal hydrodynamic modeling. II—Turbulence energy models: American Society of Civil Engineers, Journal of Hydraulic Engineering, v. 123, no. 4, p. 293–302.

Davies, A.M., and Lawrence, John, 1994, Modeling the non-linear interaction of wind and tide—its influence on current profiles: International Journal for Numerical Methods in Fluids, v. 18, p 163–188.

Davies, A.M., Luyten, P.J., Deleersnijder, Eric, 1995, Turbulence energy models in shallow sea oceanography, *in* Lynch, D.R., and Davies, A.M., eds., Quantitative skill assessment for coastal ocean models: American Geophysical Union, Coastal and Estuarine Studies, Series no. 47, p. 97–123.

Davies, A.M., and Stephens, C.V., 1983, Comparison of the finite difference and Galerkin methods as applied to the solution of the hydrodynamic equations: Applied Mathematical Modelling, v. 7, p. 226–240.

de Goede, E.D., 1991, A time-splitting method for the three-dimensional shallow water equations: International Journal for Numerical Methods in Fluids, v. 13, no. 4, p. 519–534.

de Goede, E.D., 1992, Numerical methods for the three-dimensional shallow water equations on supercomputers: Ph.D. Thesis, University of Amsterdam, 125 p.

Deleersnijder, Eric, and Beckers, J.M., 1992, On the use of the σ -coordinate system in regions of large bathymetric variations: Journal of Marine Systems, v. 3, no. 4, p. 381–390.

Delft Hydraulics Laboratory, 1974, Momentum and mass transfer in stratified flows: Delft, Netherlands, Delft Hydraulics Laboratory, Report on literature study R880 [variously paged].

DeLong, L.L., 1993, A numerical model for learning concepts of streamflow simulation, *in* Shen, H.W., Su, S.T., and Wen, Feng, eds., Proceedings of the 1993 Conference on Hydraulic Engineering: American Society of Civil Engineers, San Francisco, Calif., July 25–30, 1993, v. 2, p. 1586–1591.

Dukowicz, J.K., and Smith, R.D., 1994, Implicit free-surface method for the Bryan-Cox-Semtner ocean model: American Geophysical Union, Journal of Geophysical Research (Oceans), v. 99, no. C4, p. 7991–8014.

Durance, J.A., 1976, A three dimensional numerical model of tidal motion in a shallow sea: Mémoires de al Société Royale des Sciences de Liège, Series 6, v. 10, p. 125–132.

Duwe, K.C., Hewer, R.R., and Backhaus, J.O., 1983, Results of a semi-implicit two-step method for the simulation of markedly nonlinear flow in coastal seas: Continental Shelf Research, v. 2, no. 4, p. 255–274.

Eiseman, P.R., 1985, Grid generation for fluid mechanics computations: Annual Review of Fluid Mechanics, v. 17, p. 487–522.

Evces, C.R., and Raney, D.C., 1990, Re-examination of the Coriolis effect on the two-dimensional depth-averaged model, *in* Spaulding, M.L., ed., Proceedings of the First Estuarine and Coastal Modeling Conference: American Society of Civil Engineers, Newport, R. I., November 15–17, 1989, p. 258–267.

Fischer, H.B., List, E.J., Koh, R.C.Y., Imberger, Jorg, and Brooks, N.H., 1979, Mixing in inland and coastal waters: New York, Academic Press, 483 p.

Flokstra, C., 1976, Generation of two-dimensional horizontal secondary currents: Delft, Netherlands, Delft Hydraulics Laboratory, Report S 163, pt. II.

Forristall, G.Z., 1974, Three-dimensional structure of storm-generated currents: American Geophysical Union, Journal of Geophysical Research (Oceans), v. 79, p. 2721–2729.

Fread, D.L., 1974, Numerical properties of implicit four-point finite difference equations of unsteady flow: National Oceanic and Atmospheric Administration, National Weather Service, Office of Hydrology, NOAA Technical Memorandum NWS HYDRO-18, 38 p.

Fread, D.L., 1978, Theoretical development of implicit dynamic routing model (revised): National Oceanic and Atmospheric Administration, National Weather Service, Report for Dynamic Routing Seminar, Lower Mississippi River Forecast Center, Slidell, La., December 13–17, 1976 [variously paged].

Freeman, N.G., Hale, A.M., and Danard, M.B., 1972, A modified sigma equations' approach to the numerical modelling of Great Lakes hydrodynamics: American Geophysical Union, Journal of Geophysical Research (Oceans), v. 77, no. C6, p. 1050–1060.

Galperin, Boris, and Mellor, G.L., 1990a, A time-dependent, three-dimensional model of the Delaware Bay and River system. Part 1—Description of the model and tidal analysis: Estuarine, Coastal and Shelf Science, v. 31, no. 3, p. 231–253.

Galperin, Boris, and Mellor, G.L., 1990b, A time-dependent three-dimensional model of the Delaware Bay and River system. Part 2—Three-dimensional flow fields and residual circulation: Estuarine, Coastal, and Shelf Science, v. 31, no. 3, p. 255–281.

Gerdes, Rüdiger, 1993, A primitive equation ocean circulation model using a general vertical coordinate transformation—1. Description and testing of the model: American Geophysical Union, Journal of Geophysical Research (Oceans), v. 98, no. C8, p. 14683−14701.

Golub, G.H. and Van Loan, C.F., 1989, Matrix computations (2nd ed.): Baltimore, Md., Johns Hopkins University Press, 642 p.

Grant, W.D., and Madsen, O.S., 1979, Combined wave and current interaction with a rough bottom: American Geophysical Union, Journal of Geophysical Research (Oceans), v. 98, no. C4, p. 1797−1808.

Grant, W.D., and Madsen, O.S., 1982, Movable bed roughness in unsteady oscillatory flow: American Geophysical Union, Journal of Geophysical Research (Oceans), v. 87, no. C1, p. 469–481.

Grant, W.D., and Madsen, O.S., 1986, The continental shelf bottom boundary layer: Annual Review of Fluid Mechanics, v. 18, p. 265−305.

Gray, W.G., and Lynch, D.R., 1977, Time-stepping schemes for finite element tidal model computations: Advances in Water Resources, v. 1, no. 2, p. 83–95.

Gross, T.F., and Nowell, A.R.M., 1983, Mean flow and turbulence scaling in a tidal boundary layer: Continental Shelf Research, v. 2, no. 2/3, p. 109–126.

Haidvogel, D.B., Wilkin, J.L., Young, R., 1991, A semi-spectral primitive equation ocean circulation model using vertical sigma and orthogonal curvilinear horizontal coordinates: Journal of Computational Physics, v. 94, p. 151−185.

Haltiner, G.J., and Williams, R.T., 1980, Numerical prediction and dynamic meteorology (2nd ed.): New York, Wiley, 477 p.

Hamrick, J.M., 1992, A three-dimensional environmental fluid dynamics computer code—theoretical and computational aspects: The College of William and Mary, Virginia Institute of Marine Science, Special report no. 317 in Applied Marine Science and Ocean Engineering, Glouster Point, Va., 63 p.

Haney, R.L., 1991, On the pressure gradient force over steep topography in sigma coordinate ocean models: American Meteorological Society, Journal of Physical Oceanography, v. 21, no. 4, p. 610–619.

Hansen, D.V., and Rattray, Maurice, 1965, Gravitational circulation in straits and estuaries: Journal of Marine Research, v. 23, no. 2, p. 104–122.

Haq, A., Lick, Wilbert, Sheng, Y.P., 1974, The time-dependent flow in large lakes with application to Lake Erie: Case Western Reserve University, Department of Earth Science Technical Report, 212 p.

Heaps, N.S., 1972, On the numerical solution of the three-dimensional hydrodynamical equations for tides and storm surges: Mémoires de al Société Royale des Sciences de Liège, Series 6, v. 2, p. 143−180.

Heaps, N.S., 1974, Development of a three-dimensional numerical model of the Irish Sea: Rapports et Proces-verbaux des Réunion du Conseil International pour l'Exploration de la Mer (Reports and Verbal Processes of the Meeting of the International Council for the Exploration of the Sea), v. 167, p. 147−162.

Heaps, N.S., 1980, Spectral models for the numerical solution of the three-dimensional hydrodynamic equations for tides and surges, *in* Sündermann, Jürgen, and Holz, K.-P., eds., Lecture notes on coastal and estuarine studies—mathematical modelling of estuarine physics: Berlin, Germany, Springer, p. 75–90.

Henderson-Sellers, B., 1982, A simple formula for vertical eddy diffusion coefficients under conditions of nonneutral stability: American Geophysical Union, Journal of Geophysical Research (Oceans), v. 87, no. C8, p. 5860–5864.

Hess, K.W., 1985, Assessment model for estuarine circulation and salinity: National Oceanic and Atmospheric Administration, Technical Memorandum NESDIS AISC 3, 39 p.

Hess, K.W., 1994, Tampa Bay oceanography project—Development and application of the numerical circulation model: National Oceanic and Atmospheric Administration Technical Report NOS OES 005, 90 p.

Hill, M.C., 1990, Solving groundwater flow problems by conjugate-gradient methods and the strongly implicit procedure: American Geophysical Union, Water Resources Research, v. 26, no. 9, p. 1961–1969.

Hinze, J.O., 1975, Turbulence (2nd ed.): New York, McGraw-Hill, 790 p.

Hoffmann, K.A., 1989, Grid Generation, Chapter 8 *in* Computational fluid dynamics for engineers: Austin, Tex., Engineering Education System, p. 243–305.

Huang, J.C.K., and Sloss, P.W., 1981, Simulation and verification of Lake Ontario's mean state: American Meteorological Society, Journal of Physical Oceanography, v. 11, p. 1548–1566.

Huang, Wenrui, and Spaulding, M.L., 1995, 3D Model of estuarine circulation and water quality induced by surface discharges: American Society of Civil Engineers, Journal of Hydraulic Engineering, v. 121, no. 4, p. 300–311.

Janjic, Z.I., 1977, Pressure gradient force and advection scheme used for forecasting with steep and small scale topography: Contributions to Atmospheric Physics, v. 50, p. 186–199.

Jelesnianski, C.P., 1970, Bottom stress time history in linearized equations of motion for storm surges: American Meteorological Society, Monthly Weather Review, v. 98, p.462–478.

Jin, X.-Y., 1993, Quasi-three-dimensional numerical modeling of flow and dispersion in shallow water: Delft University of Technology, Department of Civil Engineering, Communication on Hydraulic and Geotechnical Engineering, Report 93-3, 174 p.

Johnson, B.H., 1982, Numerical modeling of estuarine hydrodynamics on a boundary fitted coordinate system, *in* Thompson, J.F., ed., Numerical grid generation— proceedings of a symposium on the numerical generation of curvilinear coordinate systems and their use in the numerical solution of partial differential equations: New York, Elsevier, p. 409–436.

Johnson, B.H., Heath, R.E., Hsieh, B.B., Kim, K.W., and Butler, H.L., 1991, User's guide for a three-dimensional numerical hydrodynamic, salinity, and temperature model of Chesapeake Bay: U.S. Army Engineer Waterways Experiment Station, Technical report no. HL-91-20, 41 p. plus appendixes.

Johnson, B.H., Kim, K.W., Heath, R.E., Hsieh, B.B., and Butler, H.L., 1993, Validation of three-dimensional hydrodynamic model of Chesapeake Bay: American Society of Civil Engineers, Journal of Hydraulic Engineering, v. 119, no. 1, p. 2–20.

Johnson, B.H., Kim, K.W., Sheng, Y.P., and Heath, R.E., 1989, Development of a three-dimensional hydrodynamic model of Chesapeake Bay, *in* Spaulding, M.L., ed., Proceedings of the Estuarine and Coastal Modeling Conference: American Society of Civil Engineers, Newport, R.I., November 15–17, 1989, p. 162–171.

Kawahara, M., Kobayashi, M., and Nakata, K., 1982, A three-dimensional multiple level finite element method considering variable water density, *in* Gallagher, R.H., Norrie, D.H., Oden, J.T., and Zienkiewicz, O.C., eds., Finite elements in fluids: Chichester, Wiley, v. 4, p. 129–156.

Keulegan, G.H., 1938, Laws of turbulent flow in open channels: National Bureau of Standards, Journal of Research, v. 121, no. 6, p. 707–741.

Killworth, P.D., Stainforth, David, Webb, D.J., and Paterson, S.M., 1991, The development of a free-surface Bryan-Cox-Semtner ocean model: American Meteorological Society, Journal of Physical Oceanography, v. 21, no. 9, p. 1333–1348.

Kincaid, D.R., Oppe, T.C., and Joubert, W.D., 1989, An introduction to the NSPCG software package: International Journal for Numerical Methods in Engineering, v. 27, no. 3, p. 589–608.

King, I.P., 1985, Strategies for finite element modeling of three dimensional hydrodynamic systems: Advances in Water Resources, v. 8, p. 69–76.

Kinnmark, I.P.E., 1986, The shallow water wave equations—formulation, analysis and application, *in* Brebbia, C.A., and Orszag, S.A., eds. Lecture notes in engineering: Berlin, Germany, Springer, 187 p.

Knudsen, M.H.C., 1901, Hydrographische Tabellen [Hydrographic tables]: Copenhagen, G.E.C. Gad, 63 p.

Koutitas, Christopher, and O'Connor, Brian, 1982, Finite element fractional steps solution of the 3-D coastal circulation model: Advances in Water Resources, v. 5, p. 167–170.

Krauss, W., and Wubber, C., 1982, A semi-spectral model on the B-plane: Deutsche Hydrographische Zeitschrift [German Hydrographic Newspaper], v. 35, p. 187–201.

Kuiper, L.K., 1981, A comparison of the incomplete Cholesky-conjugate gradient method with the strongly implicit method as applied to the solution of two-dimensional groundwater flow equations: American Geophysical Union, Water Resources Research, v. 17, no. 4, p. 1082–1086.

Kuiper, L.K., 1987, A comparison of iterative methods as applied to the solution of the nonlinear three-dimensional groundwater flow equation: Society of Industrial and Applied Mathematics, Journal of Scientific and Statistical Computing, v. 8, no. 4, p. 521–528.

Kwizak, Michael, and Robert, A.J., 1971, A semi-implicit scheme for grid point atmospheric models of the primitive equations: American Meteorological Society, Monthly Weather Review, v. 99, no. 1, p. 32–36.

Laevastu, Taivo, 1975, Multilayer hydrodynamical-numerical models, *in* Proceedings of the Symposium on Modeling Techniques—Volume II: American Society of Civil Engineers, San Francisco, Calif., September 3–5, 1975, p. 1010–1025.

Lancaster, Peter and Tismenetsky, Miron, 1985, The theory of matrices—with applications (2nd ed.): Orlando, Fla., Academic Press, 570 p.

Lardner, R.W., and Smoczynski, P., 1990, A vertical/horizontal splitting algorithm for three-dimensional tidal and storm surge computations: Proceedings of the Royal Society of London Series A, Mathematical and Physical Sciences, v. 430, no. 1879, p. 263–283.

Lardner, R.W., and Song, Y., 1992, A comparison of spatial grids for numerical modelling of flows in near-coastal seas: International Journal for Numerical Methods in Fluids, v. 14, no. 1, p. 109–124.

Launder, B.E., and Spalding, D.B., 1972, Mathematical models of turbulence: New York, Academic Press, 169 p.

Leendertse, J.J., 1967, Aspects of a computational model for long-period water-wave propagation: Rand Corporation, Santa Monica, Calif., Memorandum RM-5294-PR, 165 p.

Leendertse, J.J., 1987, Aspects of SIMSYS2D—A system for two-dimensional flow computation: Rand Corporation, Santa Monica, Calif., Report R-3572-USGS, Prepared for the U.S. Geological Survey, 80 p.

Leendertse, J.J., 1989, A new approach to three-dimensional free-surface flow modeling: Rand Corporation, Santa Monica, Calif., Memorandum R-3712-NETH/RC, Prepared for The Netherlands Rijkswaterstaat, 51 p.

Leendertse, J.J., Alexander, R.C., and Liu, S.K., 1973, A three-dimensional model for estuaries and coastal seas—Volume I, principles of computation: Rand Corporation, Santa Monica, Calif., Report R-1417-OWRR, 57 p.

Leendertse, J.J., and Liu, S.K., 1975, A three-dimensional model for estuaries and coastal seas—Volume II, aspects of computation: Rand Corporation, Santa Monica Calif., Report R-1764-OWRT, 123 p.

Leendertse, J.J., and Liu, S.K., 1977, A three-dimensional model for estuaries and coastal seas—Volume IV, turbulent energy computation: Rand Corporation, Santa Monica, Calif., Report R-2187-OWRT, 59 p.

Leith, C.E., 1968, Diffusion approximations for two-dimensional turbulence: Physics of Fluids, v. 11, no. 3, p. 671–673.

Le Provost, C., and Poncet, A., 1978, Finite element method for spectral modeling of tides: International Journal for Numerical Methods in Engineering, v. 12, p. 853–871.

Li, Y.S., and Zhan, J.M., 1993, An efficient three-dimensional semi-implicit finite element scheme for simulation of free surface flows: International Journal for Numerical Methods in Fluids, v. 16, no. 3, p. 187–198.

Liggett, J.A., 1969, Unsteady circulation in shallow, homogeneous lakes: Proceedings of the American Society of Civil Engineers, Journal of the Hydraulics Division, v. 95, no. HY4, p. 1273–1288.

Liggett, J.A., 1975, Basic equations of unsteady flow, chap. 2 *of* Mahmood, Kalid and Yevjevich, Vujica, eds., Unsteady flow in open channels: Fort Collins, Colo., Water Resources Publications, p. 29–62.

Lilly, D.K., 1965, On the computational stability of numerical solutions of time-dependent non-linear geophysical fluid dynamics problems: American Meteorological Society, Monthly Weather Review, v. 93, no. 1, p. 11–26.

Liu, S.K., and Leendertse, J.J., 1978, Multidimensional numerical modeling of estuaries and coastal seas: Advances in Hydroscience, v. 11, p. 95–164.

Luettich, R.A., Shending, Hu, and Westerink, J.J, 1994, Development of the direct stress solution technique for three-dimensional hydrodynamic models using finite elements: International Journal for Numerical Methods in Fluids, v. 19, p. 295–319.

Lynch, D.R., 1986, Basic hydrodynamic equations for lakes, chap. 2 *of* Gray, W.G., ed., Physics-based modeling of lakes, reservoirs, and impoundments: American Society of Civil Engineers, p. 17–53.

Lynch, D.R., and Werner, F.E., 1987, Three-dimensional hydrodynamics on finite elements. Part I—linearized harmonic model: International Journal for Numerical Methods in Fluids, v. 7, p. 871–909.

Lynch, D.R., and Werner, F.E., 1991, Three-dimensional hydrodynamics on finite elements. Part II—nonlinear time-stepping model: International Journal for Numerical Methods in Fluids, v. 12, P. 507–533.

Lynch, D.R., and Gray, W.G., 1979, A wave equation model for finite element tidal computations: Computers and Fluids, v. 7, p. 207–228.

Madala, R.V., and Piacsek, S.A., 1977 A semi-implicit numerical model for baroclinic oceans: Journal of Computational Physics, v. 23, no. 2, p. 167–178.

Meijerink, J.A., and van der Vorst, H.A., 1977, An iterative solution method for linear systems of which the coefficient matrix is a symmetric M-Matrix: Mathematics of Computation, v. 31, no. 137, p. 148–162.

Mellor, G.L., and Blumberg, A.F., 1985, Modeling vertical and horizontal diffusivities with the sigma coordinate system: American Meteorological Society, Monthly Weather Review, v. 113, no. 8, p. 1379–1383.

Mellor, G.L., and Ezer, Tal, 1995, Sea level variations induced by heating and cooling—an evaluation of the Boussinesq approximation in ocean models: American Geophysical Union, Journal of Geophysical Research (Oceans), v. 100, no. C10, p. 20,565–20,577.

Mesinger, F., and Arakawa, A., 1976, Numerical methods used in atmospheric models, I: World Meteorological Organization, Geneva, Switzerland, GARP Publication Series, no. 17, 64 p.

Meyer, P.D., Valocchi, A.J., Ashby, S.F., and Saylor, P.E., 1989, A numerical investigation of the conjugate gradient method as applied to three-dimensional groundwater flow problems in randomly heterogeneous porous media: American Geophysical Union, Water Resources Research, v. 25, no. 6, p. 1440–1446.

Millero, F.J., and Poisson, A., 1981, International one-atmosphere equation of state of seawater: Deep-Sea Research, v. 28A, p. 625–629.

Monin, A.S., and Yaglom, A.M., 1971, Statistical fluid mechanics—mechanics of turbulence, volume 1 (English ed.): Cambridge, Mass., The MIT Press, 769 p.

Monin, A.S., and Yaglom, A.M., 1975, Statistical fluid mechanics—mechanics of turbulence, volume 2 (English ed.): Cambridge, Mass., The MIT Press, 874 p.

Muin, Muslim, and Spaulding, M.L., 1996, Two-dimensional boundary-fitted circulation model in spherical coordinates: American Society of Civil Engineers, Journal of Hydraulic Engineering, v. 122, no. 9, p. 512–521.

Muin, Muslim, and Spaulding, M.L., 1997a, Three-dimensional boundary-fitted circulation model: American Society of Civil Engineers, Journal of Hydraulic Engineering, v. 123, no. 1, p. 2–12.

Muin, Muslim, and Spaulding, M.L., 1997b, Application of three-dimensional boundary-fitted circulation model to Providence River: American Society of Civil Engineers, Journal of Hydraulic Engineering, v. 123, no. 1, p. 13–20.

Munk, W.H., and Anderson, E.R., 1948, Notes on the theory of the thermocline: Journal of Marine Research, v. 7, p. 276–295.

Neumann, Gerhard, and Pierson, W.J., 1966, Principles of physical oceanography: Englewood Cliffs, N.J., Prentice-Hall, 545 p.

Nezu, Iehisa, and Rodi, Wolfgang, 1986, Open-channel flow measurements with a laser Doppler anemometer: American Society of Civil Engineers, Journal of Hydraulic Engineering, v. 112, no, 5, p. 335–354.

Nihoul, J.C.J., 1977, Three-dimensional model of tides and storm surges in a shallow well-mixed continental sea: Dynamics of Atmospheres and Oceans, v. 2, p. 29–47.

Nihoul, J.C.J., and Ronday, F.C., 1975, The influence of the “tidal stress” on the residual circulation—Application to the Southern Bight of the North Sea: Tellus, v. 27, no. 5, p. 484–485.

Noye, John, and Stevens, Malcolm, 1987, A three-dimensional model of tidal propagation using transformations and variable grids, *in* Heaps, N.S., ed., Three-dimensional coastal ocean models: Washington, D.C., American Geophysical Union, Coastal and Estuarine Sciences Monograph Series, v. 4, p. 41–69.

Nunes Vas, R.A., and Simpson, J.H., 1994, Turbulence closure modeling of estuarine stratification: American Geophysical Union, Journal of Geophysical Research (Oceans), v. 99, no. C8, p. 16143–16160.

O’Brien, G.G., Hyman, M.A., and Kaplan, Sidney, 1950, A study of the numerical solution of partial differential equations: Journal of Mathematics and Physics, v. 29, no. 4, p. 223–251.

Oey, L.Y., Mellor, G.L., and Hires, R.I., 1985a, A three-dimensional simulation of the Hudson-Raritan Estuary. Part I—Description of the model and model simulations: American Meteorological Society, Journal of Physical Oceanography, v. 15, no. 12, p. 1676–1692.

Oey, L.Y., Mellor, G.L., and Hires, R.I., 1985b, A three-dimensional simulation of the Hudson-Raritan Estuary. Part II—Comparison with observation: American Meteorological Society, Journal of Physical Oceanography, v. 15, no. 12, p. 1693–1709.

Oey, L.Y., Mellor, G.L., and Hires, R.I., 1985c, A three-dimensional simulation of the Hudson-Raritan Estuary. Part III— Salt flux analyses: American Meteorological Society, Journal of Physical Oceanography, v. 15, no. 12, p 1711–1720.

Officer, C.B., 1976, Physical oceanography of estuaries (and associated coastal waters): New York, Wiley-Interscience, 465 p.

Officer, C.B., 1977, Longitudinal circulation and mixing relations in estuaries, chap. 1 *of* Studies in geophysics—estuaries, geophysics, and the environment: Washington, D.C., National Academy of Sciences, p. 13–21.

Oppe, T.C., Joubert, W.D., and Kincaid, D.R., 1988, NSPCG user's guide version 1.0—A package for solving large sparse linear systems by various iterative methods: University of Texas at Austin, Center for Numerical Analysis, Report no. CNA-216, 82 p.

Owen, A., 1980, A three-dimensional model of the Bristol Channel: American Meteorological Society, Journal of Physical Oceanography, v. 10, no. 8, p. 1290–1302.

Pearson, C.E., and Winter, D.F., 1977, On the calculation of tidal currents in homogeneous estuaries: American Meteorological Society, Journal of Physical Oceanography, v. 7, p. 520–531.

Phillips, N.A., 1957, A coordinate system having some special advantages for numerical forecasting: Journal of Meteorology, v. 14, no. 2, p. 184–185.

Phillips, N.A., 1959, An example of non-linear computational stability, *in* Bolin, B., ed., The atmosphere and the sea in motion: Rossby Memorial Volume, New York, Rockefeller Institute Press, p. 501–504.

Ponce, V.M., and Yabusaki, S.B., 1980, Mathematical modeling of circulation in two-dimensional plane flow: Civil Engineering Department, Engineering Research Center, Colorado State University, Fort Collins, Report CER79-80VMP-SBY59, 289 p.

Ponce, V.M., and Yabusaki, S.B., 1981, Modeling circulation in depth-averaged flow: American Society of Civil Engineers, Journal of the Hydraulics Division, v. 107, no, HY11, p. 1501–1518.

Pond, Stephen, and Pickard, G.L., 1986, Introductory dynamical oceanography (2nd ed., reprinted with corrections): Oxford, Pergamon, 329 p.

Prandtl, Ludwig, 1925, Bericht über Untersuchungen zur ausgebildeten Turbulenz [Report about investigations on fully developed turbulence]: Zeitschrift für Angewandte Mathematik und Mechanik [Journal for Applied Mathematics and Mechanics], v. 5, p. 136–139.

Preissmann, Alexandre, 1961, Propagation des intumescences dans les canaux et rivières [Propagation of translatory waves in channels and rivers], *in* Proc. 1st Congres de l'Assoc. Française de Calcul [Proceedings 1st Congress of the French Association for Computation] Grenoble, France, p. 433–442.

Pritchard, D.W., 1956, The dynamic structure of a coastal plain estuary: Journal of Marine Research, v. 15, no. 1, p. 33–42.

Pritchard, D.W., 1971a, Three-dimensional models, *in* Ward, G.H., Jr., and Espey, W.H., Jr., eds., Estuarine modeling—An assessment, Chapter II—hydrodynamic models: Tracor, Inc., Austin, Tex. [Available from National Technical Information Service, Springfield, VA 22161 as NTIS Report PB-206 807, p. 5–21.]

Pritchard, D.W., 1971b, Two-dimensional models, *in* Ward, G.H., Jr., and Espey, W.H., Jr., eds., Estuarine modeling—An assessment, Chapter II—hydrodynamic models: Tracor, Inc., Austin, Tex. [Available from National Technical Information Service, Springfield, VA 22161 as NTIS Report PB-206 807, p. 22–33.]

Reid, R.O., Vastano, A.C., Whitaker, R.E., and Wanstrath, J.J., 1977, Experiments in storm surge simulation, *in* Goldberg, E.D., McCave, I.N., O'Brien, J.J., and Steele, J.H., eds., The Sea: New York, Wiley, v. 6, p. 145–168.

Reynolds, Osborne, 1894, On the dynamical theory of incompressible viscous fluids and the determination of the criterion: Philosophical Transactions of the Royal Society of London, Series A, no. 186, p. 123–161.

Reynolds, W.C., 1976, Computation of turbulent flows: Annual Review of Fluid Mechanics, v. 8, p. 183–208.

Rodi, Wolfgang, 1980a, Turbulence models and their applications in hydraulics—A state of the art review: Delft, Netherlands, International Association for Hydraulic Research, 104 p.

Rodi, Wolfgang, 1980b, *in* Sundermann, Jurgen, and Holz, K.-P., eds., Lecture notes on coastal and estuarine studies—mathematical modelling of estuarine physics: Proceedings of an International Symposium held at the German Hydrographic Institute, Hamburg, August 24–26, 1978, Berlin, Germany, Springer, p. 14–26.

Rodi, Wolfgang, 1987, Examples of calculation methods for flow and mixing in stratified fluids: American Geophysical Union, Journal of Geophysical Research (Oceans), v. 92, no. C5, p. 5305–5328.

Sabersky, R.H., Acosta, A.J., and Hauptmann, E. G., 1971, Fluid flow—A first course in fluid mechanics (2nd ed.): New York, Macmillan, 519 p.

Sayre, W.W., 1975, Dispersion of mass in open channel flow: Hydrology Papers, Colorado State University, Fort Collins, no. 75, 73 p.

Schaffranek, R.W., Baltzer, R.A., and Goldberg, D.E., 1981, A model for simulation of flow in singular and interconnected channels: U.S. Geological Survey, Techniques of Water Resources Investigations, book 7, chap. C3, 110 p.

Semtner, A.J., 1995, Modeling ocean circulation: Science, v. 269, p. 1379–1385.

Sen Gupta, S., Miller, H.P., and Lee, S.S., 1981, Effect of open boundary condition on numerical simulation of three-dimensional hydrothermal behavior of Biscayne Bay, Florida: International Journal for Numerical Methods in Fluids, v. 1, p. 145–169.

Sheng, Y.P., 1983, Mathematical modeling of three-dimensional coastal currents and sediment dispersion—model development and applications: U.S. Army Engineer Waterways Experiment Station, Technical report no. CERC-83-2, 288 p.

Sheng, Y.P., 1986a, Numerical modeling of coastal and estuarine processes using boundary-fitted grids, *in* Wang, S.S.Y., Shen, H.W., and Ding, L.Z., eds., Proceedings of the Third International Symposium on River Sedimentation: University of Mississippi, Jackson, Miss., March 31–April 4, 1986, p. 1426–1442.

Sheng, Y.P., 1986b, Finite-difference models for hydrodynamics of lakes and shallow seas, chap. 6 *of* Gray, W.G., ed., Physics-based modeling of lakes, reservoirs, and impoundments: American Society of Civil Engineers, p. 146–228.

Sheng, Y.P., Lick, Wilbert, Gedney, R.T., and Molls, F.B., 1978, Numerical computation of three-dimensional circulation in Lake Erie—A comparison of a free-surface model and a rigid-lid model: American Meteorological Society, Journal of Physical Oceanography, v. 8, p. 713–727.

Shubinski, R.P., and Walton, Raymond, 1982, Chesapeake Bay modeling: Proceedings of the First National U.S. Army Corps of Engineers-sponsored seminar on two-dimensional flow modeling, Hydrologic Engineering Center, Davis, Calif., July 7–9, 1981, p. 241–252.

Signell, R.P., Beardsley, R.C., Graber, H.C., and Capotondi, A., 1990, Effect of wave-current interaction on wind-driven circulation in narrow, shallow embayments: American Geophysical Union, Journal of Geophysical Research (Oceans), v. 95, no. C6, p. 9671–9678.

Signell, R.P., and Butman, B., 1992, Modeling tidal exchange and dispersion in Boston Harbor: American Geophysical Union, Journal of Geophysical Research (Oceans), v. 97, no. C10, p. 15591–15606.

Simons, T.J., 1973, Development of three-dimensional numerical models of the Great Lakes: Canada Centre of Inland Waters, Science Series report no. 12, Burlington, Ontario, 26 p.

Simons, T.J., 1974, Verification of numerical models of Lake Ontario—Part I. Circulation in spring and early summer: American Meteorological Society, Journal of Physical Oceanography, v. 4, no. 4, p. 507–523.

Simons, T.J., 1980, Circulation models of lake and inland seas: Canadian Bulletin of Fisheries and Aquatic Sciences, no. 203, 146 p.

Smagorinsky, J., Manabe, S., Holloway, J.L., 1965, Numerical results from a nine-point general circulation model of the atmosphere: Monthly Weather Review, v. 93, p. 727–768.

Smith, P.E., and Cheng, R.T., 1990, Recent progress on hydrodynamic modeling of San Francisco Bay, California, *in* Spaulding, M.L., ed., Proceedings of the First Estuarine and Coastal Modeling Conference: American Society of Civil Engineers, Newport, R. I., November 15–17, 1989, p. 502–510.

Smith, P.E., Cheng, R.T., Burau, J.R., and Simpson, M.R., 1991, Gravitational circulation in a tidal strait, Proceedings of the 1991 National Conference on Hydraulic Engineering: American Society of Civil Engineers, Nashville, Tenn., July 29–August 2, 1991, p. 429–434.

Smith, P.E., and Larock, B.E., 1993, A finite-difference model for 3-D flow in bays and estuaries, Proceedings of the 1993 National Conference on Hydraulic Engineering: American Society of Civil Engineers, San Francisco, Calif. July 25–30, 1993, p. 2116–2122.

Smith, P.E., Oltmann, R.N., and Smith, L.H., 1995, Summary report on the interagency hydrodynamic study of San Francisco Bay–Delta Estuary, California: Interagency Ecological Program for the Sacramento–San Joaquin Estuary, Technical Report no. HYDRO-IATR/95-45, California Department of Water Resources, Sacramento, Calif., 72 p.

Snyder, R.L., Sidjabat, M., and Filloux, J.H., 1979, A study of tides, set-up, and bottom friction in a shallow semi-enclosed basin. Part II—tidal model and comparisons with data: American Meteorological Society, Journal of Physical Oceanography, v. 9, p. 170–188.

Spain, Barry, 1960, Tensor calculus (3rd ed., revised): Edinburgh, Great Britain, Oliver and Boyd, New York, Interscience Publishers, 125 p.

Spall, M.A., and Robinson, A.R., 1990, Regional primitive equation studies of the Gulf Stream meander and ring formation region: American Meteorological Society, Journal of Physical Oceanography, v. 20, p. 985–1016.

Spaulding, M.L., 1984, A vertically averaged circulation model using boundary-fitted coordinates: American Meteorological Society, Journal of Physical Oceanography, v. 14, no. 5, p. 973–982.

Spaulding, M.L., Huang, Wenrui, and Mendelsohn, Daniel, 1990, Application of a boundary fitted coordinate hydrodynamic model, *in* Spaulding, M.L., ed., Proceedings of the First Estuarine and Coastal Modeling Conference: American Society of Civil Engineers, Newport, R. I., November 15–17, 1989, p. 27–39.

Spaulding, M.L., and Isaji, T., 1987, Three-dimensional continental shelf hydrodynamic model including wave-current interaction, *in* Nihoul, J.C.J., and Jamart, B.M., eds., Three-dimensional models of marine and estuarine dynamics: Amsterdam, Netherlands, Elsevier, p. 405–426.

Stansby, P.K., and Lloyd, P.M., 1995, A semi-implicit Lagrangian scheme for 3-D shallow water flow with a two-layer turbulence model: International Journal for Numerical Methods in Fluids, v. 20, p. 115–133.

Stelling, G.S., 1984, On the construction of computational methods for shallow water flow problems: Rijkswaterstaat Communication, The Hague, Netherlands, no. 35, 226 p.

Stelling, G.S., Wiersma, A.K., and Willemse, J.B.T.M., 1986, Practical aspects of accurate tidal computations: American Society of Civil Engineers, Journal of Hydraulic Engineering, v. 112, no. 9, p. 802–817.

Stelling, G.S., and van Kester, J.A.T.M., 1994, On the approximation of horizontal gradients in sigma co-ordinates for bathymetry with steep bottom slopes: International Journal for Numerical Methods in Fluids, v. 18, p. 915–935.

Stronach, J.A., Backhaus, J.O., Murty, T.S., 1993, An update on the numerical simulation of oceanographic processes in the waters between Vancouver Island and the mainland—the GF8 model: Oceanography and Marine Biology Annual Review, UCL Press, v. 31, p. 1–86.

Sündermann, Jürgen, 1975, A threedimensional model of a homogeneous estuary: American Society of Civil Engineers, Proceedings of the Fourteenth Coastal Engineering Conference, v. III, June 24–28, 1974, Copenhagen, Denmark, p. 2337–2354.

Tee, K.-T., 1979, The structure of three-dimensional tide generating currents. Part I—oscillating currents: American Meteorological Society, Journal of Physical Oceanography, v. 9, p. 930–944.

Tee, K.-T., 1987, Simple models to simulate three-dimensional tidal and residual currents, *in* Heaps, N.S., ed., Three-dimensional coastal ocean models: American Geophysical Union, Washington, D.C., Coastal and Estuarine Sciences Monograph Series, v. 4, p.125–147.

Tennekes, Hendrik, and Lumley, J.L., 1972, A first course in turbulence: Cambridge, Mass., The MIT Press, 300 p.

Thacker, W.C., 1977, Irregular grid finite-difference techniques—Simulations of oscillations in shallow circular basins: American Meteorological Society, Journal of Physical Oceanography, v. 7, no. 2, p. 284–292.

Thompson, J.F., and Johnson, B.H., 1986, Generation of adaptive boundary-fitted coordinates for use in coastal and estuarine modeling, *in* Wang, S.S.Y., Shen, H.W., and Ding, L.Z., eds., Proceedings of the Third International Symposium on River Sedimentation: University of Mississippi, Jackson, Miss., March 31–April 4, 1986, p. 1397–1406.

Thompson, J.F., Warsi, Z.U.A., and Mastin, C.W., 1985, Numerical Grid Generation: New York, Elsevier, 483 p.

Turner, J.S., 1973, Buoyancy effects in fluids: Cambridge, Great Britain, Cambridge University Press, 368 p.

Uittenbogaard, R.E., van Kester, J.A.T.M., and Stelling, G.S., 1992, Implementation of three turbulence models in TRISULA for rectangular horizontal grids: Delft Hydraulics, Delft, Netherlands, Prepared for the Tidal Waters Division of the Dutch Ministry of Transport, Public Works and Water Management, 169 p.

Unesco, 1979, Ninth report of the joint panel on oceanographic tables and standards: Unesco Technical Papers in Marine Science, no. 30, 31 p.

Unesco, 1981, Tenth report of the joint panel on oceanographic tables and standards: Unesco Technical Papers in Marine Science, no. 36, 24 p.

Vallentine, H.R., 1967, Applied hydrodynamics (2nd ed.): New York, Plenum Press, 296 p.

Verwey, Adrianus, 1971, Mathematical model for flow in rivers with realistic bed configuration: Delft, Netherlands, Delft Hydraulics Laboratory, International Courses in Hydraulic and Sanitary Engineering, Report Series no. 12.

Viollet, P.L., 1988, On the numerical modeling of stratified flows, *in* Dronkers, J.J., and van Leussen, Wim, eds., Physical processes in estuaries: Berlin, Germany, Springer, p. 257–277.

Walters, R.A., 1988, A finite element model for tides and currents with field applications: Communications in Applied Numerical methods, v. 4, p. 401–411.

Walters, R.A., 1992, A three-dimensional, finite element model for coastal and estuarine circulation: Continental Shelf Research, v. 12, no. 1, p. 83–102.

Walters, R.A., 1997, A model study of tidal and residual flow in Delaware Bay and River: American Geophysical Union, Journal of Geophysical Research (Oceans), v. 102, no. C6, p. 12689–12704.

Walters, R.A., and Foreman, M.G.G., 1992, A 3D, finite element model for baroclinic circulation on the Vancouver Island continental shelf: Journal of Marine Systems, v. 3, no. 6, p. 507–518.

Wang, D.-P., 1982, Development of a three-dimensional, limited-area (island) shelf circulation model: American Meteorological Society, Journal of Physical Oceanography, v. 12, p. 605–617.

Wang, K.H., 1994, Characterization of circulation and salinity change in Galveston Bay: American Society of Civil Engineers, Journal of Engineering Mechanics, v. 120, no. 3, p. 557–579.

Wang, P.F., 1992, Review of equations of conservation in curvilinear coordinates: American Society of Civil Engineers, Journal of Engineering Mechanics, v. 118, no. 11, p. 2265–2281.

Welander, P., 1957, Wind action on a shallow sea—some generalizations of Ekman's theory: Tellus, v. 9, p. 45–52.

Westerink, J.J., and Gray, W.G., 1991, Progress in surface water modeling: U.S. National Report to the International Union of Geodesy and Geophysics 1987–1990, Reviews of Geophysics, supplement, Contributions in Hydrology, American Geophysical Union, p. 210–217.

Wilders, P., van Stijn, T.L., Stelling, G.S., and Fokkema, G.A., 1988, A fully implicit splitting method for accurate tidal computations: International Journal for Numerical Methods in Engineering, v. 26, no. 12, p. 2707–2721.

Willemse, J.B.T.M., Stelling, G.S., and Verboom, G.K., 1985, Solving the shallow water equations with an orthogonal coordinate transformation: Delft Hydraulics Communication No. 356, Presented at the International Symposium on Computational Fluid Dynamics: Tokyo, Japan, September 9–12, 1985, 12 p.

Wills, A.P., 1958, Vector analysis, with an introduction to tensor analysis (1st ed., reprinted with corrections): New York, Dover Publications, 285 p.

Wilson, B.W., 1972, Seiches: Advances in Hydroscience, v. 8, p. 1–94.

Wolf, J., 1983, A comparison of a semi-implicit with an explicit scheme in a three-dimensional hydrodynamic model: Continental Shelf Research, v. 2, no. 4, p. 215–229.

Yen, B.C., 1973, Open-channel flow equations revisited: American Society of Civil Engineers, Journal of the Engineering Mechanics Division, v. 99, no. 5, p. 979–1009.

Young, D.M., 1971, Iterative solution of large linear systems: New York, Academic Press, 570 p.

Zalesak, S.T., 1979, Fully multidimensional flux-corrected transport algorithms for fluids: Journal of Computational Physics, v. 31, p. 335–362.

Zeinkiewicz, O.C., 1997, The finite element method (3rd ed.): London, McGraw Hill, 787 p.

Appendixes

Appendix A - Coriolis Acceleration

This section presents a derivation of the Coriolis acceleration term appearing in the equation of motion. A general treatment of the Coriolis acceleration for particle motion in a rotating reference frame can be found in many standard textbooks on mechanics (for example, Beer and Johnston, 1962). The derivation here is specifically for tidally-driven flows in estuaries and discusses the form of the Coriolis term that is in common use. Vector notation is used in this section, although not elsewhere in this report, because it is an especially natural and compact notation for deriving the Coriolis acceleration. Vectors are identified with bold-face type. In particular, heavy use is made of the vector cross product which is defined in any standard textbook on vector analysis, such as Wills (1958).

Consider the earth's center as the origin of a reference frame E$x'y'z'$ (*fig. A.1*) that is fixed in space (neglecting the motion of the earth's center as it travels through space). The estuarine reference frame Oxyz is fixed to the surface of the earth and is rotating with angular velocity Ω about the earth's axis. Let P be the position of a material element of fluid that is moving with the flow in the estuary. The position of P is defined at any instant by the vector $\mathbf{r}$ in the rotating frame and the vector $\mathbf{r}'$ in the fixed frame. By simple vector addition one can write

$$\mathbf{r}' = \mathbf{R} + \mathbf{r}\,, \tag{A.1}$$

where $\mathbf{R}$ is the position vector of the point O at the origin of the rotating frame and has a magnitude equal to the earth's radius.

The absolute velocity $\mathbf{v}'$ of the point P relative to the fixed frame is obtained by differentiating A.1,

$$\mathbf{v}' = \frac{d\mathbf{r}'}{dt} = \frac{d\mathbf{R}}{dt} + \frac{d\mathbf{r}}{dt}\,. \tag{A.2}$$

The first term on the right side of this expression is the velocity of the origin of the rotating reference frame Oxyz. From elementary mechanics, the velocity of rigid-body rotation about a fixed axis is defined by the vector cross product

$$\frac{d\mathbf{R}}{dt} = \Omega \times \mathbf{R}\,. \tag{A.3}$$

The second term on the right side of A.2 is the velocity of P relative to a nonrotating frame having the same orientation as E$x'y'z'$, but with the origin at the point O. In this case, the velocity is defined by

$$\frac{d\mathbf{r}}{dt} = \Omega \times \mathbf{r} + \left(\frac{d\mathbf{r}}{dt}\right)_r\,, \tag{A.4}$$

where $(d\mathbf{r}/dt)_r$ is the rate of change of $\mathbf{r}$ with respect to the rotating frame Oxyz and $\Omega \times \mathbf{r}$ is induced by the rotation. Substituting A.3 and A.4 into A.2 gives the absolute velocity as

$$\mathbf{v}' = \Omega \times \mathbf{R} + \Omega \times \mathbf{r} + \left(\frac{d\mathbf{r}}{dt}\right)_r\,. \tag{A.5}$$

Differentiating this expression again using A.3 and the operator (d/dt) defined by A.4 gives an expression for the absolute acceleration

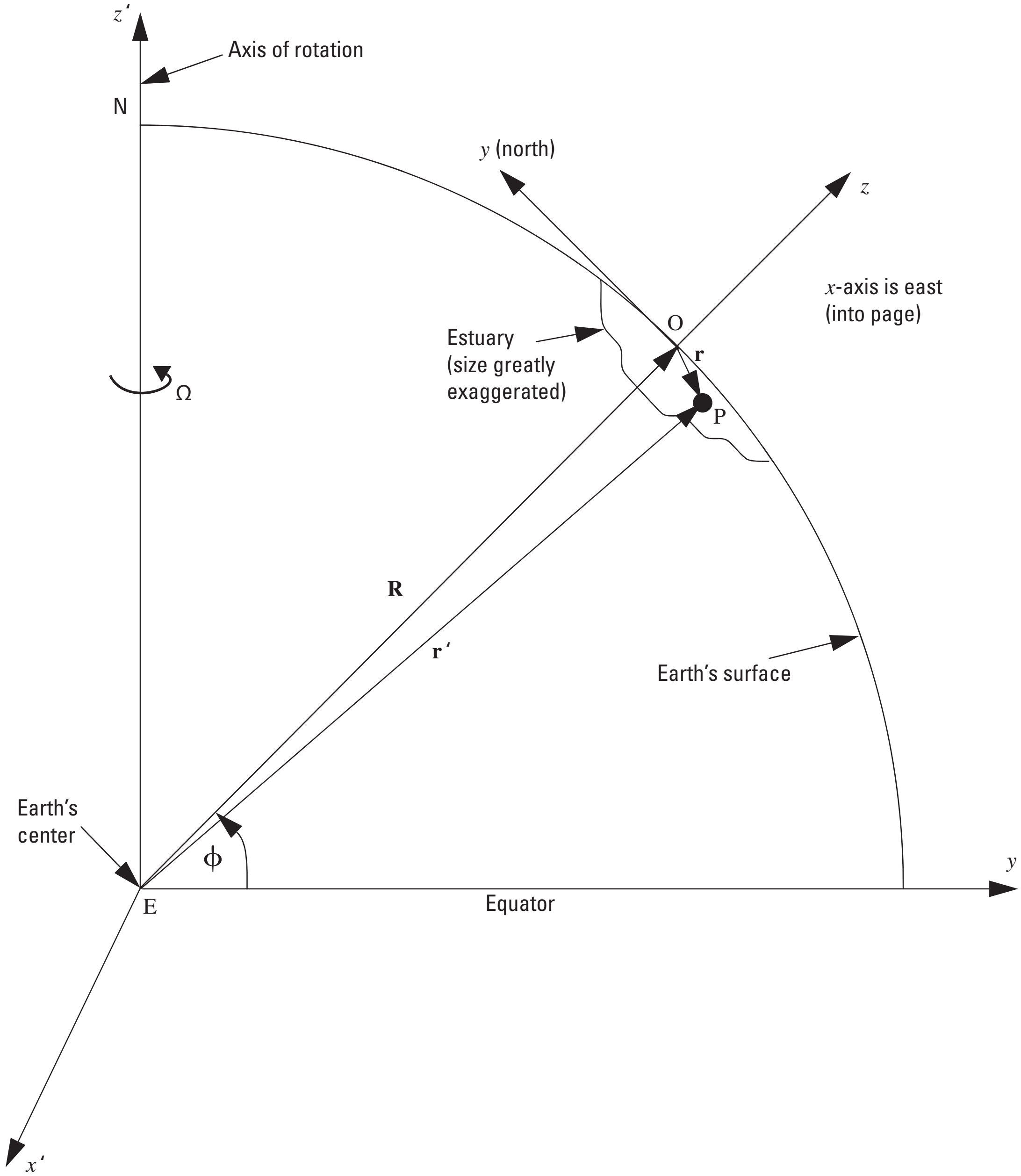

Figure A.1. Estuarine reference frame Oxyz shown fixed to the earth's surface at latitude ϕ and rotating about the earth's axis with angular velocity Ω.
The earth's center is the origin of a reference frame E$x'y'z'$ that is considered to be fixed in space.

$$
\begin{aligned}
\mathbf{a}' &= \frac{d\mathbf{v}'}{dt} = \frac{d(\Omega \times \mathbf{R})}{dt} + \frac{d(\Omega \times \mathbf{r})}{dt} + \frac{d}{dt}\left(\frac{d\mathbf{r}}{dt}\right)_r \\
&= \frac{d\Omega}{dt} \times \mathbf{R} + \Omega \times \frac{d\mathbf{R}}{dt} + \frac{d\Omega}{dt} \times \mathbf{r} + \Omega \times \frac{d\mathbf{r}}{dt} + \Omega \times \left(\frac{d\mathbf{r}}{dt}\right)_r + \left(\frac{d^2\mathbf{r}}{dt^2}\right)_r \\
&= \frac{d\Omega}{dt} \times \mathbf{R} + \Omega \times (\Omega \times \mathbf{R}) + \frac{d\Omega}{dt} \times \mathbf{r} + \Omega \times (\Omega \times \mathbf{r}) + 2\Omega \times \left(\frac{d\mathbf{r}}{dt}\right)_r + \left(\frac{d^2\mathbf{r}}{dt^2}\right)_r \quad .
\end{aligned}
\tag{A.6}
$$

Now setting $d\Omega / dt = 0$ for steady rotation of the earth, and defining $(d\mathbf{r}/dt)_r = \mathbf{v}$ and $(d^2\mathbf{r}/dt^2)_r = \mathbf{a}$ as the velocity and acceleration, respectively, relative to the rotating frame, one obtains the following expression relating the absolute acceleration in the fixed frame to the relative acceleration in the rotating frame:

$$
\mathbf{a}' = \mathbf{a} + \Omega \times (\Omega \times \mathbf{R}) + \Omega \times (\Omega \times \mathbf{r}) + 2\Omega \times \mathbf{v} \quad . \tag{A.7}
$$

For motion in even the largest estuary, $\mathbf{r}$ is much less than $\mathbf{R}$ and the term $\Omega \times (\Omega \times \mathbf{r})$ can safely be neglected. The term $\Omega \times (\Omega \times \mathbf{R})$ is the centripetal acceleration directed towards the earth's axis at the point O′ (*fig. A.2*). The true gravitational acceleration at the earth's surface is $\mathbf{g} = \mathbf{g_0} - \Omega \times (\Omega \times \mathbf{R})$ where $\mathbf{g_0}$ is the nonrotating gravitational acceleration. The centripetal acceleration is therefore already incorporated into the equation of motion in the gravitational body force, as normally defined, so long as the z-axis is assumed to lie along the line of action of $\mathbf{g}$.

Equation A.7 has now been reduced to

$$
\mathbf{a}' = \mathbf{a} + 2\Omega \times \mathbf{v} \tag{A.8}
$$

In terms of the Eulerian velocity field, $\mathbf{u}(\mathbf{x},t)$, specified in coordinates relative to the rotating frame, this expression becomes

$$
\mathbf{a}' = \frac{\partial \mathbf{u}}{\partial t} + (\mathbf{u} \cdot \nabla)\mathbf{u} + 2\Omega \times \mathbf{u} \tag{A.9}
$$

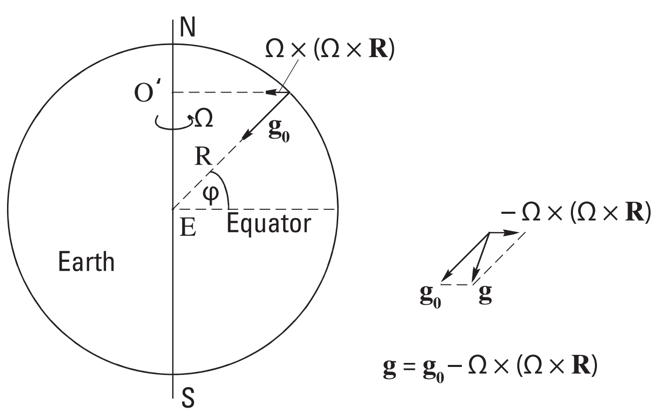

Figure A.2 The earth's rotation causes a centripetal acceleration $\Omega \times (\Omega \times \mathbf{R})$ that affects the local acceleration of gravity g at the earth's surface.
The nonrotating gravitational acceleration is g_0.

where the advective acceleration $(\mathbf{u} \cdot \nabla)\mathbf{u}$ is introduced by the Eulerian specification of the flow. Equation A.9 states that the equation of motion in the rotating frame is equivalent to that in an absolute frame so long as it is assumed that a pseudo body force per unit mass represented by $(-2\Omega \times \mathbf{u})$[54] acts upon the fluid. This pseudo body force is known as the Coriolis acceleration (force/unit mass) and is often significant in estuarine modeling.

In Cartesian coordinates using $\mathbf{u} = u\mathbf{i} + v\mathbf{j} + w\mathbf{k}$ and $\Omega = \Omega_x\mathbf{i} + \Omega_y\mathbf{j} + \Omega_z\mathbf{k}$, the acceleration terms are

$$\frac{\partial u}{\partial t} + u\frac{\partial u}{\partial x} + v\frac{\partial u}{\partial y} + w\frac{\partial u}{\partial z} - 2\Omega_z v + 2\Omega_y w \ , \tag{A.10}$$

$$\frac{\partial v}{\partial t} + u\frac{\partial v}{\partial x} + v\frac{\partial v}{\partial y} + w\frac{\partial v}{\partial z} + 2\Omega_z u - 2\Omega_x w \ , \text{ and} \tag{A.11}$$

$$\frac{\partial w}{\partial t} + u\frac{\partial w}{\partial x} + v\frac{\partial w}{\partial y} + w\frac{\partial w}{\partial z} + 2\Omega_x v - 2\Omega_y u \ . \tag{A.12}$$

For a reference frame chosen using the z-axis vertically-upward, but using the horizontal axes rotated by an angle θ, the components of Ω are dependent on both the latitude ϕ and the rotation θ by

$$\begin{aligned} \Omega_x &= |\Omega| \cos\phi \sin\theta, \\ \Omega_y &= |\Omega| \cos\phi \cos\theta \ , \text{ and} \\ \Omega_z &= |\Omega| \sin\phi. \end{aligned} \tag{A.13}$$

When the x-axis is toward the east and the y-axis is toward the north ($\theta = 0°$), these reduce to

$$\begin{aligned} \Omega_x &= 0 \ , \\ \Omega_y &= |\Omega| \cos\phi, \text{ and} \\ \Omega_z &= |\Omega| \sin\phi \ . \end{aligned} \tag{A.14}$$

In a shallow estuary, the vertical velocity component w is typically very small, and therefore the two Coriolis terms involving w in the horizontal momentum equations (A.10 and A.11) are usually neglected. Frequently the term $(\Omega_x v - \Omega_y u)$ in the z-momentum equation is also neglected because it is considered to be small in comparison with $\mathbf{g}$. Pond and Pickard (1986, p. 40) point out, however, that, although $(\Omega_x v - \Omega_y u)$ may be small compared with $\mathbf{g}$, it may not always be small compared with the difference between the pressure term in the z-momentum equation and $\mathbf{g}$. Evces and Raney (1990) formulated a 2-D vertically-averaged hydrodynamic model that included the z-component Coriolis term and estimated it may correct the total Coriolis term for a high tidal range estuary near latitude $\phi = 45°$ by10 percent. The correction will be most pronounced at high latitudes ($\phi > 45°$) and in some instances may warrant inclusion in a model applied at lower latitudes. For the model discussed herein, however, the term is neglected, as is customary. In this case, the form of the acceleration terms in the rotating reference frame are most commonly expressed as

$$\frac{\partial u}{\partial t} + u\frac{\partial u}{\partial x} + v\frac{\partial u}{\partial y} + w\frac{\partial u}{\partial z} - fv \tag{A.15}$$

[54] Using the subscript notation from Chapter 2 of this report, the Coriolis acceleration $2\Omega \times \mathbf{u}$ is written as $2\varepsilon_{ijk}\Omega_j\mathbf{u}_k$.

$$\frac{\partial v}{\partial t} + u\frac{\partial v}{\partial x} + v\frac{\partial v}{\partial y} + w\frac{\partial v}{\partial z} + fu \tag{A.16}$$

$$\frac{\partial w}{\partial t} + u\frac{\partial w}{\partial x} + v\frac{\partial w}{\partial y} + w\frac{\partial w}{\partial z} \quad , \tag{A.17}$$

where $f = 2\Omega_z = 2|\Omega| \sin \phi$ is called the Coriolis parameter and is equal to 1.03×10^{-4} sec^{-1} at $\phi = 45°$. Because the area of study is usually less than a few degrees of latitude for estuarine problems, the Coriolis parameter is held fixed at its value at the point of contact with a tangent plane to the earth. The tangent plane is called the f-plane, and this approximation is referred to as the f-plane approximation.

Appendix B - Equation of State

To evaluate the pressure gradient terms in the equations of motion and to assess the water column stability under stratified conditions, the density field must be determined. An equation of state is needed to define the dependence of density on salinity (s) and temperature (Θ). Because water is slightly compressible, the density also depends to a small degree on pressure; this dependence is eliminated by considering the density as a potential density evaluated at atmospheric pressure.

Many of the pre-1980 formulas for the equation of state are based on the well-known hydrographic tables prepared by Knudsen (1901). In 1980 a new International Equation of State (IES 80)(Millero and Poisson, 1981; Unesco, 1981) was introduced using the Practical Salinity Scale, 1978 (Unesco, 1979), which is based on electrical conductivity measurements. The use of IES 80 is now recommended over the Knudsen tables.

Two options are available in the 3-D model for the equation of state. For both, density is computed in kg/m^3, salinity is expressed according to the Practical Salinity Scale, and temperature is expressed in degrees Celsius. The first option is IES 80 as given by (rearranged from the formula presented by Pond and Pickard [1986], p. 310)

$$\rho(s, \Theta) = a + (s \times (b + \sqrt{s} \times (c + \sqrt{s} \times d))) , \tag{B.1}$$

where

$$a = a_0 + (\Theta \times (a_1 + \Theta \times (a_2 + \Theta \times (a_3 + \Theta \times (a_4 + \Theta \times a_5))))),$$

$$b = b_0 + (\Theta \times (b_1 + \Theta \times (b_2 + \Theta \times (b_3 + \Theta \times b_4)))),$$

$$c = c_0 + (\Theta \times (c_1 + \Theta \times c_2)),$$

$$d = d_0,$$

and the coefficients are

$a_0 = 999.842594,$	$a_1 = 6.793952 \times 10^{-2},$	$a_2 = -9.095290 \times 10^{-3},$
$a_3 = 1.001685 \times 10^{-4},$	$a_4 = -1.120083 \times 10^{-6},$	$a_5 = 6.536332 \times 10^{-9},$
$b_0 = 8.24493 \times 10^{-1},$	$b_1 = -4.0899 \times 10^{-3},$	$b_2 = 7.6438 \times 10^{-5},$
$b_3 = -8.2467 \times 10^{-7},$	$b_4 = 5.3875 \times 10^{-9},$	$c_0 = -5.72466 \times 10^{-3},$
$c_1 = 1.0227 \times 10^{-4},$	$c_2 = -1.6546 \times 10^{-6},$	$d_0 = 4.8314 \times 10^{-4}.$

The second option is for the case when density can be taken as a function of salinity only (temperature is uniform). In this case, a simple linear relation is used, as proposed by Hansen and Rattray (1965):

$$\rho(s) = \rho_r(1 + ks), \tag{B.2}$$

where ρ_r and k are coefficients. For the 3-D test case in this report, the two coefficients ρ_r and k were determined by fitting equation 2 to IES 80 for a specified temperature and range of salinity. For example, for $\Theta = 17\ ^{o}C$ and salinity in the range 10–20, the optimized coefficients are

$$\rho_r = 998.7959 \quad \text{and} \quad k = 0.000763\,.$$

The coefficient ρ_r is close to the density of fresh water in kg/m^3. Because density is computed often in the model computations, it is advantageous to use equation 2 whenever possible to speed up model performance.

Appendix C - The σ Transformation

In this section, the transformation of the 3-D governing equations from a z-coordinate system (x, y, z, t) to a vertically normalized, σ-coordinate system $(\hat{x}, \hat{y}, \sigma, \hat{t})$ is outlined. By choosing the free surface as $\sigma = 0$ and the bottom as $\sigma = -1$, the transformation between coordinate systems is defined as

$$\hat{x} = x, \quad \hat{y} = y, \quad \sigma = \frac{z - \zeta(x, y, t)}{h(x, y) + \zeta(x, y, t)} = \frac{z - \zeta}{H}, \quad \hat{t} = t, \tag{C.1}$$

where $H = h + \zeta$ (*fig. C.1*). An example of a σ grid in z-coordinate space and σ-coordinate space is shown schematically in *figure C.2*. Because the σ axis is vertical while the constant σ surfaces are sloping, the coordinate transformation is nonorthogonal.

The dependent variables u, v, ρ, and s transform straightforwardly between coordinate systems as

$$\hat{G}(\hat{x}, \hat{y}, \sigma, \hat{t}) = G(x, y, z = H\sigma + \zeta, t)$$

where G represents any of the four variables. Under the transformation, the new velocities $\hat{u}$ and $\hat{v}$ are still the horizontal (Cartesian) components of the velocity vector and are not measured along the sloping σ surfaces. The dependent variables H and ζ are not functions of the transformed vertical coordinate, so they can be used interchangeably with $\hat{H}$ and $\hat{\zeta}$. For the transformed vertical velocity, the following definition is adopted:[55]

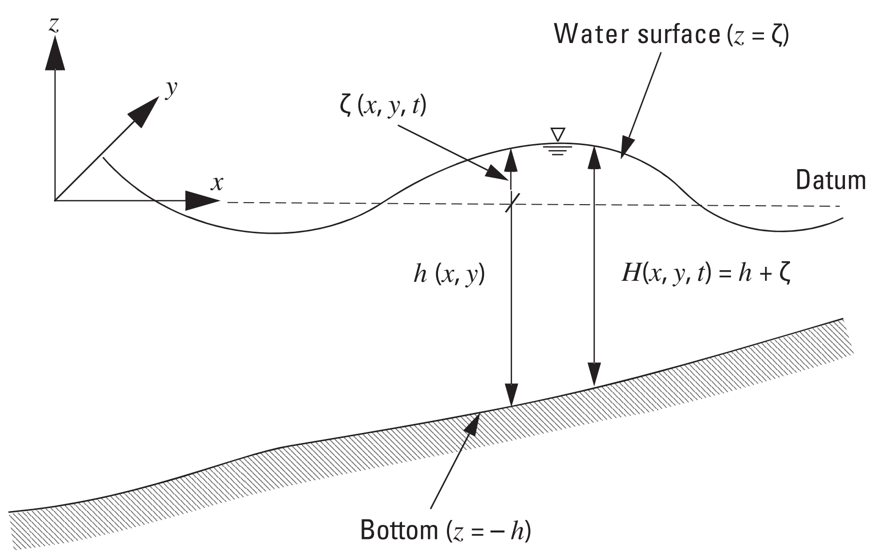

Figure C.1. Definition sketch for the estuarine free surface, bottom, and total depth (H) in a z-coordinate system.

[55]Several authors, such as Blumberg and Mellor (1987) and Stelling and van Kester (1994), choose to define the transformed vertical velocity as $\omega = H(D\sigma / Dt)$ so that it has units of (length/time). The definition of ω in equation C.2 has units of (1/time).

$$\omega = \frac{D\sigma}{Dt}. \tag{C.2}$$

The original vertical velocity w is related to ω by

$$w = \frac{Dz}{Dt} = \frac{D}{Dt}(H\sigma + \zeta) = H\omega + \sigma\frac{DH}{Dt} + \frac{D\zeta}{Dt}\ . \tag{C.3}$$

Expanding the operators D / Dt in the above expression leads to

$$w = H\omega + u\left(\sigma\frac{\partial H}{\partial x} + \frac{\partial \zeta}{\partial x}\right) + v\left(\sigma\frac{\partial H}{\partial y} + \frac{\partial \zeta}{\partial y}\right) + \left(\sigma\frac{\partial H}{\partial t} + \frac{\partial \zeta}{\partial t}\right)\ . \tag{C.4}$$

An expression for $\partial w / \partial\sigma$ can be shown to be

$$\frac{\partial w}{\partial \sigma} = H\frac{\partial \omega}{\partial \sigma} + \left(\frac{\partial \zeta}{\partial t} + u\frac{\partial H}{\partial x} + v\frac{\partial H}{\partial y}\right) + \sigma\left(\frac{\partial H}{\partial x}\frac{\partial u}{\partial \sigma} + \frac{\partial H}{\partial y}\frac{\partial v}{\partial \sigma}\right) + \left(\frac{\partial \zeta}{\partial x}\frac{\partial u}{\partial \sigma} + \frac{\partial \zeta}{\partial y}\frac{\partial v}{\partial \sigma}\right)\ . \tag{C.5}$$

By applying the familiar chain rule of calculus, the first-order derivatives in z coordinates are expressed in terms of σ coordinates by the following operators:

$$\frac{\partial}{\partial x} = \frac{\partial}{\partial \hat{x}} - \frac{\sigma}{H}\frac{\partial H}{\partial \hat{x}}\frac{\partial}{\partial \sigma} - \frac{1}{H}\frac{\partial \zeta}{\partial \hat{x}}\frac{\partial}{\partial \sigma}\ , \tag{C.6}$$

$$\frac{\partial}{\partial y} = \frac{\partial}{\partial \hat{y}} - \frac{\sigma}{H}\frac{\partial H}{\partial \hat{y}}\frac{\partial}{\partial \sigma} - \frac{1}{H}\frac{\partial \zeta}{\partial \hat{y}}\frac{\partial}{\partial \sigma}\ , \tag{C.7}$$

$$\frac{\partial}{\partial z} = \frac{1}{H}\frac{\partial}{\partial \sigma}, \text{ and} \tag{C.8}$$

$$\frac{\partial}{\partial t} = \frac{\partial}{\partial \hat{t}} - \frac{\sigma}{H}\frac{\partial H}{\partial \hat{t}}\frac{\partial}{\partial \sigma} - \frac{1}{H}\frac{\partial \zeta}{\partial \hat{t}}\frac{\partial}{\partial \sigma}\ . \tag{C.9}$$

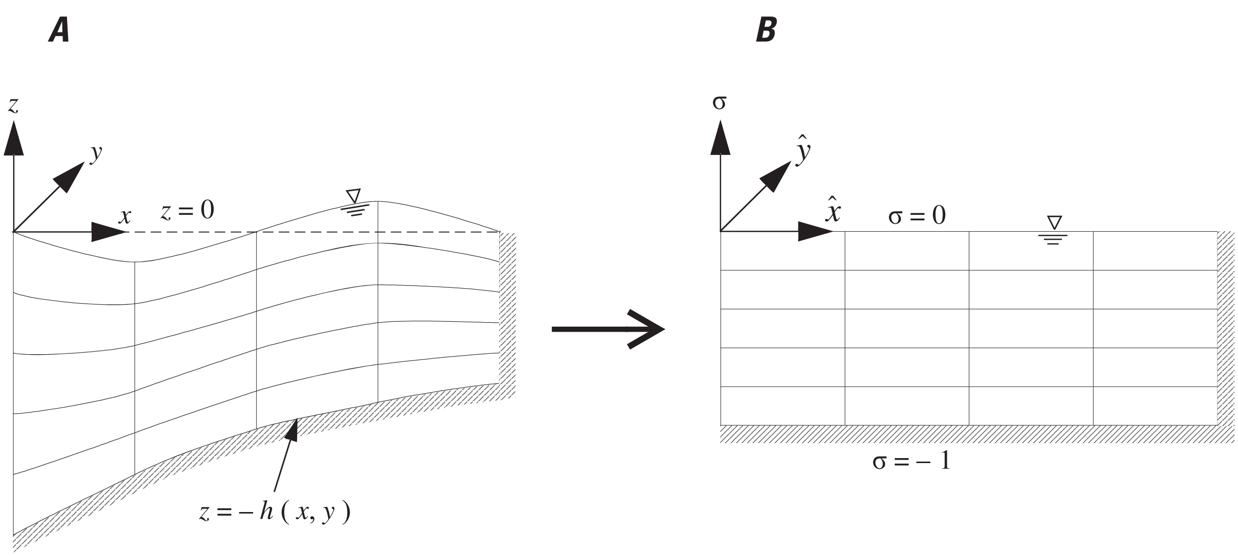

Figure C.2. Schematic of a σ-grid shown in (*A*) z-coordinate space and (*B*) σ -coordinate space.

Differential operators for the second-order, spatial derivatives are also needed in transforming the diffusion terms. In complete form these are (Sheng, 1983, p. 224)

$$\frac{\partial}{\partial x}\left(\frac{\partial}{\partial x}\right) = \frac{1}{H}\left[\frac{\partial}{\partial \hat{x}}\left(H\frac{\partial}{\partial \hat{x}}\right) - \frac{\partial}{\partial \sigma}\left(\sigma\frac{\partial H}{\partial \hat{x}}\frac{\partial}{\partial \hat{x}}\right) - \sigma\frac{\partial}{\partial \hat{x}}\left(\frac{\partial H}{\partial \hat{x}}\frac{\partial}{\partial \sigma}\right)\right.$$
$$+ \frac{1}{H}\left(\frac{\partial H}{\partial \hat{x}}\right)^2\frac{\partial}{\partial \sigma}\left(\sigma^2\frac{\partial}{\partial \sigma}\right) - \frac{\partial}{\partial \hat{x}}\left(\frac{\partial \zeta}{\partial \hat{x}}\frac{\partial}{\partial \sigma}\right) - \frac{\partial \zeta}{\partial \hat{x}}\frac{\partial^2}{\partial \sigma \partial \hat{x}}$$
$$\left. + \left(\frac{\partial \zeta}{\partial \hat{x}}\right)^2\frac{1}{H}\frac{\partial^2}{\partial \sigma^2} + \frac{2}{H}\frac{\partial \zeta}{\partial \hat{x}}\frac{\partial H}{\partial \hat{x}}\frac{\partial}{\partial \sigma}\left(\sigma\frac{\partial}{\partial \sigma}\right)\right] , \tag{C.10}$$

$$\frac{\partial}{\partial y}\left(\frac{\partial}{\partial y}\right) = \frac{1}{H}\left[\frac{\partial}{\partial \hat{y}}\left(H\frac{\partial}{\partial \hat{y}}\right) - \frac{\partial}{\partial \sigma}\left(\sigma\frac{\partial H}{\partial \hat{y}}\frac{\partial}{\partial \hat{y}}\right) - \sigma\frac{\partial}{\partial \hat{y}}\left(\frac{\partial H}{\partial \hat{y}}\frac{\partial}{\partial \sigma}\right)\right.$$
$$+ \frac{1}{H}\left(\frac{\partial H}{\partial \hat{y}}\right)^2\frac{\partial}{\partial \sigma}\left(\sigma^2\frac{\partial}{\partial \sigma}\right) - \frac{\partial}{\partial \hat{y}}\left(\frac{\partial \zeta}{\partial \hat{y}}\frac{\partial}{\partial \sigma}\right) - \frac{\partial \zeta}{\partial \hat{y}}\frac{\partial^2}{\partial \sigma \partial \hat{y}}$$
$$\left. + \left(\frac{\partial \zeta}{\partial \hat{y}}\right)^2\frac{1}{H}\frac{\partial^2}{\partial \sigma^2} + \frac{2}{H}\frac{\partial \zeta}{\partial \hat{y}}\frac{\partial H}{\partial \hat{y}}\frac{\partial}{\partial \sigma}\left(\sigma\frac{\partial}{\partial \sigma}\right)\right] \text{, and} \tag{C.11}$$

$$\frac{\partial}{\partial z}\left(\frac{\partial}{\partial z}\right) = \frac{1}{H}\frac{\partial}{\partial \sigma}\left(\frac{1}{H}\frac{\partial}{\partial \sigma}\right) . \tag{C.12}$$

In deriving operators C.6 to C.12, use was made of the identities

$$\frac{\partial \sigma}{\partial x} = -\left(\frac{\sigma}{H}\frac{\partial H}{\partial x} + \frac{1}{H}\frac{\partial \zeta}{\partial x}\right) ,$$

$$\frac{\partial^2 \sigma}{\partial x^2} = -\frac{\sigma}{H}\frac{\partial^2 H}{\partial x^2} + \frac{2\sigma}{H^2}\left(\frac{\partial H}{\partial x}\right)^2 + \frac{2}{H^2}\frac{\partial \zeta}{\partial x}\frac{\partial H}{\partial x} - \frac{1}{H}\frac{\partial^2 \zeta}{\partial x^2} \text{, and}$$
$$\left(\frac{\partial \sigma}{\partial x}\right)^2 = \frac{\sigma^2}{H^2}\left(\frac{\partial H}{\partial x}\right)^2 + \frac{2\sigma}{H^2}\frac{\partial \zeta}{\partial x}\frac{\partial H}{\partial x} + \frac{1}{H^2}\left(\frac{\partial \zeta}{\partial x}\right)^2 ,$$

and similar identities for the gradient of σ with respect to *y*.

Using these operators, the 3-D equations in *z* coordinates presented in Chapter 2 (equations 2.38, 2.49, 2.50, and 2.42) are transformed into the σ-coordinate system:

Continuity equation,

$$\frac{\partial \zeta}{\partial t} + \frac{\partial H\hat{u}}{\partial \hat{x}} + \frac{\partial H\hat{v}}{\partial \hat{y}} + H\frac{\partial \omega}{\partial \sigma} = 0 \quad ; \tag{C.13}$$

Momentum equations,

$$\frac{\partial H\hat{u}}{\partial\hat{t}} + \frac{\partial H\hat{u}\hat{u}}{\partial\hat{x}} + \frac{\partial H\hat{u}\hat{v}}{\partial\hat{y}} + H\frac{\partial\hat{u}\omega}{\partial\sigma} - fH\hat{v} = -gH\frac{\partial\zeta}{\partial\hat{x}}$$

$$-\frac{gH}{\rho_0}\left[H\frac{\partial}{\partial\hat{x}}\int_{\sigma}^{0}\hat{\rho}\,d\sigma' + \frac{\partial H}{\partial\hat{x}}\int_{\sigma}^{0}\sigma\frac{\partial\hat{\rho}}{\partial\sigma}d\sigma'\right]$$

$$+\frac{\partial}{\partial\hat{x}}\left(HA_H\frac{\partial\hat{u}}{\partial\hat{x}}\right) + \frac{\partial}{\partial\hat{y}}\left(HA_H\frac{\partial\hat{u}}{\partial\hat{y}}\right) + H.O.T. + \frac{\partial}{\partial\sigma}\left(\frac{A_V}{H}\frac{\partial\hat{u}}{\partial\sigma}\right) \text{ and} \tag{C.14}$$

$$\frac{\partial H\hat{v}}{\partial\hat{t}} + \frac{\partial H\hat{u}\hat{v}}{\partial\hat{x}} + \frac{\partial H\hat{v}\hat{v}}{\partial\hat{y}} + H\frac{\partial\hat{v}\omega}{\partial\sigma} + fH\hat{u} = -gH\frac{\partial\zeta}{\partial\hat{y}}$$

$$-\frac{gH}{\rho_0}\left[H\frac{\partial}{\partial\hat{y}}\int_{\sigma}^{0}\hat{\rho}\,d\sigma' + \frac{\partial H}{\partial\hat{y}}\int_{\sigma}^{0}\sigma\frac{\partial\hat{\rho}}{\partial\sigma}d\sigma'\right]$$

$$+\frac{\partial}{\partial\hat{x}}\left(HA_H\frac{\partial\hat{v}}{\partial\hat{x}}\right) + \frac{\partial}{\partial\hat{y}}\left(HA_H\frac{\partial\hat{v}}{\partial\hat{y}}\right) + H.O.T. + \frac{\partial}{\partial\sigma}\left(\frac{A_V}{H}\frac{\partial\hat{v}}{\partial\sigma}\right) ; \tag{C.15}$$

Salt transport equation,

$$\frac{\partial H\hat{s}}{\partial\hat{t}} + \frac{\partial H\hat{u}\hat{s}}{\partial\hat{x}} + \frac{\partial H\hat{v}\hat{s}}{\partial\hat{y}} + H\frac{\partial\omega\hat{s}}{\partial\sigma} =$$

$$\frac{\partial}{\partial\hat{x}}\left(HD_H\frac{\partial\hat{s}}{\partial\hat{x}}\right) + \frac{\partial}{\partial\hat{y}}\left(HD_H\frac{\partial\hat{s}}{\partial\hat{y}}\right) + H.O.T. + \frac{\partial}{\partial\sigma}\left(\frac{D_V}{H}\frac{\partial\hat{s}}{\partial\sigma}\right) . \tag{C.16}$$

The higher order terms (*H.O.T.*) in equations C.14, C.15, and C.16 are those due to all but the first term on the right sides of operators C.10 and C.11. The *H.O.T.* contain horizontal gradients of the water depth and water surface slope and often are neglected in practice (Mellor and Blumberg, 1985). Neglecting these terms is convenient because their inclusion can add considerably to the cost of running a model and can lead to a less stable and accurate numerical formulation. In regions of steep bottom slopes, however, the omission of the *H.O.T.* in solving the salt transport equation can cause spurious vertical diffusion of salt, especially in cases where significant salt stratification is present. In these cases the complete transformation must be included or a special numerical solution strategy, such as the finite-volume method applied to a σ grid by Stelling and van Kester (1994), should be used.

Appendix D - Expansion of Explicit Finite-Difference Terms

The explicit finite-difference terms in the 3-D momentum and salt transport equations are represented in abbreviated form in equations 4.23, 4.24, and 4.43. The expanded form of these terms using the leapfrog scheme is presented here. For the *x*-momentum equation (eq. 4.23), the finite-difference expressions for the advection, Coriolis, baroclinic density gradient, and horizontal diffusion terms are

$$
\begin{aligned}
(ADV_x)^n_{i+\frac{1}{2},j,k} &= \left(\frac{\partial(Uu)_k}{\partial x} + \frac{\partial(Vu)_k}{\partial y} + (uw)\Big|^{k-\frac{1}{2}}_{k+\frac{1}{2}}\right)^n_{i+\frac{1}{2},j} = \\
&+ \frac{1}{4\Delta x}((U^n_{i+\frac{3}{2},j,k} + U^n_{i+\frac{1}{2},j,k}) \cdot (u^n_{i+\frac{3}{2},j,k} + u^n_{i+\frac{1}{2},j,k}) \\
&- \ (U^n_{i+\frac{1}{2},j,k} + U^n_{i-\frac{1}{2},j,k}) \cdot (u^n_{i+\frac{1}{2},j,k} + u^n_{i-\frac{1}{2},j,k})) \\
&+ \frac{1}{4\Delta y}((V^n_{i+1,j+\frac{1}{2},k} + V^n_{i,j+\frac{1}{2},k}) \cdot (u^n_{i+\frac{1}{2},j+1,k} + u^n_{i+\frac{1}{2},j,k}) \\
&- \ (V^n_{i+1,j-\frac{1}{2},k} + V^n_{i,j-\frac{1}{2},k}) \cdot (u^n_{i+\frac{1}{2},j,k} + u^n_{i+\frac{1}{2},j-1,k})) \\
&+ \frac{1}{4}((w^n_{i+1,j,k-\frac{1}{2}} + w^n_{i,j,k-\frac{1}{2}}) \cdot (u^n_{i+\frac{1}{2},j,k-1} + u^n_{i+\frac{1}{2},j,k}) \\
&- \ (w^n_{i+1,j,k+\frac{1}{2}} + w^n_{i,j,k+\frac{1}{2}}) \cdot (u^n_{i+\frac{1}{2},j,k} + u^n_{i+\frac{1}{2},j,k+1})) \quad ,
\end{aligned}
\tag{D.1}
$$

$$
\begin{aligned}
(COR_x)^n_{i+\frac{1}{2},j,k} &= (fV_k)^n_{i+\frac{1}{2},j,k} = \\
&+ \frac{f}{4}(V^n_{i+1,j+\frac{1}{2},k} + V^n_{i,j+\frac{1}{2},k} + V^n_{i+1,j-\frac{1}{2},k} + V^n_{i,j-\frac{1}{2},k}) \quad ,
\end{aligned}
\tag{D.2}
$$

$$
\begin{aligned}
(BCLINIC_x)^n_{i+\frac{1}{2},j,k} &= \left(\frac{h_k}{\rho_k}\left(\frac{gh_1}{2}\frac{\partial\rho_1}{\partial x} + \sum_{m=2}^{k}\left(\frac{gh_{m-1}}{2}\frac{\partial\rho_{m-1}}{\partial x} + \frac{gh_m}{2}\frac{\partial\rho_m}{\partial x}\right)\right)\right)^n_{i+\frac{1}{2},j} = \\
&+ \frac{g}{2}((h^n_{i+1,j,k} + h^n_{i,j,k}) \cdot (\rho^n_{i+1,j,k} + \rho^n_{i,j,k})^{-1}) \\
&\times \frac{1}{2\Delta x}((h^n_{i+1,j,1} + h^n_{i,j,1}) \cdot (\rho^n_{i+1,j,1} - \rho^n_{i,j,1}) \\
&+ \sum_{m=2}^{k}((h^n_{i+1,j,m-1} + h^n_{i,j,m-1}) \cdot (\rho^n_{i+1,j,m-1} - \rho^n_{i,j,m-1}) \\
&+ (h^n_{i+1,j,m} + h^n_{i,j,m}) \cdot (\rho^n_{i+1,j,m} - \rho^n_{i,j,m}))) \quad \text{, and}
\end{aligned}
\tag{D.3}
$$

$$(HDIFF_x)^{n-1}_{i+1/2,j,k} = \left(\frac{\partial}{\partial x}\left(A_H h\frac{\partial u}{\partial x}\right)_k + \frac{\partial}{\partial y}\left(A_H h\frac{\partial u}{\partial y}\right)_k\right)^{n-1}_{i+1/2,j} =$$

$$+\frac{1}{(\Delta x)^2}(h^{n-1}_{i+1,j,k}A^{n-1}_{H\ i+1,j,k}(u^{n-1}_{i+3/2,j,k} - u^{n-1}_{i+1/2,j,k})$$

$$- h^{n-1}_{i,j,k}A^{n-1}_{H\ i,j,k}(u^{n-1}_{i+1/2,j,k} - u^{n-1}_{i-1/2,j,k}))$$

$$+\frac{1}{8(\Delta y)^2}(((h^{n-1}_{i+1,j+1,k} + h^{n-1}_{i,j+1,k})\cdot(A^{n-1}_{H\ i+1,j+1,k} + A^{n-1}_{H\ i,j+1,k})$$

$$+(h^{n-1}_{i+1,j,k} + h^{n-1}_{i,j,k})\cdot(A^{n-1}_{H\ i+1,j,k} + A^{n-1}_{H\ i,j,k}))$$

$$\times(u^{n-1}_{i+1/2,j+1,k} - u^{n-1}_{i+1/2,j,k})$$

$$-((h^{n-1}_{i+1,j,k} + h^{n-1}_{i,j,k})\cdot(A^{n-1}_{H\ i+1,j,k} + A^{n-1}_{H\ i,j,k})$$

$$+(h^{n-1}_{i+1,j-1,k} + h^{n-1}_{i,j-1,k})\cdot(A^{n-1}_{H\ i+1,j-1,k} + A^{n-1}_{H\ i,j-1,k}))$$

$$\times(u^{n-1}_{i+1/2,j,k} - u^{n-1}_{i+1/2,j-1,k})) \quad . \tag{D.4}$$

For the y-momentum equation (eq. 4.24), the finite-difference expressions are

$$(ADV_y)^n_{i,j+1/2,k} = \left(\frac{\partial(Uv)_k}{\partial x} + \frac{\partial(Vv)_k}{\partial y} + (vw)\Big|^{k-1/2}_{k+1/2}\right)^n_{i,j+1/2} =$$

$$+\frac{1}{4\Delta x}((U^n_{i+1/2,j+1,k} + U^n_{i+1/2,j,k})\cdot(v^n_{i+1,j+1/2,k} + v^n_{i,j+1/2,k})$$

$$-\ (U^n_{i-1/2,j+1,k} + U^n_{i-1/2,j,k})\cdot(v^n_{i,j+1/2,k} + v^n_{i-1,j+1/2,k}))$$

$$+\frac{1}{4\Delta y}((V^n_{i,j+3/2,k} + V^n_{i,j+1/2,k})\cdot(v^n_{i,j+3/2,k} + v^n_{i,j+1/2,k})$$

$$-\ (V^n_{i,j+1/2,k} + V^n_{i,j-1/2,k})\cdot(v^n_{i,j+1/2,k} + v^n_{i,j-1/2,k}))$$

$$+\frac{1}{4}((w^n_{i,j+1,k-1/2} + w^n_{i,j,k-1/2})\cdot(v^n_{i,j+1/2,k-1} + v^n_{i,j+1/2,k})$$

$$-\ (w^n_{i,j+1,k+1/2} + w^n_{i,j,k+1/2})\cdot(v^n_{i,j+1/2,k} + v^n_{i,j+1/2,k+1})) \quad , \tag{D.5}$$

$$(COR_y)^n_{i,j+1/2,k} = (fU_k)^n_{i,j+1/2,k} =$$

$$+\frac{f}{4}(U^n_{i+1/2,j+1,k} + U^n_{i-1/2,j+1,k} + U^n_{i-1/2,j,k} + U^n_{i+1/2,j,k}), \tag{D.6}$$

$$(BCLINIC_y)^n_{i,j+½,k} = \left(\frac{h_k}{\rho_k}\left(\frac{gh_1}{2}\frac{\partial\rho_1}{\partial y} + \sum_{m=2}^{k}\left(\frac{gh_{m-1}}{2}\frac{\partial\rho_{m-1}}{\partial y} + \frac{gh_m}{2}\frac{\partial\rho_m}{\partial y}\right)\right)\right)^n_{i,j+½} =$$

$$+\frac{g}{2}((h^n_{i,j+1,k} + h^n_{i,j,k})\cdot(\rho^n_{i,j+1,k} + \rho^n_{i,j,k})^{-1})$$

$$\times\frac{1}{2\Delta y}((h^n_{i,j+1,1} + h^n_{i,j,1})\cdot(\rho^n_{i,j+1,1} - \rho^n_{i,j,1})$$

$$+\sum_{m=2}^{k}((h^n_{i,j+1,m-1} + h^n_{i,j,m-1})\cdot(\rho^n_{i,j+1,m-1} - \rho^n_{i,j,m-1})$$

$$+(h^n_{i,j+1,m} + h^n_{i,j,m})\cdot(\rho^n_{i,j+1,m} - \rho^n_{i,j,m})))\quad , \tag{D.7}$$

$$(HDIFF_y)^{n-1}_{i,j+½,k} = \left(\frac{\partial}{\partial x}\left(A_H h\frac{\partial v}{\partial x}\right)_k + \frac{\partial}{\partial y}\left(A_H h\frac{\partial v}{\partial y}\right)_k\right)^{n-1}_{i,j+½} =$$

$$+\frac{1}{8(\Delta x)^2}(((h^{n-1}_{i+1,j+1,k} + h^{n-1}_{i+1,j,k})\cdot(A^{n-1}_{H\,i+1,j+1,k} + A^{n-1}_{H\,i+1,j,k})$$

$$+(h^{n-1}_{i,j+1,k} + h^{n-1}_{i,j,k})\cdot(A^{n-1}_{H\,i,j+1,k} + A^{n-1}_{H\,i,j,k}))$$

$$\times(v^{n-1}_{i+1,j+½,k} - v^{n-1}_{i,j+½,k})$$

$$-((h^{n-1}_{i,j+1,k} + h^{n-1}_{i,j,k})\cdot(A^{n-1}_{H\,i,j+1,k} + A^{n-1}_{H\,i,j,k})$$

$$+(h^{n-1}_{i-1,j+1,k} + h^{n-1}_{i-1,j,k})\cdot(A^{n-1}_{H\,i-1,j+1,k} + A^{n-1}_{H\,i-1,j,k}))$$

$$\times(v^{n-1}_{i,j+½,k} - v^{n-1}_{i-1,j+½,k}))$$

$$+\frac{1}{(\Delta y)^2}(h^{n-1}_{i,j+1,k}A^{n-1}_{H\,i,j+1,k}(v^{n-1}_{i,j+3/2,k} - v^{n-1}_{i,j+½,k})$$

$$-h^{n-1}_{i,j,k}A^{n-1}_{H\,i,j,k}(v^{n-1}_{i,j+½,k} - v^{n-1}_{i,j-½,k}))\quad . \tag{D.8}$$

For the salt transport equation (eq. 4.43), the finite-difference expressions for the advection and horizontal diffusion terms are

$$(ADV_s)^n_{i,j,k} = \left(\frac{\partial(uhs)_k}{\partial x} + \frac{\partial(vhs)_k}{\partial y} + (ws)\Big|^{k-½}_{k+½}\right)^n_{i,j} =$$

$$+\frac{1}{2\Delta x}(u^n_{i+½,j,k}((hs)^n_{i+1,j,k} + (hs)^n_{i,j,k}) - u^n_{i-½,j,k}((hs)^n_{i,j,k} + (hs)^n_{i-1,j,k}))$$

$$+\frac{1}{2\Delta y}(v^n_{i,j+½,k}((hs)^n_{i,j+1,k} + (hs)^n_{i,j,k}) - v^n_{i,j-½,k}((hs)^n_{i,j,k} + (hs)^n_{i,j-1,k}))$$

$$+\frac{1}{2}(w^n_{i,j,k-½}(s^n_{i,j,k-1} + s^n_{i,j,k}) - w^n_{i,j,k+½}(s^n_{i,j,k} + s^n_{i,j,k+1}))\quad , \text{and} \tag{D.9}$$

$$
\begin{aligned}
(HDIFF_s)^n_{i,j,k} &= \left(\frac{\partial}{\partial x}\left(D_H h\frac{\partial s}{\partial x}\right)_k + \frac{\partial}{\partial y}\left(D_H h\frac{\partial s}{\partial y}\right)_k\right)^{n-1}_{i,j} = \\
&+ \frac{1}{4(\Delta x)^2}\left((h^{n-1}_{i+1,j,k} + h^{n-1}_{i,j,k}) \cdot (D^{n-1}_{H\,i+1,j,k} + D^{n-1}_{H\,i,j,k})\right. \\
&\times (s^{n-1}_{i+1,j,k} - s^{n-1}_{i,j,k}) \\
&- (h^{n-1}_{i,j,k} + h^{n-1}_{i-1,j,k}) \cdot (D^{n-1}_{H\,i,j,k} + D^{n-1}_{H\,i-1,j,k}) \\
&\left.\times (s^{n-1}_{i,j,k} - s^{n-1}_{i-1,j,k})\right) \\
&+ \frac{1}{4(\Delta y)^2}\left((h^{n-1}_{i,j+1,k} + h^{n-1}_{i,j,k}) \cdot (D^{n-1}_{H\,i,j+1,k} + D^{n-1}_{H\,i,j,k})\right. \\
&\times (s^{n-1}_{i,j+1,k} - s^{n-1}_{i,j,k}) \\
&- (h^{n-1}_{i,j,k} + h^{n-1}_{i,j-1,k}) \cdot (D^{n-1}_{H\,i,j,k} + D^{n-1}_{H\,i,j-1,k}) \\
&\left.\times (s^{n-1}_{i,j,k} - s^{n-1}_{i,j-1,k})\right) \quad .
\end{aligned}
\tag{D.10}
$$

Appendix E - Computation of the Vertical Eddy Coefficients

This appendix defines the discretized equations used in the model to compute the vertical distribution of the eddy viscosity (A_V) for diffusion of momentum and the eddy diffusivity (D_V) for diffusion of salt mass.

The eddy viscosity under neutral (unstratified) conditions is computed using the Prandtl mixing length formula (eq. 2.31) in the discretized form

$$\begin{aligned}(A_{V_0})^n_{i,j,k-½} = (\Lambda^2)^n_{i,j,k-½} \cdot \Bigg(\left(\frac{u^n_{i+½,j,k-1} - u^n_{i+½,j,k} + u^n_{i-½,j,k-1} - u^n_{i-½,j,k}}{h^n_{i,j,k-1} + h^n_{i,j,k}}\right)^2 \\ + \left(\frac{v^n_{i,j+½,k-1} - v^n_{i,j+½,k} + v^n_{i,j-½,k-1} - v^n_{i,j-½,k}}{h^n_{i,j,k-1} + h^n_{i,j,k}}\right)^2\Bigg)^{½} .\end{aligned} \tag{E.1}$$

The mixing length Λ is estimated at the layer interfaces for location i, j using equation 2.32. Equation E.1 is evaluated for A_{V_0} at each layer interface except at the free surface and bottom where the wind and frictional stresses are applied.[56]

To introduce the effect of stratification on the eddy viscosity, a stability function (eq. 2.27) is used:

$$A^n_{Vi,j,k-½} = (A_{V_0})^n_{i,j,k-½}(1 + \beta_1 Ri^n_{i,j,k-½})^{\alpha_1} . \tag{E.2}$$

The coefficients $\beta_1 = 10.0$ and $\alpha_1 = -0.5$ were used by Munk and Anderson (1948); these coefficients are variables in the model and can be adjusted for best fit of the available data. The Richardson number R_i is discretized from equation 2.28 as

$$\begin{aligned}Ri_{i,j,k-½} = \frac{-g}{(\rho^n_{i,j,k-1} + \rho^n_{i,j,k})/2} \cdot \frac{(\rho^n_{i,j,k-1} - \rho^n_{i,j,k})}{(h^n_{i,j,k-1} + h^n_{i,j,k})/2} \\ \times \Bigg(\left(\frac{u^n_{i+½,j,k-1} - u^n_{i+½,j,k} + u^n_{i-½,j,k-1} - u^n_{i-½,j,k}}{h^n_{i,j,k-1} + h^n_{i,j,k}}\right)^2 \\ + \left(\frac{v^n_{i,j+½,k-1} - v^n_{i,j+½,k} + v^n_{i,j-½,k-1} - v^n_{i,j-½,k}}{h^n_{i,j,k-1} + h^n_{i,j,k}}\right)^2\Bigg)^{-1} .\end{aligned} \tag{E.3}$$

[56]For conditions where a wind stress generates significant wave action on the free surface, the magnitude of the eddy viscosity may be larger than estimated by equation E.1 because of the turbulence associated with oscillatory water motions. In those cases a wind-wave component, as mentioned in section 2.3.1.1, should be included in the model.

Because the eddy viscosities are needed in the momentum equations at the layer interfaces lying vertically between the *u*- and *v*-points, these are determined by horizontal interpolation as follows:

$$A^n_{V i+½, j, k-½} = \frac{1}{2}(A^n_{V i, j, k-½} + A^n_{V i+1, j, k-½})$$

$$A^n_{V i, j+½, k-½} = \frac{1}{2}(A^n_{V i, j, k-½} + A^n_{V i, j+1, k-½})\,.$$

To avoid model instabilities, the eddy viscosity within the interior of the water column is not permitted to take a value below some preassigned minimum, usually about 1 cm^2/s.

The eddy diffusivity is computed from equation 2.36 as

$$D^n_{V i, j, k-½} = (A_{V_0})^n_{i, j, k-½}(1 + \beta_2 Ri^n_{i, j, k-½})^{\alpha_2}. \tag{E.4}$$

The Munk-Anderson coefficients in this case are $\beta_2 = 3.33$ and $\alpha_2 = -1.5$.